THE MAGNETOCALORIC AND ELASTOCALORIC EFFECTS IN MAGNETIC SHAPE MEMORY ALLOYS

A Dissertation

by

NICKOLAUS MARK BRUNO

Submitted to the Office of Graduate and Professional Studies of
Texas A&M University
in partial fulfillment of the requirements for the degree of

DOCTOR OF PHILOSOPHY

Chair of Committee,	Ibrahim Karaman
Committee Members,	Joseph H. Ross, Jr.
	Raymundo Arroyave
	Karl T. Hartwig
Head of Department,	Andreas A. Polycarpou

August 2015

Major Subject: Mechanical Engineering

ABSTRACT

The present work focuses on the microstructural and magneto-thermo-mechanical characterization of off-stoichiometric meta-magnetic shape memory alloys (MMSMAs) with the aim of identifying key material parameters to optimize their giant magneto- (MCE) and elastocaloric (ECE) effects. Several alloy compositions of NiFeGa, Ni(Co)MnIn, and Ni(Co)MnSn have been studied to quantify their solid state energy conversion performance, in particular the conversion of magnetic and mechanical energy into thermal energy, and to reveal how this performance is influenced by microstructural features tailored using carefully selected heat treatments. To identify how heat treatments influence the energy conversion performance of the selected alloys, a previously established thermodynamic framework, which defines the refrigerant capacity (RC) of non-shape memory alloys (SMAs), was employed with the thermodynamic relations describing first order martensitic phase transitions.

Applying the RC framework to MMSMAs demonstrated that most of the key materials parameters relating to the martensitic transition can be combined to predict the magnetic field, or mechanical stress, needed to complete the transformation across a specific operating temperature range; reducing these driving force requirements was the primary focus of the experimental part of this work. Magnetometry, calorimetry, and specialized compression tests were performed on the heat treated SMAs.

An experimental apparatus, called the magneto-thermo-mechanical characterization (MaTMeCh) device, was designed, constructed, and implemented to

reduce the magnetic field requirements needed for a complete field-induced martensitic transformation by simultaneous application of external stress and magnetic field. This device allows simultaneous control of temperature, magnetic field, and stress while measuring magnetization, strain, stress, and temperature. With the MaTMeCh device, uniaxial compressive stresses up to 200MPa, magnetic fields up to 9T, and temperatures between -100°C and 80°C can be applied to a compression specimen. Using the MaTMeCh device, cyclic stress-assisted magnetic field induced transitions demonstrated the full thermal energy conversion capabilities of cost effective meta-magnetic shape memory alloys.

Prior to magneto-thermo-mechanical characterization, numerous SMA compositions were fabricated and heat treated to promote grain growth and a specific degree of long range crystallographic order. Studies, herein, indicated that minimizing the microstructural grain constraint, by producing a large grain size to thickness (GS/t) ratio in polycrystalline SMA ribbons, ultimately reduced the magnetic field levels needed to completely harness the SMA's magnetocaloric effect. Additionally, B2 crystallographic ordering in NiCoMnIn single crystals was found to offer a more efficient magnetic to thermal energy conversion efficiency than the typical $L2_1$ ordered alloys. Larger caloric effects were measured in the alloys exhibiting a higher martensitic transformation temperature, i.e. the B2 ordered alloys. As such, B2 ordered single crystals were characterized with the MaTMeCh device, thus lending the ability to measure their maximal magnetocaloric performance.

DEDICATION

To all first generation college students.

“Every artist was first an amateur.” – Ralph Waldo Emerson

ACKNOWLEDGEMENTS

First of all, I would like to express my sincere thanks and deepest gratitude to my advisor, mentor, and friend, Professor Ibrahim Karaman. Without his support, none of this work would have been a success. Not only did Prof. Karaman serve as my academic mentor, but he also took an interest in my personal life and was understanding at times when others were not. He always keeps his students' interests and futures at heart and values both academic achievement and family. For these reasons, I am forever grateful and indebted to him.

Additionally, my project would not have been a success without the guidance of my doctoral committee including Prof. Joseph H. Ross, Prof. Raymundo Arroyave, and Prof. Ted Hartwig. I would like to thank each of them for their "open door policies" and their fruitful suggestions related to my research in shape memory alloys. I learned a great deal about physics, materials science, and engineering from each of them and spent many long nights in Prof. Ross's lab. I would like to thank him for giving me the opportunity to perform research in his lab with his equipment. Also, Prof. Ross played a role in awarding me with the NSF I.G.E.R.T. fellowship at the beginning of my tenure at Texas A&M, and therefore, he deserves a special thanks. Thank you all for your guidance and support during my doctoral career.

I would also like to thank other faculty at Texas A&M, who assisted me in some way during my doctoral program. Drs. Patrick Shamberger, Ray Guillemette, Dimitris Lagoudas, and Anup Bandyopadhyay all assisted me with performing experiments and

offered me advice in their areas of expertise. I will never forget their willingness to help nor their support.

My doctoral project was not only successful as a result of Texas A&M faculty, but also those with whom I keep contact from my past. My graduate advisors at Northern Arizona University, Prof. Constantin Ciocanel, who introduced me to shape memory alloys, and Prof. Heidi Feigenbaum were always willing to offer their advice and help on any of my difficult problems. I would like to thank them both for their willingness to help and their support during my doctoral career. Similarly, I would like to thank Prof. Yuriy I. Chumlykov from the Siberian Physical Technical Institute who visited our lab on many occasions and brainstormed with me. I learned a great deal from our discussions.

Many others are in need of thanks who played indirect roles in assisting me throughout my doctoral program. Robert Barber, Brent McMillan at Mechatronic Techniques, Holley Toschlog, Jan Gerston (my fellow Lumberjack), and my advisor from many years ago, Jeffrey Cotta, who taught me the art of engineering and design, I would like to thank each of you from the bottom of my heart.

Finally, I extend my gratitude to my backbone and most influential supporters, my family. Deep thanks goes out to my wife and daughter for their patience with me during my graduate career, in addition to my mother, father, brother, and sister. Thank you all for the mental and emotional support during my graduate career, without it, I would not have been able to finish. Last, but not least, I would like to thank my research family, the MESAM group, and the National Science Foundation (Grant No. 1108396). Many students have come and gone since I began with the MESAM group in 2011. Some, I am

still in contact with and, therefore, I would like to thank Drs. James Monroe, Krishnendu Haldar, Ebubekir Dogan, Alper Evirgen, Li-Wei Tseng, Shujuan Wang, Ji Ma, Liangfa Hu, Can Atli, Baris Emre, Suheyla Yuce, Yugin Huang, Jing-Han Chen, as well as Nick Barta, Hande Ozcan, Brian Franco, Sarah Yager, Ceylan Hayrettin, Ankush Kothalkar, Pavel Lapa, Taymaz Jozaghi, Dominic Gehring, John Harvey and all those who I have forgotten to list. I learned a great deal from our discussions and group presentations and am forever thankful for the opportunity to have had worked and spending the valuable years of my doctoral program with you.

NOMENCLATURE

A	Austenite
M	Martensite
$M \rightarrow A$	Martensite to Austenite transformation
$A \rightarrow M$	Austenite to Martensite transformation
$\mathbf{y}_i$	Generalized driving force
P	Pressure
T	Temperature
T_0	Thermodynamic equilibrium temperature
σ	Uniaxial stress
σ_{cr}	Critical uniaxial stress
σ_{tr}	Transformation stress hardening
σ_{req}	Required uniaxial stress to initiate $A \rightarrow M$
σ_{comp}^{iso}	Uniaxial stress needed to complete an isothermal $A \rightarrow M$
σ_{comp}^{ad}	Uniaxial stress needed to complete an adiabatic $A \rightarrow M$
H	Magnetic field
H_{cr}	Critical magnetic field
H_{req}	Required magnetic field to initiate $M \rightarrow A$
H_{comp}^{iso}	Magnetic field needed to complete an isothermal $M \rightarrow A$

H_{comp}^{ad}	Magnetic field needed to complete an adiabatic $M \rightarrow A$
$\mathbf{X}_i$	Generalized displacement; conjugate to $\mathbf{y}_i$
M	Magnetization
ε	Uniaxial strain
ε_{el}	Elastic uniaxial strain
ε_{tr}	Uniaxial transformation strain
V	Volume
V_0	Molar volume
S	Entropy
S_{irr}	Entropy production from irreversible processes
ξ	Transformation fraction
ρ	Mass density
C_p	Specific heat capacity
U	Internal energy
G	Gibbs free energy
Ψ	Helmholtz free energy
ΔG^{A-M}	Difference in total free energy between A and M
$\Delta G_{ch}^{A\rightarrow M}$	Chemical free energy difference between A and M
$\Delta E_{mech}^{A\rightarrow M}$	Mechanical free energy difference between A and M
$\Delta G_{el}^{A\rightarrow M}$	Elastic free energy difference between A and M

ΔE_{irr}	Irreversible free energy barrier due to dissipation
$\Delta G_{mag}^{A\to M}$	Magnetic Zeeman energy
$\Delta G_{MAE}^{A\to M}$	Magnetocrystalline anisotropy energy
δQ	Work on control volume provided by heat
δW	Work on control volume that influences volume
$\delta W'$	Work on control volume that does not influence volume
W	Work
Q_l	Work loss on control volume through heat leaks
Q_f	Frictional work
ΔS	Isothermal entropy change
M_f	Martensite finish temperature
M_s	Martensite start temperature
A_s	Austenite start temperature
A_f	Austenite finish temperature
ΔT_{ad}	Adiabatic temperature change
ΔT_{elas}	Thermal transition range
ΔT_{hys}	Thermal hysteresis
$\mathbf{D}$	Demagnetizing factor
f	Hall sensor calibration factor
μ_0	Permeability of free space

RC	Refrigerant capacity
RC^{latent}	Refrigerant capacity from latent heat
RCP	Relative cooling power
T_{work}	Maximum thermal work
η	Energy conversion efficiency ratio
η^{latent}	Energy conversion efficiency ratio from latent heat
E	Magnetostatic energy density
α	Diffusion coefficient
Δf_0	Local change in free energy
ν	Order parameter
τ	Mobility coefficient

TABLE OF CONTENTS

Page

LIST OF TABLES

Page

LIST OF FIGURES

Page

CHAPTER I

INTRODUCTION*

1.1 Motivation

Meta-magnetic shape memory alloys (MMSMAs) are one of the next generation of active materials owing to their unique magneto-thermo-mechanical energy couplings. They exhibit large magnetic field driven deformations as a result of a solid to solid structural phase transition and their functionalities are useful in sensing, magneto-resistance, refrigeration, and/or actuation. Recent discoveries have shown that these materials exhibit large magnetocaloric effects and can yield cooling capabilities comparable to existing state of the art calorific materials. While MMSMAs exhibit great promise for caloric applications, their implementation is hindered by the large magnetic fields needed to drive the martensitic transformation. It is believed, however, that this limitation can be overcome with the use of mechanical stress and a deeper understanding of the physical mechanisms that drive their solid-to-solid phase transformations.

Here, a clear distinction between the types of caloric effects is made, followed by a discussion of analysis techniques used for characterizing the refrigeration performance of solid calorific materials. Experimental apparatuses and characterization techniques are

---

*Part of the following material is reprinted with permission from Titov, I. *et al.* Hysteresis effects in the inverse magnetocaloric effect in martensitic Ni-Mn-In and Ni-Mn-Sn. *Journal of Applied Physics* **112**, (2012) 073914. Copyright (2012), AIP Publishing LLC.

Part of the following material is reprinted with permission from Macmillan Publishers Ltd: *Nature Materials*. Liu, J. *et al.* Giant magnetocaloric effect driven by structural transitions. *Nature Materials* **11**, (2012) 620. Copyright (2012).

proposed and implemented to probe the influence of thermomechanical processing on MMSMA's energy conversion capabilities. Finally, a magneto-thermo-mechanical characterization apparatus is designed, built, and implemented to measure the influence of mechanical load on the giant magnetocaloric effect.

1.2 A brief history of refrigeration

1.2.1 Solid-state refrigeration

Since the 19th century, refrigeration devices have been studied, commercialized, and optimized. In recent years there has been a shift in interest from typical liquid vapor-compression type refrigerators to those that use a solid compound as the working medium. The solid-state refrigerant can be driven by either a magnetic, mechanical, or electric field. First measured in pure nickel by Weiss and Piccard [1, 2], the magnetic field induced temperature change, or magnetocaloric effect (MCE), offered a cooling mechanism whereby no moving parts or synthetically derived liquids were needed to produce heat flow. Rather, the MCE was achieved by simply applying or removing a magnetic field to some solid magnetic material.

Following Weiss's original work, for approximately 10 years the MCE was not studied, only to be rediscovered around 1926 concurrently by Debye and Giauque [3, 4]. Between 1926 and the early 1970s, only a few magnetocaloric refrigeration devices were built. The scientific community seriously began investigating the MCE around 1973 after the discovery of ozone depletion from synthetic refrigerants containing chlorofluorocarbons (CFCs) [5]. This discovery prompted the Montreal Protocol

organized by the United Nations (UN), which then resulted in several meetings, e.g. the Earth Summit of 1992, aimed at promoting environmentally sustainable technology in countries around the world [6]. CFCs were banned in UN participating countries and their phase-out was set to begin in 1991. As an immediate, but unsustainable solution, CFCs were chemically bonded with hydrogen, resulting in substances known as hydro-chlorofluorocarbons (HCFCs). These do not decompose the ozone, but instead linger in the lower atmosphere and act as greenhouse gases. As shown in the timeline and inset in Figure 1-1, the phase-out of CFCs and HCFCs was followed by an increased interest in the MCE in the scientific community. This was partially due to the fact that environmentally harmful refrigerants were no longer available and a replacement technology was needed. One promising replacement to vapor-compression type refrigerators is solid-state refrigeration driven by the magnetocaloric effect. In fact, very large magnetocaloric effects can be measured in magnetic materials exhibiting a reversible first-order phase transformation (FOPT) as discussed in the next section.

1.2.2 The giant magnetocaloric and elastocaloric effect

In 1997, Gschneidner et al. demonstrated the potential of the giant MCE in a FOPT material, $Gd_5(Si_xGe_{1-x})_4$ [7, 8]. They showed that this alloy was capable of producing thermal energy transfer of about 2J/g across a wide temperature range (~40K). The MCE capability observed in $Gd_5(Si_xGe_{1-x})_4$ was caused by a first order magnetic field induced structural phase transformation. The alloy was also shown to exhibit a temperature change of 7K under the application of 2T [8]. Conveniently, these temperature changes were

achieved near room temperature. When the capabilities of $Gd_5(Si_xGe_{1-x})_4$ were compared to those obtained around the magnetic Curie point of conventional second-order ferromagnetic refrigerants, it was clear that the concurrent structural and magnetic transitions resulted in a "giant MCE". In literature, this term is used to distinguish between second order (magnetocaloric) and first order (giant-magnetocaloric) effects.

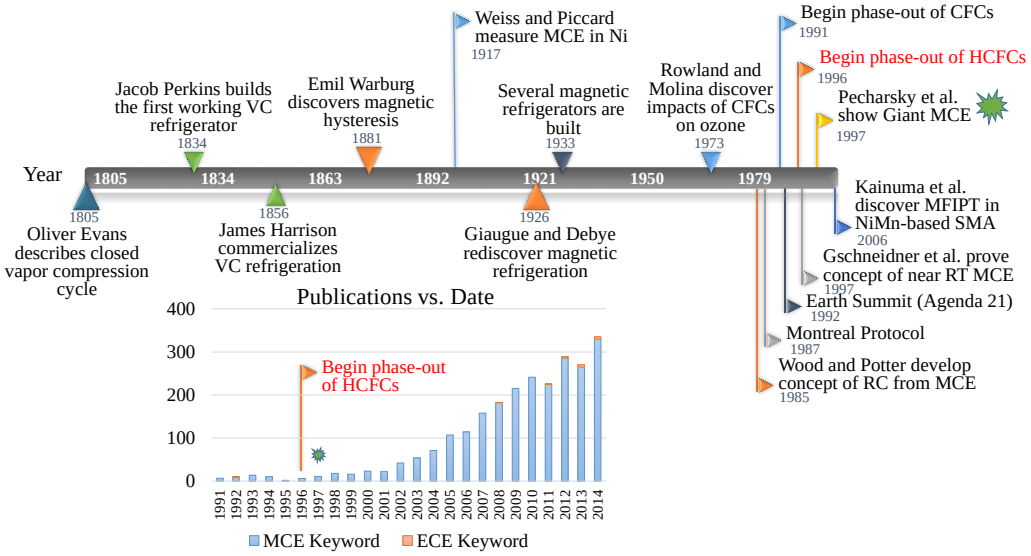

Figure 1-1: A timeline of refrigeration technology and significant events that have affected its evolution. The bottom inset shows the number of publications containing the keyword "magnetocaloric" (blue) and "elastocaloric" (orange) in the title per year since 1991 [3-9, 11, 12] determined using webofscience.com.

As shown in Figure 1-1, shortly after the phase-out of conventional CFCs, the popularity of the MCE blossomed in the scientific community. Since then, new cost effective magnetic FOPT materials, such as NiMn-based meta-magnetic shape memory alloys (MMSMAs), were discovered [9]. These materials were shown to exhibit similar

caloric effects by applying a mechanical load, i.e. the elastocaloric effect. The structural transformation induced by applying a mechanical load generates a giant elastocaloric effect (ECE) [10]. It is believed that these novel MMSMAs may offer additional benefits over the archetype $Gd_5(Si_xGe_{1-x})_4$ alloy for solid-state cooling by combining the driving mechanisms for ECE and MCE and, therefore, further scientific investigations on their physical behaviors are needed.

1.3 Thermodynamics of shape memory alloys

The following section describes the thermodynamic behavior of shape memory alloys so that physical relations can be developed describing their behavior. These relations are then employed to quantify the solid-state refrigeration performance from first order martensitic transformations observed in SMAs. As mentioned above, Gd is a popular non-SMA magnetocaloric refrigerant, but when comparing the physical mechanisms driving the magnetocaloric effect in Gd to those of shape memory alloys, the two effects cannot be explained with the same physics. Therefore, the thermodynamics of first order phase transformations are described in detail, below, and are later employed to describe the caloric effects in shape memory alloys.

1.3.1 The shape memory effect

The thermoelastic martensitic transformations in shape memory alloys (SMAs) were first discovered by Chang and Read [13] in an Au-Cd alloy. Further investigations lead to the discovery of the Ti-Ni SMA [14] and shortly after, the shape memory effect

(SME) became a widely recognized and studied phenomenon. The SME can be described by a basic illustration shown in Fig. 1-2.

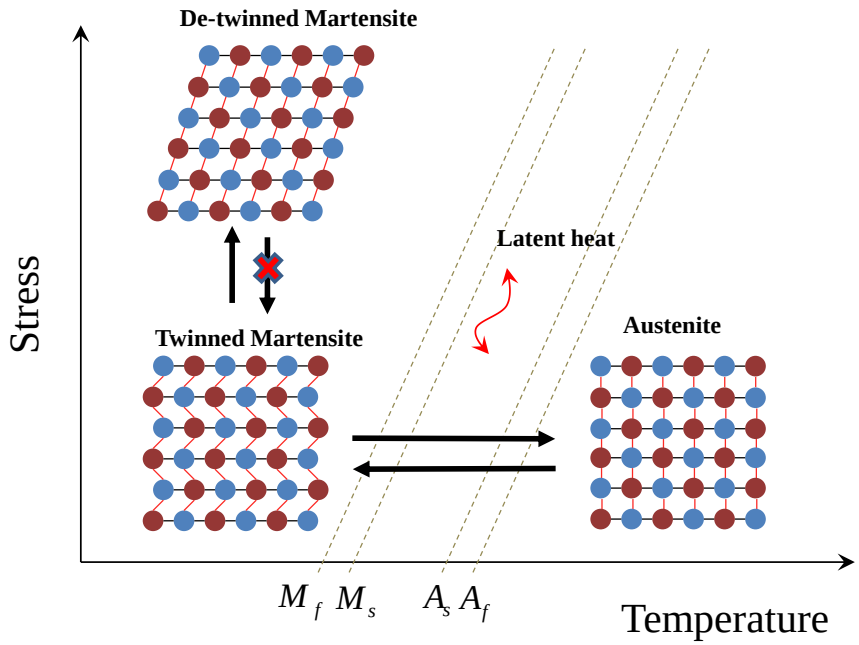

Figure 1-2: The shape memory effect (SME) is illustrated on a stress-temperature phase diagram.

Above a temperature known as the austenite finish temperature, A_f, the SMA is characterized by an austenite (A) phase. In Fig.1-2, circles represent crystal lattice sites. On cooling from A, as shown by a black arrow, the SMA begins to transform from the cubic A to a non-cubic twinned martensite (M) at the martensite start, M_s, temperature and completes the transformation at the martensite finish, M_f, temperature. The martensite that forms on cooling, nearly occupies the sample volume in such a way that

the strain energy associated with the transition is minimized; this is referred to as self-accommodation. When applying a mechanical load to self-accommodated martensite, martensitic variants reconfigure to their stress-preferred orientation giving rise to large "de-twinning" strain. Upon removing the mechanical load, the now de-twinned M does not return to its self-accommodated state. However, heating the SMA above the austenite start, A_s, temperature results in a transformation between the de-twinned martensite to austenite. Upon reaching the A_f temperature, the original shape of the material is recovered, thus the alloy is capable of 'remembering' its original austenitic shape.

The A to M transition in SMAs is commonly referred to as the forward martensitic transformation (MT) and the M to A, the reverse MT. Shape memory alloys are capable of very large recoverable strains under a bias mechanical load, and therefore, are typically well suited for actuation [15]. Here, however, the martensitic transitions are studied for their thermal properties. As shown in Fig. 1-2, a latent heat is generated from the structural transition between M and A phases. This latent heat is an indication of the amount of energy needed for the martensitic phase transformation to occur and is specific to first order transitions, whereby a change in lattice symmetry occurs. As shown in Fig. 1-2, austenite is depicted as cubic with many planes of symmetry; martensite exhibits fewer symmetry planes.

To better understand the thermodynamics of MTs, in Fig. 1-3a the free energies of the A and M phases are plotted as a function of temperature. Below some equilibrium temperature, T_0, the free energy of the M phase is lower than that of the A phase, thus, in

the ideal situation, the SMA transforms to M. Above T_0, the A phase exhibits the lowest free energy. In the figure, the minimal free energy is depicted by a dash-dot-dot line. Here, we probe at the thermodynamics of the martensitic transition, and therefore, we must fully understand the energetic contributions to the free energy, G, in Fig. 1-3a. To quantify G in the SMA illustrated in Fig. 1-3a, the internal energy must first be considered.

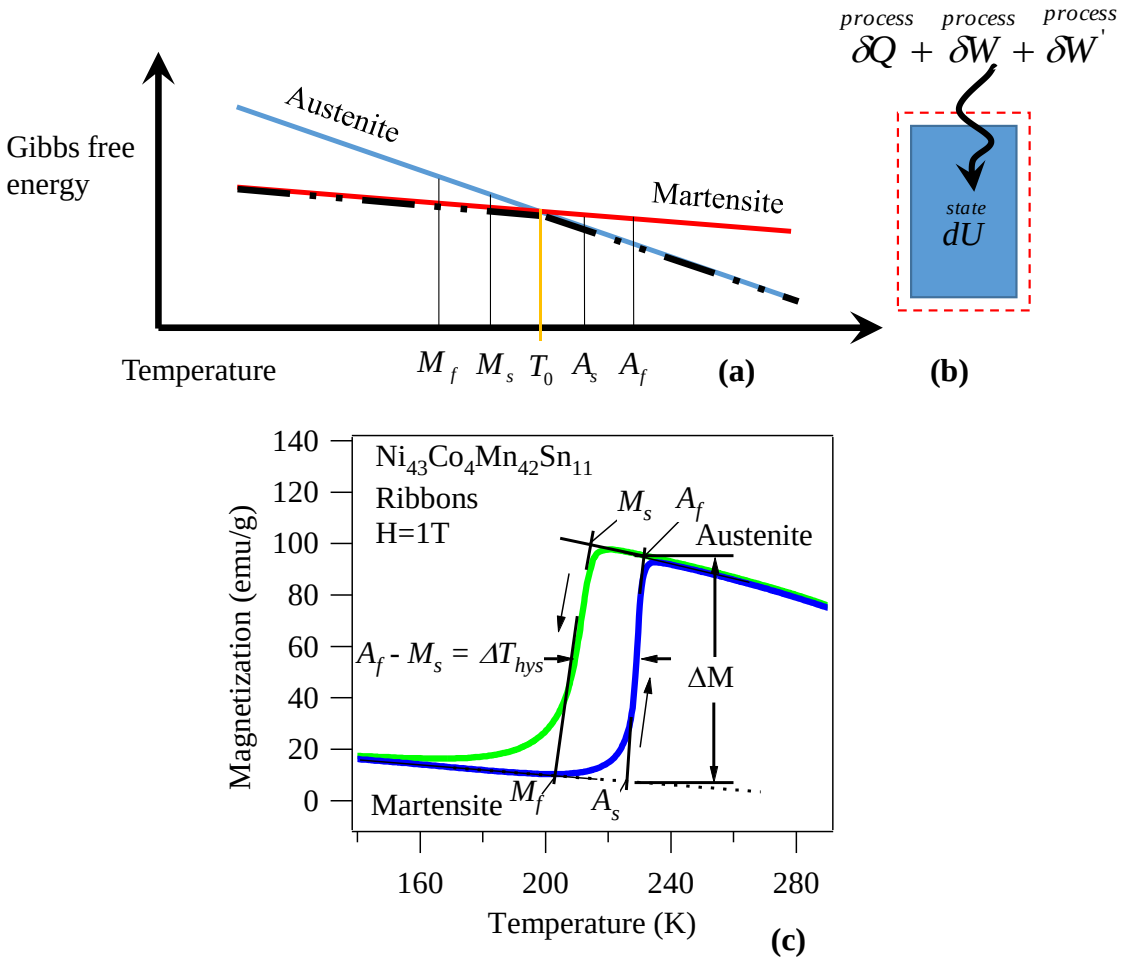

Figure 1-3: (a) The Gibbs free energy as a function of temperature across the thermoelastic martensitic transformation, (b) the MMSMA control volume, and (c) the measured thermomagnetization curve under 1T across the martensitic transformation in $Ni_{43}Co_4Mn_{42}Sn_{11}$ meta-magnetic shape memory alloy.

Consider the control volume of the SMA in Fig. 1-3b as shown by the dashed rectangle. The energy inside the control volume, U, is be defined as [16]

$$U = u(\varepsilon, S, M, V) \tag{1.1}$$

where U is a function of extensive properties (those depending on the size of the control volume) including strain, ε, entropy, S, magnetization, M, and volume, V. Any change of the extensive properties in the control volume in turn generates a change in internal energy, dU, as defined by

$$dU = \delta Q + \delta W + \delta W'. \tag{1.2}$$

In Eqn. (1.2), the change in internal energy is constrained by the first law of thermodynamics, i.e. conservation of energy, and is the sum of heat and work applied to the system through the control volume boundary. The amount of thermal energy transferred across the boundary is defined as

$$\delta Q = TdS \tag{1.3}$$

where $\delta Q = TdS$ is temperature and dS is the resulting entropy change. The internal energy can also be influenced by pressure-work applied to the control volume boundary. This pressure-work changes the volume, V, and is therefore defined as

$$\delta W = -PdV \tag{1.4}$$

where P is hydrostatic pressure and δW is negative due to convention. The negative in Eqn. (1.4) indicates that increasing the volume dilutes the internal energy. All other work terms that do not influence the volume (isochoric work terms), are represented by the $\delta W'$

term in Eqn. 1.2. In general, when including elastic and magnetic energies that don't substantially influence volume, the change in internal energy of a SMA can be expressed as

$$dU = TdS - PdV + HdM + V_0 \sigma d\varepsilon. \tag{1.5}$$

where H is magnetic field, σ is uniaxial stress, and V_0 is the molar volume.

To then quantify the Gibbs free energy, G, represented by martensite and austenite solid curves in Fig. 1-3a, a Legendre transform is applied to the internal energy in Eqn. (1.1), denoted as

$$G = U + PV - ST - MH - V_0 \sigma\varepsilon. \tag{1.6}$$

As such, G is the difference in enthalpy ($U + PV$) and the isochoric work. As shown in Fig. 1-3a, the thermoelastic martensitic transformation occurs when the M and A phases exhibit the same free energy, i.e.

$$G^A - G^M = 0 = \Delta G^{A-M} \tag{1.7}$$

where superscripts indicate the free energy of A and M phases and ΔG^{A-M} is the difference in the free energy curves. The temperature T_0, in Fig. 1-3a, is said to be a point of thermodynamic equilibrium. However, martensitic transformations in SMAs exhibit dissipation through defect generation and microstructurally stored elastic energy that needs to be overcome to trigger the transformation, thus undercooling and overheating are needed to initiate and complete the martensitic transition; this is illustrated by the transformation temperatures on either side of T_0.

As mentioned above, the SMA only transforms above and below specific transformation temperatures defined as, A_f, A_s, M_s, and M_f. These temperatures are illustrated in Fig. 1-3c above and below T_0, and indicate the amount of isochoric work needed to initiate or complete the transformation. In other words, the transformation temperatures deviate from the ideal thermodynamic equilibrium point, T_0, as a result of microstructurally stored elastic energy [15] and microstructural dissipation [15]. The magnitude of the dissipation is typically indicated by $A_f - M_s$ and is known as thermal hysteresis, ΔT_{hys}, illustrated in Fig. 1-3c.

As shown by Eqn. (1.6), G is a function of isochoric work applied to the SMA, thus $\Delta G^{A\to M}$ (Eqn. 1.7) is also a function of this work. Eqn. (1.8) quantifies the influence of the applied work terms and energy barriers that drive the martensitic transformation. The driving force quantified by Eqn. (1.8), below, must be equal to or less than zero to trigger the martensitic transition. Above and below T_0, this driving force can be defined as [17, 18]

$$\begin{aligned}\Delta G^{A\to M} &= \overbrace{-\Delta G_{ch}^{A\to M}}^{1}\overbrace{-\Delta E_{mech}^{A\to M}}^{2}\overbrace{+\Delta G_{el}^{A\to M}}^{3}\overbrace{+\Delta E_{irr}}^{4}\overbrace{+\Delta G_{mag}^{A\to M}}^{5}\overbrace{-\Delta G_{MAE}^{A\to M}}^{6} \quad T > T_0 \\ \Delta G^{M\to A} &= +\Delta G_{ch}^{M\to A} + \Delta E_{mech}^{M\to A} - \Delta G_{el}^{M\to A} + \Delta E_{irr} - \Delta G_{mag}^{M\to A} + \Delta G_{MAE}^{M\to A} \quad T < T_0 .\end{aligned} \tag{1.8}$$

In Eqn. (1.8), the first term on the right side of the equation is the difference in chemical free energy above and below T_0, the second is the mechanical contribution from externally applied forces, the third represents a combination of internal elastic energy stored across martensite plate boundaries and elastic deformations, the fourth represents

the irreversible energy dissipation generated through dislocations and microstructural defects, the fifth represents magnetic Zeeman energy, and the sixth, the magneto-crystalline anisotropy energy. Terms 5 and 6 are only applied to some magnetic shape memory alloys, as discussed later.

The ideal thermoelastic martensitic transition occurs at T_0 when $\Delta G_{ch}^{A\to M} = 0$. This can be seen by removing terms 2 through 6 in Eqn. (1.8). The $-\Delta G_{ch}^{A\to M}$ on the forward MT (top expression) indicates the A to M transition is exothermic and releases heat. On the other hand, the M to A transition absorbs energy as shown by the $+\Delta G_{ch}^{M\to A}$. Thus, the latent heat of the M to A transition causes the SMA to cool, and can be utilized in refrigeration processes.

1.3.2 Superelasticity

The sign of some of the terms in Eqn. (1.8) depend on whether the SMA starts in austenite or martensite. When in austenite, the second term is negative which implies that applying a mechanical force will decrease the free energy difference between the A and M phases. Upon applying sufficient mechanical load, $\Delta G^{A\to M}$ will eventually be driven to zero and the transformation from A to M will proceed at a temperature above T_0. This is known as a stress-induced martensitic transformation. Figure 1-4a depicts the relative changes in the Gibbs free energy when a mechanical load is applied and Fig. 1-4b, a superelastic stress-strain curve representative of the mechanical response across a stress-induced martensitic transition.

In practice, applying a mechanical load to austenite results in increasing T_0. Eventually, T_0 will equal the superelastic test temperature, T and the A to M transformation will occur. As discussed in subsequent sections, driving the martensitic

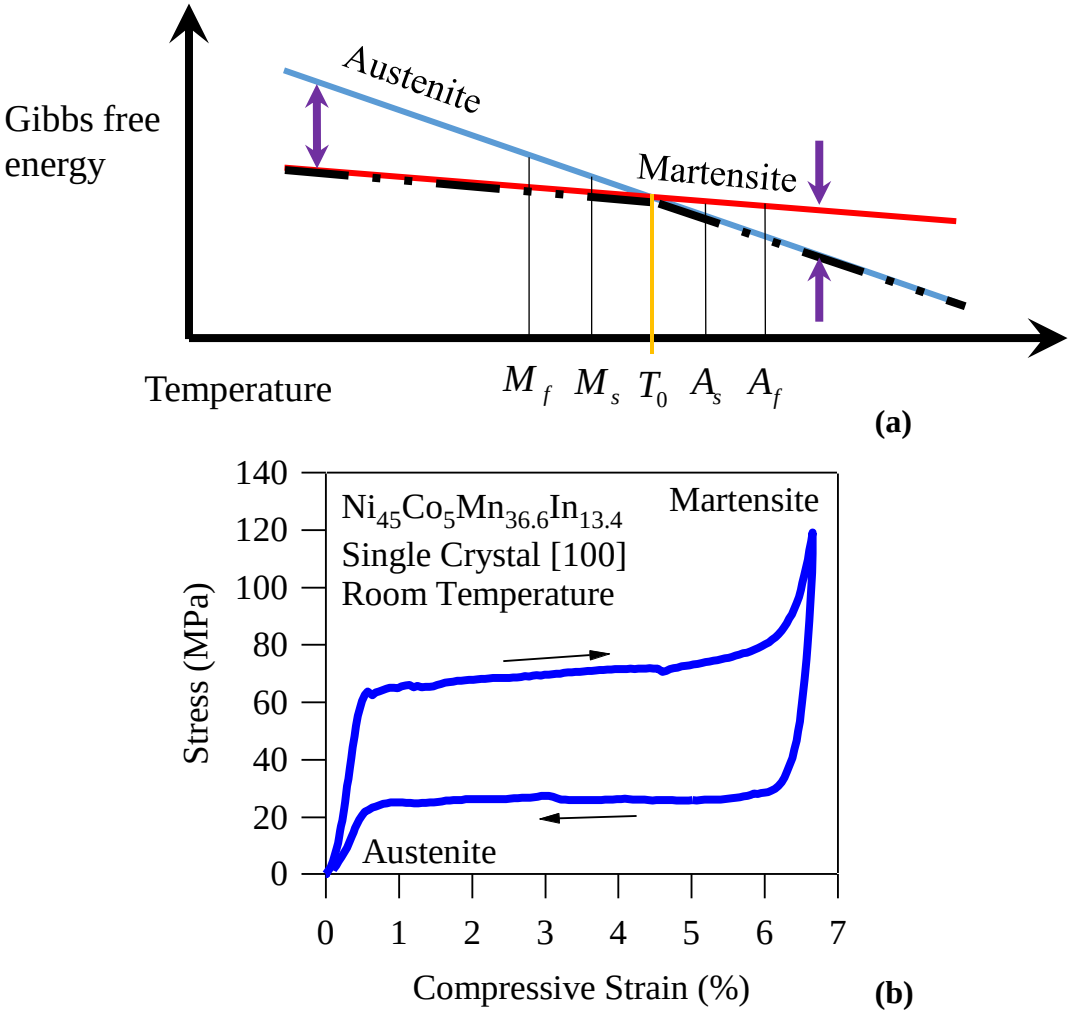

Figure 1-4: (a) The Gibbs free energy as a function of temperature for superelasticity. Upon increasing the mechanical load, the free energy difference between austenite and martensite decreases above T_0, and (b) the measured stress-strain compressive response of NiCoMnIn [001] single crystals.

transition with mechanical load can be used in solid-state refrigeration applications. It is important to note, however, cooling will only be achieved by mechanically unloading the SMA from the stress-induced martensite to austenite (M to A) phase above T_0. Heating is generated by applying the load and triggering the A to M transition.

1.3.3 Magnetic field induced transformation

Like stress-induced martensitic transformations, a magnetic field induced transformation (MFIT) in some meta-magnetic SMAs (MMSMAs) can be achieved. For this to occur, the M and A phases must exhibit a large difference in saturation magnetization. The high temperature austenite phase can be ferromagnetic when the martensite phase is non-magnetic. In other less common MMSMAs, the austenite phase is non-magnetic and martensite is ferromagnetic.

The Zeeman energy (ZE), related to term 5 in Eqn. (1.8), is defined by $G_{mag} = \int_V M \cdot H_{applied} dV$, where M is magnetization and $H_{applied}$ is an applied magnetic field [20]. In ferromagnetic materials, the magnetization saturates with small $H_{applied}$. Term 5 is then the difference between the M and A Zeeman energies and can be approximated by $\Delta G_{mag}^{A \to M} = \left(M_{austenite}^{sat} - M_{martensite}^{sat} \right) \cdot H_{applied}$ where M^{sat} is the saturation magnetization of the respective phase. This approximation assumes that both austenite and martensite phases magnetically saturate under small fields [18].

When austenite is ferromagnetic, the MFIT occurs from martensite to austenite rather than austenite to martensite as shown for superelastic loading. Fig. 1-5(a) depicts the relative shifts in Gibbs free energy when applying a magnetic field to MMSMAs in

which the high temperature austenite phase exhibits ferromagnetism as shown in Fig.1-5(b). This is observed in NiMn-based MMSMAs. Here, the magnetic field is applied to martensite. Eventually, the MFIT occurs as shown by an increasing magnetization around 30kOe up to the saturation level of the austenite phase. On releasing the field, the MMSMA transforms back to M at temperatures below M_f. On the other hand, if the martensite phase is ferromagnetic, like in some CoMnGe [21], GdSiGe [7], and FeMnGa [22] alloys, the situation is reversed and the magnetic field induced structural phase transition is driven from austenite to martensite.

Per Eqn. (1.6), applying a magnetic field to a MMSMA will result in a decrease in the Gibbs free energy of each independent phase. The decrease in G of the martensite and austenite phases occur at different rates due to the difference in saturation magnetization of each phase. Upon decreasing at different rates, $\Delta G^{M \to A}$ also decreases at temperatures below T_0 depicted by solid arrows in 1-5a. These arrows are in in different directions when compared to the stress-induced martensitic transformations discussed earlier. Eventually, the difference in free energy is driven to zero and the martensite to austenite phase transformation occurs.

All of the above discussions relate to martensitic transformations induced by a magnetic field or mechanical load. Here, it is important to note that martensitic solid-to-solid transformations imply a change in crystal symmetry, as depicted in Fig. 1-1, and as a result, the expression for the minimum Gibbs free energy is discontinuous. This is illustrated at T_0 in Figs. 1-3, 1-4, and 1-5 as a thick dash-dot-dot line. The discontinuity in Gibbs free energy is referred to as a "cusp" or a singularity. In accordance with the laws

of calculus, G is not differentiable at T_0. The consequence of this, regarding the caloric effects, are thoroughly discussed in the next section.

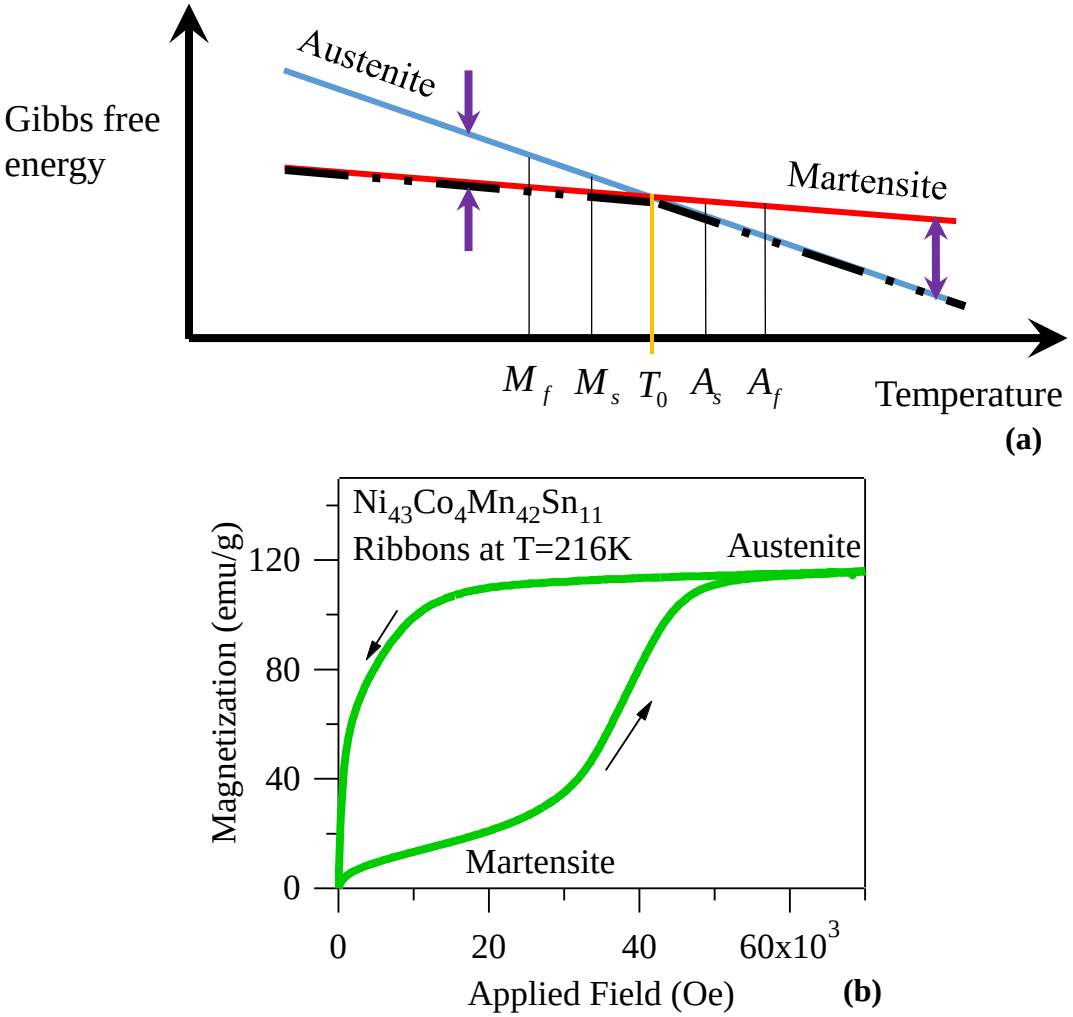

Figure 1-5: (a) The Gibbs free energy of meta-magnetic shape memory alloys during a magnetic field induced transformation (MFIT), and (b) a magnetic field induced transformation in $Ni_{43}Co_4Mn_{42}Sn_{11}$ meta-magnetic shape memory alloy.

1.4 Thermodynamic derivation of the caloric effects

"Because man's physical senses present volume, pressure, temperature, and work, in their non-thermodynamic aspects of [occupied] space, distributed force, degree of hotness, and motion-producing effort, man naturally inclines toward a distorted view of thermodynamics" [23]. However, with careful and appropriate considerations, man's distorted view of thermodynamics can be overcome and thermodynamic ambiguity can be minimized. This section aims at making a clear distinction between second order and first order caloric effects. Both of these caloric effects can be independently observed and measured in shape memory alloys. Unfortunately, there has been much confusion over the years, in literature, on how to properly quantify the caloric effects from first order transitions. The cause of this is likely due to misinterpreting thermodynamic relations, or applying them without fully understanding the assumptions used in their derivation.

1.4.1 Conventional caloric effects in shape memory alloys

A caloric, or thermal, effect is defined by a materials entropy or temperature change in response to some stimulus. For the elastocaloric effect (ECE), this stimulus is mechanical load, and in the magnetocaloric effect (MCE) the stimulus is magnetic field. The reversible heat effect generated in a material can be caused by either a change in heat capacity or a latent heat of a structural transformation.

The internal energy of a substance changes with an applied force, such as stress, temperature, and magnetic field. These forces do not depend on the size of the control volume in Fig. 1-3 and are known as intensive variables. Since we would like to determine the caloric effects resulting from a change in internal energy, we must consider the Gibbs

free energy which is independent of volume effects. The change in internal energy as a function of extensive properties has been defined in Eqn. (1.5). To then quantify the change in the MMSMAs internal energy as a function of intensive properties, a Legendre transform must be applied to U, as shown in Eqn. (1.6). The Gibbs free energy, G, in Eqn. (1.6) is the free energy of a single phase, such as martensite or austenite, and is depicted in Figs. 1-3, 1-4, and 1-5 as a line. G is known as a functional, or a function of other functions, such as U. The change in free energy, dG, can then be derived by implicitly differentiating Eqn. (1.6), applying the product rule to the functional, and substituting Eqn. (1.5) into dU. The differential of Gibbs free energy, dG, is then defined as

$$dG = VdP - SdT - \sum_{i=1}^{n} \mathbf{X}_i d\mathbf{y}_i \tag{1.9}$$

where $\mathbf{X}_i$ are extensive material properties, such as M, or ε, and $\mathbf{y}_i$ are their thermodynamic conjugates, H, or σ, respectively. Clearly, applying $\mathbf{y}_i$ will decrease G (see Eqn. 1.6) as shown by the negative sign in Eqn. (1.9).

The entropy change defining the caloric effect can then be quantified using Eqn. (1.9). This is done by employing Maxwell relations assuming pressure and intensive forces are constant, i.e. $dP = d\mathbf{y}_i = 0$. The entropy, S, is then computed as

$$-S = \left(\frac{dG}{dT} \right)_{\{P, \mathbf{y}_{n=i}\}}. \tag{1.10}$$

The forces that are assumed constant in Eqn. (1.10) are denoted by subscripts. Similarly, other extensive properties can be solved from Eqn. (1.9) using the same approach. In this case, pressure and temperature are assumed constant. Here, $\mathbf{X}_i$ is computed as

$$-\mathbf{X}_i = \left(\frac{dG}{d\mathbf{y}_i} \right)_{\{P,T,\mathbf{y}_{n\neq i}\}} \tag{1.11}$$

where P, T, and all other $\mathbf{y}_i$ are constant intensive forces.

Next, Eqns. (1.10) and (1.11) are differentiated with respect to the other independent variable. In this case, Eqn. (1.10) is differentiated with respect to $\mathbf{y}_i$ resulting in

$$-\frac{dS}{d\mathbf{y}_i} = \frac{d}{d\mathbf{y}_i}\left(\frac{dG}{dT} \right)_{\{P,\mathbf{y}_{n\neq i}\}} \tag{1.12}$$

and Eqn. (1.11) is differentiated with respect to T, resulting in

$$-\frac{d\mathbf{X}_i}{dT} = \frac{d}{dT}\left(\frac{dG}{d\mathbf{y}_i} \right)_{\{P,T,\mathbf{y}_{n\neq i}\}} . \tag{1.13}$$

Assuming that the second partial derivative of G is smooth and continuous, Schwarz' mathematical theorem can be employed which states that partial derivatives are commutative, i.e. the order of differentiation does matter. As such, the right hand side of Eqns. (1.12) and (1.13) are identical and, therefore, the left hand sides are also mathematically equivalent. The incremental entropy change, dS, can then be denoted as

$$dS = \left(\frac{d\mathbf{X}_i}{dT} \right) d\mathbf{y}_i \Rightarrow \int dS = \int \left(\frac{d\mathbf{X}_i}{dT} \right) d\mathbf{y}_i , \tag{1.14}$$

which simplifies to

$$S\big|_{\mathbf{y}_i} - S\big|_{\mathbf{y}_i=0} = \int_0^{\mathbf{y}_i} \left(\frac{d\mathbf{X}_i}{dT} \right) d\mathbf{y}_i = \Delta S(0 \to \mathbf{y}_i). \tag{1.15}$$

In Eqn. (1.15), the entropy change has been derived for any single phase exposed to the intensive force $\mathbf{y}_i$. For example, if a magnetic field, $H = \mathbf{y}_i$, is applied to austenite in a MMSMA around the magnetic Curie point, the resulting entropy change can be computed as $\int_0^H \left(\frac{dM}{dT} \right) dH$, where $\mathbf{X}_i$ is the energetic conjugate of H and is denoted as magnetization by M. Graphically, this MCE, or magnetic field induced entropy change, is illustrated in Figure 1-6.

In Figure 1-6, the entropy versus temperature diagram of a ferromagnetic material is depicted. Mathematically, these curves are described in Eqn. (1.10). Under zero magnetic field (top curve), the magnetic Curie point, T_{Curie}, is depicted as a cusp in the $S-T$ curve. According to Eqn. (1.10), the entropy curve is defined by the derivative of the Gibbs free energy with respect to temperature. Clearly, the second temperature derivative of the free energy, i.e. $\frac{dS}{dT}$, exhibits a discontinuity at T_{Curie}, thus making the ferromagnetic Curie point a second order magnetic transition. Interestingly, the assumption of commutativity, described above, no longer holds at T_{Curie}. On either side of T_{Curie}, Eqn. (1.15) is applicable for determining magnetic-field induced entropy changes.

Upon applying a magnetic field to the ferromagnetic material depicted in Fig. 1-6, the entropy decreases as a result of a reduction in heat capacity. The entropy change, $\Delta S(0 \to H)$, can be computed from the difference of the curves. $\Delta S(0 \to H)$ is typically

reported for isothermal conditions under a given applied magnetic field. On the other hand, the temperature change corresponding to the isothermal entropy change is illustrated by a red horizontal arrow labeled as $\Delta T_{ad}(0 \to H)$.

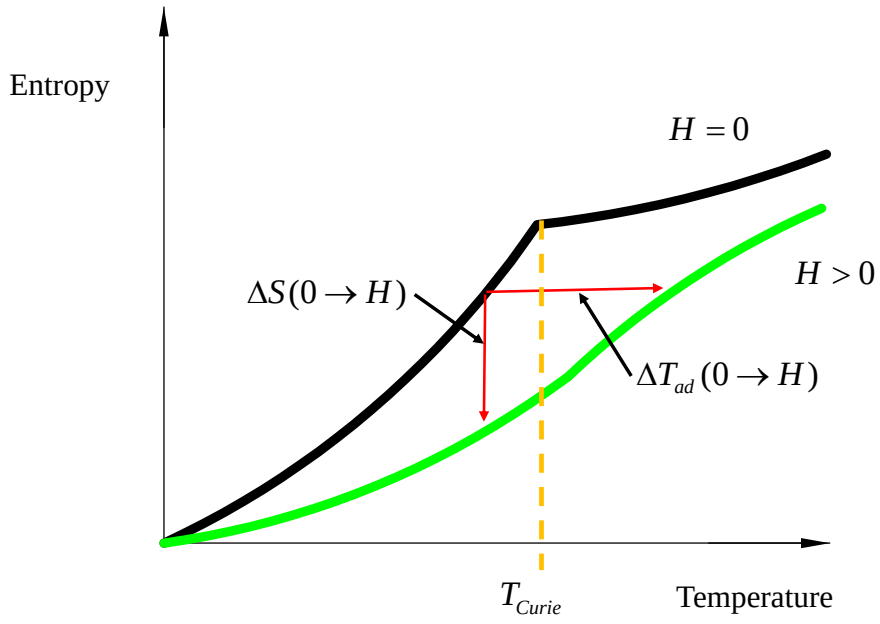

Figure 1-6: Entropy versus temperature diagram for a ferromagnetic material around the Curie point, T_C.

To compute $\Delta T_{ad}(0 \to \mathbf{y}_i)$, the total entropy, S, of the single phase is considered. Like G and U, S is a thermodynamic functional. Employing Truesdell's principle of equipresence [24], the total change in entropy, dS_{total}, is a function of all other thermodynamic quantities. As such, dS_{total} is defined as

$$dS_{total} = \left(\frac{dS}{dP}\right)dP + \left(\frac{dS}{dT}\right)dT + \sum_{i=1}^{n}\left(\frac{dS}{d\mathbf{y}_i}\right)d\mathbf{y}_i. \qquad (1.16)$$

According to Fig. 1-6, the $\Delta T_{ad}(0 \rightarrow H)$ is generated when $dS_{total} = 0$. Assuming isobaric ($dP = 0$) and isentropic ($dS_{total} = 0$) conditions, Eqn. (1.16) can be reduced to

$$0 = \left(\frac{dS}{dT}\right) dT_{ad} + \left(\frac{dS}{d\mathbf{y}_i}\right) d\mathbf{y}_i. \tag{1.17}$$

Substituting the Maxwell relation from Eqn. (1.14) into (1.17) for $\frac{dS}{d\mathbf{y}_i}$ reduces to

$$0 = \left(\frac{dS}{dT}\right) dT_{ad} + \left(\frac{d\mathbf{X}_i}{dT}\right) d\mathbf{y}_i \tag{1.18}$$

whereby the entropy change generated from applying the intensive force can be moved to the left side of the expression. This results in

$$-\left(\frac{d\mathbf{X}_i}{dT}\right) d\mathbf{y}_i = \left(\frac{dS}{dT}\right) dT_{ad}, \tag{1.19}$$

where $\left(\frac{dS}{dT}\right) = \frac{C_p}{T}$ per the second law of thermodynamics, and thus

$$-\left(\frac{d\mathbf{X}_i}{dT}\right) d\mathbf{y}_i = \left(\frac{C_p}{T}\right) dT_{ad}. \tag{1.20}$$

Finally, the terms in Eqn. (1.20) are separated and integrated resulting in

$$\Delta T_{ad}(0 \rightarrow \mathbf{y}_i) = -\int_0^{\mathbf{y}_i} \frac{T}{C_p} \left(\frac{\partial \mathbf{X}_i}{\partial T}\right)_{\{\mathbf{y}_{n \neq i}\}} d\mathbf{y}_i, \tag{1.21}$$

where the adiabatic temperature change can be computed for any isochoric driving force, $\mathbf{y}_i$, if the isobaric heat capacity and $\mathbf{X}_i$ histories are known. Oftentimes, C_p is assumed to be independent of the driving force, $\mathbf{y}_i$, and ΔT_{ad} is approximated as

$$\Delta T_{ad} \approx \frac{T}{C_p}\Delta S. \tag{1.22}$$

In summary, the conventional caloric effects generated from second order changes in heat capacity, can be quantified using the above thermodynamic framework. The entropy change can be computed from Eqn. (1.15) and the corresponding isentropic/adiabatic temperature change from Eqn. (1.21). In the context of the present work, these second order caloric effects can be computed and experimentally measured for austenite and martensite independently. That is, the above expressions and thermodynamic framework are not valid across the martensite to austenite, or austenite to martensite structural transitions because G is discontinuous.

The second order caloric effects of austenite and martensite can be computed using their free energy functions given in Eqns. (1.23) and (1.24), respectively. Here,

$$dG^A = V^A dP - S^A dT - M^A dH - \varepsilon^A d\sigma \tag{1.23}$$

and

$$dG^M = V^M dP - S^M dT - M^M dH - \varepsilon^M d\sigma \tag{1.24}$$

where the change in free energy of martensite (M) and austenite (A) are driven by pressure, temperature, applied magnetic field, and mechanical stress. Clearly, Eqns. (1.23) and (1.24) can take the place of the generalized dG in Eqn. (1.9) for the following derivation of $\Delta S(0 \to \mathbf{y}_i)$ and $\Delta T_{ad}(0 \to \mathbf{y}_i)$.

1.4.2 Giant caloric effects

As stated in the introduction, "giant" caloric effects are those generated by the latent heat of a first order structural transformation. These can be driven by superelasticity

or magnetic field induced transformations (MFITs). Here, the discussion relates to MMSMAs and the caloric effect across their martensitic transitions. Upon initiating the transformation, the free energies in austenite and martensite are equivalent (see Fig. 1-3a) and the result is a singularity point in G (see Figs. 1-3a, 1-4a and 1-5a). At this singularity, the MMSMA exhibits a change in crystal symmetry. As a result, Eqns. (1.10) through (1.22) are not valid for quantifying these caloric effects as they were derived assuming that $\frac{dG}{dT}$ is continuous.

Instead, the Clausius-Clapeyron relations must be employed to characterize the caloric effects around a first order transition. Differentiating Eqn. (1.7) results in

$$dG^A - dG^M = 0 \tag{1.25}$$

and

$$dG^A = dG^M. \tag{1.26}$$

The generalized form for dG in Eqn. (1.23) and (1.24) are then substituted into (1.26) for both martensite and austenite phases, resulting in

$$V^A dP - S^A dT_0 - \sum_{i=1}^{n} \mathbf{X}_i{}^A d\mathbf{y}_i = V^M dP - S^M dT_0 - \sum_{i=1}^{n} \mathbf{X}_i{}^M d\mathbf{y}_i. \tag{1.27}$$

Assuming the martensitic transition is not driven by hydrostatic pressure, $dP = 0$, Eqn. (1.27) simplifies to

$$-S^A dT_0 + S^M dT_0 = \mathbf{X}_i{}^A d\mathbf{y}_i - \mathbf{X}_i{}^M d\mathbf{y}_i. \tag{1.28}$$

Separating variables then results in

$$\left(-S^A + S^M\right) dT_0 = \left(\mathbf{X}_i{}^A - \mathbf{X}_i{}^M\right) d\mathbf{y}_i, \tag{1.29}$$

where the final form of the Clausius-Clapeyron relation can be denoted as

$$-\Delta S^{M\to A} = \Delta \mathbf{X}_i^{M\to A} \frac{d\mathbf{y}_i}{dT_0}. \tag{1.30}$$

In Eqn. (1.30) the entropy difference between the martensite, M, and austenite, A, phases is given. Clearly, if a change in magnitude of an extensive parameter is known across the martensitic transformation, $\Delta \mathbf{X}_i^{M\to A}$, as well as the temperature dependence of its critical driving force, $\frac{d\mathbf{y}_i}{dT_0}$, then the entropy change can be computed. The $\frac{d\mathbf{y}_i}{dT_0}$ term is generally known as the Clausius-Clapeyron slope, or the slope of a coexistence line between two phases on a phase diagram. In the case of the MCE, $\mathbf{X}_i = M$ and $\mathbf{y}_i = H$. It is important to note, however, that the value of $\frac{dH}{dT_0}$ is somewhat obscured by elastic energy and dissipation generated through the martensitic transition (see terms 3 and 4 in Eqn. (1.8)). These irreversible thermodynamic quantities result in a non-singular transformation temperature interval around T_0 and are discussed later.

As such, $\frac{dH}{dT_0}$ is typically unknown, other related parameters that can be experimentally quantified and are often employed in its stead. For example, in Fig. 1-5a, T_0 decreases with increasing applied magnetic field at a rate equal to $\left(\frac{dH}{dT_0}\right)^{-1}$. At the same time, the surrounding transformation temperatures decrease with T_0. The rates in which they decrease are not necessarily equal to that of T_0. The field sensitives of the

surrounding transformation temperatures, $\frac{dT}{dH^{M_f}}$, $\frac{dT}{dH^{M_s}}$, $\frac{dT}{dH^{A_s}}$, $\frac{dT}{dH^{A_f}}$, are easily quantifiable with simple experiments. Interestingly, each temperature exhibits its own field dependence. This indicates that the elastic energy stored across the transition and the structural dissipation (see terms 3 and 4 in Eqn. (1.8)) are not constant with field. This will be discussed in detail in a later chapter.

Nevertheless, Eqn. (1.30) is valid for determining the entropy changes across a first order transition where $\frac{dG}{dT}$ is discontinuous. Eqn. (1.30) differs from Eqn. (1.15) as the temperature derivative with respect to $\mathbf{X}_i$ is not needed to compute ΔS. If ΔS is determined using Eqn. (1.15) across FOPTs, a colossal caloric effect [25] will be found, simply as a mathematical artifact from differentiating a singularity.

The entropy versus temperature diagram for thermoelastic martensitic phase transformation in a constant magnetic field is depicted in Figure 1-7. Immediately, a clear difference is observed distinguishing Fig. 1-7 from Fig. 1-6 as the curves look dissimilar. In Fig. 1-7 entropy vs. temperature curves are illustrated under zero magnetic field, $H = 0$, and an applied magnetic field, $H > 0$. Under zero magnetic field (solid black curve) cooling from austenite produces the forward (A to M) thermoelastic transition at M_s. This is illustrated by a decrease in entropy. On reaching M_f, the transformation completes and the entropy continues to decrease with further undercooling. When heated, the reverse MT is generated at A_s and completes at A_f. In Fig. 1-7, the conventional effects are ignored in M and A.

According to Fig. 1-5, applying a magnetic field to a MMSMA results in a decrease in T_0. Thus, all of the aforementioned transformation temperatures decrease with T_0 as the magnetic field is applied. Transformation temperatures in Fig. 1-7 under a magnetic field are denoted with superscripts, H. As shown in Eqn. (1.8), $\Delta G_{mag}^{M \to A}$ is negative at $T < T_0$, and therefore, the martensitic transition can be triggered in martensite to austenite at the M_f temperature. The entropy change, $\Delta S(0 \to H)$, in Fig. 1-7 is depicted by a vertical arrow at M_f and is that generated by completing the magnetic field induced M to A transition. $\Delta S(0 \to H)$ is the difference in entropy between the austenite and martensite phases at M_f.

Unlike the response in Fig. 1-6, the $\Delta S(0 \to H)$ across the martensitic phase transformation is positive. This is accompanied by a decrease in temperature as indicated by the direction of the $\Delta T_{ad}(0 \to H)$ vector. In fact, the MCE depicted in Fig. 1-7 is inverse to the conventional effect illustrated in Fig. 1-6. Thus, giant MCE materials that exhibit a higher magnetization in austenite than the martensite phase, generate what is known as an inverse giant magnetocaloric effect (inv. GMCE).

To compute $\Delta T_{ad}(0 \to H)$ from Fig. 1-7, Eqns. (1.16) through (1.22) should not be employed as they were derived from the thermodynamic functional, S, specific to a single phase. Since a phase transformation is generated by applying a magnetic field, each term in Eqn. (1.16) is technically non-differentiable across first order transitions. Eqn. (1.22), however, is very commonly used in literature to predict the adiabatic temperature change in SMAs. Again, this is a common mistake resulting from misinterpreting the

underlying thermodynamics and not fully understanding the assumptions used when quantifying the above relations.

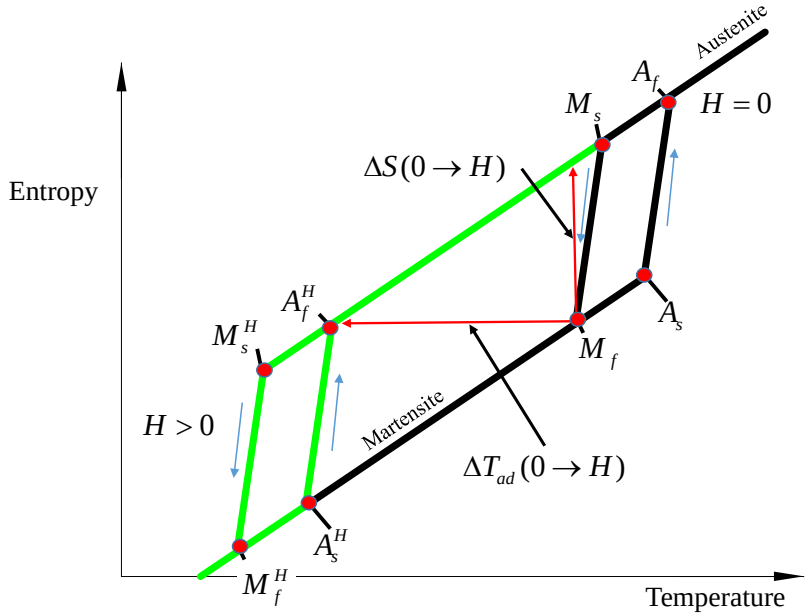

Figure 1-7: Entropy versus temperature diagram for a thermoelastic martensitic transformation.

Conveniently, there has been a recent development [26] whereby an empirical geometrical relation has been derived from entropy versus temperature diagrams to compute the $\Delta T_{ad}(0 \to H)$ of MMSMAs across MFITs. This method, although rarely reported, has been proven to be accurate within a reasonable degree [26] and will be briefly described, here. In [26], $\Delta T_{ad}(0 \to H)$ was derived using a diagram similar to that shown in Fig. 1-7, however only one leg of the hysteresis loop was considered.

In Figure 1-8, the entropy, S, versus temperature, T diagram is shown for quantifying the $\Delta T_{ad}(0 \rightarrow H)$. Only the heating curves are depicted. The solid curve represents the entropy-temperature history on heating to austenite under zero magnetic field and the dashed line represents heating to austenite under a constant magnetic field. The magnetic field, in this case, is not sufficient to complete the transformation at A_s, as would be depicted by $\Delta S^{M \rightarrow A}$ extending vertically all the way to the austenite phase, however, it is sufficient for quantifying the adiabatic temperature change. In addition, the entropy changes in A and M phases from the magnetic field dependence of heat capacity (conventional MCE) are neglected to simplify the discussion.

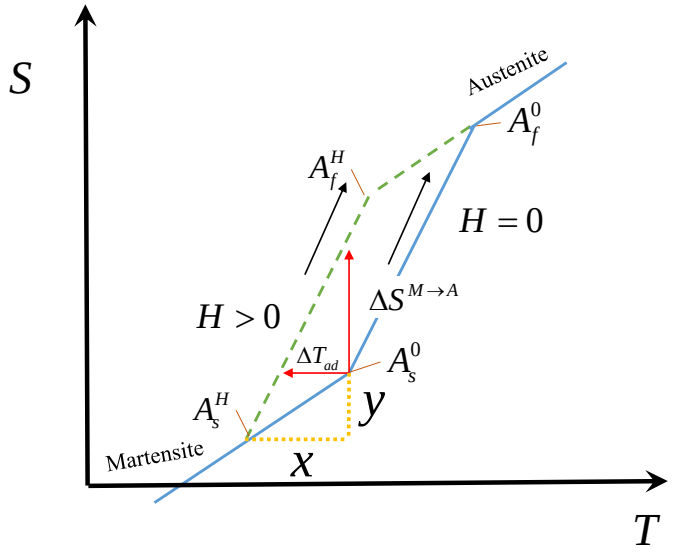

Figure 1-8: Entropy, S, versus temperature, T, diagram on the heating leg of the martensitic transition under zero and constant magnetic field, H.

Using the figure above, Porcari et al. demonstrated that the adiabatic temperature change, ΔT_{ad}, can be computed from the diagram using proportions of triangles. As such, the ratio of the isentropic legs equals the ratio of the isothermal legs,

$$\frac{\Delta T_{ad}}{x} = \frac{\Delta S^{M \to A}}{\Delta S^{M \to A} + y} \qquad \text{Inv.GMCE} \tag{1.31}$$

where $\Delta S^{M \to A}$ is the entropy change generated isothermally as computed from Eqn. (1.30). The distance x equals the decrease in the A_s temperature from applying the magnetic field, H, and is expressed as

$$x = A_s - A_s^H = \frac{dT}{dH^{A_s}} H \qquad \text{Inv.GMCE} \tag{1.32}$$

where $\frac{dT}{dH^{A_s}}$ is the field sensitivity of the A_s temperature, mentioned above. Assuming the $S-T$ response of martensite is linear and independent of magnetic field, then the parameter y is defined as

$$y \approx \frac{C_p^{martensite}}{T} x \qquad \text{Inv.GMCE} \tag{1.33}$$

where $C_p^{martensite}$ is the isobaric heat capacity of martensite and T is the temperature. Finally, solving Eqn. (1.31) for ΔT_{ad} and substituting Eqns. (1.32) and (1.33),

$$\Delta T_{ad} = \frac{\Delta S^{M \to A} \cdot \Delta T_M}{\Delta S^{M \to A} + \Delta T_M \cdot \frac{C_p^{martensite}}{T}} \quad T \le A_s \qquad \text{Inv.GMCE} \tag{1.34}$$

where ΔT_M is defined as

$$\Delta T_M = \left(\frac{dT}{dH^{A_s}} \right) H \qquad \text{Inv.GMCE} \tag{1.35}$$

and represents how far the A_s temperature has shifted by applying H. The uncertainty associated with Eqn. (1.34) has been reported to be as much as 30%-40% [26], but in this study, it will be used to predict the adiabatic temperature change of FOPTs due to its convergence with directly measured data [26]. It is important to note that Eqns. (1.31) through (1.35) are only valid for martensite to austenite magnetic field induced phase transformations, thus the equations are labeled "Inv. GMCE" to denote they are applicable only for computing ΔT_{ad} for the inverse giant magnetocaloric effect.

A similar derivation can be performed for MMSMA that exhibit a ferromagnetic martensite phase and a non-magnetic austenite phase. In this case, applying magnetic field to austenite generates a heating effect from the $A \rightarrow M$ transition. Here, $\frac{dH}{dT_0}$ is positive and, therefore, terms 5 in Eqn. (1.8) are reversed in sign, resulting in an increase in T_0 when applying a magnetic field. Using a similar diagram to Fig. 1-8, the proportions of triangles can be equated as

$$\frac{\Delta T_{ad}}{x} = \frac{\Delta S^{A \rightarrow M}}{\Delta S^{A \rightarrow M} + y} \qquad \text{GMCE} \tag{1.36}$$

where GMCE indicates the giant MCE, x is now dependent on the M_s temperature and $\frac{dT}{dH^{M_s}}$ field sensitivity resulting in

$$x = M_s^H - M_s = \frac{dT}{dH^{M_s}} H \qquad \text{GMCE.} \tag{1.37}$$

In this case, y is dependent on the isobaric heat capacity in austenite and is expressed as

$$y \approx \frac{C_p^{austenite}}{T} x \qquad \text{GMCE.} \tag{1.38}$$

Solving Eqn. (1.36) results in

$$\Delta T_{ad} = \frac{\Delta S^{A \to M} \cdot \Delta T_M}{\Delta S^{A \to M} + \Delta T_M \cdot \dfrac{C_p^{austenite}}{T}} \quad T \geq M_s \qquad \text{GMCE} \tag{1.39}$$

where

$$\Delta T_M = \left(\frac{dT}{dH^{M_s}} \right) H \qquad \text{GMCE.} \tag{1.40}$$

The thermodynamics described above are implemented for the MCE and ECE case studies in Chapter 6. In superelastic ECE studies, $\frac{dT}{dH^{M_s}}$, should is replaced with $\frac{dT}{d\sigma^{M_s}}$, defined as the critical stress-temperature slope for initiating the transformation from A to M. Here, it is important to note that implementing the incorrect equation to quantify ΔT_{ad} around a MFIT will result in large computational errors. For example, a MMSMA can exhibit typical values of $\Delta S^{M \to A} = 20 \text{J/kgK}$ under 5T, $C_p^{martensite} \approx 400 \text{J/kgK}$, at $M_f = 290K$. The A_s field sensitivity is approximately $\frac{dT}{dH^{A_s}} \approx 4 \text{K/T}$. If Eqn. (1.22) is used, ΔT_{ad} is found to be as much as 14.5K. If Eqn. (1.34) is used, however, ΔT_{ad} is computed to equal a more reasonable value of 8.4K. Eqn. (1.34) yields more realistic approximation when compared to directly measured adiabatic temperature changes [27].

Using the incorrect expression from Eqn. (1.21) results in an over approximation by almost a factor of 2.

In recent years there has been so much confusion in the literature on how to properly compute the ΔT_{ad} in MMSMAs, some researchers only rely on direct temperature measurements to quantify the MCE/ECE in MMSMAs. Alas, these measurements are somewhat difficult to perform under the required adiabadicity. For example, a few direct measurements have been reported for NiMnIn alloys [27, 28]. In [28], a NiMnIn alloy was swept through 3T while its temperature was monitored. The initial temperature of the MMSMA was set to the M_s temperature of the given sample. Example results from [28] are reported in Figure 1-9.

As shown in Fig. 1-9(a), the thermomagnetic response of the MMSMA shifts to the left under high magnetic fields. This is explained in the above sections with Fig. 1-5. Interestingly, a 1.4K temperature change was measured from applying 3T around M_s, in this particular alloy as shown in Fig. 1-9(b). Subsequent field cycling resulted in 0.5K to 0.7K temperature changes. As such, the reversibility in this alloy of achieving repeated temperature changes is poor due to the thermal hysteresis, mentioned earlier, and the stored elastic energy across the martensitic transition. Processing methods to improve the material response will be reported in a subsequent chapter.

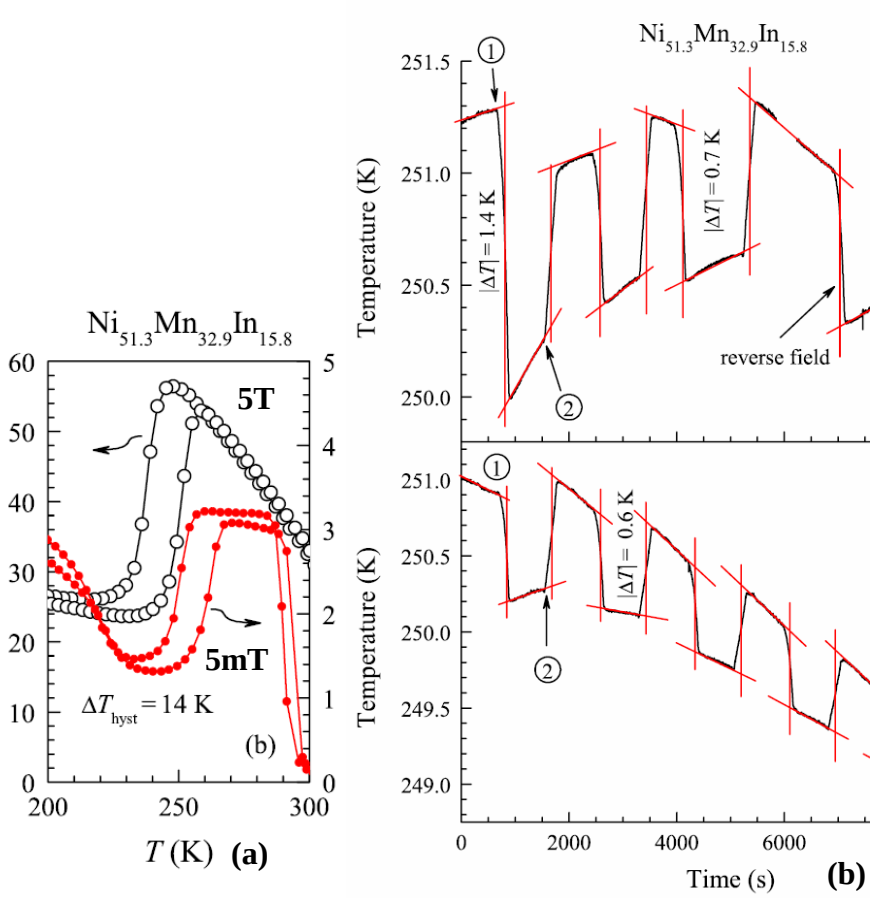

Figure 1-9: (a) The thermomagnetic response of the NiMnIn sample shown in (a) under 5T (circles) and 5mT (solid-circles) and (b) the temperature of a NiMnIn meta-magnetic shape memory alloy as a function of time during field ramping from 0T to 3T [28].

In another study, magnetic fields from a custom Halbach array was employed to generate the giant inv. MCE in MMSMA a specimen under magnetic fields up to 2T. The apparatus used to control and monitor the MMSMAs temperature is shown in Fig. 1-10 [27]. The experimental apparatus in Fig. 1-10 was pumped to high vacuum prior to being inserted into a liquid nitrogen dewar. Once in place, the temperature was controlled with the electric heaters to the desired set-point. Once the desired temperature was reached, the

magnetic field was ramped to from 0 to 2T to -2T to 0 while the temperature was measured. Example ΔT_{ad} results from the custom instrument in Fig. 1-10 are shown in Fig. 1-11 from Ref. [29].

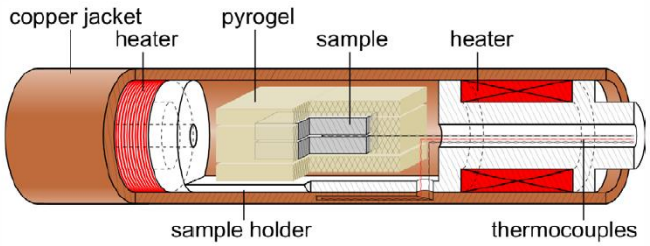

Figure 1-10: An experimental apparatus used for monitoring the adiabatic temperature change of a meta-magnetic shape memory alloy specimen. The sample is encased in pyrogel insulation and surrounded by electric heaters to control the temperature. Prior to insertion into a liquid nitrogen dewar, the sample housing was evacuated to 10^{-6} mbar. Once at the specified temperature, a Halbach array was used to ramp the magnetic field to 2T while monitoring the temperature [27] .

To measure the data in Fig. 1-11a, the MMSMA was set to the temperature indicated on the plot. Starting with $\Delta T_{ad} = 0$ at $\mu_0 H = 0$, the field was positively ramped. This resulted in cooling of about 6K at 317K. On reducing the field back to 0, the sample exhibited minimal reversibility (heating) due to the thermal hysteresis shown in Fig. 1-11(b). Subsequent cycles are represented by the negative field side of the ΔT_{ad} vs. $\mu_0 H$ diagrams. At lower temperatures, 314, 310, and 307K, the 2T applied to the MMSMA was not sufficient to induce a structural transformation. Instead, a larger field is needed to shift the thermomagnetic response (shown in Fig. 1-11(b)) farther to the left.

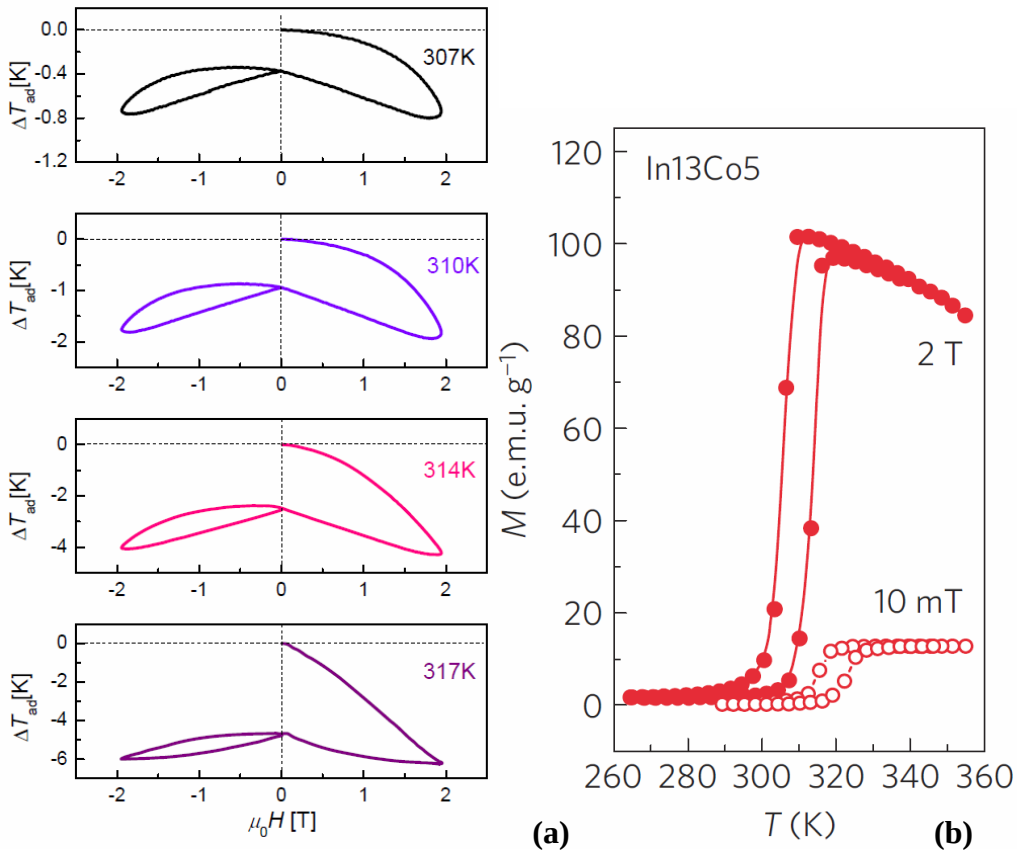

Figure 1-11: The adiabatic temperature change of $Ni_{45.2}Co_{5.1}Mn_{36.7}In_{13}$ polycrystals measured using the experimental apparatus in Fig. 1-10 (a) and (b) the thermomagnetic response of the MMSMA specimens in (a). These results are from [27] .

The next chapter discusses direct measurements of the MCE and ECE in NiMn-based MMSMAs with methods proposed by the author. Predictions of temperature changes computed by Eqn. (1.34) could be compared to the directly measured data. Experimental apparatuses were designed and retrofitted with existing instruments for MCE and ECE ΔT_{ad} measurements generated from magnetic field-induced and stress-induced martensitic transformations, respectively.

1.5 Objectives

As mentioned in the introduction, MMSMAs are promising for refrigeration applications. However, their biggest flaw is that they typically require magnetic fields larger than 2T to drive the M to A transition; the magnetic field induced transformation generates the magnetocaloric cooling and, therefore, must be driven with small magnetic fields. Permanent magnets are only capable of supplying up to 2T. Therefore, the main objective of this work is to fully transform a MMSMA under no more than 2T. This has never before been achieved, and if accomplished, will open the possibility of implementing cost effective MMSMAs in MCE applications.

It is believed this can be realized in a few ways, however. The first is by tailoring the MMSMAs microstructure with heat treatments. In doing so, the terms in Eqn. (1.8) can be controlled and perhaps 2T will induce a complete transition. Another is by finding an optimal composition which, again, would influence the terms in Eqn. (1.8). Finally, it is believed that the MMSMA will transform under 2T if a mechanical load assists the procession of transformation as a result of magneto-mechanical couplings. This is referred to as a "stress-assisted magnetic field induced transition" (SAMFIT) and will be investigated in this work.

These methods of achieving a complete transformation under 2T have driven the experimental work, herein. Therefore, this dissertation is separated into a few parts. First, the typical experimental procedures used to quantify the caloric effects in MMSMAs are discussed. These experiments will indicate whether the complete martensitic transformation has taken place under 2T. After careful review of these procedures, it was

found that magnetic and mechanical testing are typically performed separately on MMSMAs. Since MMSMAs exhibit magneto-thermo-mechanical coupling, one must measure a combination of material responses simultaneously across the martensitic transformation to fully understand their capabilities. Therefore, a materials test apparatus was designed and built to probe the multiferroic responses of MMSMAs. This test apparatus lends the ability to perform SAMFIT experiments. Subsequent chapters are intended to provide an analytical means of evaluating the MCE and ECE in MMSMA materials, improving their caloric behaviors through materials processing, and finally, some case studies are presented on the MCE and ECE in meta-magnetic and ferromagnetic SMAs. The final chapter is dedicated to explaining MMSMAs performance under simultaneously applied magnetic field and mechanical stress.

CHAPTER II

EXPERIMENTAL PROCEDURES*

2.1 Alloy fabrication

Three types of microstructures were studied in this work including bulk polycrystalline, single crystalline, and melt-spun polycrystalline. Initially, these alloys were arc-melted in an inert argon environment by collaborating researchers or personally by the author. During melting, they were flipped and re-melted at least three times to promote homogeneity. Bulk alloys and single crystals were simply removed from the arc-melter after initial melting to be heat treated, however, those intended for melt spinning were suction cast into 5mm diameter rods.

The suction cast rods were then placed in the quartz nozzle of a melt spinner. After removing the oxygen in the melt spinner, the 5mm diameter rod was induction melted in an inert environment and ejected through the quartz nozzle onto a rotating copper wheel. This procedure resulted in 30micron thick ribbon samples of various widths and lengths.

Single crystal samples, on the other hand, were prepared from large ingots with the Bridgeman technique in Tomsk, Russia. Wire EDM was used to cut compression samples from the resulting large single crystals. Samples were then electropolished, or lightly mechanically polished, to remove any brass residue that may have remained on the surface. Compression samples were typically cut to 4mm × 4mm × 8mm nominal dimensions.

---

*Part of this chapter is reprinted from *Acta Materialia*, **74**, Bruno N. *et al.* The effect of heat treatments on Ni43Mn42Co4Sn11 meta-magnetic shape memory alloys for magnetic refrigeration, 66-84, Copyright (2014), with permission from Elsevier.

Table 2-1 contains a list of the nominal compositions of the alloys in this study. They are separated into two groups, namely, NiMnIn and NiMnSn. The nominal composition in atomic percent (at.%) is tabulated on the left, and the measured, on the right. Compositions were measured using wavelength dispersive spectroscopy as discussed in a subsequent section. All alloy compositions in this dissertation are in atomic percent unless otherwise noted.

Table 2-1: Nominal and measured compositions, M_s and T_C temperatures, and e/a ratios for homogenized meta-magnetic shape memory alloys.

				Measured Composition (at.%)			
Nominal Composition (at.%)	M_s	T_c	e/a	Sn	Mn	Co	Ni
Ni_{43} $Co_4Mn_{42}Sn_{11}$ Ribbon	216	340	8.02	11.7	41.2	4.1	43.1
Ni_{43} $Co_4Mn_{42}Sn_{11}$ Bulk	279	365	8.03	11.5	41.0	4.6	43.0
$Ni_{45}Co_2Mn_{43}Sn_{10}$	343	-	8.06	10.7	43.0	1.9	44.5
$Ni_{45}Co_4Mn_{41}Sn_{10}$	375	-	8.10	10.8	40.9	4.0	44.4
$Ni_{45}Co_5Mn_{40}Sn_{10}$	406	-	8.12	10.8	39.8	5.1	44.4
$Ni_{45}Co_6Mn_{39}Sn_{10}$	408	-	8.12	10.8	39.3	5.4	44.5
$Ni_{45}Co_5Mn_{38.5}Sn_{11.5}$	340	366	8.10	12.3	37.2	5.0	45.5
$Ni_{45}Co_5Mn_{38}Sn_{12}$	282	372	8.08	12.7	37.0	5.1	45.2
Nominal Composition (at.%)	M_s	T_c	e/a	In	Mn	Co	Ni
$Ni_{48}Mn_{38}In_{14}$	265	279	7.84	14.3	38.5	-	47.2
$Ni_{50}Mn_{34.5}In_{15.5}$	264	313	7.88	15.5	34.6	-	49.9
$Ni_{50}Mn_{35}In_{15}$	300	311	7.89	15.1	35.2	-	49.8
$Ni_{50}Mn_{35.5}In_{14.5}$	331	310	7.92	14.4	35.7	-	49.9
$Ni_{50}Mn_{36}In_{14}$	346	289	7.91	14.3	36.1	-	49.5
$Ni_{45}Co_5Mn_{36.6}In_{13.4}$	260	390	7.92	13.6	36.2	4.7	45.5

2.2 Heat treatment procedures

After alloy fabrication, the MMSMAs were solution heat treated (SHT) to promote homogeneity and remove any lingering second phases. To prevent oxidation during solutionizing, the specimens were sealed in quartz tubes under 13Torr of argon. Typically, SHTs were conducted at 1173K for 24 hours and were followed by water quenching (WQ). Alloys were often wrapped in a protective tantalum foil to prevent interaction between the MMSMA and quartz containment vessel at elevated temperatures. As discussed in subsequent chapters and sections, secondary heat treatments were often performed to modify grain size and crystallographic ordering. These secondary heat treatments were performed under the same environmental conditions as the SHT process, however, the temperature and times were either lower or higher than 1173K and 24hours.

Secondary heat treatments for each base alloy in Table 2-1 are tabulated in Tables 2-2 through 2-6.

Table 2-2: The composition of the $Ni_{43}Co_4Mn_{42}Sn_{11}$ base alloy and selected secondary heat treatments. RC and FC denote rapid cooling and furnace cooling, respectively.

				Measured Composition (at.%)			
Nominal Composition (at.%)	M_s	T_c	e/a	Sn	Mn	Co	Ni
$Ni_{43}Co_4Mn_{42}Sn_{11}$ Ribbon	216	340	8.02	11.7	41.2	4.1	43.1

Solution Heat Treatment + Secondary Heat Treatment			
Temperature (K)	Time (hr)	Cooling Method	Crystal Type
(SHT) 1173K	2	RC	Ribbon
+673K FC	1	FC	
+773K FC	1	FC	
+873K FC	1	FC	
+673K RC	1	RC	
+773K RC	1	RC	
+873K RC	1	RC	

Table 2-3: The composition of the $Ni_{45}Co_5Mn_{40}Sn_{10}$ base alloy and selected secondary heat treatments. WQ and FC denote water quenching and furnace cooling, respectively.

				Measured Composition (at.%)			
Nominal Composition (at.%)	M_s	T_c	e/a	Sn	Mn	Co	Ni
$Ni_{45}Co_5Mn_{40}Sn_{10}$	406	-	8.12	10.8	39.8	5.1	44.4

Solution Heat Treatment + Secondary Heat Treatment			
Temperature (K)	Time (hr)	Cooling Mode	Crystal Type
(SHT) 1173K	2	WQ	Polycrystal
+1073K	0.5	FC	
+1073K	1	FC	
+1073K	1.5	FC	
+1073K	2	FC	
+1073K	10	FC	
+1173K	0.3	FC	
+1173K	0.7	FC	
+1173K	1	FC	
+1173K	1.3	FC	
+1173K	1.7	FC	
+1173K	1.7	FC	
+1173K	2	FC	
+1198K	0.5	FC	
+1198K	1	FC	
+1198K	2	FC	

Table 2-4: The composition of the $Ni_{48}Mn_{38}In_{14}$ base alloy and selected secondary heat treatments. WQ denotes water quenching.

				Measured Composition (at.%)			
Nominal Composition (at.%)	M_s	T_c	e/a	In	Mn	Co	Ni
$Ni_{48}Mn_{38}In_{14}$	265	279	7.84	14.3	38.5	-	47.2

Solution Heat Treatment + Secondary Heat Treatment			
Temperature (K)	Time (hr)	Cooling Mode	Crystal Type
(SHT) 1173K	24	WQ	Polycrystal
+773K	3	WQ	
+873K	3	WQ	
+973K	3	WQ	
+1073K	3	WQ	
+1123K	3	WQ	

Table 2-5: The composition of the $Ni_{50}Mn_{36}In_{14}$ base alloy and selected secondary heat treatments. WQ denotes water quenching.

				Measured Composition (at.%)			
Nominal Composition (at.%)	M_s	T_c	e/a	In	Mn	Co	Ni
$Ni_{50}Mn_{36}In_{14}$	346	289	7. 91	14.3	36.1	-	49.5

Solution Heat Treatment + Secondary Heat Treatment			
Temperature (K)	Time (hr)	Cooling Mode	Crystal Type
(SHT) 1173K	24	WQ	Polycrystal
+573K	3	WQ	
+673K	3	WQ	
+873K	3	WQ	
+973K	3	WQ	
+1073K	3	WQ	

Table 2-6: The composition of the $Ni_{45}Co_5Mn_{36.6}In_{13.4}$ base alloy and selected secondary heat treatments. WQ and FC denote water quenching and furnace cooling, respectively.

				Measured Composition (at.%)			
Nominal Composition (at.%)	M_s	T_c	e/a	In	Mn	Co	Ni
$Ni_{45}Co_5Mn_{36.6}In_{13.4}$	260	390	7.917	13.6	36.2	4.7	45.5

Solution Heat Treatment + Secondary Heat Treatment			
Temperature (K)	Time (hr)	Cooling Mode	Crystal Type
(SHT) 1173K	24	WQ	Single Crystal
(SHT) 1173K	24	FC	
+573K	3	FC	
+573K	3	WQ	
+573K	168	WQ	
+673K	3	WQ	
+673K	24	WQ	
+773K	0.08	WQ	
+773K	0.25	WQ	
+773K	0.50	WQ	
+773K	3	WQ	
+873K	3	WQ	
+873K	168	WQ	
+973K	3	WQ	
+998K	3	WQ	
+1023K	3	WQ	
+1048K	3	WQ	
+1073K	3	WQ	
+1098K	3	WQ	
+1123K	3	WQ	

2.3 Wavelength dispersive spectroscopy

The compositions of the alloys were determined using a CAMECA SX-50 electron probe microanalyzer. The microprobe employed 4 double sided diffracting crystals for

wavelength dispersive spectroscopy (WDS). Samples were prepared by mechanically polishing to 0.05 micron grit in 1 inch diameter plastic ringform mounts. Samples were encased in non-conductive epoxy within the mount. To supply an electrical ground for the electron beam within the microprobe, the prepared samples were coated with a thin layer of carbon. Ni-K_α, Mn-K_α, and Co-K_α x-rays were counted using a lithium fluoride (LIF) diffracting crystal for 20s, 20s, and 50s, respectively. Sn and In-L_α x-rays were counted using a pentaerythritol (PET) diffracting crystal with a 90s counting time. WDS measurements were taken at about 3 locations on each sample in multiple grains (if available).

2.4 Microscopy

2.4.1 Optical microscopy

Prior to compositional analysis with WDS, samples were mechanically polished and/or etched. Sample microstructures were observed and recorded with a digital microscope up to 1000X magnification.

2.4.2 Scanning electron microscopy

A FEI Quanta 600 field emission scanning electron microscope (SEM) was employed to obtain high resolution micrographs. The SEM housed an electron dispersive spectroscope (EDS), an electron backscatter diffractometer (EBSD), and an attachable backscatter electron (BSE) detector. The SEM lent the ability for quick compositional identification of microstructural inclusions and clearly visible compositional gradients or

second phases. The SEM was used for imaging, whereas the microprobe, mentioned above, mainly for compositional analysis due to its higher degree of accuracy.

2.4.3 Transmission electron microscopy

Single crystal samples were prepared for transmission electron microscopy (TEM). Plates were EDM cut such that the plate face was in the [011] austenite crystal direction, as discussed in subsequent chapters. Once cut into 400μm thick plates, samples were heat treated then mechanically ground to 100micon thickness. Thinned plates were then punched into 2mm diameter discs for TEM and twin jet polished using a 1:3 nitric acid to methanol electrolyte at 243K under 20V. Traditional dark field images were obtained from the TEM samples by diffracting the (111) reflection oriented along the [011] austenite zone axis.

2.5 SQUID magnetometry

SQUID magnetometry was performed with a Quantum Design Superconducting Quantum Interference Device (SQUID) Magnetic Property Measurement System (MPMS3). The MPMS housed a vibrating sample magnetometer (VSM). For thermomagnetic measurements, the samples were heated to 400K, cooled to 10K, and then reheated to 400K under 0.05T (or 0.01T), 1T, 3T, 5T, and 7T at a rate of 5K/min as their magnetization was measured. Isothermal magnetization curves were collected by ramping the magnetic field at either 25Oe/s or 50Oe/s.

2.6 Differential scanning calorimetry and thermogravimetric analysis

Heat flow in MMSMA samples was measured with a TA Instruments Q20 and Q2000 differential scanning calorimeter (DSC) between 93K and 450K. Samples were placed in aluminum pans during measurements and heated and cooled at 5-10K/min. Ribbons were stacked to generate larger heat signals in the Q20 DSC. Heat flow measurements provided a means to compute the latent heat of the martensitic transformation. Additionally, specific heat capacity measurements were obtained with the Q2000 DSC which employed a modulated pseudo-isothermal measurement technique. A sapphire standard was employed prior to any heat capacity measurement to verify the instrument calibration.

High temperature heat flow measurements were achieved using a TA Instruments Q600 thermogravimetric analyzer (TGA). The TGA recorded heat flow up to 1400°C and provided cooling at a rate of at most 20°C/min. High temperature heat flow measurements were performed using an alumina pan to prevent melting. Heat flow signatures at high temperatures revealed crystallographic ordering temperatures in MMSMA single crystals.

2.7 Mechanical testing

A screw driven mechanical test system (MTS) was employed for the compression tests described in this work. The MTS provided compressive loads up to 30kN while compressing the specimen as slow as 0.004mm/s. The load was measured with a load cell and the sample displacement with a high temperature extensometer with alumina tips. Special compression rods were designed for maintaining the compression sample temperature between 300°C and -120°C as discussed later. Samples were heated and

cooled across their martensitic transformation under a constant compressive load while compressive strain was recorded or isothermal compression tests were performed.

2.8 Direct magnetocaloric measurements

In the present work, an attempt was made to measure the adiabatic temperature response of $Ni_{45}Co_5Mn_{36.6}In_{13.4}$ single crystals. The only experimental instrument available capable of applying large magnetic fields was the SQUID-VSM. The SQUID-VSM is capable of providing magnetic fields up to 7T at 700Oe/s, and achieving a temperature set-point between 400K and 2K. The sample chamber can be evacuated during adiabatic temperature measurements to nearly 10^{-3}Torr .

As such, a sample insertion rod for the SQUID-VSM was modified so that a T-type thermocouple could be adhered to a MMSMA specimen during ramping of a magnetic field while under vacuum. The thermocouple was fed through the hollow sample rod and vacuum connections into a measurement computing data acquisition (DAQ) board as shown in Fig. 2-1. The sample was surrounded by pyrogel insulation during adiabatic temperature measurements.

In Fig. 2-1, the standard sample rod configuration is shown on the left. Typically, the sample rod is magnetically adhered to the moving VSM head. An aluminum cap is placed on top so the sample chamber can be evacuated during magnetization measurements at low temperatures. In a Quantum Design SQUID-VSM, sample temperature is computed from a series of temperature measurements along the sample chamber wall. In the modified configuration, however, the sample temperature is reported

directly. This allows accurate direct temperature measurements to be obtained from the magnetized sample.

The experimental test sequence used with the apparatus in Fig. 2-1 was as follows. The sample was first installed and the sample chamber was purged of air. In 5Torr He atmosphere, the temperature of the MMSMA was set to around M_f. Once the MMSMA reached the desired temperature set-point, the temperature was held constant for 5 minutes to allow the specimen to reach a thermal equilibrium with its surroundings.

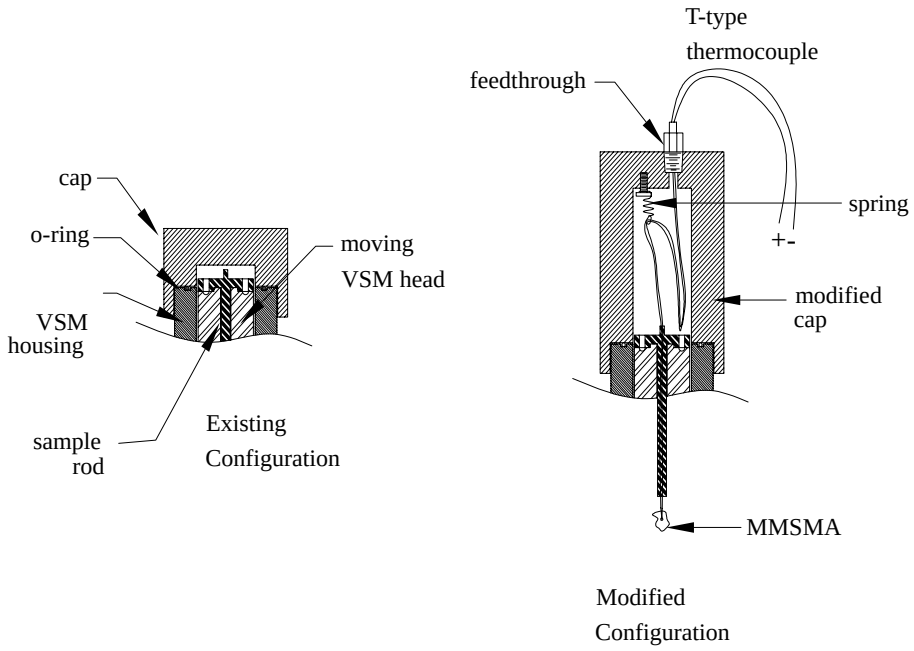

Figure 2-1: The existing (left) and modified (right) configurations of the SQUID VSM sample mounting for adiabatic temperature change measurements.

After reaching equilibrium, the sample chamber was continuously purged during the adiabatic measurements with a mechanical pump. Vacuum levels reached 10^{-3}Torr. Nevertheless, the MMSMA sample was in contact with the SQUID-VSM rod, and therefore the adiabatic conditions were somewhat compromised. The actual adiabadicity of the sample was unknown during the temperature measurements. Example results of adiabatic temperature measurements with the configuration in Fig. 2-1 are shown in Fig. 2-2 for a SHT $Ni_{45}Co_5Mn_{36.6}In_{13.4}$ single crystal.

In Fig. 2-2, the NiCoMnIn single crystal exhibited a M_f temperature of about 245K. Therefore, the sample was cooled to 245K and then the field was ramped. This should have allowed the sample to return to its martensitic state once the magnetic field was completely removed. As shown in Fig. 2-2, the sample was steady at 245K and the magnetic field was ramped (point 1) at 700Oe/s. At point 2, the sample had cooled approximately 2.5K.Upon removing the magnetic field, the MMSMA started to heat up to point 3. At point 3, the field was completely reduced to zero and the sample was allowed to rest for 200 seconds to return to 245K. Next, points 4, 5, and 6, indicate the latter for a subsequent cycle.

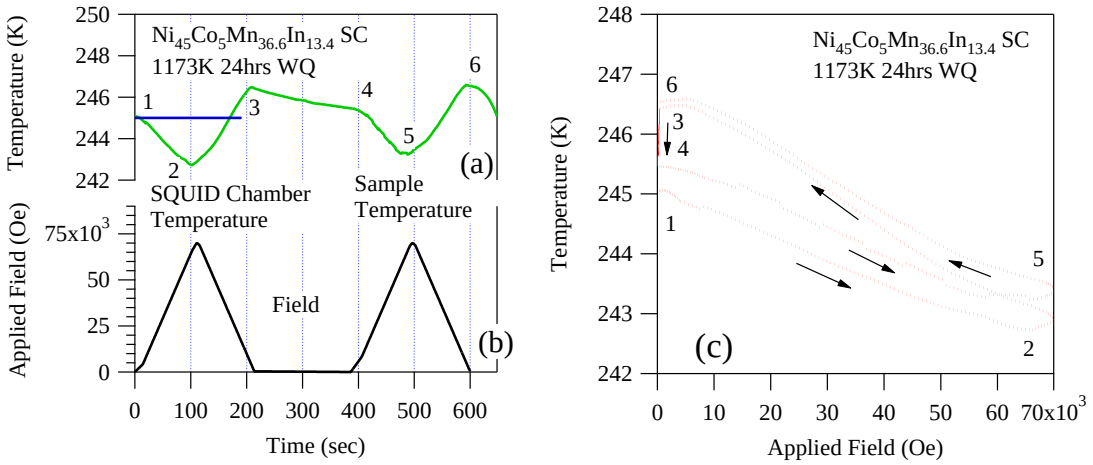

Figure 2-2: (a) The temperature vs. time history of a $Ni_{45}Co_5Mn_{36.6}In_{13.4}$ single crystal that had been homogenized at 1173K for 24hrs, (b) the magnetic field applied to the sample in (a), and, (c) the temperature versus applied field history of the sample in (a).

These points are also represented on a temperature versus applied field plot in 2-2(c). Ideally, the response in 2-2(c) should have looked like that in Fig. 1-11(a). The adiabadicity from the experimental setup in Fig. 2-1 was, unfortunately, not ideal. Over the course of 200sec the MMSMA had absorbed energy from the sample chamber. This may have been due to a poor vacuum or conduction between the sample and the sample rod. Nevertheless, some information can be extracted from the results in Fig. 2-2(c).

From point 1 to 2, the MMSMA cooled by about 2.5K. At high magnetic fields, once the MFIT was completed, the MMSMA began to heat, slightly. This slight heating may have been generated by the conventional MCE in the austenite phase. On removing the field to point 3, the sample heated to a temperature greater than 245K, indicating it had absorbed some energy during the cooling process. Instead of returning to 245K the sample returned to 246.5K due to poor adiabatic conditions. Subsequent cycles resulted in similar

behaviors. Fig. 2-3 demonstrates the measured temperature changes at different initial conditions around the martensite transformation temperatures.

As shown in Fig. 2-3, a 2K to 2.5K temperature change was measured by ramping up to 7T. It is believed that the actual temperature change was a few degrees larger than what was measured due to the poor adiabatic conditions provided by a rough vacuum. Nevertheless, these measurements are the directly measured MCE in MMSMAs. In the next section, indirect measurements are discussed which often provide a more accurate quantification of the MCE in these materials. Indirect MCE measurements are performed from isothermal experimental procedures in the rest of this work, rather than direct MCE adiabatic measurements.

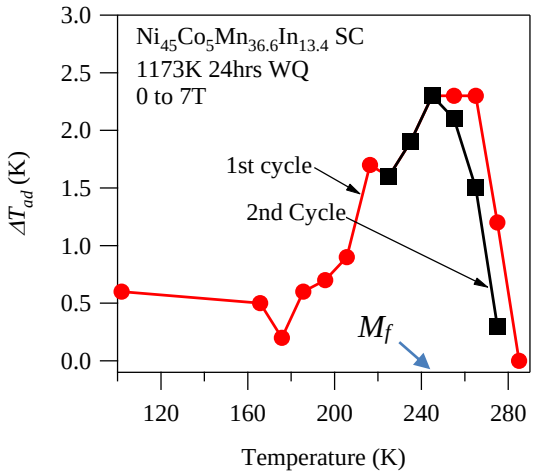

Figure 2-3: Adiabatic temperature change versus temperature for $Ni_{45}Co_5Mn_{36.6}In_{13.4}$ single crystals that had been homogenized at 1173K for 24hrs.

2.9 Direct elastocaloric effect measurements

Similarly, direct giant elastocaloric effect (ECE) measurements were made on NiFeGa single crystal magnetic shape memory alloys using custom rods with the MTS mentioned above. The giant ECE in NiFeGa magnetic shape memory alloys is generated by inducing a superelastic phase transformation. Custom compression rods were designed and fabricated for direct adiabatic temperature change measurements across martensitic transitions in MMSMAs. In addition, the compression rods, described here, were also used for indirect giant ECE measurements discussed later.

Like the SQUID-VSM, controlling the sample temperature was very important in mechanical measurements. The compression rods, therefore, were used as heat exchangers for controlling the MMSMA temperature. The general assembly of the compression rods is shown in Fig. 2-4.

The compression rod in Figure 2-4 was constructed from three components. The base was machined from 17-4PH stainless steel (SS) and a detailed schematic is shown in Fig. 2-5. A tungsten carbide (WC) rod (see Fig. 2-6) was shrunk fit into the 17-4PH SS base by cooling the WC or heating the 17-4PH SS. The dimensions reported in Figs. 2-5 and 2-6 represent those which allow the entire compression rod assembly to be safely heated and cooled between 573K and 93K. Above 573K, the WC rod loses radial contact with the 17-4PH SS base due to the differences in thermal expansion between the two materials. The temperature limit, therefore, is 573K under zero mechanical load. Exceeding this temperature can safely be achieved, however, if a compressive load is used to hold the WC insert in place, i.e. during compression tests.

Around the WC rod, a copper jacket was press fit using a machine press. The copper jacket was drilled-out along a zig-zag pattern using a drill press. A schematic of the zig-zag pattern is shown in Fig. 2-7. A total of 14 holes were drilled through each copper jacket. Channels were milled to make connections between the holes. Finally, copper rings were brazed on either side of the copper jacket to seal the zig-zag radial channel. Copper tubes were then brazed to holes connecting inlets and outlets to the channels. Figures 2-8 (a) and (b) show the copper jackets before and after brazing the top ring.

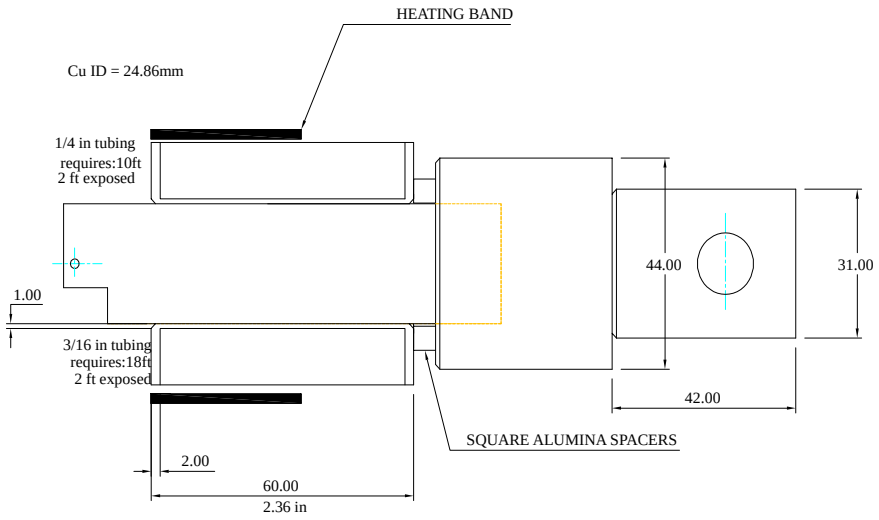

Figure 2-4: Custom compression rod assembly.

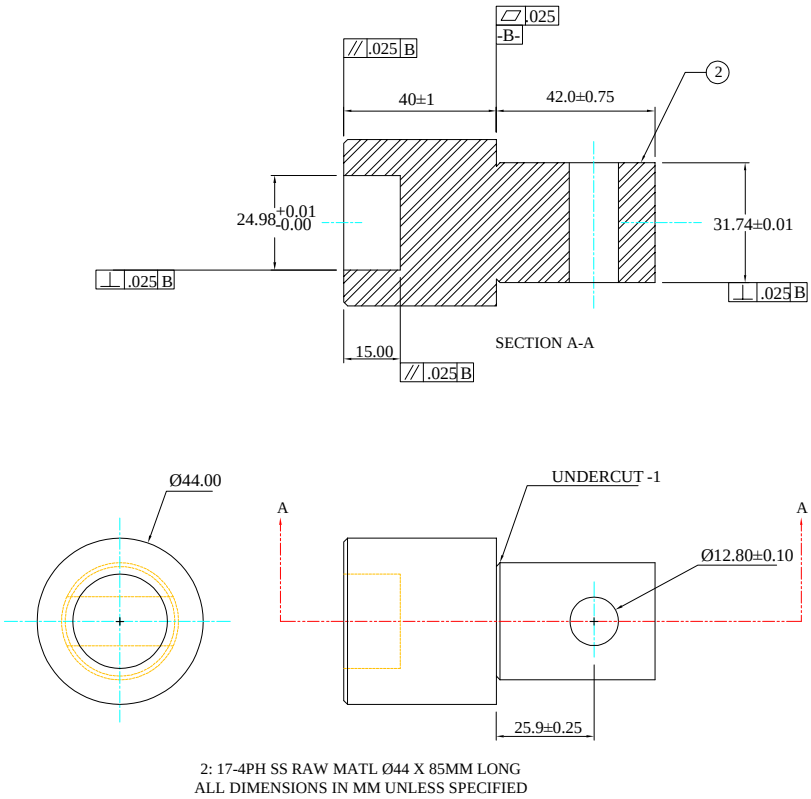

Figure 2-5: A detailed drawing of the 17-4PH stainless steel (SS) base in the custom compression rod shown in Fig. 2-4.

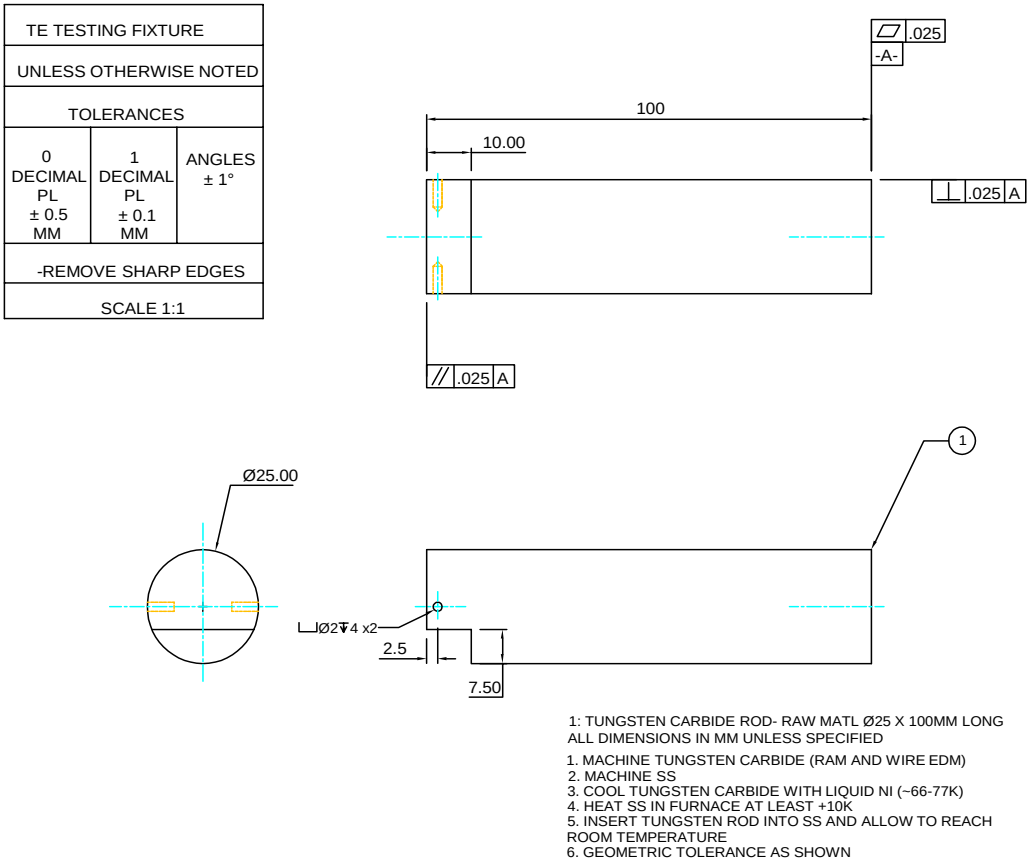

Figure 2-6: A detailed drawing of the tungsten carbide rod component in the custom compression rod in Fig. 2-4.

Two-inch diameter, two inch long, 300W Chromalox band heaters were wrapped around the copper jackets to supply heat to the test specimen through conduction as shown in Fig. 2-8b. To cool the compression rods, liquid nitrogen was flowed through the copper jacket. Cryogenic solenoid valves opened and closed to control the flow of liquid nitrogen through the channel. The heater bands and solenoid valves were activated/deactivated with

a CN8200 series OMEGA PID controller. The temperatures of the top and bottom compression rods were controlled independently.

Temperature feedback was sent to the PID controller via K-type thermocouples encased in alumina rods shown in Fig. 2-8(b). Ram electro-discharge machining, (RAM EDM) was used to generate two holes in the WC rods shown in Fig. 2-6. These holes were intended for the heads of the K-type thermocouples. One thermocouple signal was sent to the CPU and written to a file, the other sent a signal for temperature feedback to the PID controller.

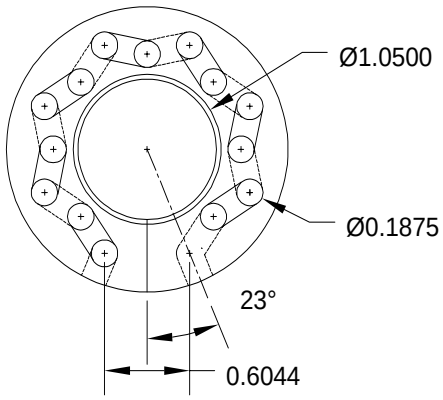

Figure 2-7: A detailed schematic for the custom copper jacket that was press-fit around the WC rod in Fig. 2-6. Dimensions are in inches.

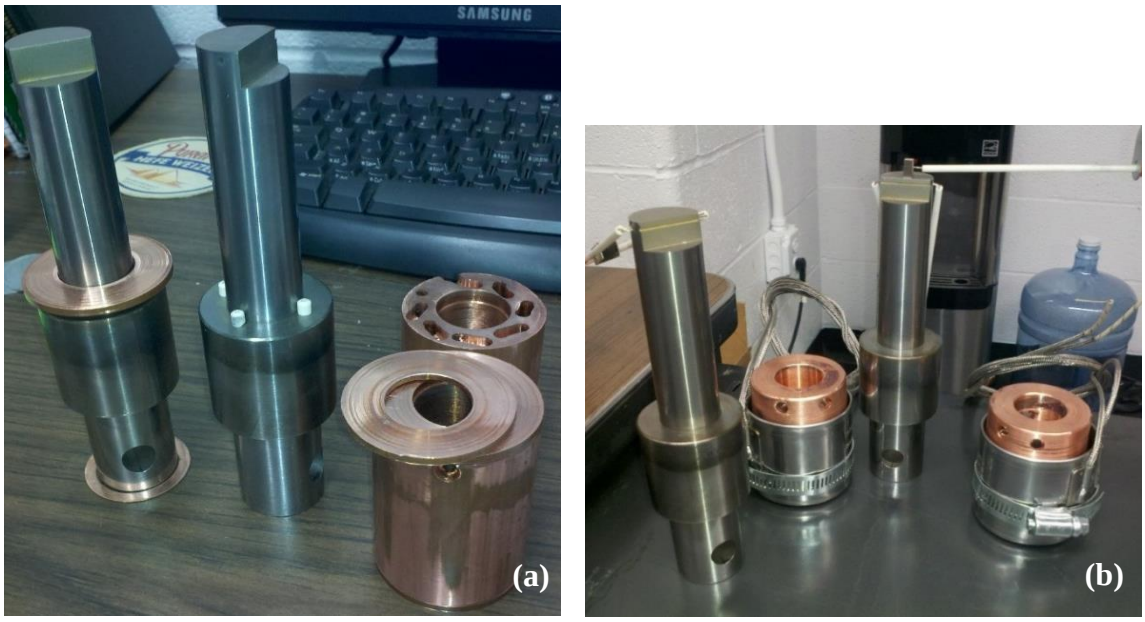

Figure 2-8: (a) custom compression rods for mechanical testing of magnetic shape memory alloy single crystals and (b) the completed rods.

As shown in Fig. 2-8(b), a "slot" was cut into the flat side of the upper and lower compression rod. This slot was intended to align the high temperature extensometer (HTEX) used in measuring compressive strain. The HTEX was zeroed by separating the measurement forks by 12.7mm which had an allowable range of ±20% strain, i.e. ±2.5mm displacement. Compression measurements were typically performed on 8mm long specimens. Therefore, these slots were cut 2mm from the compression face to allow the HTEX to remain near zeroed strain when an 8mm long sample was measured. This minimizes non-linearity errors in strain measurements.

Figure 2-9 shows the assembled compression rods on the MTS. Copper tubes were wound around the compression rods for cycling cooling water. The water acted as a protective measure from overheating the load cell (above) and rod housing. A spring

loaded thermocouple configuration was used to monitor the temperature at the surface of the compression sample as shown in Fig. 2-9. Additionally, a Lexan polycarbonate insulating box (not shown) was designed and constructed to be placed around the compression rods. The box surrounds the compression rods from either side and is latched together around the rods. This permits quick assembly and removal of the surrounding insulation. The box, however, does not touch the upper pushrod or load cell nor generate any errors in mechanical measurements.

Adiabatic temperature measurements were not performed with the quick insulating box. Instead, pyrogel was wound around the samples. NiFeGa, NiCoFeGa [29], and NiMnIn MMSMA compression samples were tested with the setup in Fig. 1-20. As discussed above, the A to M transition in these magnetic shape memory alloys can be driven using mechanical load above the A_s temperature. In the $Ni_{54}Fe_{19}Ga_{27}$ (at.%) compression samples, the A_s temperature was measured to be 284K as discussed in a later section. Here, as an example, a single crystal compression sample was loaded at 0.01mm/s ($125 \cdot 10^{-5} \varepsilon / s$) along the cubic austenite [123] direction. The adiabatic temperature changes are reported in Fig. 1-21 for initial temperatures of 293K and 311K.

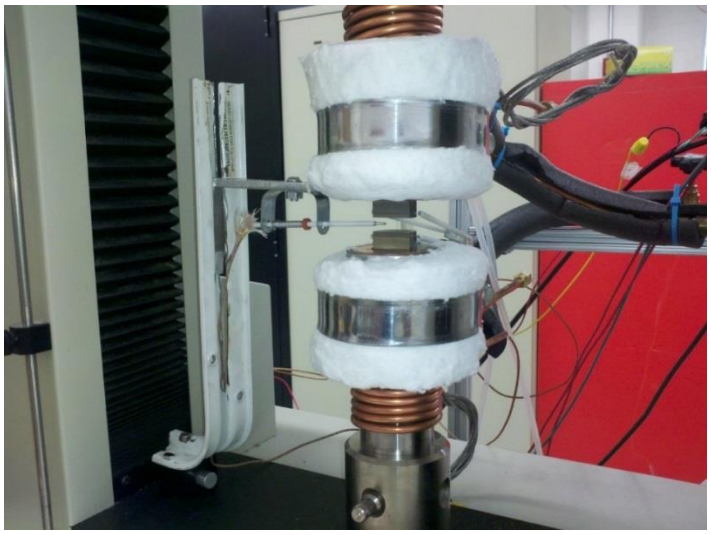

Figure 2-9: The completed custom compression setup for heating and cooling between 573K and 98K. Copper tubing was wound around the compression rods to flow cooling water in an attempt to protect the load cell (not shown) and the shrink-fit connection between the tungsten carbide and stainless steel components.

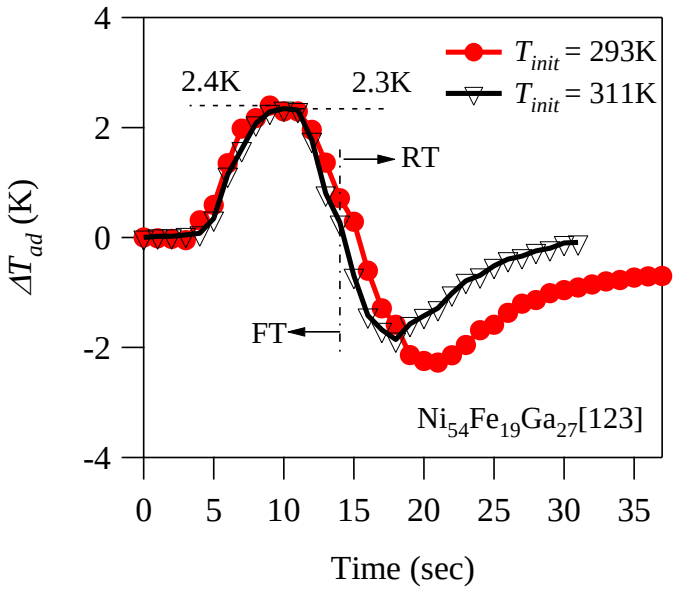

Figure 2-10: The directly measured adiabatic temperature change in $Ni_{54}Fe_{19}Ga_{27}$ (at.%) single crystals from superelastic loading/unloading along the [123] austenite crystal direction.

As shown in Fig. 2-10, the NiFeGa single crystals were compressed in the A phase. The A to M transition (forward transformation –FT) is represented by the initial heating in Fig. 2-10. Once hot, the sample was unloaded. The temperature history was recorded. Between the hottest and coolest part of the test, the NiFeGa sample exhibited an approximate 4.5K temperature decrease. This value can be computed using a thermodynamic framework discussed later. Due to the difficulties that arise when attempting to generate adiabatic environments, oftentimes indirect measurements that quantify the isothermal entropy change (see Fig. 1-7) are more accurate to quantify the caloric effect and will be the subject of most of the measurements, herein.

2.10 Indirect magnetocaloric effect measurements

In Eqn. (1.15), a generalized form for the isothermal entropy change around a second order magnetic transition was derived. In the case of the magnetocaloric effect (MCE) around a magnetic Curie point, $\mathbf{X}_i = M$ and $\mathbf{y}_i = H$ in Eqn. (1.15), thus resulting in

$$\Delta S(0 \to H) = \int_0^H \left(\frac{dM}{dT} \right) dH. \tag{2.1}$$

According to Eqn. (2.1) the isothermal entropy change shown in Fig. 1-6 can be quantified by measuring the thermomagnetic response ($M(T)$) of a magnetic material under a constant magnetic field, H, and computing its derivative. Multiplying the applied field by the temperature derivative of the thermomagnetic response results in the entropy change, which then yields information on temperature changes around the second order transition per Eqn. (1.21).

On the other hand, the giant MCE is quantified with the Clausius-Clapeyron (CC) equation given in (1.30) across first order transitions. Substituting $\mathbf{X}_i = M$ and $\mathbf{y}_i = H$, the magnetic CC equation (1.30) reduces to

$$-\Delta S^{M\to A} = \Delta M^{M\to A}\frac{dH}{dT_0} \tag{2.2}$$

where $\Delta M^{M\to A}$ is the magnetization change from martensite to austenite, and $\frac{dH}{dT_0}$ is the CC slope described in Chapter 1. The CC slope can be approximated as another directly measureable slope, such as $\frac{dH^{M_s}}{dT}$. Eqn. (2.2) will then give only a single $\Delta S^{M\to A}$ value. In practice, the entropy change as a function of temperature ($\Delta S^{M\to A}(T)$) should be measured so that additional thermodynamic analysis can be performed. This analysis is described in detail later.

The $\Delta S^{M\to A}(T)$ can be measured with magnetic isotherms [30] from the expression

$$-\Delta S(T_K, 0\to H) = \frac{1}{\Delta T_k}\left[\int_0^H M_{T_{k+1}}dH - \int_0^H M_{T_k}dH\right] \tag{2.3}$$

where T_{k+1} and T_k are test temperatures, $T_{k+1} > T_k$, $\Delta T_k = (T_{k+1} - T_k)$, and $T_K = (T_{k+1} + T_k)/2$. According to Eqn. (2.3), the entropy change caused by the field-induced transformation can be quantified by finding the difference in the magnetostatic energy density between two different magnetic responses at different temperatures (with small temperature increments), divided by the temperature increment [30]. Essentially,

$-\Delta S(T_K, 0 \rightarrow H)$ is the difference in Zeeman energy of M and A divided by temperature as discussed earlier and defined by term 5 in Eqn. (1.8). A schematic representation on how to determine ΔS from isothermal measurements is shown in Figure 2-11.

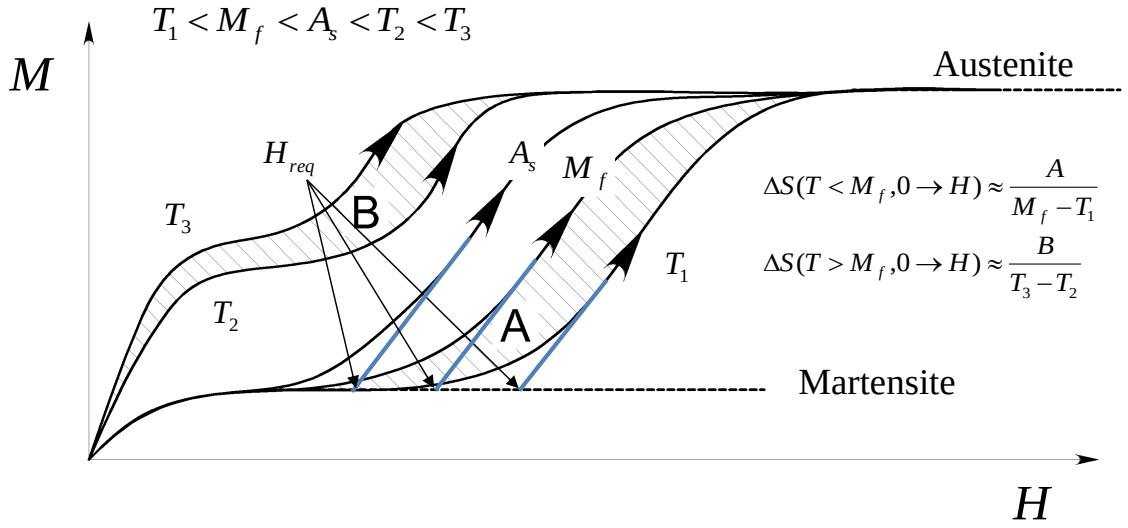

Figure 2-11: The magnetization response across a MFIT in a MMSMA [50].

Figure 2-11 depicts the isothermal magnetic response ($M-H$) of a MMSMA during field-induced $M \rightarrow A$ transformation at five different temperatures, T_1, M_f, A_s, T_2, and T_3. Here, $T_1 < M_f < A_s < T_2 < T_3$ and as the sample resides at hotter temperatures the ferromagnetic austenite phase is more stable, thus requiring less magnetic field to transform the sample from martensite to austenite as indicated by H_{req}. The entropy change is then quantified by finding the area (hatched regions) between two reverse *MT*

$M-H$ curves and dividing by the temperature increment responsible for the change (see area 'A').

Looking closely at Fig. 2-11 it can be seen that dividing area 'A' by the temperature change responsible for shifting the magnetic response is equivalent to implementing the CC equation in (2.2). For instance, area 'A' in Fig. 2-11 is essentially a rectangle defined by $\Delta M^{M\to A}$ as its height, and $H_{req}(M_f)-H_{req}(T_1)=dH$ as its base. The change in H_{req} is generated through $M_f-T_1=dT$.

It is important to note, however, that this method of computing the $\Delta S^{M\to A}(T)$ breaks down when the area between isotherms is not rectangular. If the area is not rectangular, the MMSMA transforms between a mixed (austenite and martensite) microstructure to austenite. What percentage of the microstructure is austenite and martensite is unknown, and therefore, implementing this method must be done using extreme caution.

The magnetic responses of MMSMAs when their initial microstructural state is mixed, i.e. containing both martensite and austenite phases, shown by the curves labeled T_2 and T_3. It can be seen from the $M-H$ curves labeled T_2 and T_3 that when the material is at a temperature in the two-phase region, small temperature changes may result in predicted entropy changes (shaded regions) at magnetic fields smaller than H_{req} (see area 'B' for small fields) which should not be confused for an entropy change generated from the M to A transition.

For this reason, the MMSMA must always be magnetically charged from 100% martensite, which can be achieved using a special experimental procedure, termed the discontinuous heating protocol. The discontinuous heating protocol is carried out as follows:

1. The samples were cooled to a temperature below M_f under zero magnetic field, resulting in a fully martensitic state.
2. The samples were then heated under zero magnetic field to a temperature just below the austenite start temperature without overshooting the target temperature.
3. Holding temperature constant, the magnetic field was ramped from zero to 7T and then back down to zero at a rate of 25 Oe/s, meanwhile, the magnetization was measured.
4. The temperature was then decreased to below M_f.
5. Next, the temperature was increased to the previous temperature plus 3K (without overshoot) and then step 3 was repeated.
6. Step 4 and 5 were repeated until the test temperature was very close to the austenite finish temperature.

Using the above steps, an accurate $\Delta S^{M\to A} - T$ diagram can be generated as shown in a later chapter for various case studies. These $\Delta S^{M\to A} - T$ diagrams can be further analyzed to yield information on the refrigeration performance of MMSMAs and other calorific materials.

2.11 Indirect elastocaloric effect measurements

Like the magnetocaloric effect, the elastocaloric effect (ECE) can be quantified indirectly under the assumption that uniaxial mechanical loading does not generate a volume change. In reality, this is not true unless Poisson's ratio is 0.5 [31]. For the conventional ECE in a material deformed elastically the ECE is defined as

$$\Delta S(0 \to \sigma) = \frac{1}{\rho}\int_0^{\sigma}\left(\frac{d\varepsilon_{el}}{dT}\right)d\sigma, \tag{2.4}$$

where ε_{el} is elastic uniaxial strain, σ is uniaxial applied mechanical load, and ρ is mass density. Similar to the MCE, the ECE should generate a decrease in the free energy, and therefore a decrease in entropy upon elastic loading. This will generate heating. The entropy change in (2.4) can be computed by finding the temperature derivative of uniaxial strain under a constant load, i.e. the coefficient of thermal expansion.

Using fictitious numbers to compute (2.4) one can compute the relative value of the conventional ECE compared to that of the MCE. Assuming a MMSMA with mass density of 8000kg/m^3 exhibits a coefficient of thermal expansion, $\frac{d\varepsilon_{el}}{dT}$, along some crystal direction of austenite, let us say the [001], of $5.99\cdot10^{-5}$ mm/mmK, then under 200MPa of uniaxial stress the entropy change can be computed using Eqn. (2.4). Loading the austenite single crystal from 0 to 200MPa, an entropy change of 1.5 J/kgK would be generated. Using Eqn. (1.22) and assuming the MMSMA is loaded at room temperature with $C_p \approx 400$J/kgK, the adiabatic temperature change from said loading generates

$\Delta T_{ad} \approx 1\text{K}$. Oftentimes, 1K is the temperature accuracy of the thermocouple, and therefore, the conventional ECE is negligible in MMSMAs.

On the other hand, superelastic mechanical loading through the martensitic transformation generates latent heat values similar to the MCE. As such, the CC equation in (1.30) can be expressed as

$$-\Delta S^{M\to A} = \frac{\varepsilon_{tr}{}^{M\to A}}{\rho}\frac{d\sigma_{cr}}{dT_0} \tag{2.5}$$

where the extensive property $\mathbf{X}_i$ from (1.30) has been replaced with the transformation strain, $\varepsilon_{tr}{}^{M\to A}$, and the intensive force, $\mathbf{y}_i$, with uniaxial stress, σ. It is important to note that Eqn. (2.5) defines the entropy change across the M to A transition upon releasing the mechanical load, i.e. the one that produces cooling per the above discussion.

Interestingly, some shape memory alloys exhibit a multistage stress-induced superelastic response [32]. In such a case, the entropy change from the low temperature martensite, to high temperature parent phases can be computed as the sum of each contributing transformation. The entropy change for multistage transformations can be computed as

$$-\Delta S_i^{M\to P} = \sum_{i=1}^{n}\frac{\varepsilon_{tr,i}^{M\to P}}{\rho}\cdot\frac{d\sigma_{cr}}{dT_{0\ i}} \tag{2.6}$$

where n represents the number of superelastic transitions in a the shape memory alloy, and superscript P represents a parent phase from the preceding martensite.

Eqn. (2.6) can then be represented by a set of integrals

$$-\Delta S^{M\to A}(T_K, 0\to\sigma) = \frac{1}{\rho\Delta T_k}\left[\int_0^{\sigma}\varepsilon_{T_{k+1}}d\sigma - \int_0^{\sigma}\varepsilon_{T_k}d\sigma\right] \tag{2.7}$$

where T_{k+1} and T_k are test temperatures, $T_{k+1} > T_k$, $\Delta T_k = (T_{k+1} - T_k)$, and $T_K = (T_{k+1} + T_k)/2$. It is important to note, however, that Eqn. (2.7) can only be integrated if the $\varepsilon - \sigma$ relation is a function. By definition, a function is a special type of relation in which each value in the domain (σ) corresponds to exactly one value in the range (ε), i.e. $f : \sigma \to \varepsilon$. Under some loading conditions for SMAs, however, the $\varepsilon - \sigma$ response is not a function.

For example, consider the illustrated superelastic $\sigma - \varepsilon$ response in Fig. 2-12. Upon increasing the mechanical stress, σ, a sudden drop is observed due to the rapid propagation of martensite after its nucleation. If one attempts to integrate the $\varepsilon - \sigma$ response in Fig. 2-12, rather than the $\sigma - \varepsilon$ response, Eqn. (2.7) cannot be applied. As a solution, an alternative has been proposed, here, in which a Legendre transform is used to generate a free energy potential that is reciprocal to the Gibbs free energy. Effectively, this permits the analysis of the ECE across superelastic loading in reciprocal space, whereby the $\sigma - \varepsilon$ response can be integrated to evaluate the entropy change.

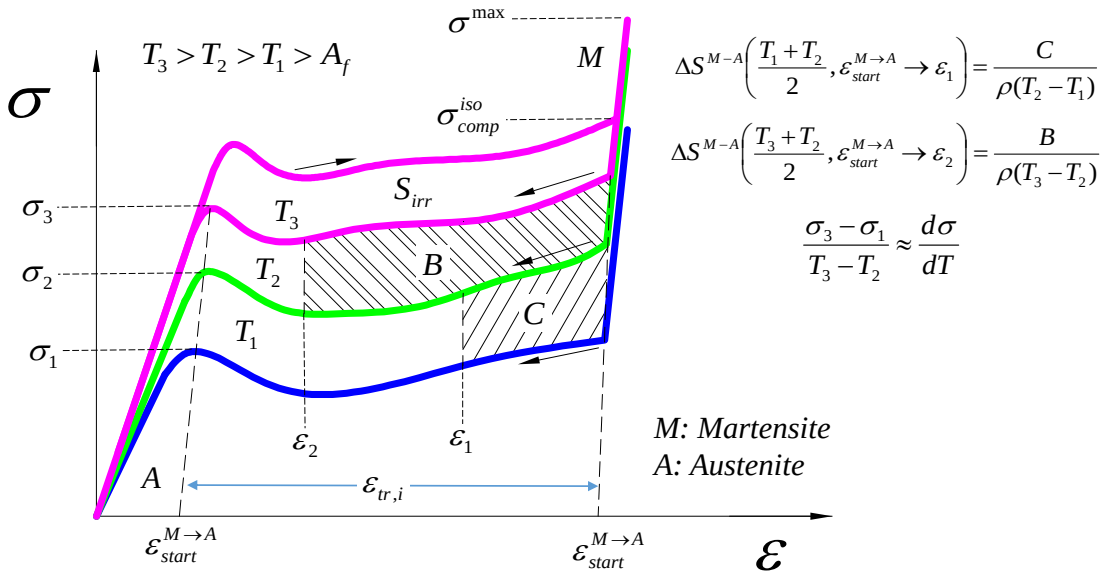

Figure 2-12: An illustration of the stress-strain response in shape memory alloys. Mechanical unloading is illustrated for T_1 and T_2, and both loading and unloading are illustrated at temperature T_3. Shaded areas, B and C, represent different levels of entropy change generated by unloading to different strain levels.

An alternative to the Gibbs free energy-derived CC (Gibbs-CC) relation shown in Eqn. (1.30), is the one that is derived from the Helmholtz free energy. For example, consider the internal energy U of SMAs as a function of extensive process variables ε and S like that in Eqn. (1.1). Instead of applying a Legendre transform to the Gibbs free energy, like Eqn. (1.6), only the heat work term is removed. This results in what is known as the Helmholtz free energy,

and
$$\begin{aligned} \Psi &= U - TS \\ d\Psi &= -SdT - PdV + HdM + \sigma d\varepsilon \end{aligned} \tag{2.8}$$

where the $\sigma d\varepsilon$ term is taken directly from dU in Eqn. (1.5) after the chain rule is applied. Like Eqn. (1.7), the free energy of M and A phases is equivalent at the point of

transformation. Thus the differential of the free energies are also equivalent at the point of transformation. This is expressed as

$$d\Psi^{Martensite} = d\Psi^{Austenite}. \tag{2.9}$$

Substituting Eqn. (2.8) into (2.9) for the A and M phases, and solving for $\Delta S_i^{M\to A}$, results in the CC equation,

$$\Delta S_i^{M\to A} = \sum_{i=1}^{n} \frac{\sigma_{tr,i}^{M\to A}}{\rho} \cdot \left(\frac{d\varepsilon_{tr}}{dT_0} \right)_{tr,i} \tag{2.10}$$

where from M to A the $\Delta S_i^{M\to A}$ must be positive, the reverse transformation hardening, $\sigma_{tr,i}^{M\to A}$, must be negative, and the CC slope, $\frac{d\varepsilon_{tr}}{dT_0}$, must also be negative. Note, the $\frac{d\varepsilon_{tr}}{dT_0}$ is not the coefficient of thermal expansion, but instead it represents how a critical strain level changes with temperature.

In practice, Eqns. (2.6) and (2.10) should compute the same entropy change of transformation for a MMSMA across superelastic loading. Both give only a single value. As mentioned before, it is important to characterize $\Delta S_i^{M\to A}$ across a wide range of temperatures for thermodynamic analysis. Therefore, Eqn. (2.10) can be expressed as

$$\Delta S^{M\to A}(T_K, \varepsilon_{start}^{M\to P_i} \to \varepsilon_{finish}^{M\to P_i}) = \sum_{i=1}^{n} \frac{1}{\rho \Delta T_k} \left[\int_{\varepsilon_{start}^{M\to P_i}}^{\varepsilon_{finish}^{M\to P_i}} \sigma_{T_{k+1}} d\varepsilon - \int_{\varepsilon_{start}^{M\to P_i}}^{\varepsilon_{finish}^{M\to P_i}} \sigma_{T_k} d\varepsilon \right] \tag{2.11}$$

where $\varepsilon_{start}^{M\to P_i}$ is the strain level at the start of the ith reverse transition, $\varepsilon_{finish}^{M\to P_i}$ is the strain level at the finish of the ith transformation, T_{k+1} and T_k are test temperatures, $T_{k+1} > T_k$,

$\Delta T_k = (T_{k+1} - T_k)$, and $T_K = (T_{k+1} + T_k)/2$. Eqn. (2.10) assumes the austenite modulus of elasticity E^A exhibits a negligible temperature dependence. Using Eqn. (2.11) the superelastic $\sigma - \varepsilon$ response of a MMSMA can be integrated to quantify the ECE across a first order transformation.

In Chapter 4, the entropy changes computed with the above Maxwell and Clausius-Clapeyron relations serve as inputs to additional thermodynamic analytic tools which are then used to compare solid-state calorific materials. Unfortunately, directly comparing the entropy change that is generated by MCE/ECE materials is a poor indicator of refrigeration performance. In second order MCE and ECE materials, applying and removing the intensive driving force $\mathbf{y}_i$, mentioned above, will result in a repeatable entropy or temperature change. In first order caloric materials, especially those exhibiting a structural hysteresis around a phase transformation, this reversibility can only be achieved under special circumstances. Due to the ability to attain different degrees of repeatability on field cycling, additional thermodynamic criteria are needed to quantify performance in MMSMAs.

2.12 The missing experimental link

When comparing capabilities and couplings of MMSMAs from section 1.3, it becomes apparent that the experimental procedures, in the above chapter, are lacking. Specifically, mechanical test instruments only probe at mechanical behavior and magnetic instruments probe only at magnetic behavior. In order to fully understand the magneto-

thermo-mechanical couplings of the MMSMA, a more robust test apparatus is needed that measures a combination of multiferroic responses.

The next chapter is dedicated to developing one such apparatus. The machine discussed below was intended to quantify the caloric effects in MMSMAs under mixed loading conditions, i.e. simultaneous field and stress. In following chapters, this test frame is used to investigate the influence of magnetic field on the superelastic behavior and caloric effects surrounding the martensitic transformation. Additionally, the test apparatus can be used to reduce the magnetic field requirement for cyclic martensitic transformation under a 2T applied magnetic field as mentioned in the Objectives section.

CHAPTER III

THE DESIGN OF A MAGNETO-THERMO-MECHANICAL TEST FRAME FOR CHARACTERIZING MAGNETIC MATERIALS

3.1 Test frame design

Modern day materials engineering is faced with increasingly complex requirements for the characterization of advanced and active materials. One particular group of active materials, namely meta-magnetic shape memory alloys (MMSMAs), exhibit many scientifically interesting phenomena [33-35] that can be studied by measuring the thermal, mechanical, and magnetic histories across their ferroic transitions [30]. Elaborate experimental methods are needed to analyze some of these effects and, therefore, such studies are rarely reported in literature [18, 36]. These measurements, however, are becoming increasingly sought after to test theoretical frameworks [18] or to calibrate novel constitutive models [19, 37, 38] and thereby improve the active material response.

MMSMAs undergo simultaneous thermoelastic (martensitic) and magnetic phase transitions. The martensitic phase transformation is the result of a change in crystal structure and is accompanied by a large recoverable strain. At temperatures above a critical point, the MMSMA transforms to the austenite (A) phase. Upon lowering the temperature, martensite (M) nucleates and propagates resulting in what is known as a forward (A to M) martensitic transformation [15]. On heating the alloy above the critical temperature from M, however, the A phase is recovered by the reverse transformation (M to A).

Interestingly, in MMSMAs the M and A phases exhibit different magnetic ordering. It has been posited that this behavior is controlled by Mn-Mn interatomic spacing [39] and its change across the phase transformation. In NiMnX (X=Sn, In, Sb), for example, the austenite phase is usually ferromagnetic [9] and the martensite phase is non-magnetic. On the other hand, in compounds such as FeMnGa [22], CoMnGe [21], and $Gd_5(Si_{1-x}Ge_x)4$ [7], the martensite phase is ferromagnetic and the austenite phase is non-magnetic. The complex nature of the thermal, magnetic, and mechanical couplings exhibited by these unique alloys lends the possibility for their implementation in numerous sensing and actuation applications, mentioned above.

3.1.1 The shape memory effect in meta-magnetic shape memory alloys

The reversible and diffusionless thermoelastic transformation observed in MMSMAs can be induced by sweeping their temperature across a critical point. On cooling from the A phase, martensite begins to nucleate at the martensite start temperature, M_s, and finishes propagating through the microstructure at the martensite finish temperature, M_f. On heating, austenite starts to form at the austenite start temperature, A_s, and finishes its transformation at the austenite finish temperature, A_f. A thermal hysteresis, defined here as $A_f - M_s$, is typically observed across the transformation and is produced by dissipation generated during the crystallographic change. Unfortunately, this structural hysteresis poses significant limitations in implementing engineering applications for shape memory alloys [18].

Often, the austenite phase in NiMnX (X=Sn, In, Sb) has a cubic Heusler lattice in which the Mn-Mn interatomic spacing results in ferromagnetic interactions. On cooling, the cubic phase transforms to a tetragonal, orthorhombic, or monoclinic martensite phase [18, 40] with lattice parameters different from those of the parent A phase. As a result, a transformation strain as large as 6.5% along certain crystal directions can be measured [18].

During the transformation process, a latent heat (or enthalpy of transformation) can be measured. It is this latent heat, as well as magnetic interactions, that lends the ability of solid-state refrigeration. The MaTMeCh device described in this work was designed to quantify the caloric effects of MMSMAs under mixed loading conditions, i.e. the magnetocaloric (magnetic field driven transformation) and the elastocaloric (stress induced transformation) effects. Superelasticity (stress induced transformations) and magnetic field driven transformations (MFIT) are briefly described below as an aid in developing the design constraints for the MaTMeCh device.

3.1.2 Superelasticity in meta-magnetic shape memory alloys

The phase transition in MMSMAs can also be triggered by applying a mechanical load at temperatures above A_s. The transformation strains can be completely recoverable when applying such loads at a temperature above A_f, temperature. These stress-induced transformations are known as superelasticity. Interestingly, the structural hysteresis mentioned above will manifest as a stress- or thermal history dependence (hysteresis) depending on the method used to transform the MMSMA. When the transformation is

driven by changes in temperature vs. mechanical load, the resulting martensite crystal structure may be different, and therefore the magnitude of the hysteresis across the martensitic transformation is a function of the method used to drive the transformation. This is caused by the differences in the martensite crystal structure that forms in stress-free conditions versus that which forms under a mechanical load.

Furthermore, in some alloys the structural dissipation is known to be anisotropic [15], thus additional complexity arises when characterizing the shape memory response in single crystals. For example, mechanical tests on CoNiGa MSMA single crystals [41] demonstrate that the [011] austenite crystal direction exhibits the largest stress hysteresis (~147MPa), in [001] the smallest (~42MPa), and in the [123] an intermediate between the other two (~119MPa). Clearly, stress hysteresis is dependent on the crystal orientation with respect to the mechanical loading. In the MMSMA materials studied, here, the dissipation anisotropy has been unclear and, therefore, the MaTMeCh device will allow us to probe at the transformation behaviors under isothermal and isofield conditions.

3.1.3 Magnetic field induced phase transformation

Finally, the M to A phase transition, specifically in MSMAs, can be driven by applying a magnetic field at temperatures below M_s [18]. A completely reversible magnetic field induced transformation (MFIT) can be achieved at temperatures below M_f [42]. The MFIT is analogous to heating the martensite phase to austenite. On removing the field, if no mechanical load is applied, martensite will self-accommodate to preserve the shape of austenite and minimize the internal elastic strain energy [18]. It is important

to note, when characterizing the MFIT in MMSMAs, that an applied mechanical stress has the potential of reducing structural hysteresis, as releasing the field from a MFIT with stress will transform the MMSMA to a stress-preferred martensite, rather than a self-accommodated one. Studies probing this behavior are rarely reported due to the difficulty of experimentation. Upon mechanically loading a MMSMA prior to MFITs, the lattice parameters change in the martensite phase. This is believed to be one of the mechanisms responsible for the mechanical load dependence of the structural hysteresis. Additionally, magnetostriction may influence lattice parameters, and influence the transformation behaviors [43]. The MaTMeCh device will allow measurement and comparison of the dissipation generated while transforming the MMSMA by different applied forces.

3.1.4 Magnetized bars

In conventional magnetometry, magnetization measurements rely on a changing magnetic flux. Either the magnetic field applied to the sample is pulsed, or the measured sample is vibrated, or extracted, through a set of inductive pickup coils. The voltage in the pickup coils is then used to measure magnetization. In the case of MMSMAs, however, the applied magnetic field is static and, during mechanical loading, the sample is unable to be vibrated or extracted from the magnetic field.

In a previous study [36], it was shown that the volume average magnetization can be determined by measuring the DC stray magnetic field surrounding a rectangular sample. Soft magnetic materials (such as MMSMAs) will demagnetize in the absence of a magnetic field. In the presence of a magnetic field, a demagnetizing field is generated surrounding the sample. A fully demagnetized rectangular sample is depicted in Fig. 3-1a.

Here, magnetic domains within the demagnetized bar, as shown by dashed lines, are oriented such that the magnetostatic energy is minimized. Arrows within the magnetic domains represent local magnetization. The stray field surrounding the sample is also at a minimum, and therefore, no magnetic flux lines are depicted.

In Fig. 3-1b, a uniform magnetic field is applied to the bar in the longitudinal direction. Upon applying the field, magnetic domains in the same direction of the applied field grow at the expense of the neighboring magnetic domains. In the case of Fig. 3-1b is we neglect any crystallographic defects that serve as pinning sites for the magnetic domain wall motion. The growth of the magnetic domain causes magnetic flux lines to appear surrounding the sample as a result of the north (N) and south (S) poles generated by the now partially magnetized sample. Upon applying a large enough longitudinal magnetic field, as in Fig. 3-1c, the magnetization of the bar is uniform. If the applied field was then rotated to a different direction, the magnetization vector would then rotate away from the longitudinal direction to co-align with the field, as long as the sample is short. In the case of Fig. 3-1c, there is no such rotation and the field is applied vertically. The configuration in Fig. 3-1c matches the proposed configuration used in the MaTMeCh device. The top surface of the sample is defined as the N end of the magnetic dipole and the bottom surface is the S pole. In this case there is a large stray field generated outside the sample due to the demagnetization of the bar. The stray field is depicted as blue arrows.

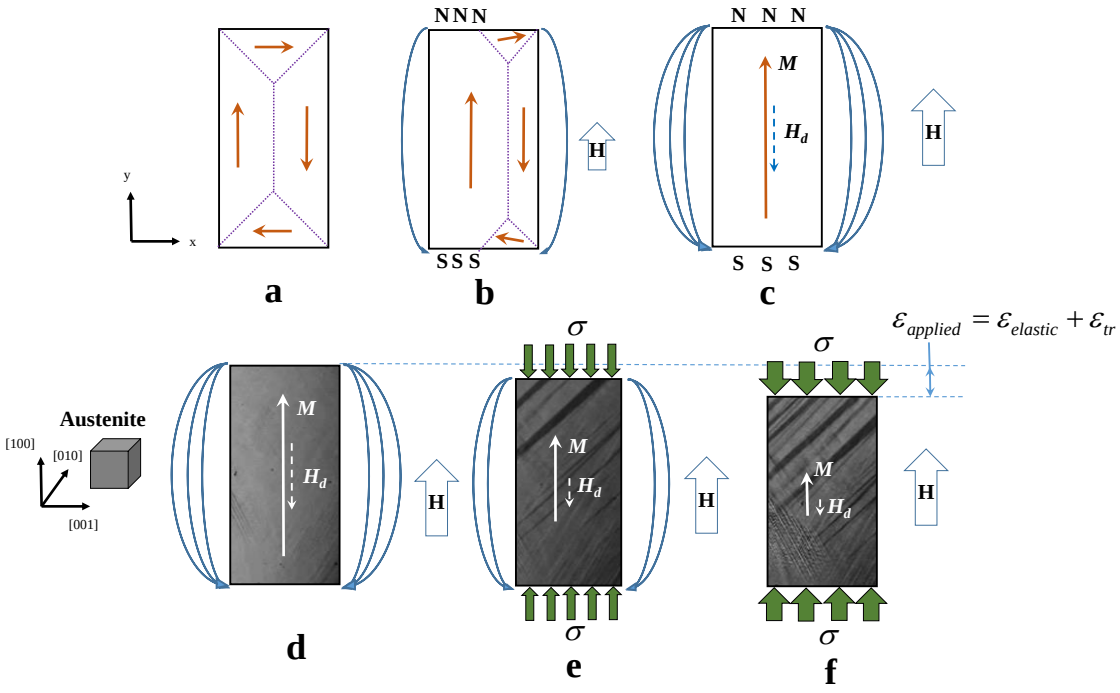

Figure 3-1: A demagnetized (a), partially magnetized (b), and uniformly magnetized (c) bar in the y direction. Internal dashed lines indicate magnetic domain walls, blue external lines represent stray magnetic field, internal solid arrows indicate magnetization, and the dashed internal arrow indicates the internal demagnetizing field. The externally applied field is represented as H. A uniformly magnetized austenite MMSMA (d), mixed austenite and martensite (e), and fully martensite (c) magnetized bars depict superelasticity in constant magnetic field, H. Solid arrows at either edge of the rectangle represent compressive stress denoted as σ.

Upon uniformly magnetizing the specimen along the longitudinal direction, a demagnetizing field can be measured. Qualitatively, this field is defined as that which opposes the applied field in an attempt to demagnetize the sample to its lower energy state shown in 3(a). The influence of such a field has a negative impact on application. Since magnetic fields are vector quantities, they are additive. Locally, the magnetized bar

experiences a smaller field than what is externally applied. Analytically, the field experienced at a material point, $\vec{H}_{effective}$, is defined as

$$\vec{H}_{effective} = \vec{H}_{applied} - \vec{H}_d \tag{3.1}$$

where $\vec{H}_{applied}$ is the applied magnetic field, H in Fig. 3-1, and $\vec{H}_d$ is the internal demagnetizing field.

Quantitatively, the average demagnetizing field is defined as

$$\vec{H}_d = \mathbf{D} \cdot \vec{M} \tag{3.2}$$

where $\mathbf{D}$ is the volume average demagnetizing factor dependent on sample geometry and $\vec{M}$ is the uniform specimen magnetization. It has been shown that for non-ellipsoidal geometries, rectangular bars for example, $\mathbf{D}$ can be computed analytically [44]. The demagnetizing factor is a tensor

$$\mathbf{D} = \begin{bmatrix} D_{xx} & 0 & 0 \\ 0 & D_{yy} & 0 \\ 0 & 0 & D_{zz} \end{bmatrix} \tag{3.3}$$

where D_{xx} corresponds to the [001] crystal direction in the macroscopic single crystal shown in Fig. 3-1d, D_{yy} to the [010] crystal direction, and the D_{zz} to the longitudinal direction. The diagonal of $\mathbf{D}$ always sums to unity. In this study, the nominal dimensions of the MMSMAs are 4mm × 4mm × 8mm, and therefore, our volume average (magnetometric) demagnetizing factors were computed to be approximately $D_{zz} = 0.19$, $D_{xx} = D_{yy} = 0.4$ using the analytical approach in [44].

In the case where zero mechanical stress is applied to the MMSMA, the sample will magnetize as shown in Fig. 3-1d in a uniform applied field. Per the discussion above, the meta-magnetic transition in MMSMAs consists of a concurrent magnetic and structural transition. Figures 3-1(d-f) depict the stress-induced meta-magnetic transition under a constant magnetic field, H, and varying mechanical load, σ, represented by large solid arrows at the N and S poles. Essentially, the magnetized austenite (Fig. 3-1d) begins to structurally transform to martensite upon mechanical loading. The temperature of the specimen is above A_f, thus superelasticity can be achieved. The magnetization of the sample is decreased as a result of the A to M transition, and is shown by fewer magnetic flux lines surrounding the specimen (Fig. 3-1e) as well as the martensite plates that form within the sample. Finally, when the stress-induced A to M transition is completed (Fig. 3-1f), the magnetic flux lines are virtually non-existent because the martensite phase in MMSMAs is non-magnetic [45]. Also note, the length of the sample is smaller in the loaded case when compared to the unloaded case. This is a result of applying a uniaxial strain which is decomposed into a transformation strain, ε_{tr}, and an elastic strain, ε_{el}. These fundamental assumptions are used in quantifying the average sample magnetization of a uniformly magnetized MMSMA specimen during isothermal/isofield compression tests and they will be discussed more in subsequent sections.

3.2 Testing principles and test frame capabilities

3.2.1 General description

A magneto-thermo-mechanical characterization (MaTMeCh) device was designed and constructed to analyze and measure the multiferroic responses explained above. The completed test rig was capable of applying 200MPa of uniaxial compressive stress to a 4mm × 4mm × 8mm sample along its longitudinal direction. Magnetic field levels between 0-9T were generated collinear to the mechanical load by an external NMR magnet surrounding the mechanical load frame. The NMR magnet was a vertical field Cryomagnetics NMR solenoid housed in a KD-601 Series LHe dewar on an 18 inch tall tripod along with a Cryomagnetics magnet controller power supply. Within the mechanical loading rig, the specimen temperature could be swept or set anywhere between -100°C and 80°C. Additionally, to prevent icing around the test rig's critical components and sensors, the sample chamber was evacuated to rough vacuum prior to experimentation.

Figure 3-2a is a cross section of the experimental apparatus and surrounding magnet dewar. The MaTMeCh device housing, labeled as "1" was of grade 2 titanium construction for its strength, machinability, and non-magnetic behavior. Three windows were cut via electro-discharge machining (EDM) at the top of the housing intended for sample installation and adjustment of sensors. Parts "2" and "3" are the bottom and top pushrods, respectively, machined from grade 2 Ti and beryllium-Copper (BeCu) for thermal conductivity and strength. A BeCu snap ring and a custom titanium spring configuration (see parts 7 and 8 in Fig. 3-2a) were used to apply a bias upward force of about 6lbf (~25N) on the MMSMA sample located in the section labeled "Detail A". This

bias force was intended to keep the MMSMA stationary during complete mechanical unloading under high magnetic field levels. Ideally, the test frame was designed so that the sample would be located in the field center and no body force was generated, however, the actual uniformity of the field was only roughly measured using our magnetic sensors as discussed later. Thus, as a safety measure, the bias force was implemented.

Above and below the sample were high strength non-magnetic ceramic inserts which were employed due to the large local stress concentration generated by compressing a small rectangular sample. Non-magnetic metals would have mechanically failed if implemented, here, due to their low yield strengths. Preliminary finite element simulations predicted approximately 200 kPSI (1.4GPa) of local stress at the sample interface when 200MPa was applied to the sample by the surrounding push rods. The bottom ceramic insert (custom sized Al_2O_3 bar) is more visible in Fig. 3-2b. Each component labeled in the schematic of Fig. 3-2a is described in the figure caption.

Individual parts of the test frame were designed using AutoCAD 2014 and 3D models were uploaded and converted to SolidWorks files to be analyzed with the SolidWorks finite element analysis software. The von Mises stress of each load bearing piece was determined under the maximum design load of 1200lbf and the computed stresses were compared with selected material yield stresses. A factor of safety of 1.5 was used in the design and sizing of the load bearing components.

A USB-2408 DAQ system with onboard cold-junction compensation was used to log temperature, mechanical load, uniaxial displacement, stray magnetic field, and applied magnetic field with a custom LabVIEW program. The actuator supplying the mechanical

compressive load communicates with the CPU via a USB-RS485 converter and is controlled with the same custom LabVIEW program. Two programs were written; one was intended for superelastic loading up to a specified load limit and the other was used to hold the mechanical load constant during temperature sweeps or field ramping. The constant load LabVIEW sequence was programmed with displacement limits in the case of sample failure.

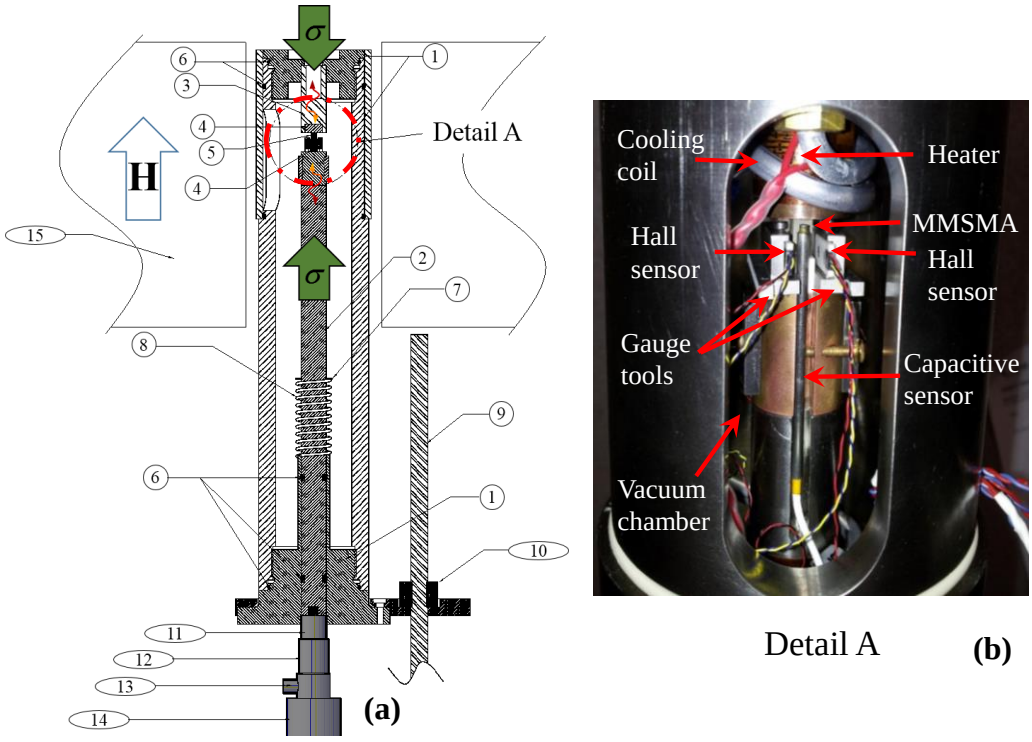

Figure 3-2: A cross-sectional view of the magneto-thermo-mechanical characterization (MaTMeCh) device (a). Parts are labeled as 1: grade 2 titanium housing, 2: bottom push-rod, 3: upper push-rod, 4: ceramic inserts, 5: MMSMA specimen, 6: O-rings, 7: BeCu snap ring, 8: titanium spring, 9: acme threaded tension rod, 10: brass nut, 11: spherical Ti-6-4 connection rod, 12: flat Ti-6-4 connecting rod, 13: load cell, 14: actuator thrust arm. Detail A from (a) is depicted in (b) to illustrate the specimen stage area during testing.

The sections below describe thermal, mechanical, and magnetic control and measurements, respectively, in more detail. Additionally, calibration is briefly discussed and, finally, a few sample results of the MaTMeCh device are presented.

3.2.2 Thermal control and measurements

To measure the shape memory effect (SME) explained above, thermal sweeps of the compression samples were achieved via conduction through the compression rods. Non-magnetic polyimide ultra-thin heater sheets with adhesive backings were wrapped around to the top and bottom compression rods. The top and bottom heaters were wired in parallel such that activation/deactivation of the heaters occurred simultaneously via a CN8200 series OMEGA Inc. PID controller. Heaters were wired using a 12-Cu lead vacuum feedthrough threaded into the bottom housing of the test rig.

Conax Technologies vacuum feed-throughs constructed of 316SS were employed to make electric connections within the sample vacuum chamber. One feed-through was used for wiring the heaters and other sensors, and the other housed 6-T-type thermocouple wire pairs. Thermocouple pairs were welded and then placed at various points in the sample chamber to monitor temperature, as well as directly on the sample surface using a Teflon string and GE varnish.

Around the strip heaters aluminum tubing was wound. Liquid nitrogen was flowed through a connection at the bottom of the sample chamber, which in turn cooled the compression rods and conducted heat away from the sample. Rubber tubing was used for connections between aluminum windings. The surrounding environment was evacuated to rough vacuum during testing. An external cryogenic solenoid valve with 304SS

construction was implemented to flow pressurized (~50psi) liquid nitrogen through the aluminum tubing and was opened and closed via the same PID controller that activated the heaters. Nitrogen liquid/gas was channeled out the top of the test frame after cooling the internal parts. PID controllers were auto-tuned to identify integral and derivative parameters. A set-point was then programmed into to the PID controllers for isothermal tests with the T-type thermocouple on the specimen supplying the temperature feedback. Additionally, a program was written in the PID controller between a lower and upper set-point such that the controller activated/deactivated the heaters and solenoid valve at appropriate times to achieve the temperature sweeps at a specified rate.

3.2.3 Mechanical measurements

Uniaxial stress-strain was measured using an Interface WMC sealed stainless-steel mini load cell and a Capacitec HPC-40 series capacitive sensor, respectively. The load cell was limited to a maximum load of 2000lbf and the capacitive sensor was capable of measuring distances up to 1.2mm from the target plate. The load cell (part 13 in Fig. 3-2a) was located outside of the strong stray field generated by the NMR magnet (part 15 in Fig. 3-2a). The small stray field on the load cell generated by the magnet (~0.2T), when charged from 0 to 9T, generated a small body force on the load cell determined by observations once the system was assembled. This produced errors in uniaxial stress measurements no larger than 5MPa during field sweeping. Uniaxial displacement was measured with the capacitive sensor next to the sample as shown in Fig. 3-2b. This configuration employed the top compression plate as the sensor electrical “ground” target plate. This configuration negated any additional strains developed along the load train. It

is important to note that capacitive sensors are immune to magnetic fields over a wide range of temperatures, but they are not immune to icing. At low temperatures ice will form at the capacitive sensing tip and influence displacement readings. This problem was addressed by evacuating the sample chamber with a roughing pump prior to testing and flushing the chamber with dry nitrogen gas.

Finally, since MMSMAs can exhibit a significant elastocaloric effect (~8K) from the stress-induced phase transformation [10], mechanical testing is often performed slowly, for isothermal tests, or quickly, for "adiabatic" tests [10]. Typically, mechanical tests involving shape memory alloys were considered isothermal when loaded at strain rates no faster than $5 \cdot 10^{-4} \frac{\varepsilon}{s}$. In this study, specimen were strained no faster than $2.5 \cdot 10^{-4} \frac{\varepsilon}{s}$ to ensure the measured response was isothermal.

A custom actuator was designed by Mechatronic Techniques, LLC under the given design constraints to supply the compressive force. The finished actuator is capable of applying a maximum of 2000lbf and 1200lbf of continuous force at every actuation velocity of interest and exhibits a 3.5in (90mm) stroke length to assist in positioning the MaTMeCh device to the appropriate height within the NMR magnet. A Nanotec PD4-N stepper motor drives a 1:100 gearbox reducer which then rotates the spindle drive via a belt. The gearbox slows the drive speed to rates acceptable for isothermal measurements as discussed later in the calibration section. As shown in Fig. 3-2a, a spherical compression fitting (part 11) was designed and threaded to the load train such that the bottom pushrod only exhibited one contact point with the mating actuator. This minimized asymmetry in

the compressive load and ensured proper parallelism with the compression sample's edge and the compression plate as well as prevented premature fracture of the specimen.

3.2.4 Magnetic measurements

In the introduction, the physical mechanisms describing uniformly magnetized rectangular bars were outlined. To measure the volume average magnetization of the MMSMA in our apparatus, during a compression test, the stray field was analyzed with the use of Hall sensors. A correlation between the horizontal field along the [001] direction (pictured in Fig. 3-1d) and a vertical magnetization in the [100] direction can be quantified for an ideal case using finite elements. This correlation can then be used for computing magnetization. Here, the magnetostatic module of COMSOL Multiphysics 4.3a was employed for magnetic simulations.

The magnetic simulations consisted of a rectangular bar in free space that was uniformly magnetized along the longitudinal direction at 120emu/g, i.e. 960,000A/m assuming a mass density of 8000kg/m^3. The 3D simulation geometry is illustrated in Fig. 3-3a. No magnetic fields were applied in the simulation, but rather a uniform magnetization in the sample geometry was applied in the 'y' direction. Only the stray field resulting from the magnetization was computed in the simulations.

Circles representing the active area of the Hall element were drawn at various distances from the sample edge, such that the centerline of the circles corresponded to the mid-plane in Z, i.e. the middle of the bottom edge, of the magnetized bar. These are also illustrated in Fig. 3-3a. Assuming the sample is uniformly magnetized in the positive y direction, a stray field is generated in the x direction as shown by the red arrows in Fig. 3-

3b. Here, the demagnetizing field at the mid-plane (in Z) is plotted and white lines represent example locations of the simulated hall sensor elements. As shown by the red arrows, some stray field passes perpendicularly through the Hall element. This magnetic field, B_X ,was then integrated (see Fig. 3-3c) over the circular areas at various distances from the sample edge and the ratio between the measured field and the magnetization was computed as [36]

$$f = \frac{B_X}{\mu_0 M_y}. \tag{3.4}$$

In Eqn. (3.4), B_X is the average magnetic field over the simulated circular area shown in Fig. 3-3c, M_y was the average sample magnetization in A/m, and μ_0 is the permeability of free space. Interestingly, for a given distance from the sample surface, f remains constant no matter the magnetization level of the magnetized bar. In other words, the horizontal field measured in the hall elements varies linearly with sample magnetization at a constant location in space. The ratios computed with Eqn. (3.4) are plotted in Fig. 3-3d as a function of distance from the sample edge for different specimen geometry. In practice, the M_y is unknown and B_X is measured at a set distance from the sample edge. The magnetization can then be computed using the simulated f values.

As shown in Fig. 3-3d, the slope of f decays with increasing distance from the sample edge. This implies that minor errors in placement of the hall sensors will result in large errors in the computed magnetization [36]. In this study, this error is minimized in three ways. First, an opposing hall sensor configuration is employed, as discussed in [36],

where it was shown that taking the average magnetization measurements from two hall sensors equally spaced from the sample edge minimizes the error from misplacing a probe during experimentation. Secondly, the Hall elements were placed at 2.1mm from the sample edge. As shown in Fig. 3-3c, the slope of f is near a minimum at this distance. Finally, gauge tools, i.e. positioning forks, were cut from aluminum stock via wire EDM to ensure the Hall sensors were placed with an accuracy of 0.1mm from the sample edge. These positioning forks are shown in Fig. 3-2b.

Additionally, the thickness of the ceramic coating on the cryogenic hall sensor was considered when designing the thickness of the positioning forks. During compression, however, the MMSMA will strain laterally. The lateral strain was measured using a micrometer when the MMSMA was strained uniaxially up to 5%. The lateral strain was measured to be only 0.25% (0.01mm displacement), thus resulting in a negligible change in D or f during the compression tests in this study.

Here, two Lakeshore HGCT-3020 Hall cryogenic hall sensors were employed with a Lakeshore model 460 3-channel gaussmeter. The change of magnetic sensitivity of the sensors was approximately 0.1% across -100°C to 80°C. The active area of the Hall sensors was reported to be 0.817mm^2 through personal communication with Lakeshore Cryotronics. An analog voltage was sent from the gaussmeter to the DAQ board which was then translated to stray field. The gauss meter applied a linear calibration curve of ±10V to -300mT to 300mT or -3T to 3T as defined by the user settings.

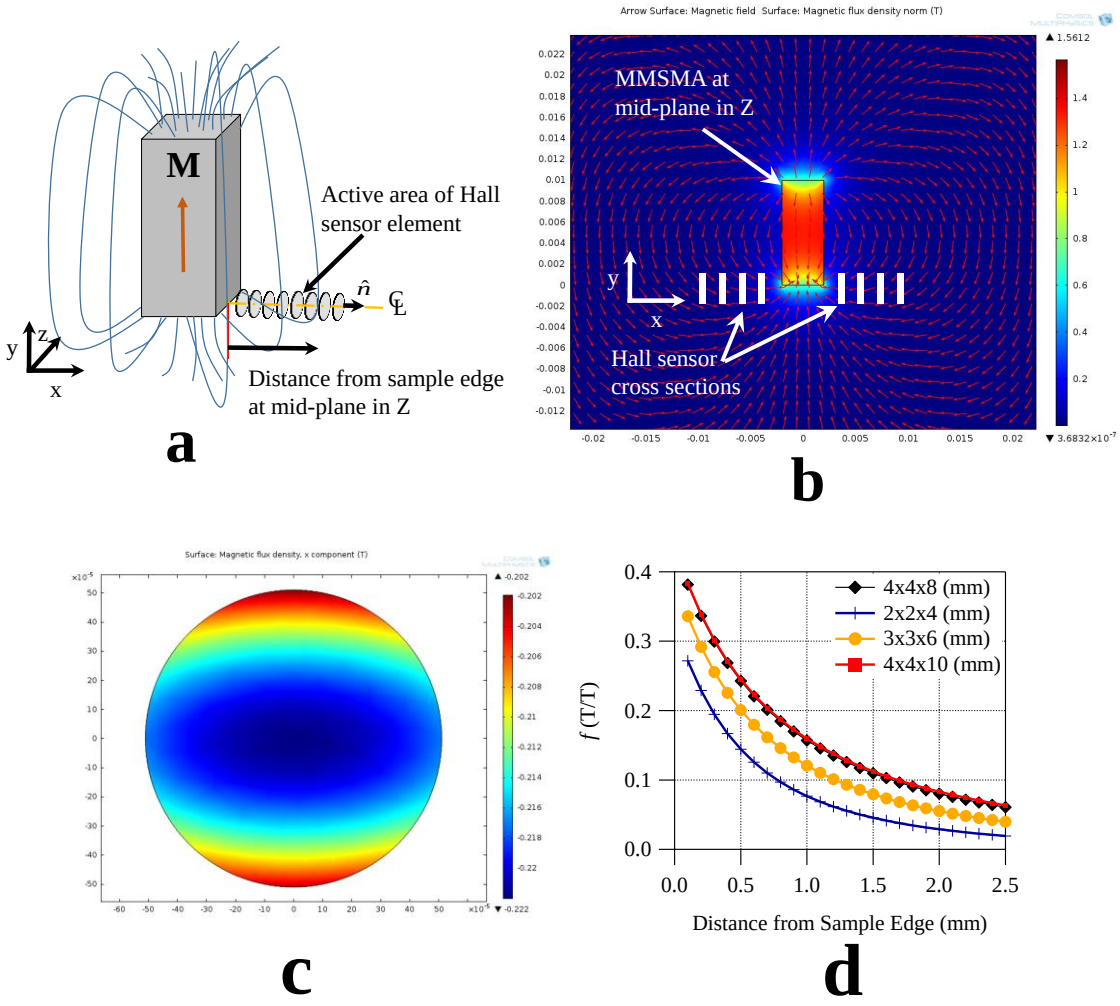

Figure 3-3: The 3D simulation geometry (a) is illustrated. Blue lines indicate magnetic flux and discs drawn with faces parallel to the sample surface represent the active hall sensor element. The normal direction of the Hall elements is indicated along the centerline as $\hat{n}$. The bar is magnetized vertically in the finite element simulation. No magnetic fields are applied. Magnetic field lines are represented as red arrows along a mid-plane slice of the sample in (b). White lines near the south pole of the magnetized sample in (b) represent cross-sections of the discs illustrated in (a). The magnetic field was integrated over these discs, as shown in (c). The ratio of the x-direction integrated magnetic field over the disk areas in (c) with uniform vertical magnetization is plotted as a function of distance to the sample edge (see Eqn. (3.4)) in (d).

3.3 Calibration

3.3.1 Magnetic calibration

To ensure that accurate magnetic measurements were collected with the MaTMeCh device, the field uniformity was first verified with the above mentioned Hall sensors. To measure the field, the sample was removed from the test rig and the hall sensor was fixed (with Kapton tape) on the Al_2O_3 sample seat to measure the vertical field.

NMR magnets are capable of producing highly uniform fields, and in this case, the test rig was designed to be extended within the bore up to a limit, such that the compression sample was within the uniform field. Not only does this ensure the field generated by the magnet matches that which is applied to the sample, but it also ensures that no body forces are generated by magnetic field gradients that could potentially move the sample during a test or generate additional stresses. In Fig. 3-4, the measured magnetic field within the bore of the magnet is plotted as a function of test frame extension. At 0, the test frame was fully extended. For all the tests conducted, described herein, the sample was located at -1.5 inches from full extension. This corresponded to approximately mid-stroke extension of the custom spindle drive actuator.

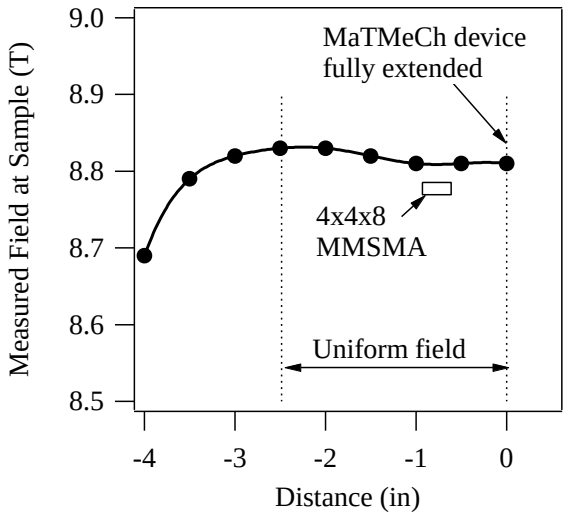

Figure 3-4: Measured vertically applied magnetic field within the superconducting NMR magnet up to the full extension of the test frame. Field begins to significantly deviate at -2.5 inches from the full extension. All tests were conducted at -1.5 inches of the full extension to ensure proper uniformity.

Next, the magnetization of whole compression specimens (~1g in mass) were measured in a Quantum Design magnetic property measurement system (MPMS) vibrating SQUID magnetometer (SQUID VSM). Measurements were collected at room temperature (~293K) under 0.01T. Longitudinally magnetizing the compression samples resulted in a measured magnetic moment of approximately 4.5emu/g. This number served as a baseline for magnetic measurements. Before starting MaTMeCh tests, the field in the superconducting NMR magnet was set to 0.01T and the LabVIEW-computed-magnetization was corrected by modifying f to match that reported by the SQUID VSM measurements.

3.3.2 Mechanical calibration

Calibration of the load cell was conducted using a set of Instron calibration weights, however, the capacitive displacement sensor used for measuring uniaxial displacement was not re-calibrated from factory conditions. Since the linear actuator was a custom build from Mechatronic Techniques LLC, manual calibration was needed.

To determine a calibration curve for the spindle drive, a capacitive displacement sensor was attached to the drive head of the actuator and a conductive steel plate was mounted above the sensor to serve as the target. The Nanotec motor was then activated at different frequencies and the displacement of the drive head was recorded in time. The calibration curve of the linear actuator is shown in Fig. 3-5. As mentioned above, a typical strain rate employed for isothermal mechanical measurements of MMSMAs is approximately $5 \cdot 10^{-4} \frac{\varepsilon}{s}$. For an 8mm long specimen, this translates to approximately 0.005mm/s. According to the calibration curve in Fig. 3-5, this corresponds to a rotation speed of 65Hz. However, we chose to use only 30Hz in the compression experiments, described in the next section, which corresponded to approximately 0.002mm/s and $2.5 \cdot 10^{-4} \frac{\varepsilon}{s}$.

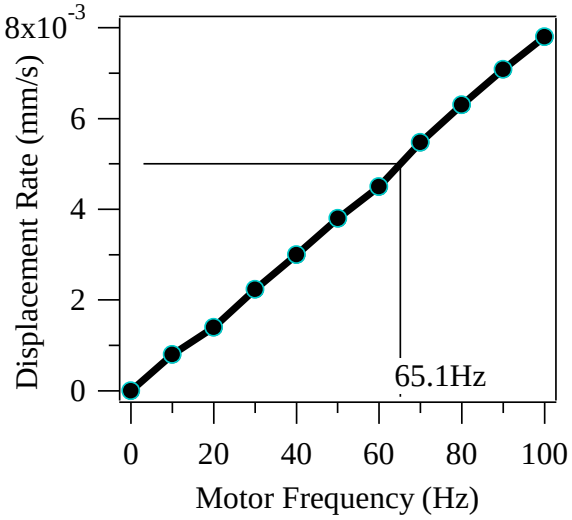

Figure. 3-5: The calibration curve for the custom spindle drive actuator from Mechatronic Techniques LLC.

3.4 Example results

3.4.1 SME in heating/cooling

Figure 3-6 shows the measured shape memory effect of a $Ni_{45}Co_5Mn_{36.6}In_{13.4}$ (at.%) single crystal under 25MPa compressive stress and 1T applied field along the [100] austenite direction. The A_f temperature of this sample was tuned by annealing [46] to be 18°C under zero stress and field conditions. The sample is heated and cooled at 2°C/min and was initially heated to 30°C. At 30°C it was assumed the sample exhibited zero compressive strain and the magnetization was measured to be approximately 81emu/g. This is comparable to SQUID measurements of a sample with similar heat treatment and composition [27]. Upon cooling, the MMSMA transforms to its martensitic phase below 10°C and exhibits approximately 5.7% transformation strain. The change in magnetization

of 92emu/g compares well with SQUID measurements under zero mechanical load. The small increase in magnetization from 30°C to 10°C, on cooling, is attributed to cooling below the Curie point of austenite. The thermal hysteresis across the transformation was measured to be approximately 11°C. Further testing will allow the shape memory effect (SME) to be measured under different fields and mechanical loads to study the influence of the hysteresis and transformation strain.

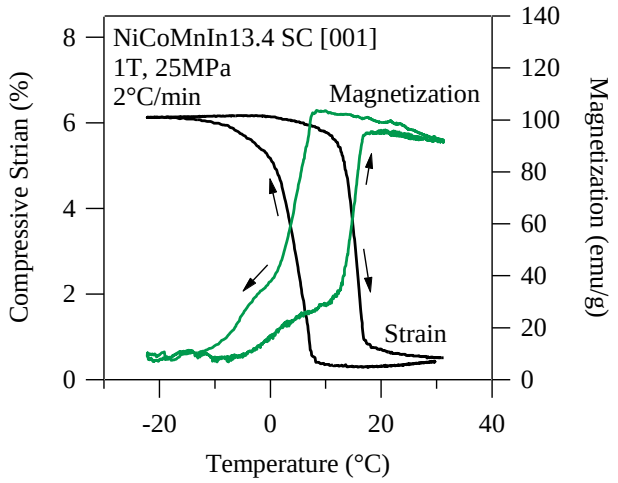

Figure 3-6: The simultaneously measured uniaxial compressive strain and average magnetization from heating and cooling at 2°C/min through the martensitic transformation in a $Ni_{45}Co_5Mn_{36.6}In_{13.4}$ single crystal. During heating and cooling, the compressive load was held constant at 25MPa and the magnetic field was 1T collinear to the [001] austenite crystal direction.

3.4.2 Superelasticity

Figure 3-7(a) shows the measured superelastic responses of a $Ni_{45}Co_5Mn_{36.6}In_{13.4}$ single crystal at 18°C under 0, 5, and 9T applied along the [100] austenite direction. In

this particular material system, the A_f temperature in zero stress or field has been identified as 18°C. Upon compressing the sample, the elastic response of austenite is measured as a 9.5GPa modulus of elasticity. At critical stress levels 40MPa, 87MPa, and 138MPa, martensite begins to nucleate in the microstructure, respectively. Under normal conditions, the MMSMA can be loaded beyond the transformation strain limit to observe the elastic response of the stress-induced martensite. In this study, however, we did not strain the material beyond 7% to protect its microstructural integrity. Loading the MMSMA into the elastic martensite regime will produce dislocations and cause premature brittle failure. This is well documented in other studies [47]. Nevertheless, the modulus of elasticity of martensite can be extracted from the data obtained during mechanical unloading and was determined to be 17.2GPa.

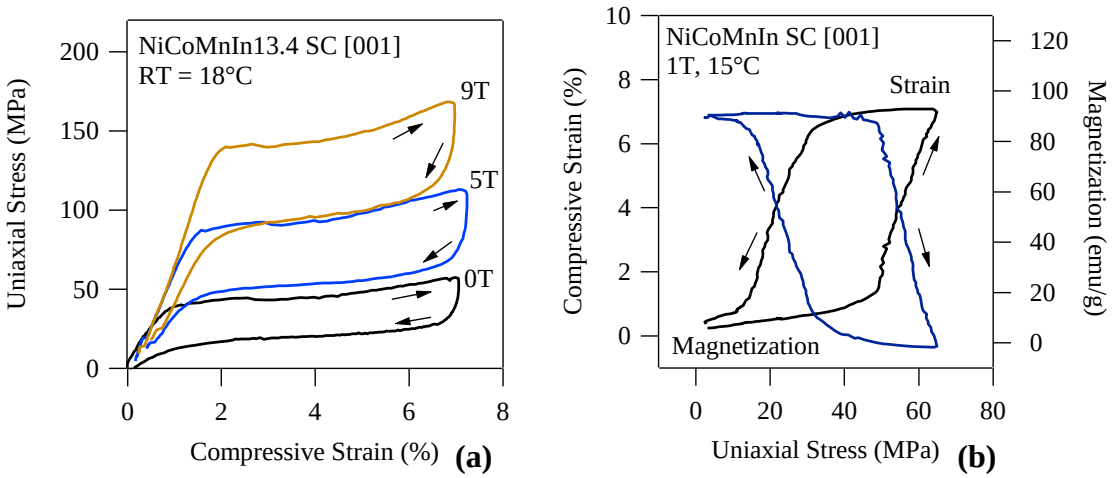

Figure 3-7: The superelastic curves for $Ni_{45}Co_5Mn_{36.6}In_{13.4}$ single crystals compressed along the [001] austenite crystal direction under 0, 5, and 9T fields; the test was conducted at a constant 18°C (a). The superelastic response and simultaneously measured stress-induced demagnetization behavior is plotted in (b) for the same single crystal under 1T at 15°C.

As expected, when large magnetic fields are applied to the specimen, larger mechanical loads are needed to induce superelasticity. This phenomenon is caused by the fact that the magnetic field stabilizes, or favors the ferromagnetic phase (austenite). In practice, applying magnetic fields to MMSMAs reduces the transformation temperatures. Since the temperature of this isothermal test was a constant 18°C, but a magnetic field was applied to the MMSMA, more energy needed to be overcome by the applied mechanical energy to initiate the transformation. This is known as magnetostress and is related to the difference in Zeeman energy between austenite and martensite [18]. From the data in Fig. 3-7a, the magnetostress was determined to be about 12.8MPa/T, only half of what was previously reported for a similar composition [18]. The small level of magnetostress was unexpected and may have been a result of the thermal treatment applied to the MMSMA to move the transformation temperature to 18°C.

Additionally, the increase in stress hysteresis with increasing magnetic field was not expected. Under 0T, the stress hysteresis was measured to be 25MPa. From increasing the field from 5T to 9T, the stress hysteresis increased from 38MPa to 47MPa. This increase could be due to a mechanical training effect from cyclic mechanical loads, or due to the selection of martensite variants produced by applying magnetic fields in the [001] direction. More studies are needed to identify the cause of increasing stress hysteresis with larger applied magnetic fields.

Finally, to demonstrate the magnetization measurement capabilities of the MaTMeCh device during isothermal/isofield compression, Figure 3-7b shows the superelastic and magneto-structural coupling of the same compression sample at 15°C

under 1T applied collinear to load. The mechanisms defining this type of test are illustrated in Figs. 3-1(d-f). Again, the sample was only compressed to 7% strain to prevent premature failure. Since 1T was applied, the transformation temperatures of the MMSMA experienced a decrease, thus, the sample transforms from A to M at 50MPa at 15°C rather than 40MPa (in 0T) at 18°C as illustrated in Fig. 3-7a. The magnetization is measured to drop approximately 90emu/g across the stress-induced martensitic transformation.

3.4.3 Magnetic field induced strain

The completely reversible magnetic field induced transformation under 52MPa constant load is shown in Figure 3-8. Prior to field ramping, at 18°C, the MMSMA was compressed to its martensitic state from austenite. Once the sample was completely comprised of martensite, the field was ramped from zero to 6T at approximately 50Oe/s (0.3T/min). This is comparable to the field ramping rates used in the above mentioned SQUID magnetometer for isothermal measurements. Under about 4.1T the stress-induced M to A transition began and it finished around 5.3T. On removing the field, the A to M transition began slightly below 2T and completed around 0T. The magnetic hysteresis under 52MPa was measured to be about 4.0T and the reversible MFIS was measured to be about 5.4%. Further studies will be conducted using the MaTMeCh device to identify the role of mechanical load on the magnetic hysteresis observed in MFIT experiments.

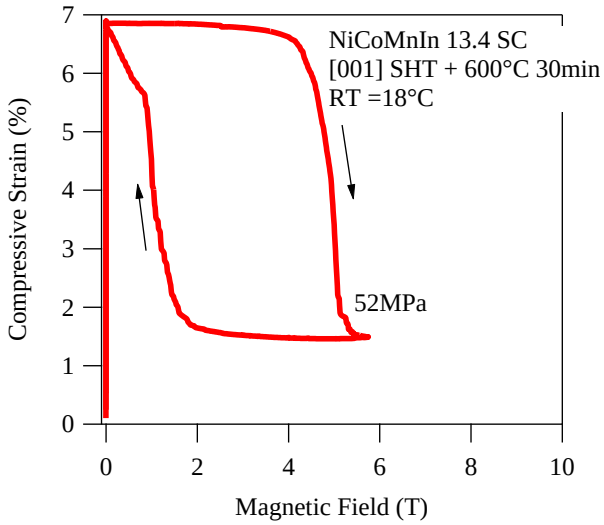

Figure 3-8: The fully recoverable magnetic field induced strain (MFIS) of a $Ni_{45}Co_5Mn_{36.6}In_{13.4}$ single crystal uniaxially compressed under 52MPa along the [001] austenite crystal direction. The test was conducted at 18°C.

3.5 Conclusions

A magneto-thermo-mechanical characterization (MaTMeCh) device was designed, assembled, and implemented for studying the martensitic transformation behaviors of meta-magnetic shape memory alloy single crystals. The robust device accommodates -100°C to 80°C test temperatures, 0-200MPa uniaxial compressive loads, and 0-9T collinear-to-load magnetic fields. Uniaxial stress, strain, volume average magnetization, applied magnetic field, and temperature are measured simultaneously. The mechanical load and magnetic field are driven independently, therefore, the MaTMeCh device is suitable for studying the effects of mixed loading conditions on single crystalline, or polycrystalline, compression bar samples. In this report was have discussed the shape memory effect, superelasticity, and magnetic field inducted meta-magnetic transitions, in

detail, and these served as a baseline for the MaTMeCh device design criteria. Finally, the testing capabilities were demonstrated by a few example data sets. Systematic studies are underway on $Ni_{45}Co_5Mn_{36.6}In_{13.4}$ single crystals and more experimental results will be presented at a later date.

CHAPTER IV

THE DEVELOPMENT OF A PERFORMANCE CRITERIA FOR FINDING OPTIMAL MATERIALS PROPERTIES*

4.1 Overview

Since the discovery of second order magnetic transitions, the magnetocaloric effect has been of interest to the scientific community. It was well known that these second order effects could be quantified using equilibrium thermodynamics, with the equations in Chapter 1, but the thermodynamic relations describing their performance in refrigeration processes were not formally developed until the 1980's. These relations were originally derived assuming that the magnetocaloric working refrigerant exhibited a second order magnetic transition. As demonstrated above the governing equations for second and first order magnetic transitions need to be derived separately simply due to the differences in the underlying physics that generate the two caloric effects, i.e. changing heat capacity in second order transitions and the latent heat of a structural transformation in first order transitions.

The objective of this chapter is to extend an existing thermodynamic framework that quantifies the refrigeration performance from second order transitions in non-shape memory alloys (SMAs), to the first order transitions exhibited by SMAs by employing the governing equations for first order phase transformations (FOPTs) into a previously

---

*Part of this chapter is reprinted from *Acta Materialia*, **74**, Bruno N. *et al.* The effect of heat treatments on Ni43Mn42Co4Sn11 meta-magnetic shape memory alloys for magnetic refrigeration, 66-84, Copyright (2014), with permission from Elsevier.

derived performance criteria. It will be shown that extending the framework can be achieved by employing a few reasonable assumptions and that making these assumptions ultimately reveals important materials parameters that are easily tuned in the SMA with thermal processing. Substituting expressions for the entropy change and adiabatic temperature change from FOPTs into the performance criteria has never before been done, and as a result, the refrigeration performance in MMSMAs was found to be controlled by only a few materials parameters. Modifying these parameters, in turn, changes the refrigeration performance, thus revealing the possibility of optimizing their MCE or ECE responses.

Specifically, the refrigeration performance of a SMA magneto- or elastocaloric refrigerant depends on the irreversibility that arises from the structural hysteresis and elastic strain energy storage across FOPTs. In addition, their operating temperatures in a thermodynamic cycle must be carefully considered. Here, quantities including the refrigerant capacity (RC), relative cooling power (RCP), the magnitude of critical driving forces for field cycling, and other efficiency ratios are discussed and developed. A simple relation is derived and used later in this work to describe the MMSMAs energy conversion efficiency around the FOPTs.

4.2 Wood and Potter's refrigerant capacity

In 1987, Wood and Potter developed the idea of refrigerant capacity (RC) to describe the refrigeration performance of materials exhibiting second order magnetic transitions. This parameter describes how much thermal energy can be transferred through a temperature gradient by a working magnetocaloric material. Thermal energy is defined

by the first term of Eqn. (1.5), and therefore, "thermal work" is generated by moving this thermal energy across a temperature gradient.

Figure 4-1 shows how the RC is computed from an entropy vs. temperature diagram for conventional non-SMA magnetocaloric refrigerants [12]. On the top of Fig. 4-1, the entropy vs. temperature diagram (see Fig. 1-6) for a ferromagnetic material is depicted around its Curie temperature, T_{curie}. The magnetic Curie temperature is labeled by an orange dashed line. On the entropy vs. temperature diagram (Top), the black curve indicates the entropy of the material under zero magnetic field, and the green curve indicates a decrease in the entropy due to the applied field, $H > 0$. On the lower half of Fig. 4-1, the entropy change vs. temperature is plotted corresponding to the difference in the entropy curves on the top half of the figure.

As shown by the bottom half of Fig. 4-1, an entropy change, ΔS_c, is achievable at temperature T_c, and an entropy change of ΔS_h is achievable at temperature T_h. These temperatures correspond to the cold and hot reservoirs of a magnetocaloric refrigeration cycle, respectively. In [12], the refrigeration capacity (RC) was defined as the product of the entropy change achieved at the cold reservoir of a refrigeration cycle and the temperature gradient, i.e. the difference in temperature of the hot and cold reservoirs, $\Delta T = T_h - T_c$. This is shown by the shaded region on the bottom of Fig. 4-1 and is defined by

$$W_{rev} = RC = \Delta S_c \cdot \Delta T. \tag{4.1}$$

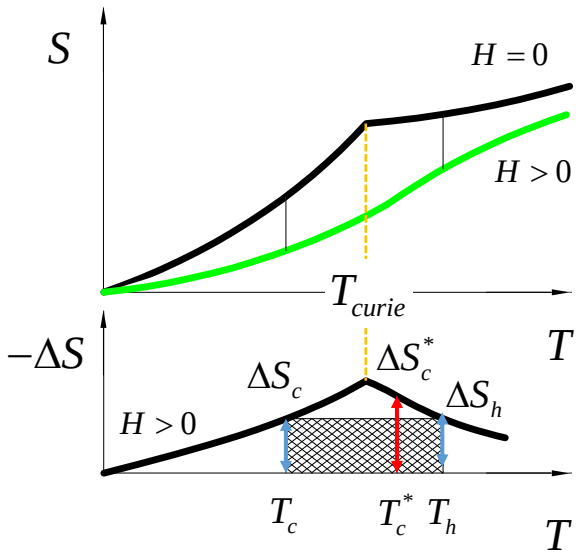

Figure 4-1: (Top) Entropy versus temperature curves for zero (black) and constant (green) magnetic fields around a magnetic Curie point, T_{curie}, and (bottom) the difference between the curves in (Top).

The goal of much present-day research is to increase the RC in state of the art MCE materials [48]. One might assume that changing the cold temperature reservoir to a temperature greater than T_c, say to T_c^* in Fig. 4-1, may increase the RC due to the fact that $\Delta S_c^* > \Delta S_c$. This would result in an increase in Eqn. (4.1). It was shown in [12], however, that this violates the second law of thermodynamics and that the entropy change at the hot temperature reservoir must always be greater than or equal to that at the cold reservoir, $\Delta S_h > \Delta S_c$. This implies that the hot and cold temperature reservoirs for a given refrigeration cycle must be selected very carefully for non-SMA calorific materials to maximize the RC.

In the best case, i.e. a completely reversible MCE, the entropy change at the temperature reservoirs are equal, that is to say $\Delta S_c = \Delta S_h$. However, in real processes, irreversibility is generated in the form of heat, and the entropy change at the hot temperature reservoir will always be greater than that at the cold, $\Delta S_c \leq \Delta S_h$. Taking this into consideration, the real work performed on the magnetocaloric material over a refrigeration cycle can be computed as [12]

$$W_{real} = \Delta S \cdot \Delta T + S_{irr} T_h - Q_l - Q_f \tag{4.2}$$

where S_{irr} is the entropy produced by all irreversible processes and released at T_h, Q_l is the work loss to heat leaks in the refrigeration cycle, and Q_f is the work lost to friction.

4.2.1 Coefficient of performance

In [12] a thermodynamic figure of merit was developed to determine the optimal operating temperature range in non-SMA MCE refrigerants. This figure of merit, η, was the ratio of reversible work (Eqn. 4.1) to real work (Eqn. 4.2) over one thermodynamic cycle, i.e.

$$\eta = \frac{W_{rev}}{W_{real}}. \tag{4.3}$$

Often, ratios like the one shown in Eqn. (4.3) are used to quantify the efficiency of a thermodynamic process. Later it will be demonstrated that a similar ratio can be used to probe at the energy conversion efficiency of the MMSMA across FOPTs.

4.3 Pecharsky and Gschneidner's relative cooling power

In 2000, Pecharsky and Gschneidner developed a similar thermodynamic parameter to the one in Eqn. (4.1) for comparing the performance of magnetocaloric refrigerants [49]. Instead of naming the performance term the "refrigerant capacity", they described it as the "relative cooling power" (RCP) and explicitly stated in [49] that the RCP has no physical meaning. Instead, the RCP is only useful for comparing MCE materials. Figure 4-2 is an example of how the RCP can be computed from entropy change versus temperature diagrams for a Gd single crystal [49].

In [49], the RCP of MCE materials was determined by multiplying the maximal entropy change at the ferromagnetic Curie temperature, $\Delta S^{\max}$, to a temperature range arbitrarily selected at full width-half maximum (FWHM) of the ΔS vs. T curve . This is shown in Fig. 4-2 by a horizontal solid like and two vertical dashed lines.

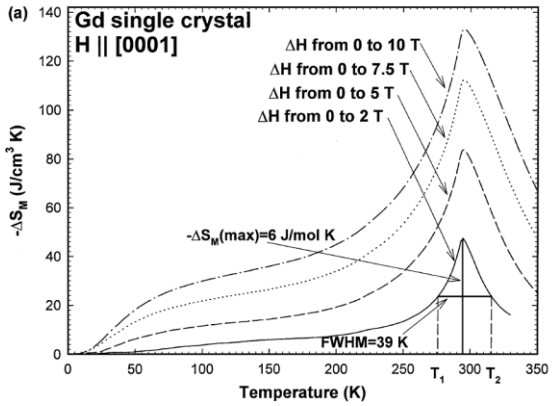

Figure 4-2: The entropy change vs. temperature diagram for Gd single crystals taken from [49]. The relative cooling power (RCP) is computed by multiplying the maximal entropy change to the temperature range of full width-half maximum of the entropy change curve.

Fig. 4-2 shows a peak in $-\Delta S$ around 300K for Gd single crystals corresponding to the Curie point of Gd. Each curve represents the entropy change generated by applying different field levels. The lowest solid curve is the entropy change generated from applying 2T. The RCP can then be computed from this diagram by [49]

$$RCP(S) = -\Delta S^{\max} \cdot \delta T_{FWHM} \tag{4.4}$$

where δT_{FWHM} is the temperature difference between full width-half maximum (FWHM) of the ΔS vs. T curve. For the 2T curve in Fig. 4-2, the RCP is computed to be 234 J/cm3.

Although this shares the same units as the RC, described above, it does not share the same meaning. In Eqn. (4.1), the temperature gradient was selected carefully to represent that which energy was transferred in a thermodynamic cycle. In addition, the entropy change at the hot and cold sources were bound by the second law of thermodynamics. In the case of RCP, however, the temperature range has no physical implications and the entropy change used in its computation can only occur at the T_{Curie} .

Since the RCP has no uses other than to compare MCE refrigerants, it was shown that it can also be determined from adiabatic temperature change vs. temperature diagrams as

$$RCP(T) = -\Delta T_{ad} \cdot \delta T_{FWHM} \tag{4.5}$$

with units of K^2. In Eqn. (4.5), ΔT_{ad} is the adiabatic temperature change (see Eqn. (1.21)) of the MCE refrigerant corresponding to the $\Delta S^{\max}$ in Eqn. (4.4). Since the entropy change considered in Eqn. (4.4) is not that at the hot or cold reservoir, as it was in [12] for the RC, the RCP cannot be used to analyze a thermodynamic cycle. In addition, thermodynamic

losses are neglected in its computation which further reduces its usefulness in quantifying the performance of MCE materials. The next sections will discuss, in detail, the consequence of using the RCP to analyze MMSMA refrigeration performance. Using the RCP as a measure of refrigeration performance is commonly done in literature, thus, misleading results are often reported in magnetocaloric studies. Here, a few alternatives to the RCP are developed specifically intended to be used to compare the refrigeration performance of MMSMAs that exhibit a thermal hysteresis.

4.4 Magnetocaloric cycles and reversibility in MMSMAs

In sections 4.3 and 4.4, the RC and RCP are defined. Both of these parameters were originally derived for second order phase transforming materials. If used properly, the RC quantifies the thermal work generated by the MCE refrigerant. The RCP is a metric designed only for comparing non-SMA materials. Both generally assume that the isothermal entropy change, generated in a magnetocaloric material under a given magnetic field, is repeatable with field cycling. In meta-magnetic shape memory alloys (MMSMAs) the entropy change is only repeatable with field cycling at very specific initial temperatures and, therefore, Eqns. (4.1) and (4.4) should be used with extreme caution.

To illustrate the temperature dependence of the repeatable entropy change in MMSMAs, a Brayton cycle is depicted in Fig. 4-3. Figure 4-3 illustrates the idealized entropy vs. temperature ($S - T$) diagrams around a first order thermoelastic martensitic transformation upon cooling and subsequent heating, with (blue curve) and without (green curve) applied magnetic field, H. The S - T curve shifts to lower temperatures upon application of the field. The field reduces the transformation temperatures of the

MMSMAs and stabilizes the austenite where the austenite is ferromagnetic and the magnetic ordering of martensite is not magnetic. These idealized responses neglect the contribution of magnetic entropy to the total entropy in austenite and martensite phase regions, and thus, the conventional MCE behavior of martensite and austenite phases, for the sake of simplicity and ease of understanding the thermodynamic cycle. In addition, the diagrams assume, the forward transition range ($M_s - M_f$) is equal to the reverse transition range ($A_f - A_s$). The average of these transformation ranges, defined as $\Delta T_{elas} = \left[\left(A_f - A_s \right) + \left(M_s - M_f \right) \right] / 2$ is used in the following discussion. The transformation ranges are typically controlled by microstructurally stored elastic energy (see Eqn. (1.8)), and therefore the transformation range is denoted using the subscript "elas".

As shown in Fig. 4-3, the MMSMA initially begins the depicted Brayton cycle [50] at M_f (point 1 in the figure), or the hot reservoir of the cycle, T_{hot} . The schematics under the *S* – T plot in Fig. 4-3 represent microstructures of the material at specified points or regions in the *S* – *T* diagram. Upon the field application, H_{comp}^{ad} , which is sufficient to induce a complete adiabatic reverse martensitic transformation at M_f ($M: \text{Martensite} \rightarrow A: \text{Austenite}$), the sample exhibits endothermic behavior and cools to T_{cold} (point 3) if insulated from external heat sources. This temperature change is shown in the figure by the line $T_{hot} \rightarrow T_{cold}$ (region 2) and is directly related to the transformation entropy change. Next, the sample is exposed to the refrigerated volume and allowed to absorb energy, thus heating the sample comprised of field-induced austenite (see

$T_{cold} \rightarrow T_{\text{refrigerator}}$, point 4 in the figure). The sample is then removed from the refrigerated volume and the field is released under insulated conditions warming up the sample due to the forward transformation ($A \rightarrow M$), which is an exothermic process ($T_{\text{refrigerator}} \rightarrow T_{end}$, region 5). At this point (point 6 in the figure), the sample is exposed to ambient temperature and releases heat from the temperature T_{end} to T_{hot}, returning the sample to a temperature below or equal to M_f, which allows the process to be repeated. As shown on the abscissa in Figure 4-3, the operating temperatures which define the Brayton cycle are $T_{hot} \leq M_f$ and $T_{cold} = T_{hot} - \Delta T_{ad}$, where T_{cold} is the temperature that is achieved due to adiabatic magnetization of the sample and ΔT_{ad} is the adiabatic temperature change upon the field application (is $\Delta T_{ad}^{\max}$, if the transformation is complete) defined in Eqn. (1.34).

Clearly, if the RC from section 4.2 was computed for the MMSMA, the hot and cold temperature reservoirs of a thermodynamic cycle would be limited by its transformation temperatures. This was also observed in [51]. For the cycle in Fig. 4-3, the thermal work produced from field cycling can be defined by the size of the shaded area. Interestingly, for the cycle to be repeatable with field cycling, and in that sense equivalent to one attainable with second order magnetocaloric materials, the thermal hysteresis areas of the $S - T$ diagram should not contribute to useful thermal work. Neglecting the thermal work produced within the thermal hysteresis during computation of the RC allows for an accurate comparison of performance between second and first order magnetic transitions.

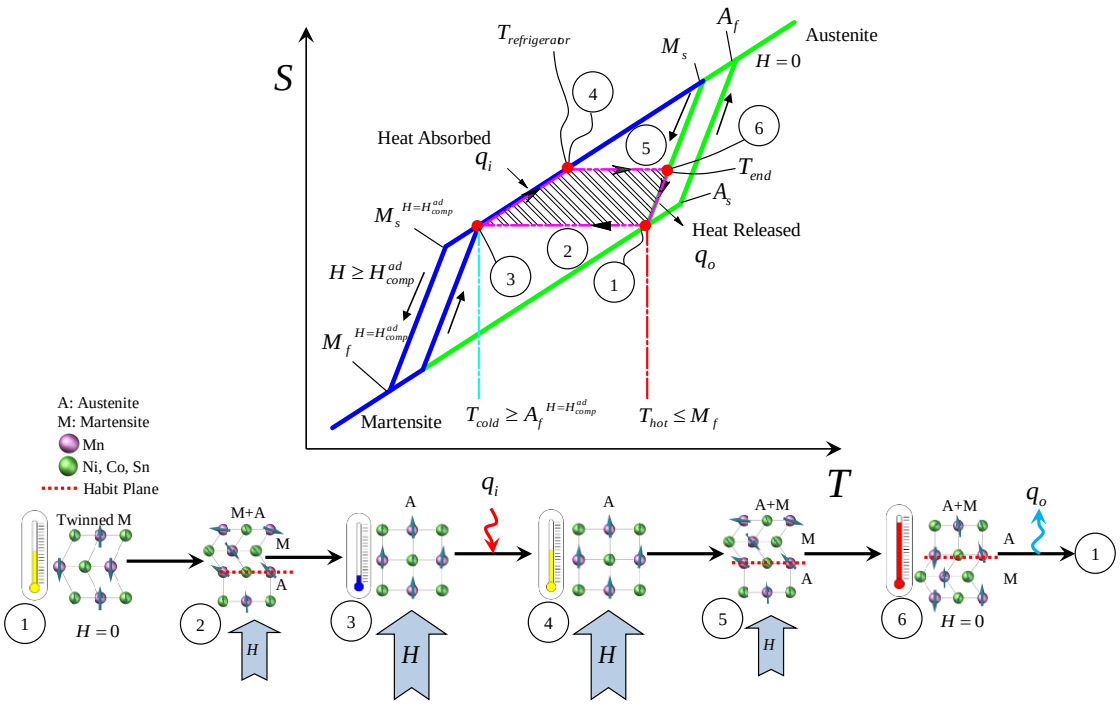

Figure 4-3: Example MCE Brayton cycle discussed in the text; The sample starts under zero magnetic field at M_f at point 1. An applied field nucleates austenite (region 2) and cools the sample to point 3. The sample absorbs energy to point 4 within the refrigerated volume. The sample is then removed from the refrigerated volume and adiabatic demagnetization occurs in region 5 to point 6. At point 6 the sample is allowed to cool to M_f from T_{end}. The hatched region indicates the work performed by the Brayton Cycle. The schematics underneath the S – T plot show the representative microstructure at a given point or region [50].

In the cycle depicted in Fig. 4-3, the ΔS_c is ambiguous as the MMSMA tends to heat from point 3 to point 4. This makes quantifying the entropy change at some isothermal reservoir, impossible. In fact, the MMSMA in Fig. 4-3 absorbs energy along an isofield line, instead of along an isotherm. Therefore, the next section is dedicated to quantifying

what is called the maximum thermal work [50] attainable in MMSMAs from their first order phase transformations.

4.5 Maximum thermal work in shape memory alloys

MMSMAs should theoretically be able to perform more thermal work than that specified by the shaded region within the Brayton cycle in Figure 4-3. This is illustrated in Figure 4-4 for a given applied magnetic field capable of inducing a complete adiabatic structural transformation, H_{comp}^{ad}. The theoretical maximum work, T_{work}, that a MMSMA can perform, is independent of thermodynamic cycles and is defined as the area of the shaded region in the ΔS vs. T plot in Figure 4-4b. However, this area is limited by the MMSMA transformation temperatures as mentioned above. Figure 4-4b is constructed based on the ideal $S-T$ diagrams shown in Figure 4-4a: at a given temperature, $\Delta S = S^{\text{Austenite at } H=H_{comp}^{ad}} - S^{\text{Martensite at } H=0}$, where $S^{\text{Martensite at } H=0}$ is the entropy of martensite under $H=0$, which fully transforms to austenite under $H=H_{comp}^{ad}$, and $S^{\text{Austenite at } H=H_{comp}^{ad}}$ is the entropy of the austenite under $H=H_{comp}^{ad}$, which transforms back to martensite under $H=0$. The temperatures limiting the shaded region were extended down from Figure 4-4a and areas of thermal transformation hysteresis, i.e. two phase regions, were not considered to contribute to reversible work upon field cycling.

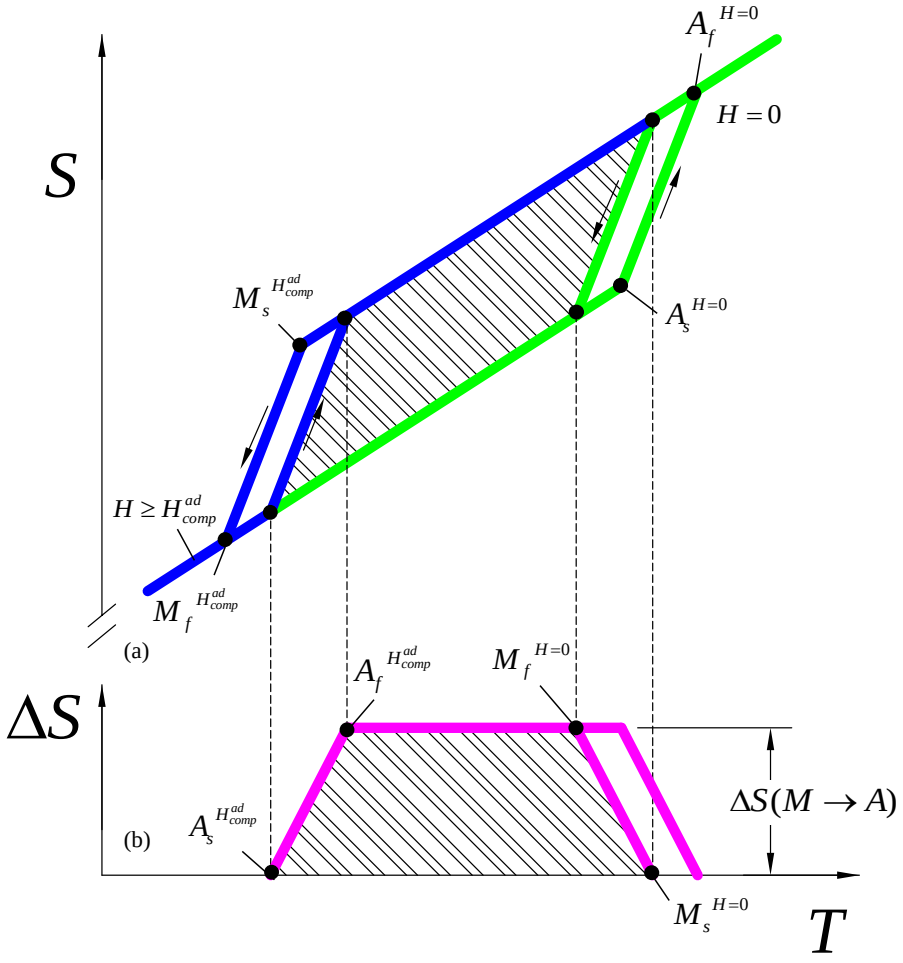

Figure 4-4: (a) Entropy vs. temperature plot for a meta-magnetic SMA under zero and H_{comp}^{ad} magnetic fields near the thermoelastic transformation. (b) Entropy change vs. temperature plot where the shaded region indicates T_{work}. The rectangular shaded region between $M_f^{H=0}$ and $A_f^{H=H_{comp}^{ad}}$ indicate the T_{work} in the temperature range where the total entropy change is reversible. The areas of the transformation hysteresis indicate the operating temperature ranges where the forward and reverse entropy changes during isothermal magnetization experiments are not the same, and are therefore cyclically irreversible [50].

It is clear from Figure 4-4b that the transformation temperatures and ΔS dictate the size of the shaded region that is used to determine the useful work, or T_{work}. Upon

closer inspection of Figure 4-4b, the elastic transformation ranges ($A_f^{H=H_{comp}^{ad}} - A_s^{H=H_{comp}^{ad}}$ and $M_s^{H=0} - M_f^{H=0}$) also contribute to the shaded region by amount $\Delta S \cdot \Delta T_{elas}$, however these operating temperatures can only be accessed if special thermodynamic processes are used that allow martensite to form at the start of each cycle. In addition, it can be seen that within the operating temperature range of $M_f^{H=0}$ and $A_f^{H=H_{comp}^{ad}}$, the maximum entropy change of the MSMA is achieved, and thus is capable of contributing to the T_{work} by the amount $\Delta S \cdot \Delta T_{ad}^{\max}$. For the Brayton cycle in Fig. 4-3, only part of this value was captured and it is believed that special thermodynamic cycles, possibly involving mechanical stress or regenerative cycles, can be used to access the entire theoretical values.

The example cycle in Figure 4-3 and depiction of T_{work} in Figure 4-4 clearly indicate the importance of studying the critical materials parameters to enhance the MCE/ECE in MMSMAs. It is shown in Figure 4-4 that a large T_{work} can be achieved if samples exhibit large adiabatic temperature changes, have large entropy changes across transformation, and have broad elastic transformation ranges.

Once the $\Delta S - T$ diagrams are constructed for a given MMSMA, the T_{work} is computed as the area of the shaded region in Figure 4-4b. The T_{work} is dependent not only on magnetic field, but also the martensitic transformation temperatures and is defined, here, as

$$T_{work}(H,T) = \Delta S^{M \to A} \cdot \left(\Delta T_{ad}^{M \to A} + \Delta T_{elas} \right) - \frac{S_{irr}}{2} \cdot \left(\Delta T_{ad}^{M \to A} + \Delta T_{elas} \right) \qquad (4.6)$$

where $\Delta T_{ad}^{\max}$ is the maximum adiabatic temperature change, ΔT_{elas} is the average of the forward and reverse elastic transformation ranges mentioned earlier, and $S_{irr} \cdot (\Delta T_{ad}^{\max} + \Delta T_{elas})$ is the thermodynamic loss upon the forward and reverse phase front motion associated with the transformation hysteresis. It is important to include this entropy production to avoid violating the second law of thermodynamics as discussed earlier.

Using the $\Delta S - T$ diagram in Fig. 4-4b to compute the RCP in Eqn. (4.4), it can be seen the RCP will over-predict the available thermal work in the MMSMA because it includes thermal work transferred across the thermal hysteresis. For example, the ΔS value in Eqn. (4.4) for MMSMA is simply the entropy change across the martensitic transformation, $\Delta S^{M \to A}$, and the full width half maximum δT_{FWHM} encompasses the thermal hysteresis. Including the thermal hysteresis while computing the RCP commonly done in literature, but as can be seen here, the results misleading.

The computed RC in Eqn. (4.1), however, gives the same value as the first term of T_{work}, i.e. the maximal thermal work generated from the latent heat of the martensitic transition. In T_{work}, terms have been added to include work obtained within the elastic transformation ranges, losses due to transformation hysteresis, and limitations have been set on T_{hot} and T_{cold} to correspond to the martensite transformation temperatures. Note that the adiabatic temperature change can be approximated using Eqns. (1.34) or (1.39).

The S_{irr} term in Eqn. (4.6) approximates the cooling power losses from the entropy production during the transformation process. The entropy production from the

transformation hysteresis is the hysteresis loss defined in [42] divided by the temperature of the isothermal magnetization tests [52] as,

$$S_{irr} = \frac{\xi(H) \cdot \Delta S^{M \to A} \cdot \Delta T_{hys}}{T} \tag{4.7}$$

which, if $\xi(H) = 1$, approximates entropy production for a complete transformation cycle. For magnetic fields that induce only partial transformation, the percent transformation, $\xi(H)$, is $0 < \xi(H) < 1$. In Eqn. (4.7), S_{irr} can be roughly determined by multiplying the transformation entropy, $\Delta S^{M \to A}$, by the thermal hysteresis of transformation, ΔT_{hys} under zero magnetic field and dividing by the temperature of the isothermal field-induced transformation. Only half the S_{irr} is considered in Eqn. (4.6) because in the refrigeration cycle, like that shown in Figure 4-3, the transformation front propagates only once during the cooling step ($T_{hot} \to T_{cold}$), but S_{irr} takes into account both forward and reverse phase front motion. Upon releasing the magnetic field outside of the refrigerated volume, the other half of frictional dissipation associated with the complete transformation is produced. This second half does not affect how much the sample will cool upon field ramping, but as shown in Figure 4-4b, the hysteresis does limit the operating temperatures and thus reduces T_{work}. Lastly, it is important to note that this approximation of entropy production from the martensitic transformation is assumed to be independent of rate. This, however, is not true in general and suggests a more accurate model must be developed in future studies to account for the rate dependence of entropy production.

4.6 Critical driving forces and magnetic field levels

In MMSMAs, the driving forces needed to transform the MMSMA are an essential consideration when quantifying refrigeration performance. The driving force is used in computing the work input of a refrigeration cycle or that which is needed to cool the sample, and also in computing efficiency ratios like that shown in Eqn. (4.3). In general, a driving force of $\mathbf{y}_{i,comp}^{ad}$ is required to complete the cyclic adiabatic transformation of the MMSMA at either the M_f or A_f temperature. Other important driving forces include those needed to induce and/or complete the isothermal transformation, $\mathbf{y}_{i,req}$ and $\mathbf{y}_{i,comp}^{iso}$, respectively. These force levels will be quantified, here, and then used later to compute the energy conversion efficiency of FOPTs.

The critical magnetic field levels needed to achieve MFIT are derived, first, followed by those needed for the stress induced transformations. In the case of magnetic field induced transformations, where martensite is non-magnetic and austenite is ferromagnetic, the transformation temperatures decrease with applied magnetic field as shown in Figure 4-5a. In Fig. 4-5a the right-most curve is the measured thermomagnetization curve of NiCoMnSn under 0.05T, denoted as H_1. On increasing the magnetic field to 7T, H_2, the curve shifts left. As shown by the red dotted line, increasing the field sufficiently will shift the temperature to be equal to the M_f temperature. If the

field is ramped isothermally at M_f, the transformation will take place under high enough fields. Therefore, applying a large enough magnetic field will generate the reverse M to A transformation at any temperature below A_s.

The generalized force, $\mathbf{y}_{i,req}$, needed to initiate the transformation the MMSMA at a temperature below A_s is defined as

$$\mathbf{y}_{i,req} = \left(A_s - T\right) \cdot \left| \frac{d\mathbf{y}_i^{A_s}}{dT} \right| \quad \forall T \le A_s \tag{4.8}$$

where $d\mathbf{y}_i^{A_s} / dT$ is the inverse of the A_s temperature's sensitivity to the applied driving force

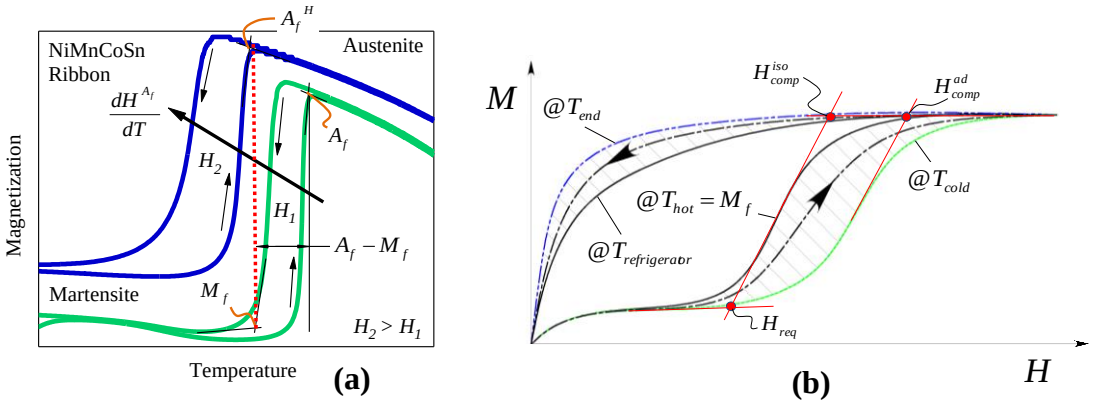

Figure 4-5: The thermomagnetic response of NiCoMnSn under zero magnetic field (green) and 7T (blue) (a) and an illustration of magnetization isotherms corresponding to temperatures in Fig. 4-3 (b) [50].

To completely transform the MMSMA under isothermal conditions at a temperature below A_s, the generalized force $\mathbf{y}_{i,comp}^{iso}$ can be computed as

$$\mathbf{y}_{i,comp}^{iso} = \left(A_f - T\right) \cdot \left| \frac{d\mathbf{y}_i^{A_f}}{dT} \right| \quad \forall T \le A_s . \tag{4.9}$$

Finally, if the transformation is adiabatic and the MMSMA exhibits a temperature change across the transformation, the generalized force needed to complete the transformation can be defined as

$$\mathbf{y}_{i,comp}^{ad} = \left(A_f - T + \Delta T_{ad}\right) \left| \frac{d\mathbf{y}_i^{A_f}}{dT} \right| \quad \forall T \le A_s , \tag{4.10}$$

where unlike Eqn. (4.9), the adiabatic temperature change is added to increase the required driving force by an amount equal to $\Delta T_{ad} \cdot d\mathbf{y}_i^{A_f} / dT$.

The critical driving forces for MFITs are illustrated in Figure 4-5b. The influence of the adiabatic temperature change can be observed by the dash-dot line connecting the two magnetization curves at $T = T_{hot}$ and $T = T_{cold}$. Figure 4-5b depicts the magnetic responses of a meta-magnetic SMA at different states in Figure 4-3. The magnetic response at M_f shows the magnetic field, H_{req}, needed to start the transformation. If the sample is to transform under isothermal conditions, the field required to complete the transformation would be defined by the same magnetization curve, and is labeled as H_{comp}^{iso}. However, the sample is insulated while the field is applied and an endothermic reaction occurs, as shown in Figure 4-3, thus the magnetic response is shifted to the right while the

sample cools and ultimately requires H_{comp}^{ad} to complete the transformation. From Figs. 4-3 and 4-5b, it can be deduced that $T_{hot} \le M_f$ and $T_{cold} \ge A_f^{H=H_{comp}^{ad}}$.

In the case of completely reversible MFITs at M_f, the generalized forces in Eqns. (4.8), (4.9) and (4.10), can be computed as magnetic field levels given as

$$H_{req} = \left(A_s - M_f\right) \cdot \left| \frac{dH^{A_s}}{dT} \right|, \tag{4.11}$$

$$H_{comp}^{iso} = \left(A_f - M_f\right) \cdot \left| \frac{dH^{A_f}}{dT} \right|, \tag{4.12}$$

and

$$H_{comp}^{ad} = \left(A_f - M_f + \Delta T_{ad}\right) \left| \frac{dH^{A_f}}{dT} \right|, \tag{4.13}$$

respectively, where the temperature T has been replaced with M_f and $\mathbf{y}_i$ with H. Using Eqns. (4.11), (4.12), and (4.13), the percent of transformed MMSMA is defined, (when $T_{hot} = M_f$) as

$$\xi(H) = \frac{H - H_{req}}{H_{comp}^{ad} - H_{req}} \times 100 \quad \textit{where} \quad H_{req} < H < H_{comp}^{ad} \tag{4.14}$$

where H is constrained between the minimum field required to induce transformation and the field required to attain complete transformation. For $H < H_{req}$ and $H > H_{comp}$, $\xi(H)$ obviously equals 0 and 1, respectively when considering only the reverse transformation. The fraction of transformation can then be used to determine T_{work}, and S_{irr} under any given field or transformed volume fraction.

Analogously, Eqns. (4.11) through (4.14) can be derived for superelasticity. In the general case of only A to M transformation, these expressions are

$$\mathbf{y}_{i,req} = \left(T - M_s\right) \cdot \frac{d\mathbf{y}_i^{M_s}}{dT} \quad \forall T \geq M_s \,, \tag{4.15}$$

$$\mathbf{y}_{i,comp}^{iso} = \left(T - M_f\right) \cdot \frac{d\mathbf{y}_i^{M_f}}{dT} \quad \forall T \geq M_s \,, \tag{4.16}$$

and

$$\mathbf{y}_{i,comp}^{ad} = \left(T - M_f + \Delta T_{ad}\right) \cdot \frac{d\mathbf{y}_i^{M_f}}{dT} \quad \forall T \geq M_s \,. \tag{4.17}$$

In the case of reversible superelasticity, they are defined as

$$\sigma_{req} = \left(T - M_s\right) \cdot \frac{d\sigma^{M_s}}{dT} \quad \forall T \geq A_f \,, \tag{4.18}$$

$$\sigma_{comp}^{iso} = \left(T - M_f\right) \cdot \frac{d\sigma^{M_f}}{dT} \quad \forall T \geq A_f \,, \tag{4.19}$$

and

$$\sigma_{comp}^{ad} = \left(T - M_f + \Delta T_{ad}\right) \frac{d\sigma^{M_f}}{dT} \quad \forall T \geq A_f \,. \tag{4.20}$$

In the next section, the above expressions for FOPTs are substituted into the RC framework in Eqn. (4.3). Essentially, Eqn. (4.3) can be used to identify key materials parameters that enhance performance. These can be modified using thermomechanical processing in MMSMAs. Eqns. (4.8) through (4.20) can be used to compute the applied work on the MMSMA, which is then compared to the MMSMAs capability to perform useful thermal work.

4.7 Ratios for identifying key material characteristics to enhance the giant caloric effects

As shown in Figure 4-3, the thermal work generated by the MMSMA is limited by the thermodynamic cycle in which it is employed. In Eqn. (4.6), we identified the maximum thermal work attainable by MMSMAs, however, some important parameters did not contribute to T_{work}. To identify material parameters that can be modified via thermal processing treatments, discussed in the next chapter, the performance criteria of the MMSMA must be decoupled from the thermodynamic cycle like was done for the T_{work} parameter, above. Additionally, the magnetic field levels needed to transform the MMSMA should contribute to the performance criteria of MMSMAs which was not considered in the T_{work} parameter. Employing Eqn. (4.3) will lend the ability to combine T_{work} and the driving forces defined in Eqns. (4.8) through (4.20).

Here, the refrigerant capacity (RC) resulting from the martensitic transformation is quantified in MMSMAs assuming that the latent heat of the structural transformation is the only contributor. This "RC^{latent}" is then divided by the work needed to generate the latent heat. In other words, a ratio similar to the one in Eqn. (4.3), η^{latent}, is computed between the chemical energy change at the point of transformation and the work input needed to generate the chemical energy change.

In the case of MFITs, the energy conversion efficiency is defined by RC^{latent} divided by the Zeeman energy (term 5 in Eqn. (1.8)) and for superelasticity, RC^{latent} divided by the mechanical strain energy described by term 2 in Eqn. (1.8). This ratio

quantifies the energy conversion efficiency of the MMSMA. According to the first law of thermodynamics, i.e. conservation of energy, the energy applied to the MMSMA should result in the same amount of energy output per the control volume in Fig. 1-2. In the ideal case, η^{latent} will equal unity. In real processes, however, this is never reached due to dissipation. The energy ratios developed, here, quantify the ideality of the stress or magnetic field induced transformations.

Careful review of Figs. 4-3 and 4-4 indicates that the critical temperature points on the entropy change vs. temperature diagram are defined by the martensitic transition temperatures for a thermodynamic cycle. This implies that for quantifying the RC for the latent heat of the structural transformation, that $\Delta T = \Delta T_{ad}^{M\to A} = T_h - T_c$ [53]. According the developments in [12], the entropy changes at the hot and cold temperature reservoirs of a refrigeration cycle must satisfy the condition $\Delta S_h \geq \Delta S_c$. As shown in Fig. 4-4b, the entropy change at both hot and cold reservoirs in SMAs are nearly equal to the entropy change of the martensitic transformation, $\Delta S^{M\to A}$. The RC^{latent} of the SMA for some thermodynamic cycle under the conditions shown in Fig. 4-4b is therefore defined as

$$W_{rev} = \Delta S_c \left(M_f - A_f^{H=H_{comp}^{ad}} \right) = RC^{latent} \tag{4.21}$$

and assuming $\Delta S_c = \Delta S^{M\to A}$ and $\Delta T_{ad}^{M\to A} = M_f - A_f^{H=H_{comp}^{ad}}$,

$$RC^{latent} = \Delta S^{M\to A} \cdot \Delta T_{ad}^{M\to A}. \tag{4.22}$$

With the above considerations, $\Delta S^{M\to A}$ and $\Delta T_{ad}^{M\to A}$ used in Eqns. (4.22) can be decomposed to identify important materials parameters that influence the T_{work} in Eqn.

(4.6), or the RC^{latent} in SMAs. Substituting Eqns. (1.30) and (1.34) into (4.22), the RC^{latent} is defined as

$$RC^{latent} = \left(\Delta \mathbf{X}_i^{M \to A} \frac{d\mathbf{y}_i}{dT_0} \right) . \left[\frac{\Delta \mathbf{X}_i^{M \to A} \frac{d\mathbf{y}_i}{dT_0} \cdot \Delta T_M}{\Delta \mathbf{X}_i^{M \to A} \frac{d\mathbf{y}_i}{dT_0} + \Delta T_M \cdot \frac{C_p^{martensite}}{T}} \right] \quad T \le A_s \tag{4.23}$$

where ΔT_M is equal to the shift in the A_f temperature with applied force, i.e. $\Delta T_M = \frac{dT}{d\mathbf{y}_i^{A_f}} \mathbf{y}_i$. In Eqn. (4.23) it is assumed the complete martensite transformation occurs, and therefore, RC^{latent} also corresponds to the complete transformation under $\mathbf{y}_i$, in Eqn. (4.9). Here, it is important to note that the $\Delta T_{ad}^{M \to A}$ in Eqn. (1.34) is computed using the isothermal entropy change, $\Delta S^{M \to A}$, and the driving force needed to induce the complete isothermal transformation, $\mathbf{y}_{i,comp}^{iso}$.

Next, to find the energy conversion efficiency ratio, η^{latent}, Eqn. (4.23) is divided by the energy needed to generate the RC^{latent},

$$E = \int_0^{\mathbf{y}_{i,comp}^{ad}} \mathbf{X}_i d\mathbf{y}_i . \tag{4.24}$$

For MFITs, $\mathbf{X}_i = M$, $\mathbf{y}_i = H$ and Eqn. (4.24) is the Zeeman energy and, here, is roughly approximated as

$$E \approx \frac{\Delta M^{M \to A} \cdot H_{comp}^{ad}}{2}, \tag{4.25}$$

where $\Delta M^{M\to A}$ is the magnetization difference between M and A phases and H_{comp}^{ad} is the magnetic field needed to completely transform the MMSMA under adiabatic conditions at M_f (see Eqn. 4.13). Next, η^{latent} is computed by substituting $\mathbf{X}_i = M$ and $\mathbf{y}_i = H$ into (4.23), dividing Eqn. (4.23) by (4.25), and simplifying. This reduces to

$$\eta^{latent} = \frac{1}{1+\frac{dT}{dH^{A_f}}\frac{C_p^{mart}}{2\Delta M^{M\to A}}\left(\frac{A_f}{M_f}-1\right)} \tag{4.26}$$

where the energy conversion efficiency, η^{latent}, is a function of the CC slope, $\frac{dT}{dH^{A_f}}$, martensite heat capacity, C_p^{mart}, magnetization change, $\Delta M^{M\to A}$, thermal hysteresis, and elastic transition ranges through the $\frac{A_f}{M_f}$ ratio. Any deviation from unity, computed from Eqn. (4.26), indicates the MFIT in the MMSMA is not ideal. Similarly, for the superelastic transformations, the energy conversion efficiency ratio can be approximately quantified as

$$\eta^{latent} = \frac{1}{1+\frac{dT}{d\sigma^{M_f}}\frac{C_p^{aust}}{2\varepsilon_{tr}^{A\to M}}\left(\frac{A_f}{M_f}-1\right)}. \tag{4.27}$$

Using Eqns. (4.26) and (4.27), the influence of thermomechanical processing on the energy conversion capabilities in MMSMAs can be quantified. However, these expressions do not allow the dissipative and non-ideal elastic effects to be separated into individual contributions. Instead, only one number is computed and its difference with unity signifies the ideality of the stress or magnetically induced transformation.

The equations governing FOPTs have never before been employed to quantify the energy conversion efficiency as was done here, in Eqns. (4.21) through (4.27). The next chapter uses this framework and describes the experimental procedures and processing techniques that can be employed to influence the materials parameters in Eqns. (4.26) and (4.27). Processing and fabrication methods that influence the sample microstructure and the transformation characteristics can be utilized to improve energy conversion capabilities in MMSMAs. In doing so, these refrigerants can exhibit the highest energy conversion efficiency.

CHAPTER V

TUNABILITY OF MAGNETIC SHAPE MEMORY ALLOY BEHAVIOR

5.1 Introduction

Many scientifically interesting problems have arisen through past attempts to control reversible martensitic transformations (MTs). As discussed above, reversible MTs often occur from a cubic austenite phase, to a low temperature martensite phase of lower symmetry. It has been observed that the MT can be preceded by a softening in the transverse acoustic phonon branch (TA_2) and a change in elastic compliance along certain austenitic crystallographic directions [54]. Interestingly, this phenomenon has been linked to the shape of the austenite crystal Fermi surface and is dependent on composition and electronic structure [55]. Therefore, the temperature in which the MT occurs may depend on both composition, which influences the electronic structure, crystallographic ordering, and the thermodynamic contributions discussed in Chapter 1.

In the next sections, MMSMA composition and the influence of heat treatments on the MMSMA response are investigated. Heat treatments are employed to control the magnitude of the thermodynamic driving forces derived in Eqn. (1.8), and to manipulate the magnetoelastic couplings in a single MMSMA composition through crystallographic ordering. The experimental characterization of the MT following heat treatments demonstrates the tunability of the MMSMA. The characteristics surrounding the tuned MT are then used as inputs to quantify the effect of the thermal treatments on the energy conversion efficiency in Eqn. (4.26).

5.2 Meta-magnetic shape memory alloy compositions and e/a ratios

The M_s and T_C for each composition in Table 2-1 were determined from differential scanning calorimetry or magnetometry, discussed earlier. In some samples T_C is not reported because it was either not resolved by calorimetry or it resided at temperatures higher than the limit of the magnetometer (400K). Additionally, the ratio of valence electrons to number of atoms (e/a ratio) was computed for each alloy using the measured composition and is tabulated in Table 2-1.

In metallurgy, the e/a ratio is commonly reported in alloys that exhibit a strong electronic dependence on their physical properties. As mentioned above, the physical properties of the MMSMA are controlled by the electronic Fermi surface in MMSMAs. Therefore, this method has been adopted for MMSMAs which exhibit a large change in transformation characteristics under small compositional variations [39, 56]. Figure 5-1 depicts linear trends in the M_s temperatures for NiMnX (X=Ga, In, Sn, Sb) alloys as a function of their e/a ratio from [57].

The solid lines in Fig.5-1 were computed from first principles calculations in [57] and assume the MMSMA transforms from a stoichiometric $L2_1$ austenite to $L1_0$ martensite. It has been well documented [57] that experimentally changing the MMSMA composition away from stoichiometry, or including a quaternary addition such as Co, may result in a metastable non-$L1_0$ martensite phase, thus misaligning the M_s temperature with the predicted results.

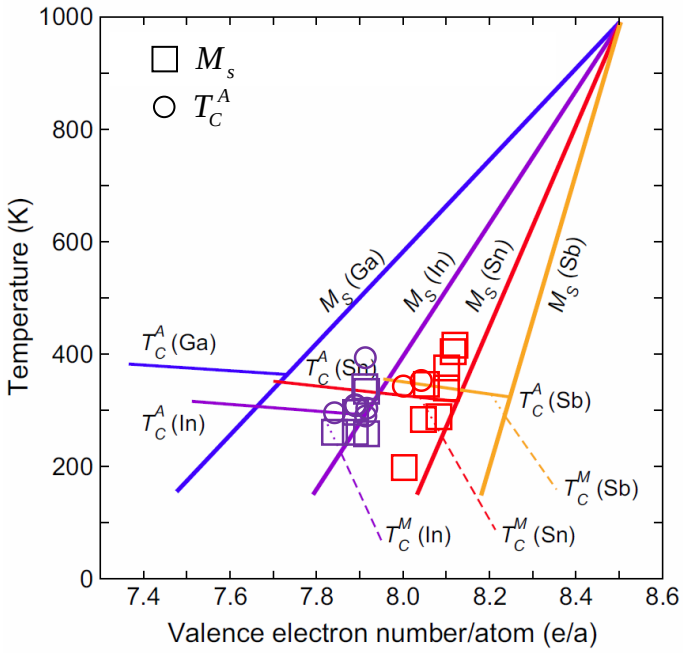

Figure 5-1: The M_s (square) and T_C (circle) temperatures for the solution heat treated alloys in Table 2-1 plotted as a function of e/a ratio over theoretical lines [58].

The M_s (squares) and T_C (circles) temperatures for the solution heat treated (SHT) alloys in Table 2-1 have been overlaid on the plot in Fig. 5-1. The M_s and T_C temperatures of the NiMnIn alloys overlap those predicted, however, there is a large degree of uncertainty. The M_s temperatures in the NiCoMnSn alloys exhibit the same slope as the predicted curve, but all of the transformation temperatures are shifted to lower e/a ratios. This may be a consequence of alloying NiMnSn with Co. Further studies are needed to verify the cause of this shift.

A few of the above alloys were selected for further thermal treatments to identify the variation in M_s and T_C under a constant e/a ratio. The variation in these temperatures

after thermomechanical processing represented the influence of thermodynamics, or crystal ordering, on the MT. Two NiCoMnSn alloys were systematically heat treated, as shown in Tables 2-2 and 2-3, and their critical M_s and T_C plotted in Figure 5-2.

The critical M_s and T_C temperatures for each of the secondary heat treated alloys in Tables 2-2 and 2-3 were identified and plotted with their corresponding e/a ratios (which were constant for each composition) as shown in Fig. 5-2. Interestingly, $Ni_{45}Co_5Mn_{40}Sn_{10}$ did not exhibit much variation in the M_s temperature with the heat treatments tabulated in Table 2-3. As discussed later, these treatments were intended to increase grain size in polycrystalline ribbons and maintain a constant crystallographic order. These annealing treatments, on the $Ni_{45}Co_5Mn_{40}Sn_{10}$ alloy, were performed at temperatures above or at 1073K. Furnace cooling was employed to minimize formation of anti-site defects and vacancies following the thermal processing. Any change in the M_s temperature in Fig. 5-2 for the $Ni_{45}Co_5Mn_{40}Sn_{10}$ alloy was not a result of changing crystal order or vacancy concentration, but the change may have been a result of other thermodynamic contributions discussed later.

On the other hand, a notable spread in the M_s temperature was found for the $Ni_{43}Co_4Mn_{42}Sn_{11}$ composition under a constant e/a ratio. The thermal treatments on this alloy were over a wider temperature range and they employed both slow-furnace and rapid cooling. Rapid cooling is defined by quenching the alloy in a quartz vial, by plunging a hot quartz ampoule from furnace temperatures into room temperature water. The quartz was not broken during the quench to protect the integrity of the thin ribbons. Interestingly,

the quenching procedure and wide range of annealing temperatures may have resulted in the formation of vacancies and/or anti-site defects and a change in crystallographic order whereby a corresponding change in M_s was measured. More detailed results of the systematic heat treatments on the NiCoMnSn alloys are presented in Chapter 6.

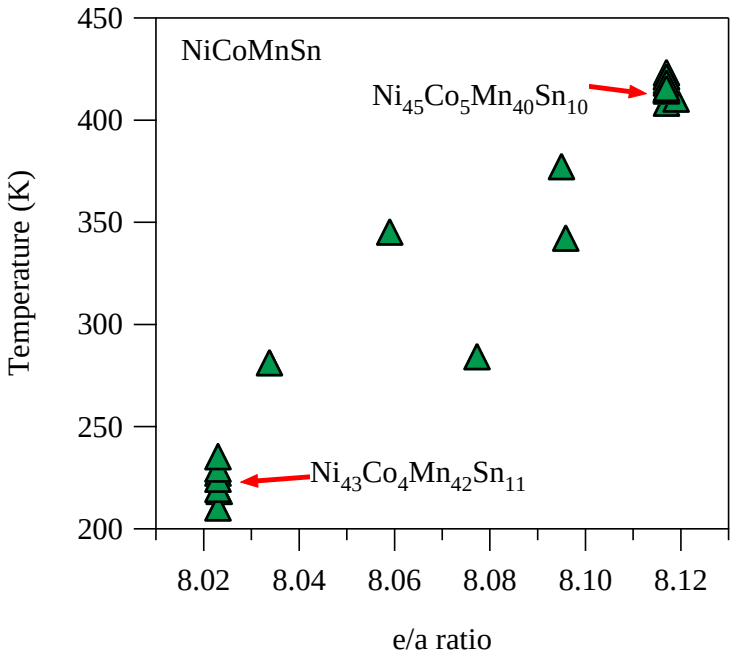

Figure 5-2: The M_s temperatures as a function of valence electron to atom (e/a) ratio for the NiCoMnSn alloys in Tables 2-2 and 2-3.

The composition and critical temperatures of three secondarily heat treated NiMnIn alloys are shown in Tables 2-4 and 2-5. The alloys in Table 2-4 and Table 2-5 were polycrystalline and did not contain cobalt. These alloys were heat treated for only 3 hours at various temperatures and quenched in water. On the other hand, a cobalt-containing single crystalline $Ni_{45}Co_5Mn_{36.6}In_{13.4}$ alloy was heat treated under the

conditions listed in Table 2-6. Most often the alloy was heat treated for only 3 hours, but for a few instances different times were employed.

Figure 5-3 shows the spread in the critical M_s and T_C temperatures for the NiMnIn(Co) alloys tabulated in Chapter 2 for each heat treatment. The e/a ratios were computed using the compositions measured with WDS. Unlike the NiCoMnSn alloy system, the In containing MMSMA did not exhibit a clear linear trend in M_s temperatures over a wide e/a range. In addition, for a constant e/a ratio, the $Ni_{48}Mn_{38}In_{14}$ alloy demonstrated small changes in M_s, suggesting that this alloy was electronically stable and that only minimal changes in crystallographic ordering were achieved by annealing. The $Ni_{45}Co_5Mn_{36.6}In_{13.4}$ single crystalline alloy, on the other hand, exhibited the largest spread in M_s and T_C temperatures of all the selected base alloys. These results suggest that Co may play a role in the tunability of NiMnIn MMSMAs. In an attempt to identify the mechanisms responsible for the spread in M_s and T_C temperatures, depicted in Figs. 5-2 and 5-3, the following sections take a closer look at the microstructure and crystal ordering in these alloys.

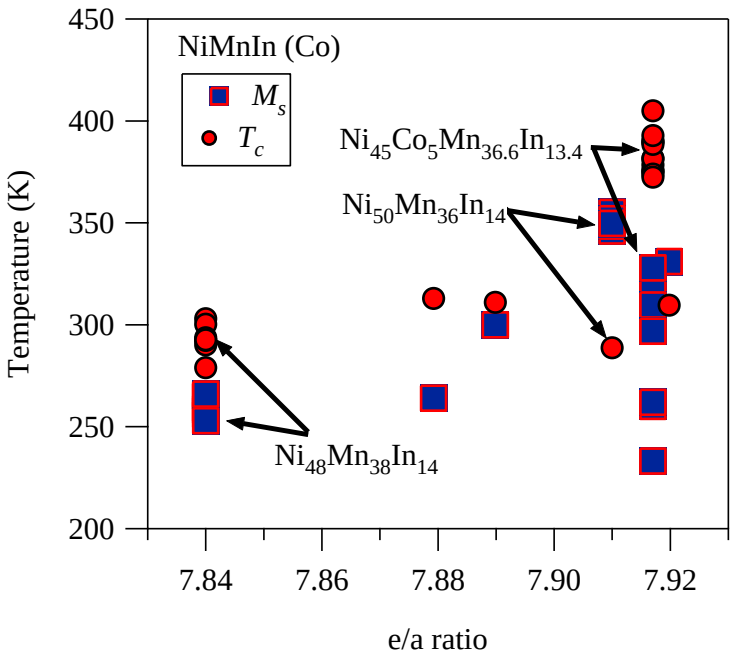

Figure 5-3: The M_s (square) and T_C (circle) temperatures for the NiMnIn(Co) alloys as a function of valence electron to atom (e/a) ratio.

5.3 Microstructural barriers

As shown in the Figures 1-3, 1-4, and 1-5, and described by Eqn. (1.8), the martensitic transformation temperatures depend on non-chemical (elastic and dissipation) contributions to the free energy. The microstructural storage of elastic energy across the martensitic transition results in broad transition ranges and a deviation of an ideal thermoelastic transformation. Similarly, defect generation and other dissipative effects generate a thermal hysteresis resulting in further deviation from the ideal response.

In both A to M and M to A transformations represented by Eqn. (1.8), the ΔE_{irr} is positive indicating that additional energy must be overcome for both forward and reverse transformations. The ΔG_{el}, on the other hand, is stored in the microstructure during the A to M transformation, and is recovered by the M to A transformation [17]. This energy storage and release has been shown to be partially responsible for differences in the latent heat measured by calorimetry between forward and reverse transformations [17]. In terms of improving the giant calorific effects of MMSMAs, small elastic energy should be stored in the microstructure. If the stored elastic energy is too large, no enthalpy change would be measured in calorimetry because the chemical energy change would be stored elastically [17]. To study the influence of elastic energy storage through microstructural barriers on the MCE performance, the low hysteresis $Ni_{45}Co_5Mn_{40}Sn_{10}$ alloy in Table 2-3 was subject to grain growth with carefully selected annealing treatments. The martensitic transformation characteristics are discussed, in detail, in subsequent sections.

5.3.1 Experimental procedures

Four compositions near $Ni_{45}Mn_{40}Co_5Sn_{10}$ (at.%) were synthesized via arc melting in a protective argon atmosphere. Ribbons were prepared and their compositions measured with WDS as described in Chapter 2. The ribbon compositions were measured to be $Ni_{44.5\pm0.15}Mn_{43\pm0.20}Co_{1.9\pm0.02}Sn_{10.7\pm0.07}$ at.%, $Ni_{44.4\pm0.35}Mn_{40.9\pm0.29}Co_{4\pm0.08}Sn_{10.8\pm0.03}$ at.%, $Ni_{44.4\pm0.08}Mn_{39.8\pm0.12}Co_{5.1\pm0.03}Sn_{10.8\pm0.07}$ at.%, and $Ni_{44.5\pm0.15}Mn_{39.3\pm0.21}Co_{5.4\pm0.06}Sn_{10.8\pm0.04}$ at.%. Henceforth, these alloys are abbreviated as Co2, Co4, Co5, and Co6, respectively.

Differential scanning calorimetry (DSC) was conducted on the ribbon samples using a TA Instruments Q20 calorimeter by stacking more than 10 mg of ribbons in an aluminum pan. The temperature was swept at 5K/min between 353K and 453K. The martensitic transformation temperatures, (M_s, M_f, A_s, and A_f) were extracted from the DSC measurements using the line intersection method. This method is demonstrated on the Co5 cooling curve in Fig. 5-4 where the cooling curves of each as-spun sample are shown. The Co5 ribbons were selected for the grain size study due to the lowest transformation hysteresis and the largest latent heat of transformation.

To promote grain growth in the as-spun ribbons, different Co5 ribbons were annealed at under the conditions in Table 2-3. The above mentioned samples were annealed in a partial argon atmosphere within quartz tubes that had been washed at least 3 times with argon and purged to vacuum (3×10^{-4}Torr) between washing. The ribbons were encased in tantalum foil to prevent their interaction with the quartz tube and a titanium sponge was sealed within the same tube as an oxygen getter. The ribbons were furnace cooled after annealing to produce similar crystallographic ordering and vacancy

concentrations on cooling. One additional heat treatment was conducted at 1173K in high vacuum (1×10^{-5} Torr) for 100min on separate ribbons, which were allowed to rest on the quartz tube during the heat treatment without tantalum foil or a titanium sponge and were subsequently furnace cooled.

All the ribbons' microstructures were investigated using a FEI Quanta 600 field emission scanning electron microscope (SEM). A backscatter electron (BSE) detector was used to collect images of the grains on the sample surfaces and ribbon cross sections after cleaving the ribbons transversely. Images of ribbon cross sections were collected using a secondary electron (SE) detector and second phases or inclusions were identified using the energy dispersive spectrometer (EDS) in the SEM.

The grain size of the ribbon samples were measured from BSE images. A histogram of the measured grain diameters was plotted, a Gaussian curve was fit to the diameter data, and the average grain diameters were determined to be the maximum of the fitted peak. The grain diameter was then referred to as grain size (*GS*). The thicknesses of the ribbons were also measured from the SE image cross sections and then the GS to thickness ratio (*GS/t*) was used as a measure of grain constraint [59, 60].

5.3.2 Transformation temperatures and latent heat of martensitic transformation

In the ribbons, DSC scans were used to determine the transformation temperatures and latent heats of transformation. As shown in Fig. 5-4, the substitution of cobalt for manganese increases the transformation temperatures. The entropy changes across the martensitic transformation, $\Delta S^{A\to M}=\int_{M_f}^{M_s}\frac{C_p}{T}dT$, were computed using the heat flow

measurements from the heating and cooling runs. For the Co2, Co4, Co5, and Co6 samples the entropy change upon the A to M transformation was computed to be 42, 41, 47, and 42 J/kgK, respectively. This can also be seen from the DSC curves as the height and width of each peak. Increasing Co beyond 5 at.% resulted in a latent heat of transformation comparable to the compositions with lower Co percentages.

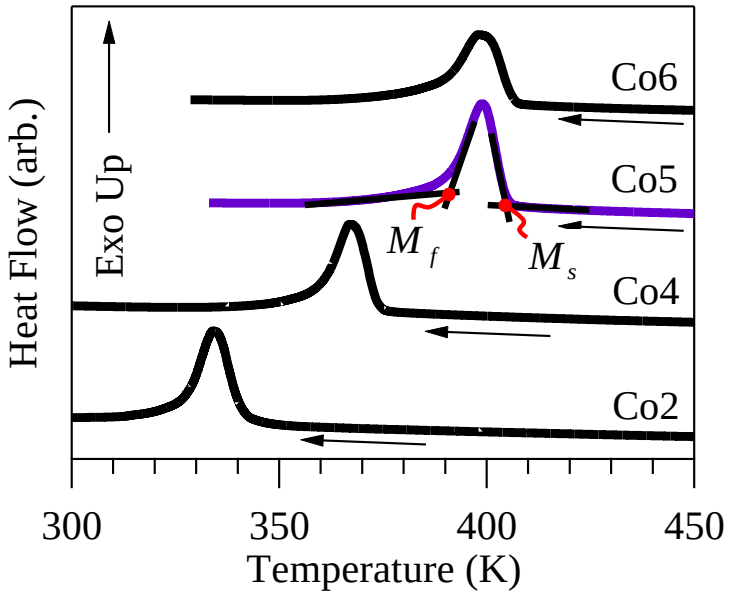

Figure 5-4: Heat flow histories across the forward martensitic transformation for the Co2, Co4, Co5, and Co6 alloys described in the text.

Since the Co5 ribbon has the largest latent heat of transformation and the lowest transformation hysteresis among the compositions studied, it was selected for further annealing treatments. After annealing, DSC was conducted on the ribbons before SEM imaging. The average measured grain size, transformation ranges for forward ($M_s - M_f$)

and reverse ($A_f - A_s$) transformations, and the M_s temperatures are tabulated in Table 5-1 for each of the heat treated ribbons.

Table 5-1: Transition ranges, M_s temperature, and parameters representing the energetics of the martensitic transformation, in $Ni_{45}Co_5Mn_{40}Sn_{10}$ (at.%) annealed ribbons.

Annealing Treatment	Time (min)	M_s (K)	$M_s - M_f$ (K)	$A_f - A_s$ (K)	$A_f - M_s$ (K)	GS (μm)	$\Delta G_{el}^{A\to M} / Q_{tr}$ (%)	$\Delta E_{irr} / Q_{tr}$ (%)
	30	410	8.7	6.2	8.5	6.5	1.06	2.0
	60	411	8.8	6.7	9.0	7.3	1.07	2.2
1073K	90	411	8.6	6.5	8.7	8.1	1.05	2.1
	120	411	8.6	6.3	9.2	8.3	1.05	2.2
	600	412	8.9	6.8	9.1	10.4	1.08	2.2
	20	412	8	5.8	7.7	15	0.97	1.8
	40	413	8	6.1	7.2	17	0.97	1.7
	60	413	7.7	5.3	7.8	18.6	0.93	1.8
1173K	80	413	7.9	6.2	8.3	20.4	0.96	2.0
	100	413	7.9	6.5	7.9	17.7	0.96	1.9
	100[I]	412	22	23	6.9	22.8	2.67	1.7
	120	414	7.7	7.2	7.9	23.3	0.93	1.9
	30	413	7.6	5.9	7.7	19.2	0.92	1.8
1198K	60	413	7.5	6	8.0	23.0	0.91	1.9
	120	414	6.6	5.5	7.2	36.2	0.80	1.7

[I]1173K 100min in 1×10^{-5} torr vacuum and the ribbons were allowed to rest on the quartz tube.

Table 5-1 demonstrates that the M_s temperature only marginally increases with annealing time and temperature. The transition ranges are not always decreasing with annealing time. Annealing the ribbons at 1073K had little effect on the martensitic transition characteristics in Table 5-1 when annealed for less than 600 minutes. A higher annealing temperature had a greater influence on the transition range. Interestingly, the

reverse transition range, $A_f - A_s$, does not seem to be clearly effected by the annealing treatment.

5.3.3 Microstructure and grain size

Fig. 5-5 (a)-(f) show the micrographs of a ribbon face and its cross-section for the 1073K, 1173K and 1198K 2hr heat treated ribbons. It is clear from Fig. 5-5(a) and (b) that 1073K was not sufficient to promote grain growth to an extent large enough so that the grains completely extended through the thickness of the ribbon samples. On average the *GS* of the 1073K annealed ribbons was 8.1μm while the ribbon thicknesses were about 31μm. The annealing treatments for 2 hours at 1173K and 1198K seem to have promoted grain growth sufficiently such that the grains could grow completely through the thickness of the cross section of the ribbon. Differences in grain size are obvious from different annealing treatments as shown in Figs. 5-5(a), (c), and (e). The average grain size of each heat treatment case is listed in Table 2-6. Lastly, all the samples tested were martensitic at room temperature.

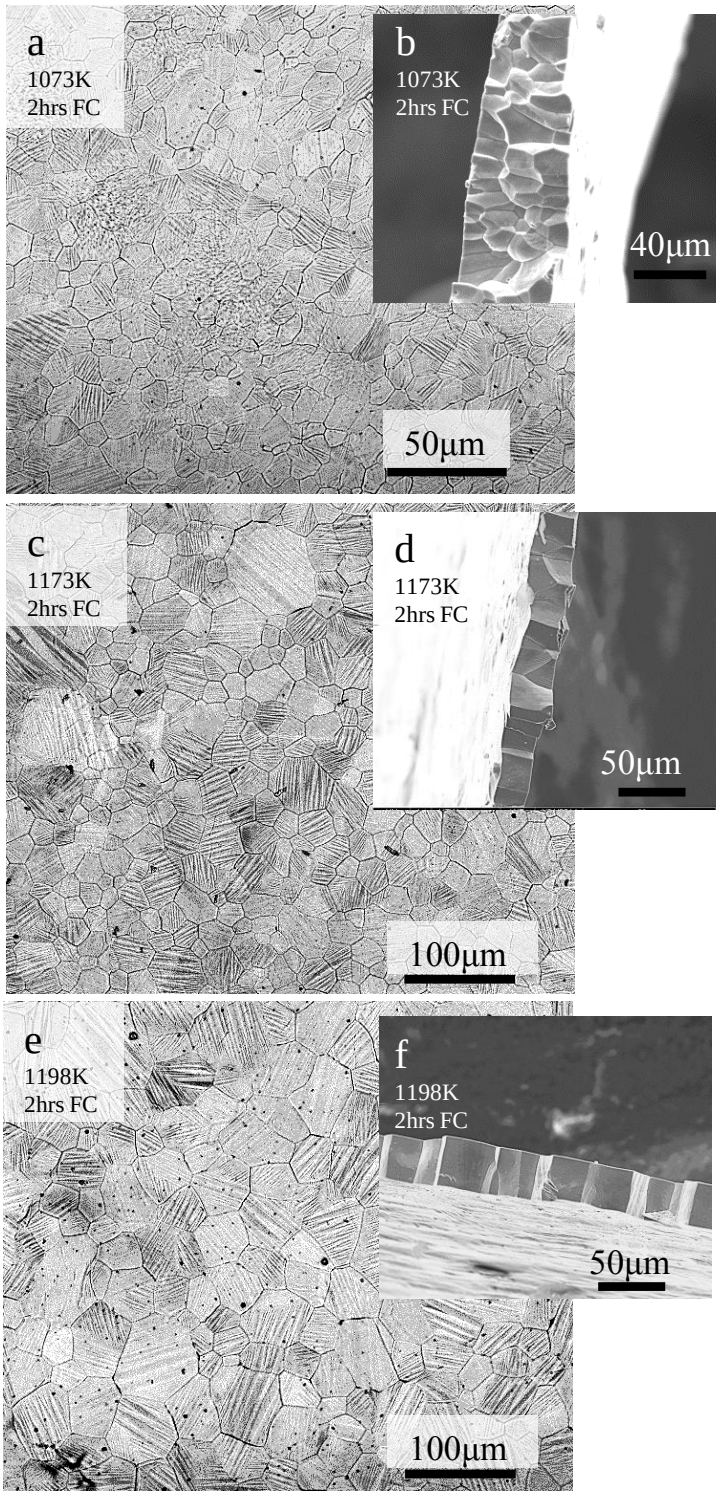

Figure 5-5: Backscattered electron images of $Ni_{45}Co_5Mn_{40}Sn_{10}$ ribbons after annealing and furnace cooling from 1073K (a) and (b), 1173K (c) and (d), and 1198K (e) and (f) for 2 hours.

5.3.4 Thermodynamic contributions to the transformation characteristics

To better understand the role of microstructure on magnetic refrigeration, we first need to explain how microstructural features influence the energetics of the martensitic transformation. In the theory of martensitic transformation, the local free energy balance for the forward martensitic transformation is described in Eqn. (1.8). With the absence of the terms 2-6 in Eqn. (1.8), the transformation would be an ideal first order phase transformation at temperature T_0. Large ΔE_{irr} values are the indication of thermal transformation hysteresis, as opposed to the ideal first order response where $\Delta E_{irr} = 0$, and large $\Delta G_{el}^{A \to M}$ values result in large transition ranges (ΔT_{elas}), also deviating from the ideal response.

In earlier works, ΔE_{irr} was shown to be related to the compatibility between the transforming phases, phase front motion during the transformation, and plastic deformation to accommodate the transformation shear and volume change. The elastic strain energy contribution, $\Delta G_{el}^{A \to M}$, on the other hand, was shown to be related to the level of compatibility between austenite and martensite phases as well as the interaction at interfaces between different martensite variants [61]. Following these descriptions, we build most of our discussion pertaining to the effect of grain size and microstructural features on the transition range and hysteresis in MMSMAs.

As defined in [61], the magnitude of $\Delta G_{el}^{A \to M}$ can be expressed as $0.5 \cdot \Delta S^{A \to M}(M_s - M_f)$ or $0.5 \cdot \Delta S^{A \to M} \Delta T_{elas}$. This value is an indication of how much elastic strain energy must be overcome to transform the MMSMA. In MCE applications,

the elastic strain energy stored through the transformation is overcome by applying magnetic fields per Eqn. (1.8). Reducing $\Delta G_{el}^{A\to M}$ ultimately reduces the required magnetic fields to trigger the M to A transition.

For comparative purposes between heat treated alloys, a measure of microstructurally stored elastic energy is needed. A convenient metric that compares this elastic energy barrier to the energy that is converted to heat through the MCE, is $\Delta G_{el}^{A\to M} / Q_{tr}$ where Q_{tr} is the latent heat of the martensitic transformation, $Q_{tr} = \Delta S^{A\to M} M_s$ [17]. Conveniently, this ratio eliminates the need to find the entropy change across the martensitic transformation, which may be a function of atomic ordering, but still gives a relative comparison of performance between different MMSMAs or different microstructural conditions. Minimizing this ratio is favorable for MCE applications. The ratio $\Delta G_{el}^{A\to M} / Q_{tr}$, calculated for the ribbon samples is shown in Table 5-1.

In Table 5-1, it is shown that $\Delta G_{el}^{A\to M} / Q_{tr}$ decreases with increasing temperature and time of the heat treatment. In other words, this parameter decreases with increasing grain size indicating a smaller amount of strain energy is stored in the microstructure when larger grains are present. It is believed that smaller grains cause more nucleation sites for martensite, and therefore lead to a higher density of martensite/martensite and martensite/austenite phase boundaries and higher stored elastic strain energy.

The magnitude of energy dissipation, ΔE_{irr}, on the other hand, can be computed by the expression $\Delta E_{irr} = \Delta S^{A\to M} \Delta T_{hys}$ [42]. Using the ratio of the energy dissipation to

the latent heat of the martensitic transformation, the fraction of energy lost to heat (not converted to MCE cooling), across the martensitic transformation can be expressed as $\Delta E_{irr} / Q_{tr}$. Again, this value should be minimized to produce a favorable MCE in MMSMAs. Not only will reducing this value amplify MCE cooling, but it will also reduce the magnetic field levels required to transform the MMSMA by reducing $A_f - M_f$ discussed in Chapter 2. The ratio of energy dissipation to latent heat of transformation, $\Delta E_{irr} / Q_{tr}$, is also shown in Table 5-1 for each ribbon.

Although it was our aim to keep dissipation, or ΔT_{hys}, as constant as possible by furnace cooling and maintaining crystallographic ordering our samples, some differences were still observed between different heat treatments as shown in Table 5-1. It seems that larger grain sizes or high *GS/t* ratios reduce $\Delta E_{irr} / Q_{tr}$. Although there is some scatter, $\Delta E_{irr} / Q_{tr}$ does not exhibit the same level of reduction with grain size increase as $\Delta G_{el}^{A \to M} / Q_{tr}$.

5.3.5 Effect of GS/t on the martensitic transition range

In Fig. 5-6a, it is shown in Co_5 ribbons that the $M_s - M_f$ transition range decreases with increasing *GS/t*. Originally, $M_s - M_f$ for the 1073K heat treated ribbons was about 9K. Increasing the annealing time at this temperature had a minor effect on the transition range and *GS/t.* The standard deviation (2σ) of the grain size, as apparent in Fig. 5b from the width of the peaks, also did not exhibit much change. *GS/t* was around 0.2 for each of the ribbons annealed at 1073K. The low standard deviation in each ribbon sample annealed

at 1073K indicates that either the grains were at a size in which their surface energy was near an equilibrium at this annealing temperature, or the atomic diffusivity was too slow.

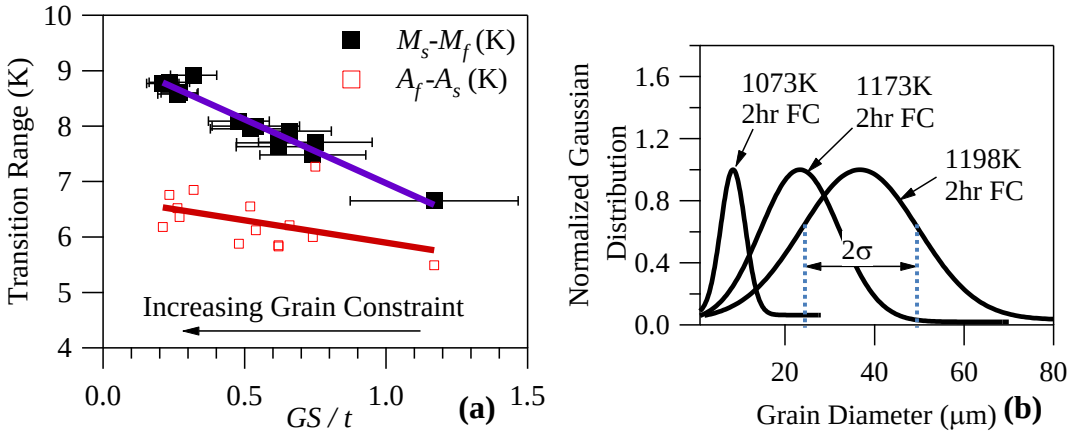

Figure 5-6: Martensitic transition ranges as a function of grain size to thickness ratio in $Ni_{45}Mn_{40}Co_5Sn_{10}$ annealed ribbons (a). Error bars indicate ± one standard deviation (σ) from the Gaussian regression data shown in (b).

In this condition, each grain (with the exception of those on the ribbon surface) was completely in contact with its neighboring grains on all sides, as shown in Fig. 5-5b, and therefore any volume change that occurred due to the martensitic transformation would produce a tendency for martensite to self-accommodate. The self-accommodation process, in turn, produces many interacting martensite interfaces and stores additional microstructural elastic energy, per Eqn. (1.8). In ribbons with longer and higher temperature annealing treatments, on the other hand, the grains only contacted their neighbors along their circumference as shown in Figs. 5-5d and f. These larger grains grew

completely though the thickness of the ribbon and exhibit two free surfaces where no interaction with neighboring grains could occur.

In the 1173K heat treated samples the standard deviation of the grain size distribution increased. This indicates that increasing the annealing temperature did not promote growth in all of the grains, but that a select few grew at the expense of others. Although the standard deviation of the grains grew with *GS/t*, $M_s - M_f$ was measured to be 8K to 7.5K. The 1173K heat treatments listed in Table 2-6 result in a linear decrease of $M_s - M_f$ with increasing *GS/t* between the range of 0.5<*GS/t*<0.7.

A further decrease in $M_s - M_f$ was observed along with higher *GS/t* ratios, 0.7<*GS/t*<1.2, after annealing at a higher temperature, 1198K. Although *GS/t* is less than unity for all cases as shown in Fig. 5-6a, all of the heat treatments at 1173K and above promoted grain growth through the cross section, as shown in Figs.5-5d and f. Grains in this case experienced smaller grain constraint than for the ribbons heat treated at 1073K.

For the complete martensitic transformation, the change in volume in $Ni_{45}Mn_{40}Co_5Sn_{10}$ was computed to be -1.59% using the conventional Clausius-Clapeyron relation derived from the Gibbs free energy of martensite and austenite; i.e. $\Delta S_{tr}(dT/dP) = \Delta V_{tr}$. Here, $\Delta S_{tr} \approx 47$ J/kgK as given in the experimental results section, and dT/dP was found to be approximately -0.042 K/MPa for NiMnSn alloys [40, 45]. This volume change results in an inhomogeneous stress gradient along grain boundaries and as the martensite forms, a self-accommodation process has to take place to minimize the local free energy. The self-accommodation of martensite, in turn, produces more

interacting martensite/martensite or martensite/austenite boundaries that contribute to the elastic strain energy. The density of twin boundaries and interfaces (number of boundaries for a given area) increases with decreasing grain size as seen in Figure 5-5. Larger grains allow larger martensite plates to form, and therefore the density of these interfaces is less.

Finally, it is shown in Fig. 5-6a that $A_f - A_s$ is not affected by grain size to the same extent as $M_s - M_f$. However, there is a slight decrease in $A_f - A_s$ as *GS/t* increases. In addition, the reverse transformation range, $A_f - A_s$, is always less than that of the forward transformation, $M_s - M_f$. It is believed that most of the stored elastic energy from the forward transition is recovered, and therefore results in a smaller reverse transition range [62] as observed here.

5.3.6 Other microstructural effects on the martensitic transition range

We have shown above that promoting grain growth decreases the transition range, and this is also expected to reduce the overall magnetic field requirement to complete an isothermal magnetic field-induced martensitic transformation per Eqn. (4.12). In order to consistently achieve this, heat treatments of this alloy should be conducted carefully and the microstructure should be composed of a single phase with no inclusions. Contaminating the microstructure with second phases or inclusions is detrimental to the transformation characteristics of shape memory alloys.

In past studies [27, 40, 50, 63, 64], heat treatments have been performed on NiMn-based SMA powders [63], melt-spun ribbons [50, 64], and bulk polycrystals [27, 40]. In such cases, separating the sample from the wall of the containment vessel with a non-

reactive agent during a heat treatment can be difficult and is often neglected. As explained in the experimental section, two similar 100min heat treatments were conducted at 1173K with one set of ribbon samples allowed to rest on the quartz tube under high vacuum during the entirety of the annealing treatment, and the other set encased in tantalum foil in argon atmosphere with titanium sponge used as an oxygen getter. Fig. 5-7a shows a micrograph of the samples that were allowed to touch the quartz during annealing, and Fig. 5-7b shows the microstructure of the samples wrapped in tantalum foil. Clearly, the former samples grew inclusions during the heat treatment and those wrapped in tantalum foil did not. It was shown in [65] and [66] that the standard Gibbs free energy of formation for $MnSiO_3$ is lower than that of SiO_2 (quartz) (See Fig. 5-7c). EDS analysis confirmed that these inclusions were rich in Si and Mn, indicating that they were indeed $MnSiO_3$. The result of allowing the samples to rest on the quartz tube during heat treatment was the microstructural contamination shown in Fig. 5-7a.

The effect of the inclusions on the martensitic transition range is significant. DSC scans were conducted on both of these ribbons to determine their transition ranges. $M_s - M_f$ and $A_f - A_s$ of the contaminated samples were 22K and 23K, respectively, whereas these ranges were 7.9K and 6.5K for the ribbons shown in Fig. 5-7b. The set of ribbons that were not contaminated had a *GS/t* ratio of about 0.5, but those with the manganese silicate contamination had GS/$t \approx 0.73$.

Although the contaminated ribbons exhibited a larger grain size which should have allowed larger martensite plates to form and decreased the stored elastic strain energy [Eqn. (1.8)], the inclusions prevented this, as shown by the size of martensite twins in Fig.

5-7a. Interestingly, the thermal hysteresis (approximated as $A_f - M_s$) in the contaminated ribbons was about the same as in the clean samples. The contaminated ribbons exhibited a thermal hysteresis of 7.3K and the clean ribbons, 7.9K. This is somewhat surprising as the matrix composition should affect the compatibility between austenite and martensite [40] around the composition gradient. The second phase particles should also have some impact on the thermal hysteresis. Interestingly, $\Delta E_{irr} / Q_{tr}$ is about the same in the contaminated sample as the rest of the samples tested, the reason of which is not clear.

On the other hand, the silicates seem to affect the self-accommodation process of martensite and the size of the martensite twins, and thus the transition range, through the higher density of phase/twin fronts. With increasing twin boundary density induced by either small grains or small distances between inclusions, the elastic strain energy contribution to the martensitic transformation increases in these alloys.

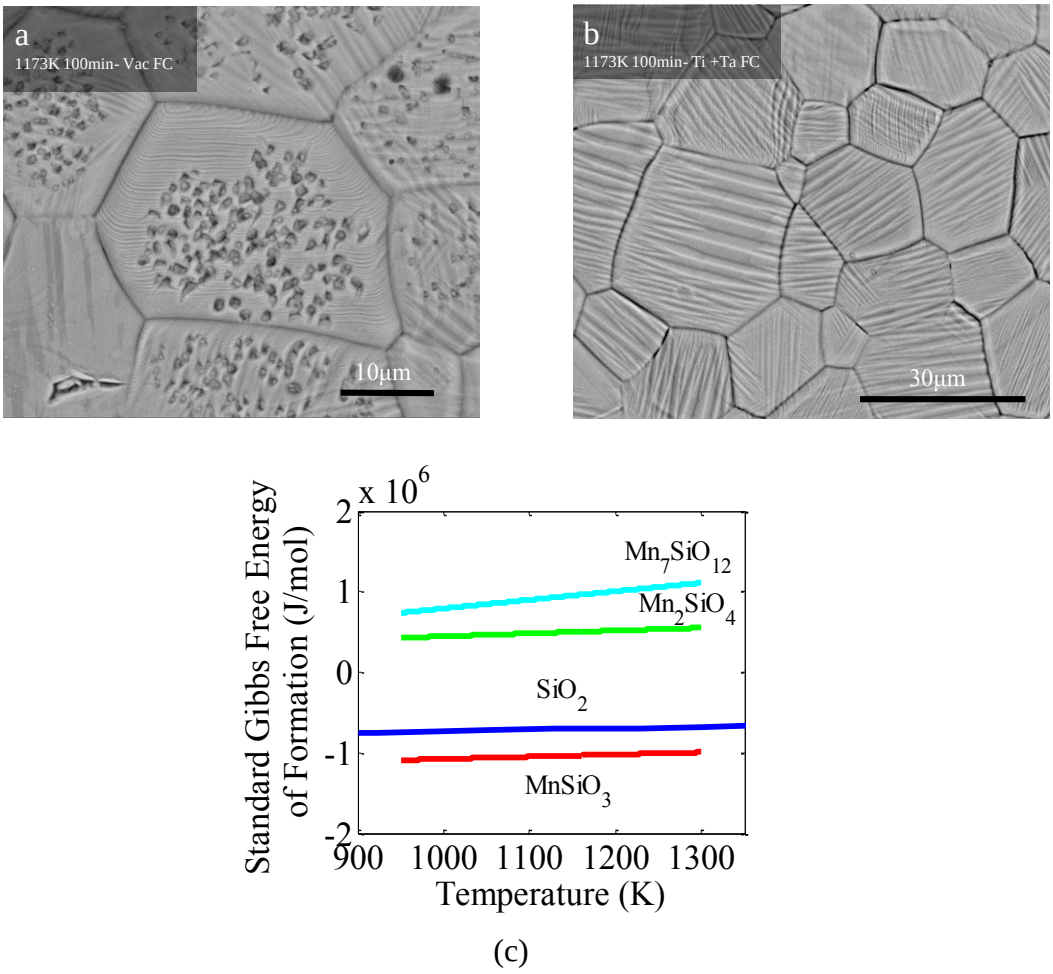

(c)

Figure 5-7: $Ni_{45}Mn_{40}Co_5Sn_{10}$ ribbons annealed at 1173K for 100min in high vacuum (1×10^{-5} torr) resting on the quartz vial (a), in partial argon atmosphere wrapped in tantalum foil using a titanium oxygen getter (b), and the standard Gibbs free energy of formation for manganese silicates shown in (a) and quartz within the temperature range of the annealing treatments as determined from [65] and [66]. Manganese silicates shown in (a) are assumed to be $MnSiO_3$ as shown by the minimal standard Gibbs free energy in (c).

5.3.7 Effect of GS/t on H_{comp}^{iso} *and* η^{latent}

Although significant scatter is observed in $A_f - A_s$, decreasing $M_s - M_f$ resulted in a smaller overall temperature range that must be overcome to complete the transformation ($A_f - M_f$) as discussed in Chapter 4 using Eqn. (4.12) and depicted in Fig. 5-8. Decreasing this temperature range ultimately decreases the required magnetic field to complete the field-induced transformation at temperature M_f. Using the Clausius-Clapeyron slope given in [40] for the same alloy composition (-0.384*T/K*), the magnetic field required to complete the isothermal martensitic transformation at temperature M_f is plotted in Fig. 5-8. It can be seen that decreasing $A_f - M_f$ by only a few Kelvin also decreases the magnetic field requirement by approximately 2T. The samples with *GS/t* close to 0.32 required about 7T to complete the reversible field-induced transformation at M_f, while those with a *GS/t* ratios near 0.62 and 1.7 required fields of about 6T and 5.1T, respectively.

Reducing the required field by 2T is significant as it would require substantially lower magnetic energy to transform the MMSMA and leads toward the possibility of using permanent magnet technology for solid-state MMSMA refrigeration applications. Although the lowest field capable of completely transforming the MMSMA in this study was shown to be 5.1T, about 3T larger than permanent magnet capabilities, reducing the magnetic field requirements using carefully selected heat treatments will allow a larger fraction of the transformation to occur from field cycling and, in turn, increase the energy conversion efficiency ratio of the MMSMA.

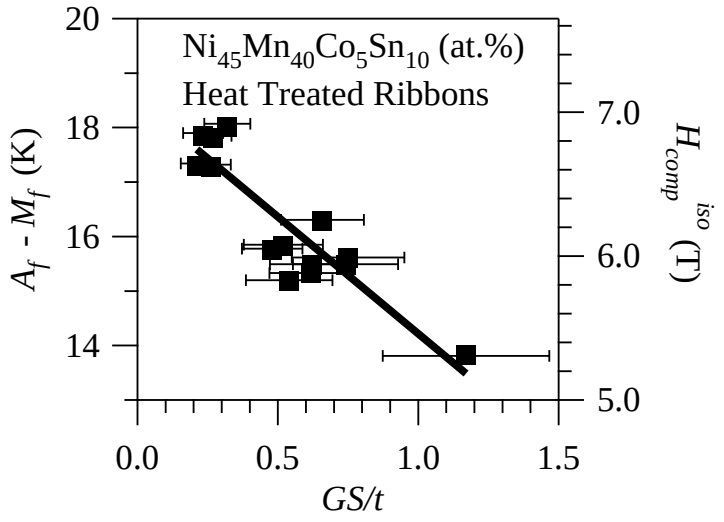

Figure 5-8: $A_f - M_f$ and H_{comp}^{iso} dependencies on grain size to thickness ratio (GS/t) in $Ni_{45}Co_5Mn_{40}Sn_{10}$ annealed ribbons.

Figure 5-9 shows the grain constraint dependence of the η^{latent} parameter developed in Eqn. (4.26). Here, η^{latent} was computed with measured values in Table 5-1, $\Delta S^{M\to A} = \Delta M^{M\to A}\dfrac{dH^{A_f}}{dT} = 45.7\text{J/kgK}$ measured from calorimetry, and $C_p^{Mart} \approx 390\text{J/kgK}$ which is a typical value for intermetallic MMSMAs at room temperature. As mentioned earlier, larger η^{latent} values indicate that for a given latent heat of martensitic transformation, less Zeeman energy is required to generate it, therefore the martensitic transformation converts energy more efficiently with large η^{latent}. According to the data in Figs. 5-8 and 5-9, reducing the magnetic field requirement to completely transform the MMSMA results in an increase in the conversion efficiency of approximately 7%.

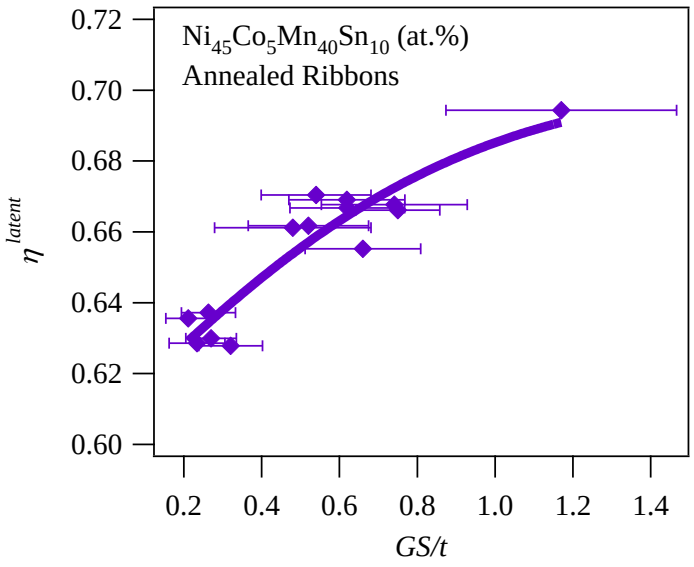

Figure 5-9: The magnetic to thermal energy conversion efficiency from Eqn. (4.26) of $Ni_{45}Co_5Mn_{40}Sn_{10}$ annealed ribbons as a function of grain size to thickness ratio.

The data in Fig. 5-9 indicates that although the effect is not very large, increasing the *GS/t* ratio in MMSMAs improves the energy conversion efficiency through magnetic field induced transformations in NiCoMnSn MMSMAs. Higher efficiency ratios may be attainable with larger GS/t ratios, however, additional studies need to be performed over a wider range of GS/t for a given composition. In addition, the data in Fig. 5-8 indicates that the required magnetic field needed for a complete isothermal and reversible martensitic transformation can be reduced by as much as 2T. This reduction is a result of increasing the grain size for a ribbon of constant thickness and reducing the $\Delta G_{el}^{A\rightarrow M}$ term in Eqn. (1.8).

5.4 Crystal structure and order

5.4.1 Review of the $L2_1$ to B2 transition in NiMnIn Alloys

Here, a single composition of $Ni_{45}Co_5Mn_{36.6}In_{13.4}$ is heat treated to manipulate the crystallographic order in austenite, and therefore, the electronic state. Single crystals, instead of polycrystals, are studied to negate the influence of grain size on the thermodynamics driving the martensitic transformation, discussed above. Thermal treatments for the NiCoMnIn alloy are tabulated in Table 2-6.

In past studies [67], it has been reported that some compositions of NiMnIn exhibit a change in crystallographic order from a $L2_1$ Heusler phase to a B2 cubic phase on heating above a critical temperature, $T^{L2_1/B2}$. The $L2_1$ superlattice is denoted as a Fm3m structure (space group 225). The $L2_1$ and B2 crystal orders are depicted in Figure 5-10 as simulated by PowderCell.

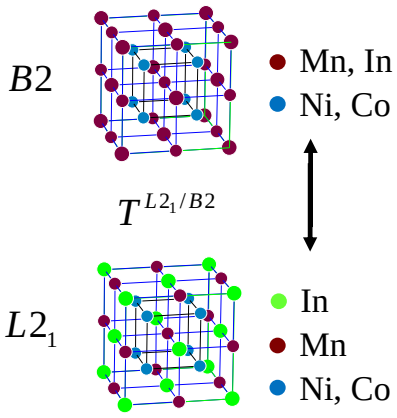

Figure 5-10: B2 and $L2_1$ ordered crystal structures in NiCoMnIn alloys.

At temperatures below a critical point, Mn and In atoms migrate to designated sublattice sites. The perfect Heusler structure is described with In and Mn atoms occupying the 4a and 4b Wykoff sublattice sites [68]. In the B2 structure, however, Mn and In are randomly distributed between the two.

Diffraction offers a means to quantify the long range crystal order in these materials. The structure factor of the unit cell in Fig. 5-10 can be written as a function of effective scattering factors for each sublattice site [68]. In short, odd reflections (111, 311, 331, etc…) are characteristic of $L2_1$ long range order, even reflections (200, 222, 420, etc…) are characteristic of B2 order, and the fundamental reflections (220, 400, 440, etc…) are characteristic of A2 order. The relative intensity of these reflections can be used to compute a degree of long range crystal order. For example, the normalized diffraction pattern of a perfect Heusler alloy ($Ni_{45}Co_5Mn_{25}In_{25}$) is depicted in Figure 5-11 as simulated with PowderCell.

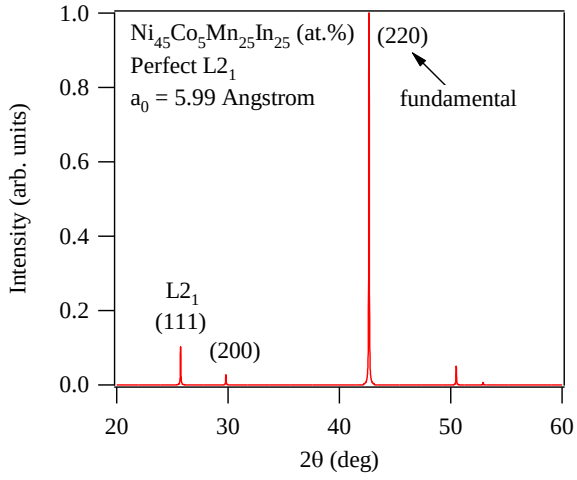

Figure 5-11: The normalized simulated x-ray diffraction peaks of the perfect $L2_1$ structure in Fig. 5-10.

In Fig. 5-11, the ratio of intensity at the (111) reflection around $2\theta \approx 26^{\circ}$ to the fundamental reflection gives relative degree of long range $L2_1$ order. The relative intensity of the (200) reflection can be used to quantitatively characterize degree of long range B2 order, and the (220) fundamental peak is invariant of order. In practice, this can be used to visualize the $L2_1$ morphology with transmission electron microscopy (TEM). Here, we observe the $L2_1$ morphology in heat treated NiCoMnIn alloys exhibiting differing degrees of long range $L2_1$ order.

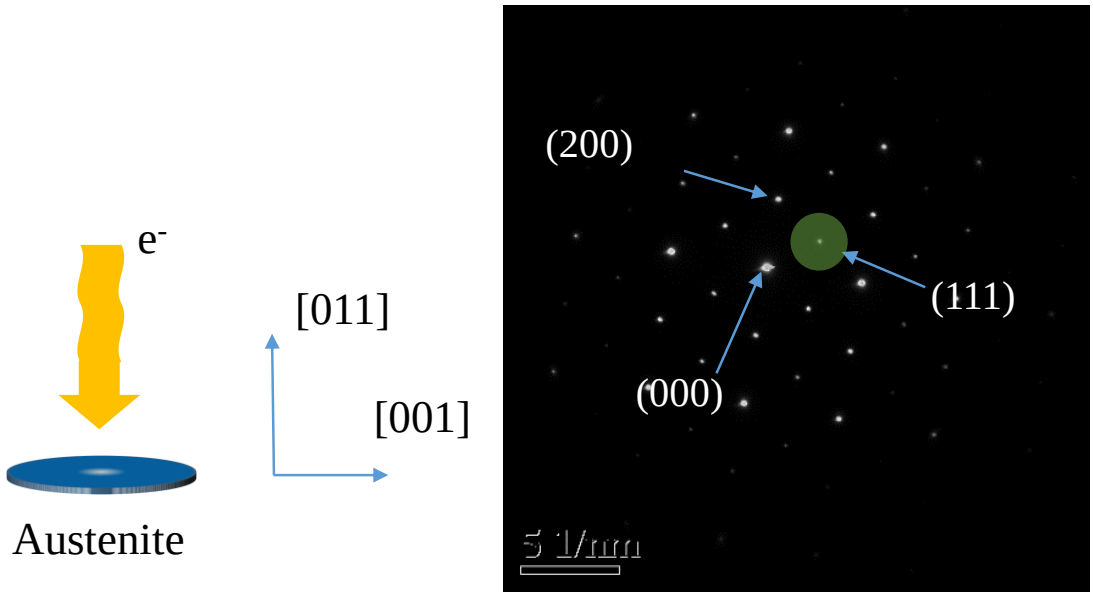

(a) **(b)**

Figure 5-12: An illustration of the MMSMA TEM sample oriented such that the [011] zone axis parallel to the electron beam (a) and the resulting diffraction pattern of the [011] zone axis. The (111) reflection is investigated for dark field imaging to visualize $L2_1$ morphology.

In TEM, the [011] austenite zone axis (Fig. 5-12a) can be diffracted with the electron beam to generate the pattern shown in Fig. 5-12b. In Fig. 5-12b, the diffraction pattern of a $L2_1$ Heusler phase is shown. The transparent spot is labeled as (000). The B2(200) and L21(111) diffraction spots are indicated by arrows. In TEM, the electron beam can be positioned through an aperture to align only with the (111) spot. This is represented as the green semi-transparent circle around the (111) reflection. The resulting "dark field image", which will be shown later, represents the spatial variation of the (111) peak intensity, i.e. $L2_1$ morphology.

5.4.2 Experimental procedures

Single crystalline $Ni_{45}Co_5Mn_{36.6}In_{13.4}$ nom. at.% MMSMA were synthesized as described in Chapter 2. A master sample was cut into compression samples with electro-discharge machining (wire EDM) which were then sealed in a quartz vial under partial vacuum/argon atmosphere (~14 torr). The samples were then solution heat treated. During the solutionizing heat treatment, the master sample was wrapped in tantalum foil to prevent the formation of precipitates from interacting with the surrounding quartz. In addition, a titanium sponge was sealed in the quartz vial during all of the heat treatments as an oxygen getter.

WDS was performed on the solutionized single crystals at multiple locations and the composition was determined to be $Ni_{45.6}Co_{4.82}Mn_{36.0}In_{13.55}$ at.% with a ± 1 at.% accuracy of the reported values. After solution heat treating the single crystal, small pieces were isolated using a low speed diamond saw and subsequently resealed with the same procedure. Secondary annealing treatments were performed at 573, 673, 773, 873, 973,

998, 1023, 1048, 1073, 1098, and 1123K for 3 hours followed by a water quench (WQ). To identify the influence of crystallographic ordering on the martensitic transformation characteristics, the magnetic response of each sample was measured using a Quantum Design superconducting quantum interference device with a vibrating head (SQUID-VSM) using the methods described in Chapter 2.

From these measurements, the martensitic transformation temperatures (martensite finish, M_f, martensite start, M_s, austenite start, A_s, and austenite finish, A_f) were determined as shown in Fig 5-13. The change in magnetization across the martensitic transformation with 1T applied field, ΔM, was also extracted as depicted in Fig. 5-13. The austenite Curie temperature, T_{Curie}, was extracted by finding the temperature derivative of the magnetization under the smallest field measured (~0.01T-0.05T) as shown by the inset of Fig. 5-13.

In Fig. 5-13, the thermomagnetic response of the 1173K 24hrs + 1073 3hrs WQ sample is shown. On cooling from 400K, the ferromagnetic austenite phase transforms to a non-magnetic martensite phase at temperature M_s. The forward (A to M) transformation is completed at M_f. On heating, the martensite transforms to austenite at temperature A_s and finishes at A_f resulting in the thermal hysteresis ($A_f - M_s$) typically observed from first-order solid to solid phase transformations. The thermomagnetic data in Fig. 5-13 also provides the transition range ($M_s - M_f$) discussed earlier.

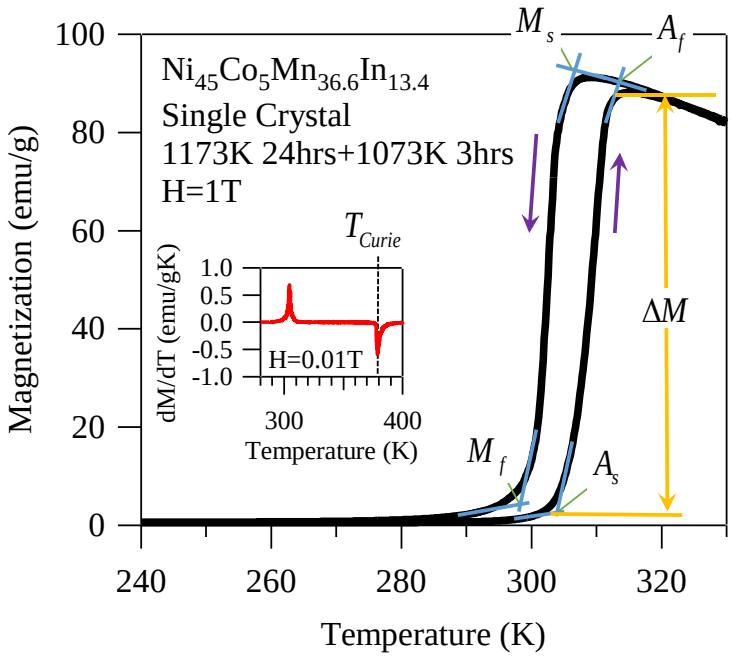

Figure 5-13: The thermo-magnetization curve of $Ni_{45}Co_5Mn_{36.6}In_{13.4}$ at.% single crystal after annealing at 1173K for 24 hours followed by 1073K for 3hrs. Heating/cooling was performed at 5K /min. The inset shows the derivative of the thermomagnetization curve under 0.01T revealing the austenite Curie temperature (T_{Curie}) at the minimum of the high temperature peak.

After the aforementioned parameters were extracted from the data, the heat capacity (C_p^{mart}) was measured for each sample at a temperature equal to its M_f temperature using a TA instruments Q2000 differential scanning calorimeter (DSC). At each test temperature the heat capacity of a sapphire standard was measured (in 2 separate tests) and used to calibrate the DSC instrument; this calibration was then used to "correct" the measured heat capacity of the MMSMA. Heat capacity measurements were then used to compute the adiabatic temperature change (ΔT_{ad}), derived in Eqn. (1.34).

A TA instruments SDT/Q600 thermo-gravimetric analyzer (TGA) was employed for high temperature heat flow logging to determine the $L2_1$ to B2 ordering temperature ($T^{L2_1/B2}$). In the TGA, a sample previously aged at a low temperature to promote $L2_1$ ordering was heated in a ceramic pan with a lid up to 773K and then to 1073K at 10K/min. During the heating from 773K to 1073K the heat flow was recorded. The minimum of an endothermic peak in this temperature range indicated a change in crystal symmetry resulting from the change in atomic configurations at the ordering temperature. The minimum of the captured endothermic peak was found to be at 900K, thus providing the $T^{L2_1/B2}$ for the $Ni_{45}Co_5Mn_{36.6}In_{13.4}$ alloy in this study.

5.4.3 Results

Before heat treating the samples, the $L2_1$/B2 ordering temperature was identified using a thermo-gravimetric analyzer (TGA), i.e. a high temperature differential scanning calorimeter. The sample measured in the TGA was first ordered to the $L2_1$ phase in a protective argon atmosphere by furnace cooling from 1173K across the unknown ordering temperature. The sample was then heated at 10K/min in a ceramic pan between 773K and 1073K, concurrently the heat flow was recorded as depicted in Figure 5-14.

As shown in Fig. 5-14, a negative peak was measured around 900K. The negative peak indicates that an endothermic reaction occurs and is an expected result of ordering from $L2_1$ to B2. Specifically, the $L2_1$ ordered crystal is characterized by a lower configurational entropy (atomic disorder) than the B2 phase. On heating, the alloy undergoes an increase in configurational entropy, thus resulting in an endothermic reaction. As shown in Fig. 5-14, the order/disorder transformation occurs at

$T^{L2_1/B2} = 900K$ which corroborates well with values reported in literature for a similar alloy composition [69].

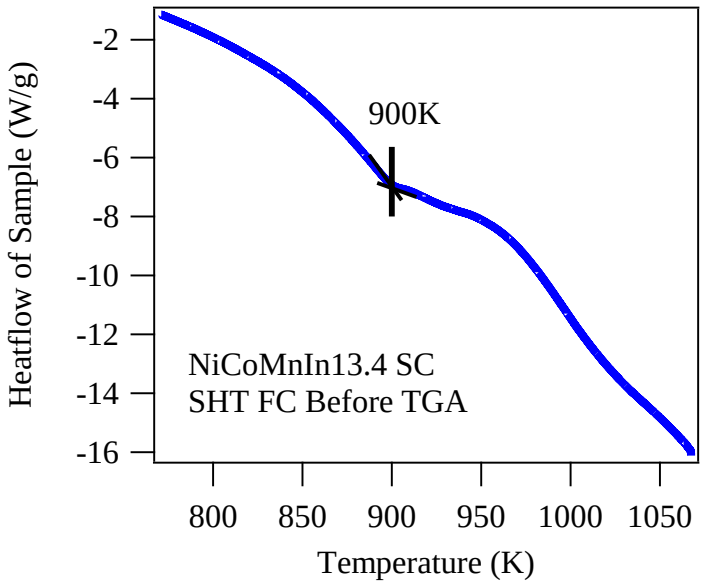

Figure 5-14: Heat flow of $Ni_{45}Co_5Mn_{36.6}In_{13.4}$ single crystals furnace cooled from 1173K prior to heat flow measurements. The sample was heated at 10K/min and the minimum at 900K indicates the $L2_1$ to B2 ordering temperature.

It is well known that in off-stoichiometric Heusler alloys, like the MMSMA studied here, crystallographic ordering influences the martensitic transformation temperatures and $\Delta G_{el}^{A\to M}$ in Eqn. (1.8) [68]. In effect, crystal ordering influences the enthalpy and the calorific effects of the MMSMA, and therefore, is a major consideration when tailoring the MMSMA response with heat treatments.

To study the influence of crystal order on the martensitic transformation characteristics, the experiments described above were employed. Magnetic

characterization was performed around the martensitic transformation and some heating/cooling histories are shown in Fig. 5-15a. In most of the samples, the martensitic transformation is generated on cooling from 400K to 100K under 1T as depicted by the large decrease in magnetization around the martensite start temperature (M_s). At temperatures above M_s, a gradual decrease in magnetization is measured in austenite on heating which can be attributed to the T_{Curie} of the ferromagnetic austenite. At temperatures below M_s, on the other hand, the magnetization levels describe that of martensite and depend on the thermal treatment. Here, we categorize the magnetic order of martensite as frustrated anti-ferromagnetism, which was measured in [45] with polarized neutrons, and later relate some of the discussion toward how the magnetization levels of martensite indirectly influence the energy conversion efficiency (see Eqn. (4.26) in MMSMA.

The X=573K thermomagnetization curve, in Fig. 5-15a, shows an "arrested transformation" where 1T is capable of stabilizing austenite at temperatures below M_f. Here, the transformation attempts to proceed on cooling around 200K, but cannot. There has been active discussion in the literature aimed at identifying why this arrest occurs. Some believe that the aggregate microstructural features such as antiphase boundaries (APBs), magnetic clusters, and martensitic nuclei are responsible [45, 70]. These microstructural features may also influence the martensitic transformation temperatures and are later discussed in detail.

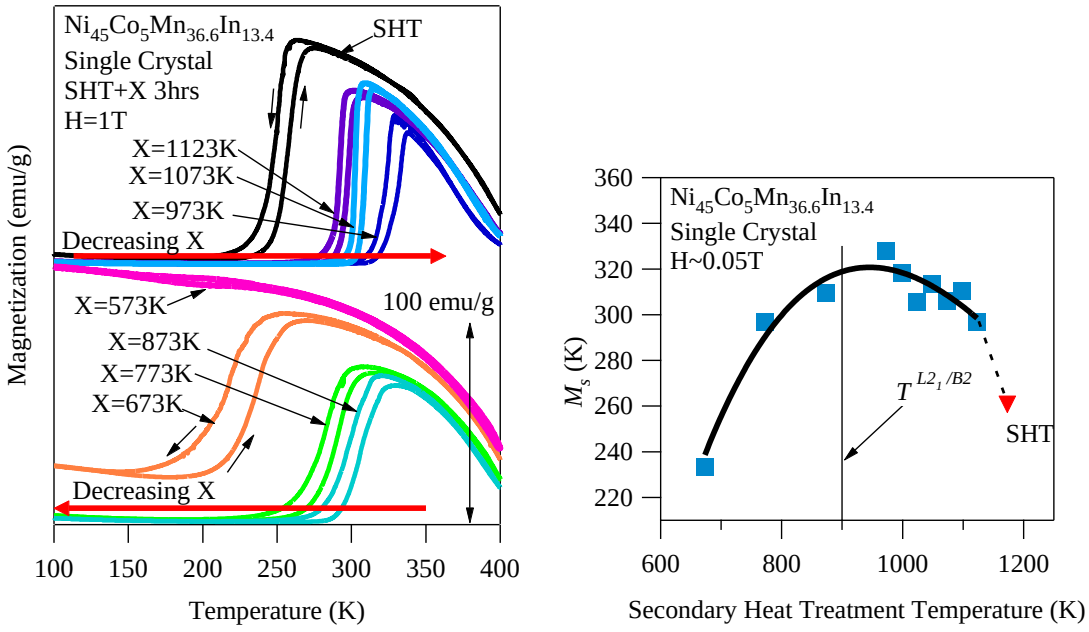

Figure 5-15: Thermo-magnetization curves under 1T 5K/min heating/cooling (a) and martensite start temperature, M_s, under ~0.05T of $Ni_{45}Co_5Mn_{36.6}In_{13.4}$ at.% single crystals that have been solutionized (SHT) at 1173K for 24 hours and then annealed at 1073, 973, 873, 773, 673K, and 543K for 3hrs.

The M_s temperatures, as extracted from Fig. 5-15a, are shown in Fig. 5-15b and vary as a function of secondary heat treatment temperature. This variation, also shown in Fig. 5-3, is attributed to the degree of long range crystal order in the MMSMA resulting from the heat treatment. In addition, high temperature quenching may generate higher vacancy concentration and anti-site defects in the austenite phase. Both of these would influence the $\Delta G_{el}^{A\rightarrow M}$ in Eqn. (1.8), thus the transformation temperatures are expected to change.

As shown in Fig. 5-16, the T_{Curie} varies linearly with M_s. This phenomenon has been reported to be linked to the degree of order in NiMnIn alloys [46], and therefore is indirect evidence that the degree of order in these alloys has changed with heat treatments. The T_{Curie} of the solution heat treated-1173K 24hrs (SHT), 1173K 24hrs + 573K 3hrs (573), and 1173K 24hrs + 673K 3hrs (673) WQ annealed samples are elevated compared to those of the other annealing treatments. Some speculations regarding this behavior are discussed in subsequent sections.

Since the objective of the current study was to identify the influence of crystal order on the energy conversion efficiency in MMSMAs, the magnetization change from M to A and the CC slope were needed from the above data as inputs to Eqn. (4.26). The product of these parameters is the entropy change from M to A (Eqn. 1.30). The $\Delta M^{M \to A}$ and dH^{A_f} / dT were extracted from the data above and are plotted in Figure 5-17.

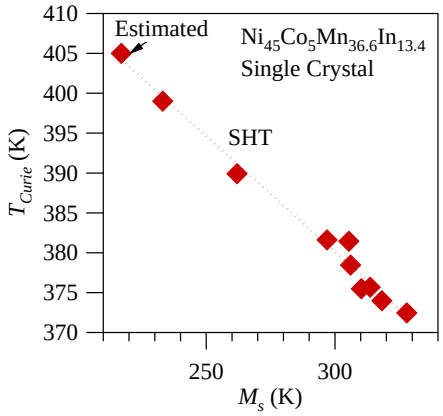

Figure 5-16: The austenite Curie temperature (T_{Curie}) vs. martensite start (M_s) temperature $Ni_{45}Co_5Mn_{36.6}In_{13.4}$ at.% single crystals that have been solutionized (SHT) at 1173K for 24 hours and then annealed at 1073, 973, 873, 773, 673K, and 543K for 3hrs.

In Fig. 5-17a, the magnetization change, $\Delta M^{M\to A}$, from M to A is plotted as a function of secondary heat treatment temperature. According to reports in literature, Co-free NiMnIn alloys [46] have been shown to decrease $\Delta M^{M\to A}$ with decreasing secondary annealing temperature. These heat treatments were also reported to decrease M_s. It was believed that this decrease was related to a larger degree of ferromagnetic order in the aggregate magnetic interactions below M_f [45]. The data presented here shows a similar decrease from quenching between 1173K and 900K, however, when heat treating below $T^{L2_1/B2}$, the $\Delta M^{M\to A}$ is recovered to nearly the original SHT level. Therefore, the following discussion is broken into two parts. The first will focus on the influence of 3hr. heat treatments in the temperature range $T^{L2_1/B2} < T < 1173\text{K}$, and the second on the influence of heat treating NiCoMnIn at temperatures below $T^{L2_1/B2}$.

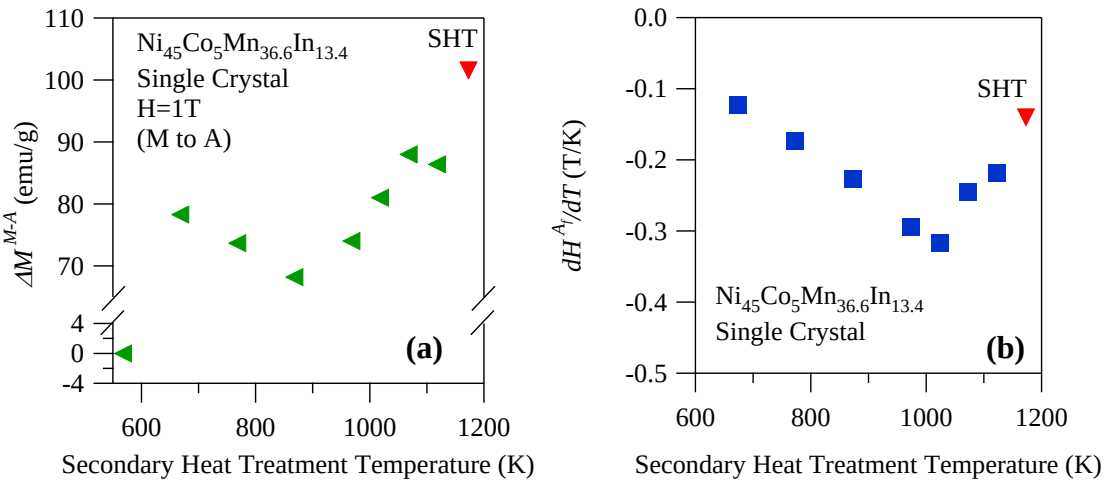

Figure 5-17: The magnetization changes ($\Delta M^{M\to A}$) across the martensitic transition (a) and austenite-finish phase diagram slopes (b).

On heat treating the $Ni_{45}Co_5Mn_{36.6}In_{13.4}$ single crystals at temperatures below 1173K, but above 900K, the M_s temperature tends to slightly increase with decreasing heat treatment temperature. This increase in M_s can be attributed to the reduction of vacancy concentration and anti-site defects resulting from lower temperature annealing above $T^{L2_1/B2}$. Perhaps the alloy orders to some degree, as well. It is well known that reducing the vacancy concentration and anti-site defects will effectively reduce lattice strain in the austenite sublattice ($\Delta G_{el}^{A\to M}$), and therefore the M_s temperature will increase. This is also observed with increasing grain size [59, 60] and was discussed earlier. Here, however, the specimens are single crystals and the austenite/martensite or martensite/martensite interface boundaries should be the only other contributors to the strain energy storage across the MT.

On increasing the M_s temperature, the transformation then occurs closer to the austenite Curie point, T_{Curie}. At the T_{Curie}, magnetization drops off, and therefore an increase in M_s corresponds to a drop in $\Delta M^{M\to A}$. In turn, the drop in $\Delta M^{M\to A}$ is an indication that the magnetic Zeeman energy difference ($\Delta G_{mag}^{A\to M}$ in Eqn. 1.8) has decreased, and thus, the transformation temperature sensitivity (dT/dH) to magnetic field is expected to decrease. This was explained in Chapter 1.

In Fig. 5-17b, the austenite-finish phase diagram slope, $\frac{dH^{A_f}}{dT}$ (Clausius-Clapeyron slope) is plotted as a function of heat treatment temperature. This particular slope was plotted due to its importance in Eqn. (4.26). As expected, the dT/dH decreases

as M_s increases and $\Delta M^{M\to A}$ decreases. The $\left|\frac{dH^{A_f}}{dT}\right|$ exhibits a maximum with the 1073K 3hrs secondary heat treatment.

Interestingly, the increase in M_s and the corresponding decrease in $\Delta M^{M\to A}$ from quench temperatures between 900K and 1173K result in a sharper forward martensitic transformation, $M_s - M_f$. The forward martensitic transition range, the total transition range, $A_f - M_f$, and the thermal hysteresis, $A_f - M_s$, are plotted as a function of heat treatment temperature in Fig. 5-18a. The author believes that heat treating at temperatures below 1173K but above 900K results in a smaller elastic energy barrier that must be overcome to propagate the forward martensitic transition due to the expected decrease in vacancy concentration and reduction of anti-site defects. As mentioned in the introduction, the elastic energy barrier contribution to Eqn. (1.8) is defined by $\Delta G_{el}^{A\to M}$. In [61], the magnitude of $\Delta G_{el}^{A\to M}$ was approximated by $\frac{\Delta S}{2}\cdot(M_s - M_f)$, hence, a reduction in $M_s - M_f$ corresponds to a decrease in $\Delta G_{el}^{A\to M}$.

Reducing $\Delta G_{el}^{A\to M}$, in effect, increases the latent heat measured by calorimetry [17]. Since no magnetic field is applied in a calorimeter, the measured latent heat (enthalpy) is a function of elastic and chemical contributions, including that from dissipation. The computed entropy change, $\Delta S^{M\to A}$, corresponds to the sum of these contributions. Under zero magnetic field, the $\Delta S^{M\to A}$ was determined for the heat treated alloys as shown in Fig. 5-18b. Interestingly, $\Delta S^{M\to A}$ increases as a result of the lower

temperature secondary heat treatments within the 1173K and 900K range. In zero magnetic field, the $\Delta G_{mag}^{A\to M}$ contribution in Eqn. (1.8) can be neglected. Therefore, the increase in $\Delta S^{M\to A}$ at temperatures above $T^{L2_1/B2}$ are attributed to a reduction in the elastic enthalpy contribution [17] as indicated by the decreasing $M_s - M_f$ in Fig. 5-18a. On the other hand, at temperatures below $T^{L2_1/B2}$, the $\Delta S^{M\to A}$ starts to decrease. This may be an indication that $\Delta G_{el}^{A\to M}$ increases, which is confirmed with the increase in $M_s - M_f$ below $T^{L2_1/B2}$, in Fig. 5-18a.

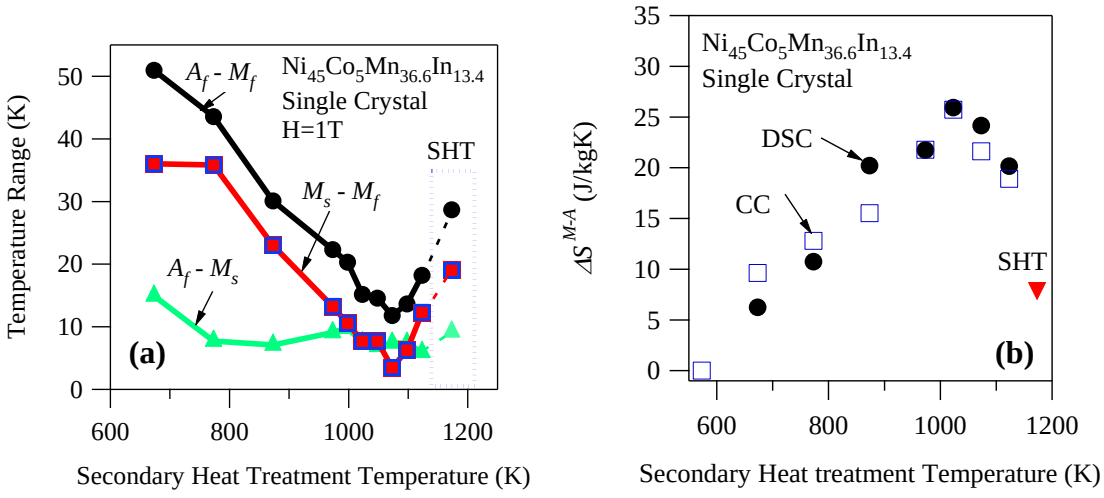

Figure 5-18: The characteristic transformation temperature ranges (a) and the transformation entropy change, $\Delta S^{M\to A}$ for the heat treated $Ni_{45}Co_5Mn_{36.6}In_{13.4}$ single crystals.

When heat treating the $Ni_{45}Co_5Mn_{36.6}In_{13.4}$ alloy below $T^{L2_1/B2}$ for 3 hours, the M_s temperature begins to decrease (see Fig. 5-15b). It is believed that this is a result of

ordering from a B2 to $L2_1$ crystal structure. On ordering to $L2_1$, the ferromagnetic interactions in austenite become stronger [45], thus T_{Curie} increases as shown in Fig. 5-16. It is commonly believed that lower temperature heat treatments order the lattice and promotes the Mn-Mn ferromagnetic interactions [45, 71]. The influence of these interactions are also believed to be carried over to the martensite phase because the martensitic transformation is diffusionless and the next nearest neighbors do not change across the transition. On cooling to martensite from austenite, the magnetic interactions obviously change across the transition due to a change in lattice parameters, but they may still result in a higher overall magnetization level below M_f [46]. Interestingly, the largest magnetization change occurs in the SHT sample (~100 emu/g). Considering that it was not subjected to an ordering treatment, this high change in magnetization may be the result of anti-site defects, high configurational disorder, or vacancies, however, the exact reason still remains unclear.

With a decrease in M_s, and an increasing T_{Curie} driven by $L2_1$ ordering, the $\Delta M^{M\to A}$ is expected to increase with heat treatments below $T^{L2_1/B2}$. This increase in $\Delta M^{M\to A}$ is confirmed with the data shown in Fig. 5-17a. Accordingly, this indicates an increase in the magnetic Zeeman energy, $\Delta G_{mag}^{A\to M}$, and a higher sensitivity in $\frac{dT}{dH}$, i.e. smaller $\left|\frac{dH^{A_f}}{dT}\right|$. The decrease in $\left|\frac{dH^{A_f}}{dT}\right|$ is also confirmed experimentally in Fig. 5-17b.

Upon reaching a specific degree of long range order with low temperature heat treatments, the martensitic transformation becomes completely arrested. As shown in Fig.

5-15a, the $\Delta M^{M\to A}$ resulting from the X=573 heat treatment, is essentially zero under 1T. In fact, other reports indicate that $\Delta S^{M\to A}$ is also nearly zero [72], indicating that the transformation does not occur, or that the elastic enthalpy and dissipation contributions cancel the chemical enthalpy measured in calorimetry. For the $Ni_{45}Co_5Mn_{36.6}In_{13.4}$ single crystals studied, here, it is believed $\Delta S^{M\to A}$ is nearly zero from applying the CC relation in Eqn. 1.30. In Fig. 5-18b, the $\Delta S^{M\to A}$ values computed with the CC relation for all other heat treatments agree well with those computed from enthalpy data measured with calorimetry.

The microstructural mechanism responsible for the arrested transformation in these alloys is investigated in the next section, but first, the energy conversion efficiency for the above 3hr. heat treated alloys are computed using Eqn. (4.26). The parameters required to compute Eqn. (4.26) include $\Delta M^{M\to A}$, $\frac{dH^{A_f}}{dT}$, A_f, M_f, and C_p^{mart}. These parameters are plotted in Figs. 5-17, 5-18, and 5-19. The C_p^{mart} was measured at the M_f temperature and is plotted for a few heat treatment cases in Fig. 5-19a.

The typical specific heat capacity of an intermetallic alloy is nearly 400J/kgK above the Debye temperature. As shown in Fig. 5-19, the measured heat capacity is, indeed, around 400J/kgK. The heat capacity is assumed to follow the Debye model, as depicted in Fig. 5-19b, where the limit of the phonon contribution to the total entropy is 6 cal/molK (3R). In Fig. 5-19b, the Debye temperature, Θ_D, was assumed to equal 322K as reported in another study for the same alloy composition [70]. At temperatures above 250K, the measured C_p^{mart} was, on average, larger than the theoretical limit of the

vibrational contribution, indicating that perhaps the magnetic contributions to C_p^{mart} are larger at elevated temperatures. Further investigations are needed to corroborate the data in 5-19b.

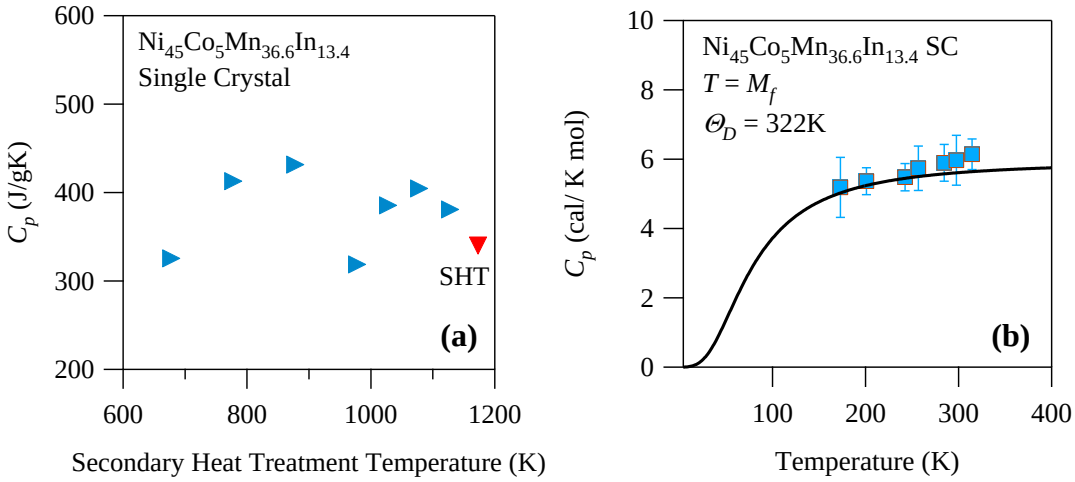

Figure 5-19: The specific heat capacity as a function of 3 hour heat treatment temperature (a) and the specific heat capacity for each heat treatment as a function of temperature added to a plot of a Debye curve (b) for $Ni_{45}Co_5Mn_{36.6}In_{13.4}$ single crystals. Data points in (a) and (b) were measured at the M_f temperature of the heat treated alloy.

Finally, η^{Latent} was computed for each heat treatment case and is shown in Fig. 5-20. In Fig. 5-20, the data point corresponding to the solution heat treated alloy (SHT) and the $L2_1$/B2 ordering temperature, $T^{L2_1/B2}$, are labeled. Interestingly, a maximum is observed at a temperature above $T^{L2_1/B2}$ indicating that the energy conversion efficiency resulting from the aforementioned heat treatments is the best in B2 ordered $Ni_{45}Co_5Mn_{36.6}In_{13.4}$ alloys. This seems to be a result of minimizing the elastic energy

contribution, $\Delta G_{el}^{A\to M}$, by decreasing vacancy concentration in a B2 ordered alloy with the help of secondary heat treatments.

The magnetization change, in this case, is neither maximum nor minimum with respect to Figure 5-17a, however, the $\left|\frac{dH^{A_f}}{dT}\right|$ is maximum. Since $\Delta M^{M\to A}$ defines the magnetic Zeeman energy, $\Delta G_{mag}^{A\to M}$, which then controls the magnitude of $\left|\frac{dH^{A_f}}{dT}\right|$, the $\left|\frac{dH^{A_f}}{dT}\right|$ should not be minimum nor maximum if $\Delta M^{M\to A}$ was its only controlling factor. Conversely, the $\left|\frac{dH^{A_f}}{dT}\right|$ parameter seems to be also influenced by the $\Delta G_{el}^{A\to M}$ term in Eqn. (1.8). Therefore, when employing η^{Latent} to determine the maximum energy conversion efficiency through MFITs, all the contributions to the free energy are considered. Thus, Eqn. (4.26) a powerful tool for quickly identifying the best energy converter through parameter optimization.

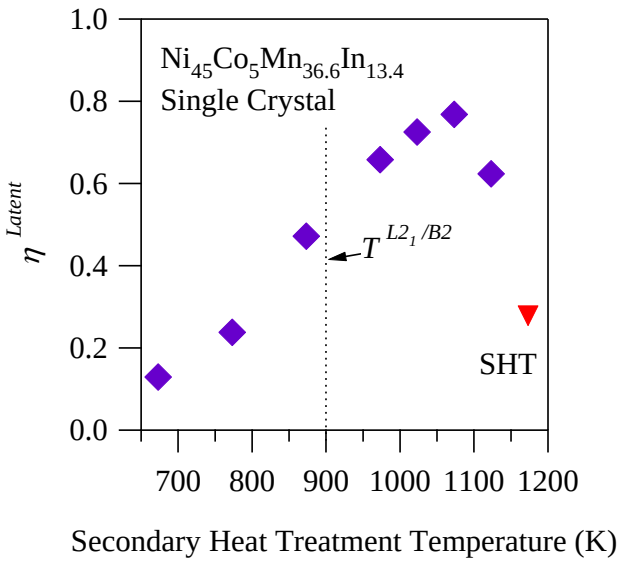

Figure 5-20: The magnetic-to-thermal energy conversion efficiency in $Ni_{45}Co_5Mn_{36.6}In_{13.4}$ single crystals subject to 3 hour thermal treatments followed by water quenching.

As such, the SHT+1073K 3hrs WQ alloy has been identified to be the best magnetic-to-thermal energy converter for all the mentioned heat treatments in $Ni_{45}Co_5Mn_{36.6}In_{13.4}$. This is attributed to the B2 crystallographic order, the location of M_s with respect to T_{Curie}, and the vacancy concentration and anti-site defects which control $\Delta G_{el}^{A\rightarrow M}$. Heat treatments above $T^{L2_1/B2}$ and below 1173K essentially decrease any stored strain energy in the lattice, and at the same time, maintain the thermal hysteresis at nearly 10K.

For the SHT+1073K 3hrs WQ heat treatment, the adiabatic temperature change and magnetic field needed to generate the complete the adiabatic transformation can be computed from Eqns. (1.34) and (4.13), respectively. These data are plotted in Fig. 5-21a

and b for the aforementioned heat treatments. In Fig. 5-21a, the B2 ordered alloys exhibit a computed adiabatic temperature change of approximately -6 to -8K. This corresponds well with direct measurements reported in studies on similar alloy compositions [27]. On approaching the ordering temperature, the computed adiabatic temperature change increases, indicating that $L2_1$ ordered alloys will perhaps exhibit a larger temperature change than the B2 ordered alloys. This may be attributed to the fact that their M_f temperatures are lower, and therefore their C_p^{mart}'s are also lower. However, when selecting a heat treatment for a specific MCE application the ΔT_{ad} is not the only consideration. Instead, those concerning the magnetic field levels needed to generate the ΔT_{ad} are often more important.

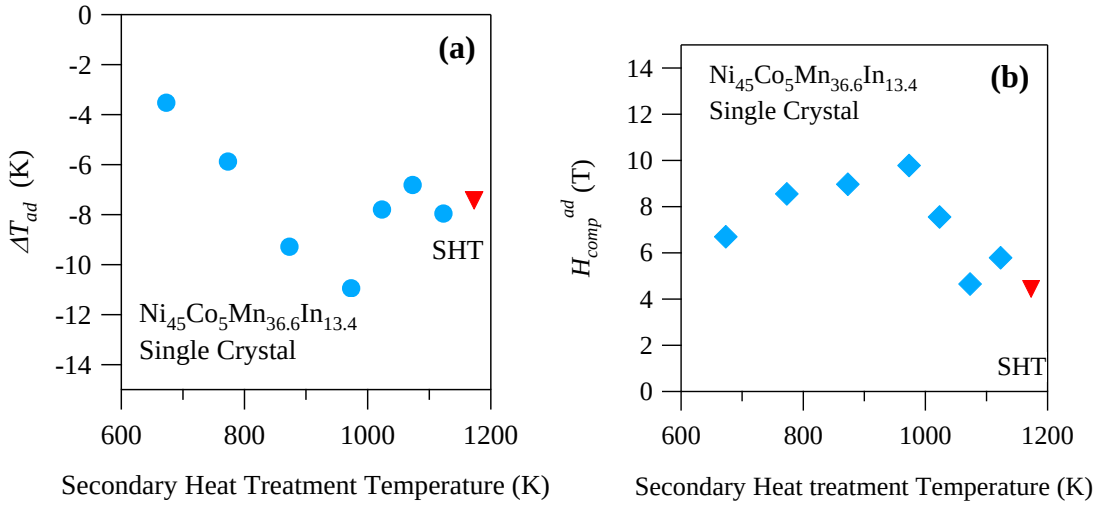

Figure 5-21: The computed adiabatic temperature change (a) and magnetic field needed to complete the adiabatic transformation at temperature M_f (b) for $Ni_{45}Co_5Mn_{36.6}In_{13.4}$ single crystalline 3 hour heat treated alloys.

In Figure 5-21b, the magnetic field level needed for the adiabatic transformation at M_f is plotted for each heat treatment case. This is the field level needed to drive the refrigeration process in Fig. 4-3. Interestingly, the B2 ordered alloys that had been treated above 1000K for 3hrs exhibit smaller magnetic field requirements. At first glance, the SHT alloy looks to be the best alloy for MCE applications, however, the $\Delta S^{M\to A}$ generated by applying the magnetic field is quite small compared to the 1073K heat treated alloy, as shown in Fig. 5-17b. This is due to the low M_s temperature and high $\Delta G_{el}^{A\to M}$ believed to be generated by anti-site defects and vacancies resulting from the quench procedure. Using the data in Figs. 5-21, magnetocaloric processes can be designed by selecting the best performing MMSMA, or for a MMSMA that exhibits the best adiabatic temperature change and/or smallest magnetic field requirement for some MCE processes.

5.4.4 Observing microstructural defects in arrested NiCoMnIn

The final section of this chapter deals with identifying and observing microstructural precursors that indicate the martensitic transformation is arrested. The martensitic transformation in NiCoMnIn alloys can be suppressed by employing low temperature secondary thermal treatments as depicted by the X=573 magnetothermal curve in Fig. 5-15. The M_s temperature, in the case of arrested alloys, is normally very low and away from room temperature. Therefore, this phenomenon typically does not influence near room temperature refrigeration schemes.

As discussed in the previous section, ordering the MMSMA to $L2_1$ increases the T_{Curie} in austenite and decreases M_s. This corresponds to an increase in $\Delta M^{M\to A}$ and

$\Delta G_{mag}^{A\to M}$, thus decreasing the $\left|\frac{dH^{A_f}}{dT}\right|$. Surprisingly, very low heat treatment temperatures (≈573K) that were intended to order the alloy to $L2_1$, resulted in very low measured $\Delta M^{M\to A}$ as shown by the data point in Fig. 5-17a for the 573K heat treatment. This has been the topic of major discussion in the literature, and is believed to be related to glassy behaviors in MMSMAs. In short, the magnetoelastic couplings that arise from low temperature heat treatments tend to disrupt the martensitic transformation, and therefore, austenite does not transform to martensite at low temperatures. Careful review of Fig. 5-3 indicates that the sensitivity of tuning the NiMnIn alloy may be related to the presence of cobalt in the NiMnIn system. For the Co-free $Ni_{48}Mn_{38}In_{14}$ alloy, the martensitic transformation is not substantially tuned with thermal processing, but the transformation can still be suppressed with low temperature heat treatments as discussed later.

Here, we probe the austenitic microstructure in an attempt to identify a feature indicative of arrested transformations. The alloys studied, here, were subject to heat treatments like those mentioned in Chapter 2. However, to determine the time dependence on the $L2_1$ to B2 transformations, various thermal treatments are employed for different durations. Sample microstructures heat treated for different durations were observed with transmission electron microscopy (TEM), as described in the experimental section. Microstructural TEM observations were then related to the thermomagnetic responses measured with SQUID magnetometry.

Thermal treatments employed for this study are tabulated in Table 2-6. Initially, the dark field images of $L2_1$ morphology and the thermomagnetic responses were

compared between SHT and SHT + 573K 3hrs or 1 week alloys. Figure 5-22a depicts the thermomagnetic responses of the alloys under 1T and 5-22b, c, and d the corresponding dark field images of $L2_1$ morphology in room temperature austenite.

In Figures 5-22b, c, and d the bright morphology corresponds to microstructural $L2_1$ ordering, and dark regions indicate ordering other than $L2_1$, including B2 or $D0_3$. Interestingly, the $L2_1$ morphology looks almost identical in these cases with slightly larger morphology produced in the 573K 3hrs and 1wk cases. The thermomagnetic responses between the SHT and secondary heat treated alloys, however, are substantially different in 5-22a. The 573K 3hrs and 1wk heat treated alloys exhibit similar arrested responses as indicated by low $\Delta M^{M\to A}$ values at low temperatures. The 1 week heat treatment was sufficient to completely arrest the transformation and only 3 hours was not. According to the dark field images in Fig. 5-22, the size of the $L2_1$ morphology may be responsible for the thermomagnetic response of the MMSMA. That is, larger $L2_1$ morphology might influence the transformation.

To further probe at the microstructure, $Ni_{45}Co_5Mn_{36.6}In_{13.4}$ was heat treated at 673K for 3hours and 24hours, and then compared with the solutionized case. The thermomagnetic response of these alloys are shown in figure 5-23a. The $L2_1$ morphology for these cases are shown in 5-23b and c. Interestingly, the $L2_1$ morphology in Fig. 5-23b coarsened from the SHT case to a greater degree in 3hours at 673K than for 3hours at 573K shown in Fig. 5-22c. After SHT, the 673K 3hrs heat treatment decreased the M_s temperature, decreased $\Delta M^{M\to A}$, and increased the transition range. This is an indication that the $\Delta G_{el}^{A\to M}$ from Eqn. (1.8) also increased.

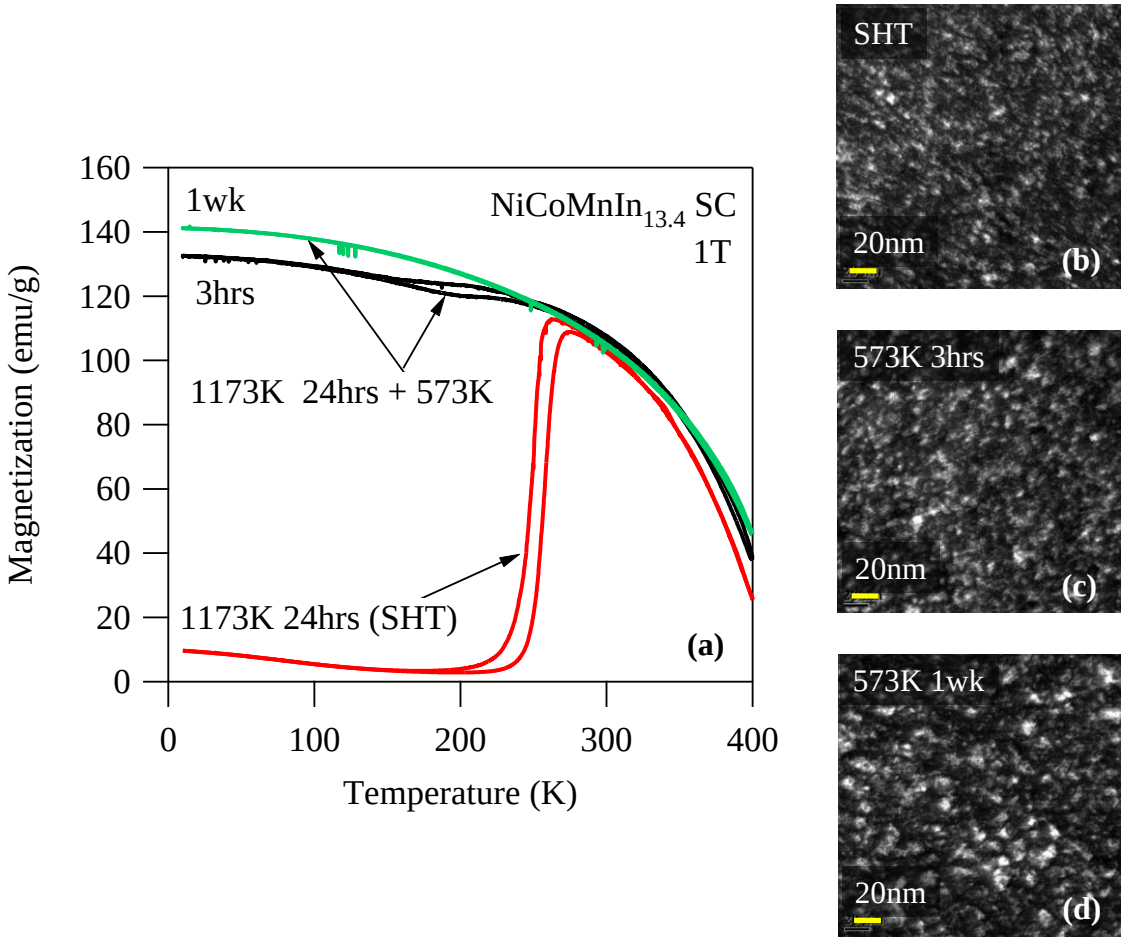

Figure 5-22: The thermomagnetic responses of a 1173K 24hour water quenched (SHT), SHT + 573K 3hrs, and SHT + 573K 1 week $Ni_{45}Co_5Mn_{36.6}In_{13.4}$ alloy under 1T (a), and their corresponding $L2_1$ morphologies in (b), (c), and (d), respectively.

Heat treating for a longer duration of 24hours, resulted in an even courser $L2_1$ morphology characterized by the thermomagnetic response depicted in Fig. 5-23a. The 24hour heat treatment, in this case, arrested the transformation completely. Upon closer inspection of Figs. 5-23b and c, non-uniformities are observed littering the $L2_1$ morphology in the 24hrs heat treatment case. The non-uniform contrast seems to indicate the degree that the martensitic transformation will be arrested. Highly dense contrast

differences correspond to more arrested transformations. Considering these non-uniformities are only slightly present in the 3hrs heat treatment case, the increased magnetization of the martensite phase (shown in Fig. 5-23a) can be attributed to partial arrested martensitic transformation. In addition, an increased degree of $L2_1$ order is generated from the SHT case, as depicted by larger $L2_1$ morphology, and therefore, martensite may exhibit stronger ferromagnetic interactions as determined for Co-free NiMnIn alloys [46]. In the 573K heat treated cases shown in 5-22, the $L2_1$ morphology was too small to observe the contrast difference within the $L2_1$ domains.

Therefore, we attempted to further increase the $L2_1$ domain size with higher temperature, shorter heat treatments to clearly observe the contrast difference structure responsible for arresting the transformation. The influence of additional thermal treatment on $L2_1$ morphology was studied by secondarily heat treating solutionized $Ni_{45}Co_5Mn_{36.6}In_{13.4}$ alloys at 773K for 15min, 30min, and 3hrs. The thermomagnetic responses of the heat treated alloys are depicted in Fig. 5-24a.

As shown in Fig. 5-24a, heat treating for 3 hours at 773K resulted with an increase in M_s which is also depicted in Fig. 5-15b. The $L2_1$ morphology for this heat treatment case was quite large as indicated by the bright regions in Fig. 5-24b. Here, the bright morphology are separated by black walls, known as antiphase boundaries (AFPs). In this case, these APBs are characterized by B2 crystal order and are formed with approximately 10nm thickness to reduce the free energy between $L2_1$ domains [73]. At some points, the APBs appear to be thicker than 10nm because they are skewed out of plane parallel to the electron beam through the thickness of the TEM sample.

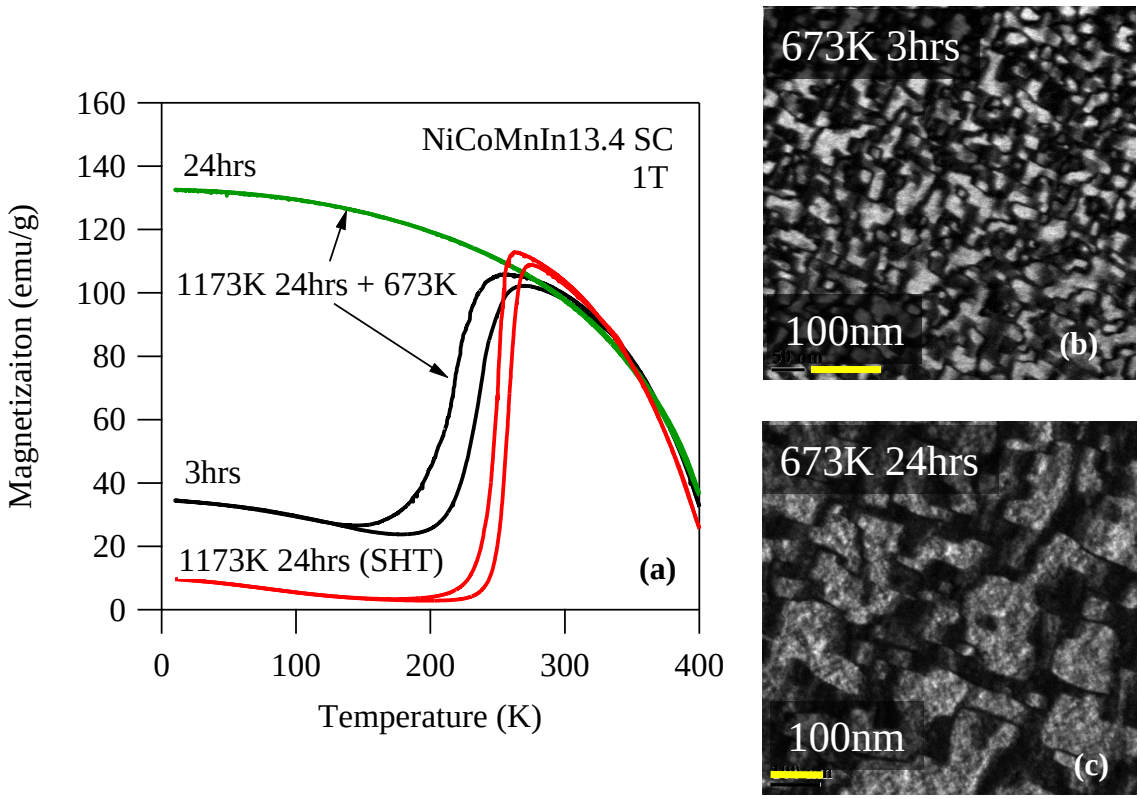

Figure 5-23: The thermomagnetic responses of a 1173K 24hour water quenched (SHT), SHT + 673K 3hrs, and SHT + 673K 24 hours $Ni_{45}Co_5Mn_{36.6}In_{13.4}$ alloy under 1T (a), and the corresponding $L2_1$ morphologies for the secondarily heat treated alloys in in (b) and (c), respectively.

Heat treating the alloy at 773K for 30 minutes, on the other hand, only slightly increases the M_s from the SHT case. The transformation range, $M_s - M_f$, substantially grows from the SHT case, and the magnetization level measured below M_f was about 45 emu/g. This elevated level of magnetization may indicate that some degree of $L2_1$ ordering had occurred within 30min, thus increasing the magnetic ordering in martensite. In addition, the large magnetization at low temperatures can be attributed to a partially

arrested martensitic transformation where austenite persisted in the microstructure below M_f.

Interestingly, the thermomagnetic responses corresponding to the 1173K 24hrs + 773K 30min heat treatment case (Fig. 5-24c) looks similar to that of the 1173K 24hrs + 673K 3hours (Fig. 5-23b). From these heat treatments, the size of the $L2_1$ domains separated by B2 APBs are different. In addition, the $L2_1$ morphology resulting from the 773K 30min heat treatment is littered with the non-uniformities first discussed in the 673K 24hrs alloy in Fig. 5-23c. It is believed that since the $L2_1$ domains are larger in the 773K 30min sample than the 673K 3hrs sample, the contrast difference is more visible. The contrast difference in the 673K 3hours case may not be observable because the $L2_1$ domains are too small and the ordering that produces contrast non-uniformities is hidden in the dark B2 morphology.

The main difference between the thermomagnetic responses of the 773K 30min and 673 3hrs cases is the thermal hysteresis around the martensitic transformation. The 673K 3hrs case exhibits larger hysteresis. This may be attributed to smaller $L2_1$ domains separated by B2 APBs, but more microstructural investigations are needed to identify the cause of the differences in thermal hysteresis.

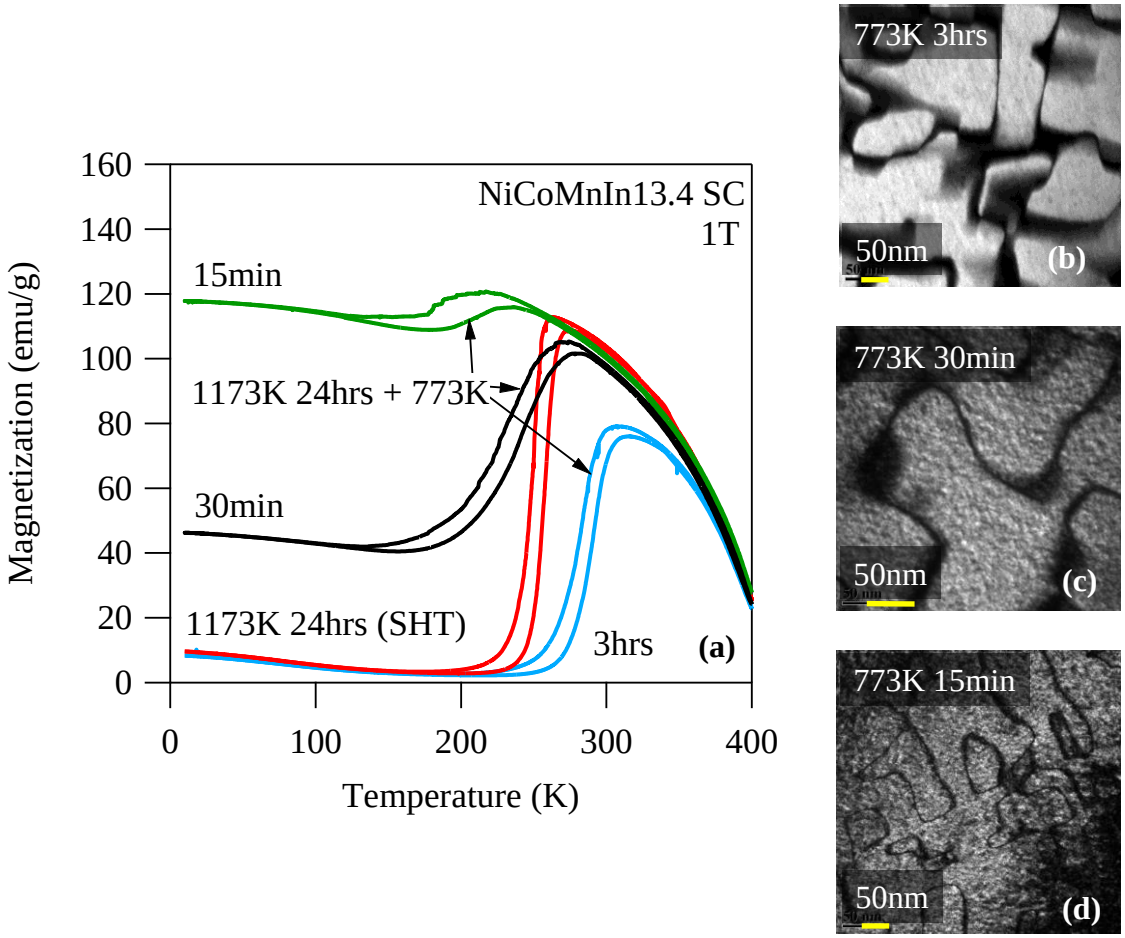

Figure 5-24: The thermomagnetic responses of a 1173K 24hour water quenched (SHT), SHT + 773K 3hrs, SHT + 773K 30min, and SHT + 773K 15min $Ni_{45}Co_5Mn_{36.6}In_{13.4}$ alloy under 1T (a), and their corresponding $L2_1$ morphologies in (b), (c), and (d), respectively.

Finally, the most arrested case of the 773K heat treatments was measured from the 15 minutes heat treatment, as shown in Fig. 5-24a. The $L2_1$ morphology of the 1173K 24hrs + 773K 15min sample is shown in 5-24d. The contrast difference within the $L2_1$ domains, in this case, are even denser than that resulting from the 773K 30min case. The density of the microstructural non-uniformities from the 773K 15min case is nearly

equivalent to the 673K 24hours heat treatment in 5-23c. B2 APBs are clearly present in the 773K 15min case, but local disorder is the microstructural feature indicating that the transformation is arrested.

The time/temperature dependent microstructures depicted in Figs. 5-24 and 5-23 give an indication on how $L2_1$ domains form from a B2 ordered matrix. Initially, the alloy is collectively disordered and characterized by a B2 crystal structure in the SHTed state. At elevated temperatures, below $T^{L2_1/B2}$, the alloy orders toward $L2_1$ according to the Allen-Cahn equation [74],

$$\frac{\partial \nu}{dt} = -\alpha \frac{\partial \Delta f_0}{d\nu} + \tau \nabla^2 \nu \tag{5.1}$$

where ν is a long range order parameter, t is time, α is a positive kinetic coefficient, $\frac{\partial \Delta f_0}{d\nu}$ is the spatial derivative of the excess free energy due to interfaces, and τ is a diffusion coefficient defined by $2\alpha\kappa$. The diffusion coefficient τ is dependent on κ, which is known as the gradient energy coefficient.

In the NiCoMnIn system, studied here, TEM observations indicate a clear spatial gradient in the order parameter, and thus the first term on the R.H.S. of Eqn. (5.1) is non-zero. In addition, the mobility coefficients, τ and α, contribute to the time dependence of ordering. In the micrographs above, certain regions of the microstructure initially order more quickly than others. The microstructural feature (contrast non-uniformity) is observed within a $L2_1$ matrix, thus suggesting that the size of the $L2_1$ domain is not responsible for arresting the transformation. Additional studies, however, are needed to

identify the rate of local ordering in NiCoMnIn alloys and the temperature dependence of the mobility coefficients, τ and α.

5.4.5 Conclusions:

In summary, the magneto-structural property relations in NiCoMnIn alloys were investigated using transmission electron microscopy (TEM) and SQUID magnetometry in attempts to observe the microstructural defects responsible for arresting the martensitic transformations. A precursor microstructural feature in room temperature dark field images of austenite was observed in arrested alloys. This features was observed in $L2_1$ domains which were separated by B2 antiphase boundaries. This microstructural feature was not observed in the alloys heat treated for 3hours. $L2_1$ ordering, however, was demonstrated to occur within 3 hours at temperatures above 573K and the resulting martensitic transformation was found to progress regardless of the $L2_1$ domain size. On the other hand, the martensitic transformation is arrested when $L2_1$ morphology is degraded with high temperature-short duration heat treatments. The microstructural feature responsible for suppressing the transformation in the 573K 3hours alloy was not visible in the dark field images due to the small size of the $L2_1$ domains which typically illuminate them.

In terms of magnetic or solid-state refrigeration, a few points can be made on the above findings.

1. Arrested $Ni_{45}Co_5Mn_{36.6}In_{13.4}$ alloys cannot perform in magnetically driven refrigeration applications. Therefore, these arrested alloys have no use in MCE

applications. More work is needed to quantify the applicability of arrested alloys for elastocaloric applications.

2. The most efficient energy conversion ratio can be achieved in a $Ni_{45}Co_5Mn_{36.6}In_{13.4}$ alloy first solutionized and then subsequently re-heat treated at 1073K for 3 hours. This was related to the reduction in strain energy associated with dislocations and anti-site defects above the ordering temperature. These exhibit larger entropy changes, nearly 8K temperature changes, and require nearly 4-6T to drive the transformation.
3. Generally, B2 ordering via heat treatments will yield a better magnetocaloric refrigerant in $Ni_{45}Co_5Mn_{36.6}In_{13.4}$.

In the next chapter, a few case studies are presented for the giant MCE and ECE in the alloys tabulated in Chapter 2. The optimal annealing treatment in $Ni_{45}Co_5Mn_{36.6}In_{13.4}$ single crystals defined by Eqn. (4.26) is investigated further and entropy change versus temperature diagrams are constructed for a few heat treatment cases. Additionally, the energy conversion efficiency of the heat treated alloys listed in Chapter 2 are computed from the experimentally determined key materials parameters, discussed earlier.

CHAPTER VI

CRITICAL ANALYSES OF GIANT MAGNETOCALORIC AND ELASTOCALORIC EFFECTS IN SELECTED MAGNETIC SHAPE MEMORY MATERIALS*

6.1 Introduction

The following chapter is dedicated to discussing the measured calorific responses around martensitic transformations in a few selected magnetic shape memory alloys. For each alloy and heat treatment, the parameters in Eqns. (4.26) or (4.27) were identified through the procedures described in Chapter 2 and the energy conversion efficiency was computed to reveal the optimal thermoprocessing condition. Entropy change versus temperature diagrams were generated for a few heat treatment cases in NMnX (X=Sn, In). Additionally, the influence of crystallographic anisotropy on the elastocaloric effect was studied in as-grown $Ni_{54}Fe_{19}Ga_{27}$ single crystals. It will be shown in subsequent sections that superelastic curves from $Ni_{54}Fe_{19}Ga_{27}$ pose analytical problems when computing the ECE as discussed in Chapter 2. These problems can be overcome by implementing Eqns. (2.8) through (2.11).

---

*Part of this chapter is reprinted from *Acta Materialia*, **74**, Bruno N. *et al.* The effect of heat treatments on Ni43Mn42Co4Sn11 meta-magnetic shape memory alloys for magnetic refrigeration, 66-84, Copyright (2014), with permission from Elsevier.

6.2 $Ni_{43}Co_4Mn_{42}Sn_{11}$ (at.%)

6.2.1 Introduction

Bulk polycrystalline $Ni_{43}Mn_{42}Co_4Sn_{11}$ (at %) alloys were prepared using the procedures in Chapter 2. Some induction melted samples were homogenized in argon at 1173K (above the reported $L2_1$ ordering temperature [75]) for 24 hours and quenched in ice water. The melt-spun ribbon samples made from the bulk alloys and were subsequently heat treated as described in Chapter 2.

Microstructural compositional analysis was performed with WDS and thermomagnetic measurements with a Quantum Design SQUID-VSM magnetometer. These measurements were used in determining martensitic transformation temperatures and transformation hysteresis. All thermomagnetic measurements began with zero field heating to 400K and were followed by FC-FH. For qualitative comparison of the effect of the secondary heat treatments, the change in magnetization across the transformation, $\Delta M^{M\to A}$, was determined from the difference of the magnetization levels at A_f and A_s from the thermomagnetization curves under 0.05T.

Isothermal magnetization responses were measured at small temperature intervals and the forward ($A\to M$) and reverse ($M\to A$) paths were separated so that Eqn. (2.3) could be applied to construct an entropy change diagram. Only the reverse transformation was considered because the $M\to A$ transformation was associated with the endothermic response responsible for the cooling. In these experiments, the applied field was ramped at 25 Oe/s and the magnetic responses were considered to be isothermal because this rate

is sufficiently low to prevent temperature changes from the latent heat of the transformation. The $\Delta S^{M \to A}$ was plotted over a range of temperatures from the isothermal magnetization curves, which then allowed T_{work} to be computed using Eqn. (4.6). Isothermal magnetization measurements also provided a means to validate the critical fields H_{comp}^{iso}, H_{comp}^{ad} and H_{req} computed with Eqns. (4.11), (4.12), and (4.13).

Thermomagnetic transformation temperatures measured under 0.05T were then compared to those measured with DSC. For DSC analysis, the temperature was ramped at 2K/min. In order to compute ΔT_{ad} in Eqn. (4.6), the heat capacity was measured using a Quantum Design Physical Property Measurement System (PPMS) between 10K and 250K by a pulsed-relaxation method-continuous heating scheme.

6.2.2 Results

Magnetic characterization of the $Ni_{43}Mn_{42}Co_4Sn_{11}$ samples was performed and the thermomagnetic results are compared in Figure 6-1a. The figure shows the thermomagnetization curves of the solutionized bulk, and as-spun and solutionized ribbon samples under 0.05T. The as-cast bulk specimen did not exhibit a notable meta-magnetic phase transition, thus the results are not shown. The austenite phase of the bulk sample is ferromagnetic (FM) for a narrow temperature interval on heating until its Curie temperature, T_{Curie}, is reached. The T_{Curie} of the austenite was determined to be about 365K. The martensite exhibits a small magnetic susceptibility, which in past studies has been attributed to short-range frustrated antiferromagnetic interactions by neutron polarization measurements [45, 76]. The frustrated antiferromagnetic response is shown

by the low magnitude of magnetization from 4.2K to 160K. Around 200K the sample started transforming to the highly magnetic austenite as a result of the reverse transformation. Both as-spun (A-S) and solutionized ribbons exhibited good meta-magnetic shape memory characteristics with a sharp transition between the austenite and martensite. The changes in magnetization across MT ($\Delta M^{M\to A}$), transformation ranges (ΔT_{elas}), temperature hysteresis (ΔT_{hys}), and their sum (ΔT_{comp}) were extracted from Figure 6-1a. The data indicate that the solutionized bulk sample exhibits the smallest thermal hysteresis, but the ribbon samples exhibit the smallest transformation range.

In addition, the Clausius-Clapeyron (CC) slopes were determined using the thermomagnetization results like that seen in Figure 6-1(c) for the solutionized ribbon samples. The corresponding phase diagrams are shown for the solutionized bulk and ribbon samples in Figure 6-1(d). These results will later be used to discuss the effect of microstructure on the performance parameters summarized earlier.

Differing from the samples in the bulk form, the ribbons exhibit a large $\Delta M^{M\to A}$ with the application of very low magnetic fields. In addition, the ribbons show the smallest ΔT_{comp} which is desired for efficient refrigeration performance per Eqns. (4.6). On the other hand, the solutionized bulk sample exhibits the smallest ΔT_{hys}. Since the refrigeration performance parameters can be improved by decreasing ΔT_{hys}, the solutionized $Ni_{43}Mn_{42}Co_4Sn_{11}$ ribbons were exposed to secondary heat treatments in attempt to further reduce their ΔT_{hys} as can typically be done for NiMnIn alloys [46].

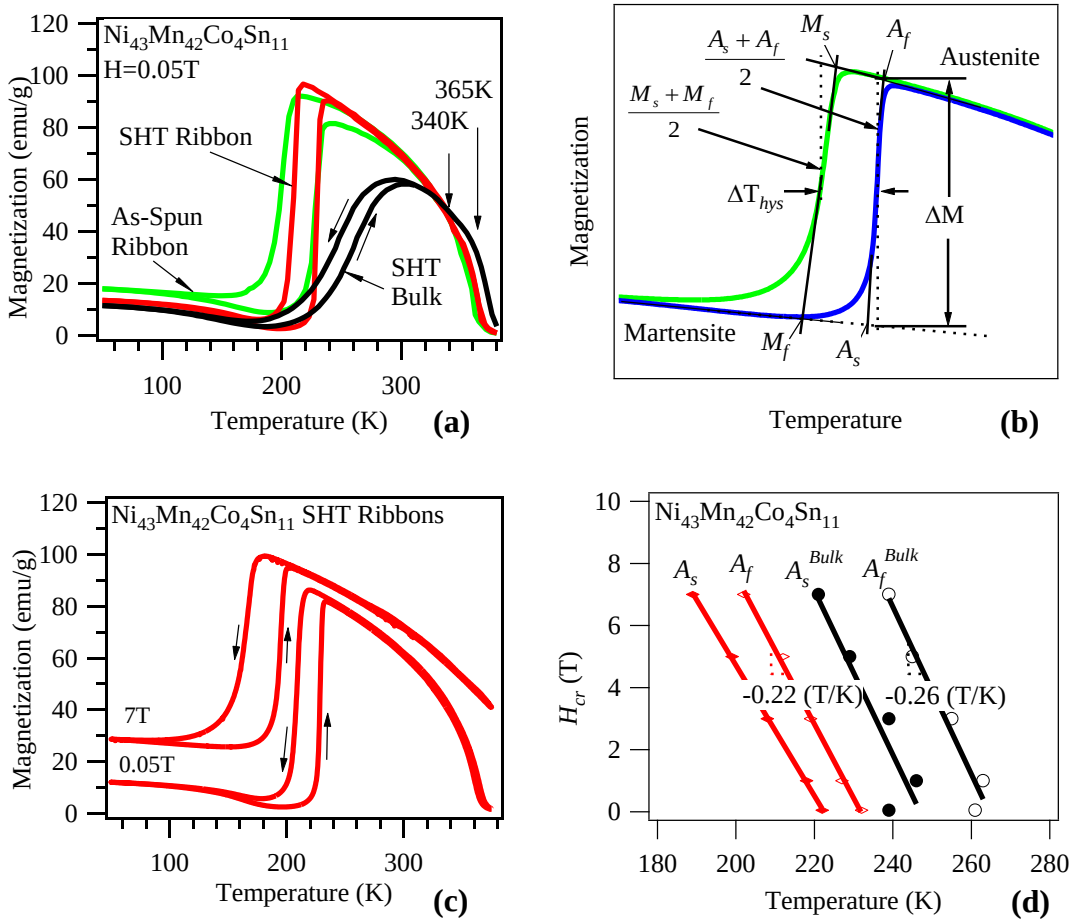

Figure 6-1: (a) 0.05T thermo-magnetization curves of $Ni_{43}Mn_{42}Co_4Sn_{11}$ polycrystalline samples in as-spun ribbon, bulk solutionized at 1173K for 1 day, and ribbon solutionized at 1173K 2 hrs. (b) Schematic showing how some of the parameters in Table 1 were determined using the results in (a). (c) Thermo-magnetization curves of the solutionized ribbon samples under 0.05T and 7T which were used to construct the critical field-temperature phase diagram in (d). (d) includes the critical field – temperature phase diagrams for the solutionized bulk and ribbon samples [50].

In [46], it was shown that ΔT_{hys} is related to $L2_1$ ordering, and therefore secondary heat treatments were performed at temperatures (673K, 773K, 873K) below the reported $B2/L2_1$ ordering temperature for 1 hr to promote $L2_1$ ordering. At each temperature,

ribbons were rapidly quenched (RQ) or furnace cooled (FC). Characteristic features of the martensitic transformation after secondary heat treatments are determined directly from the experiments or calculated using the equations in Chapters 1 and 2, and tabulated in Table 6-1. The critical field vs. temperature phase diagrams for the completion of the martensite to austenite transformation in the secondary heat treated ribbons are shown in Figure 6-2(a), which are extracted from the thermomagnetization curves. Later, these phase diagrams will be used to compute the H_{comp}^{iso} parameter.

Table 6-1: Martensitic transformation (*MT*) characteristics of the secondary heat treated ribbons. FC denotes furnace cooling; RQ denotes rapid quenching and the *MT* temperature is determined as $T_0 = (M_s + A_f)/2$ [50].

Annealing Treatment	$\frac{dH^{A_s}}{dT}$ (T/K)	$\frac{dH^{A_f}}{dT}$ (T/K)	M_f (K)	M_s (K)	A_s (K)	A_f (K)	T_0 (K)	ΔT_{hys} (K)	ΔT_{elas} (K)	H_{comp}^{iso} (T)	H_{comp}^{ad} (T)	H_{req} (T)	T_c (K)
673K FC	-0.14	-0.23	193	208	217	225	217	21	11	7.56	9.6	3.4	368
773K FC	-0.17	-0.23	185	217	214	230	223	23	26	11.2	13.3	4.9	367
873K FC	-0.19	-0.26	189	225	216	243	234	22	31	13.9	17.0	5.0	366
673K RQ	-0.16	-0.25	210	222	229	238	230	17	10	6.9	9.5	3.1	361
773K RQ	-0.18	-0.27	209	227	230	240	233	17	14	8.2	11	3.8	360
873K RQ	-0.22	-0.24	213	233	232	246	240	16	17	8.0	10.1	4.3	360
1173K SHT	-0.19	-0.22	198	216	224	233	224	21	13	7.6	9.6	5	340

As seen in Table 6-1, secondary heat treatments resulted in slight changes in transformation temperatures, thermal hysteresis, and magnetic field sensitivity of A_s and A_f, but on average, the $\Delta M^{M \to A}$ across the transformation remained approximately the

same and therefore was not included in the table. The RQ samples exhibited an increase in transformation temperatures, whereas the FC samples showed a decrease in transformation temperatures as compared to the solution heat treated ribbons. This suggests that slight changes in atomic ordering were dependent on the cooling rate of the secondary heat treated ribbons.

The product of the slopes of the CC lines in Figure 6-2(a) and the $A_f - M_f$ computed from Table 6-1 yielded the H_{comp}^{iso} following Eqn. (4.11), which is also tabulated in Table 6-1. The solutionized ribbon that was secondarily heat treated at 673K for 1 hour and then RQ was found to exhibit the smallest H_{comp}^{iso} of 6.9T whereas the solutionized ribbon sample originally had a H_{comp}^{iso} of 7.6T.

Figure 6-2(b) shows the 7T thermo-magnetization curves of the $Ni_{43}Mn_{42}Co_4Sn_{11}$ as-spun, solutionized (SHT), and solutionized plus 673K 1hr RQ ribbons (SHT+673K(RQ)). The 0.05T thermo-magnetization curve for the SHT+673K(RQ) sample is shown in the inset. As can be seen in the inset, the 7T field does not lead to a large change in the magnetization of austenite, and the large applied field reduces $\Delta M^{M \to A}$ across *MT* as the magnetization of martensite increased more than that of the austenite. We attribute this to the short range antiferromagnetic interactions of martensite [45, 76, 77] making magnetic saturation of martensite difficult. Large fields decrease the transformation temperatures, as expected. The CC slopes, dH^{A_s} / dT and dH^{A_f} / dT, for the SHT+673K(RQ) ribbons were determined to be -0.16 T/K and -0.25 T/K, respectively, from thermomagnetization curves.

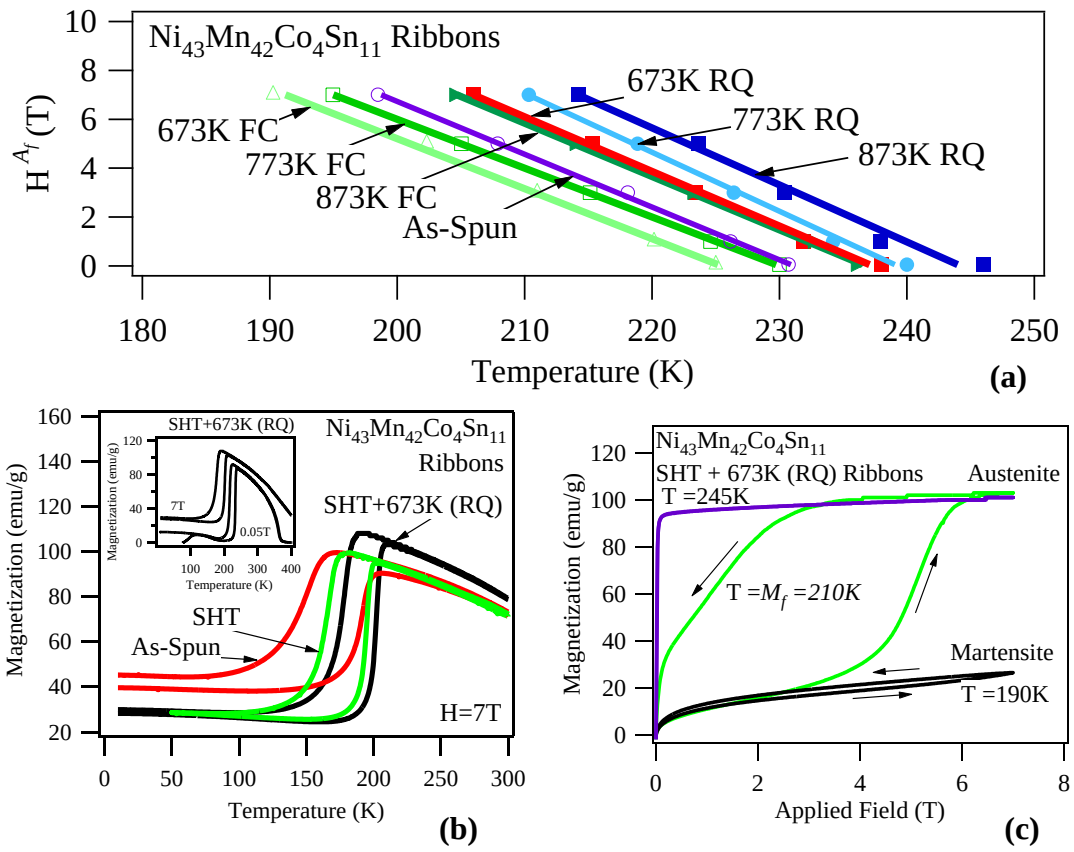

Figure 6-2: (a) The critical field-temperature phase diagram for the completion of the martensite to austenite phase transformation for the secondary heat treated ribbons. (b) Thermo-magnetization curves of the $Ni_{43}Mn_{42}Co_4Sn_{11}$ as-spun, SHT, and SHT+673K(RQ) ribbons in the field of 7T; Inset: 0.05T and 7T thermo-magnetization curves of SHT+673K(RQ) ribbons, (c) Isothermal magnetization curves of the SHT+673K(RQ) ribbons. Magnetization isotherms were measured at temperatures much less than M_f (=190K), at M_f =210K, and above A_f =245K [50].

To verify the validity of Eqns. (4.11) and (4.12), the isothermal magnetic response of the $Ni_{43}Mn_{42}Co_4Sn_{11}$ SHT+673K(RQ) ribbons was measured under applied magnetic fields up to 7T at a temperature (=190K) much below M_f, at M_f (=210K), and a temperature (=245K) above A_f, using martensite as the initial phase in the former two cases. The response is shown in Figure 6-2(c). The magnetization values at low temperatures are small. Small magnetic hysteresis is observed at T =190K since the field is not sufficient to induce a large structural transformation and the sample is mainly comprised of short range frustrated antiferromagnetic martensite. The small hysteresis may be attributed to a low concentration of magnetic domains rotating at low applied fields or a small volume fraction of phase transformation. The response near M_f shows magnetic hysteresis upon unloading the field indicating structural transformation has taken place. At temperatures above A_f, no magnetic hysteresis is observed indicating that the field does not induce a transformation from austenite to another phase, and austenite is purely ferromagnetic.

More importantly, the isothermal magnetization curves in Figure 6-2(c) verify the validity of Eqn. (4.11) for the SHT+673K(RQ) ribbons. In Table 6-1, H_{comp}^{iso} and H_{req} were predicted to be 6.9T and 3.1T, respectively, using the thermo-magnetization results. As can be seen from the isothermal magnetization curve at $T = M_f$ in Figure 6-2(c), these magnetic fields reasonably match the experimentally observed ones in the figure for the $M \rightarrow A$ transformation.

The latent heat and heat capacity were determined for the SHT ribbon samples using DSC and the PPMS mentioned earlier. As shown in Figure 6-3(a), the $\Delta S^{M\to A}$ was determined to be 18J/kgK from the area of the endothermic peak ($\Delta S^{M\to A} = \int (C_p / T) dT$). In addition, the transformation temperatures match those obtained from 0.05T thermo-magnetic measurements for the SHT ribbons.

The Clausius-Clapeyron (CC) relation can also be used to find $\Delta S^{M\to A}$. The CC relation is defined by Eqn. (1.30). To further verify that the $\Delta S^{M\to A}$ was about 18 J/kgK, the above equation was used, where $\Delta M^{M\to A}$ was found, from magnetic data like that shown in Figure 6-2(c) at $T = M_f$, to be 84.1 emu/g and dH^{A_f} / dT was determined to be -0.22 T/K from thermo-magnetic measurements. The CC relation predicted the transformation entropy of 18.6 J/kgK, which is in good agreement with the DSC measurements. This indicates that either Eqn. (1.30) or the experimental results shown in Fig. 6-3(a) can be used to determine $\Delta S^{M\to A}$.

In Fig. 6-3(b), the heat capacity data are shown. The data provide an accurate measure of the heat capacity bracketing the hysteresis region, although the first-order transition region itself is not reproduced by the pulse-relaxation technique. These values are used to determine the adiabatic temperature change near T_0 as required in Eqn. (4.6) to compute the T_{work}. At higher temperatures the data approach the classical $3Nk_B$ per mole as expected, plus a small electronic term. Using $\Delta S^{M\to A}$ of 18 J/kgK and a C_p of 434 J/kgK at 190K (near M_f), and a T_0 of 224K from Table 6-1, $\Delta T_{ad}^{\max}$ is computed from

Eqn. (1.22) to be 9.3K. This implies that if T_{hot} is considered to be equal to M_f =198K as in Fig. 2-3, T_{cold} would be 188.6K (i.e. $T_{hot} - \Delta T_{ad}$). The T_{work} contribution within the temperature range permitting the complete field induced entropy change ($A_f^{H=H_{comp}^{ad}}$ to $M_f^{H=0}$) is defined as $\Delta S^{M\to A} \cdot \Delta T_{ad}^{\max} - \left(S_{irr} \cdot \Delta T_{ad}^{\max}\right)/2$. Here we found S_{irr} equals to 1.9 J/kgK when $T = M_f$ in Eqn. (4.7). This leads to the T_{work} of 159 J/kg for the SHT ribbons in this temperature range. However, when considering the entropy changes in the elastic regions of transformation, the maximum possible reversible T_{work} is computed using $\Delta S^{M\to A} \cdot \Delta T_{ad}^{\max} + \Delta S^{M\to A} \cdot \Delta T_{elas} - S_{irr}(\Delta T_{ad}^{\max} + \Delta T_{elas})/2$ (Eqn. (4.6)). For the SHT ribbons, this total reversible T_{work} is 389 J/kg.

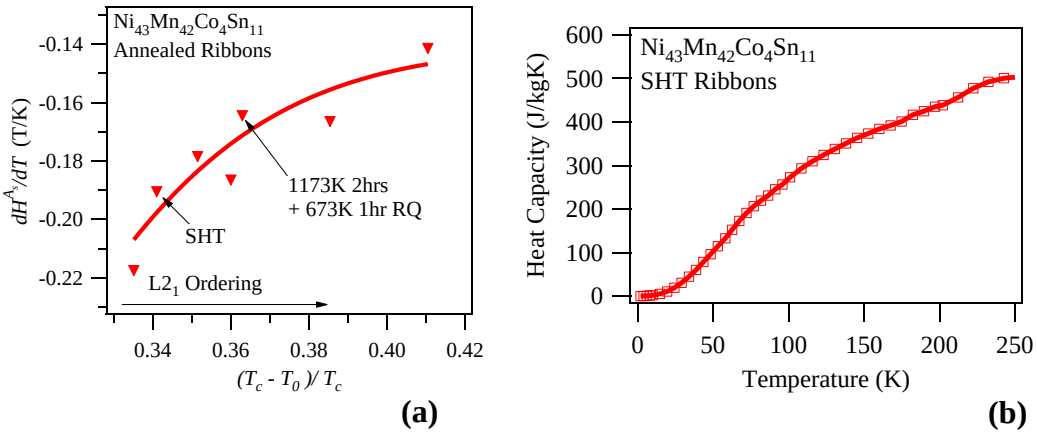

Figure 6-3: (a) A_s field sensitivity as a function of the normalized difference between T_{Curie} and T_0 for the secondary heat treated ribbon samples of $Ni_{43}Mn_{42}Co_4Sn_{11}$ alloys and (b) heat capacity measurements of SHT ribbons on cooling [50].

In the SHT+673K(RQ) ribbon samples, the entropy change across transformation was calculated using the CC equation (Eqn. 1.30) as explained for the SHT sample above. The $\Delta M^{M\to A}$ was measured at $T=\left(A_f+A_s\right)/2$ to be 79 emu/g, and the CC slope (dH^{A_f}/dT) to be -0.25 T/K. Eqn. (1.30) then results in $\Delta S^{M\to A}$ of 19.7 J/kgK. Assuming the heat capacity does not significantly change after the secondary heat treatments, $\Delta T_{ad}^{\max}$ is found to be 10.4K, thus the H_{comp}^{ad} (from Eqn. (4.13)) then equals 9.5T for the SHT+673K(RQ) ribbon which is slightly lower than that of the SHT ribbons. The T_{work} contribution within the temperature range permitting the complete entropy change ($A_f^{H=H_{comp}^{ad}}$ and $M_f^{H=0}$) is calculated to be 196 J/kg, with S_{irr} being equal to 1.5 J/kgK when $T=M_f$ in Eqn. (4.7). Including the entropy changes in the elastic regions of transformation, the total reversible T_{work} is calculated to be 385 J/kg for the SHT+673K(RQ) ribbon.

Comparing the SHT ribbons with those exposed to secondary heat treatments, it was found that the transformation entropy change increases as a result of these heat treatments, H_{comp}^{iso} decreases for the RQ samples, and $A_f^{H=H_{comp}^{ad}}$ to $M_f^{H=0}$ (temperature region where the complete reversible entropy change can be achieved) grows at the expense of the elastic transformation regions $A_f^{H=H_{comp}^{ad}}-A_s^{H=H_{comp}^{ad}}$ and $M_s^{H=0}-M_f^{H=0}$. These findings suggest that the material can be easily tailored for a given cycle with simple heat treatments to permit not only a certain cooling capacity under a given field, but also that

the field levels required to achieve refrigeration and their operating temperatures can be modified.

Figure 6-4(a) shows the $\Delta S^{M\to A}$ curves from the discontinuous heating protocol described in Chapter 2 for the SHT ribbons. Here, $\Delta S^{M\to A}$ from the field induced transformation, over the entire temperature range, seemed to plateau at a value (18 J/kgK) that matches that measured in DSC. This indicates that the transformation entropy is not largely a function of magnetic field and entropy production from hysteresis is relatively small compared to the entropy change of the *MT*. In addition, a clear growth of the $\Delta S-T$ diagram to lower temperatures is observed as the fields become larger. This is due to the negative CC slope.

A schematic of the $\Delta S-T$ diagram shown in Fig. 4-4 has been drawn over the data to indicate how the $\Delta S-T$ diagram should look to experimentally verify the computed T_{work} from the first two terms of Eqn. (4.6). Clearly, the magnitude of the entropy change is consistent with the theoretical diagram, but a majority of measurements still reside outside the temperatures of interest enclosed by the black trapezoid in Fig. 6-4. Again, this is due to the large ΔT_{elas}, ΔT_{hys}, and H_{comp}^{iso} (or H_{comp}^{ad}) exhibited by the SHT ribbons. This can also be viewed as the inability to sufficiently decrease the transformation temperatures with the applied field of 7T. Reducing ΔT_{elas} and ΔT_{hys} would effectively overlap theoretical $\Delta S-T$ and experimentally captured $\Delta S-T$ curves with small applied magnetic fields.

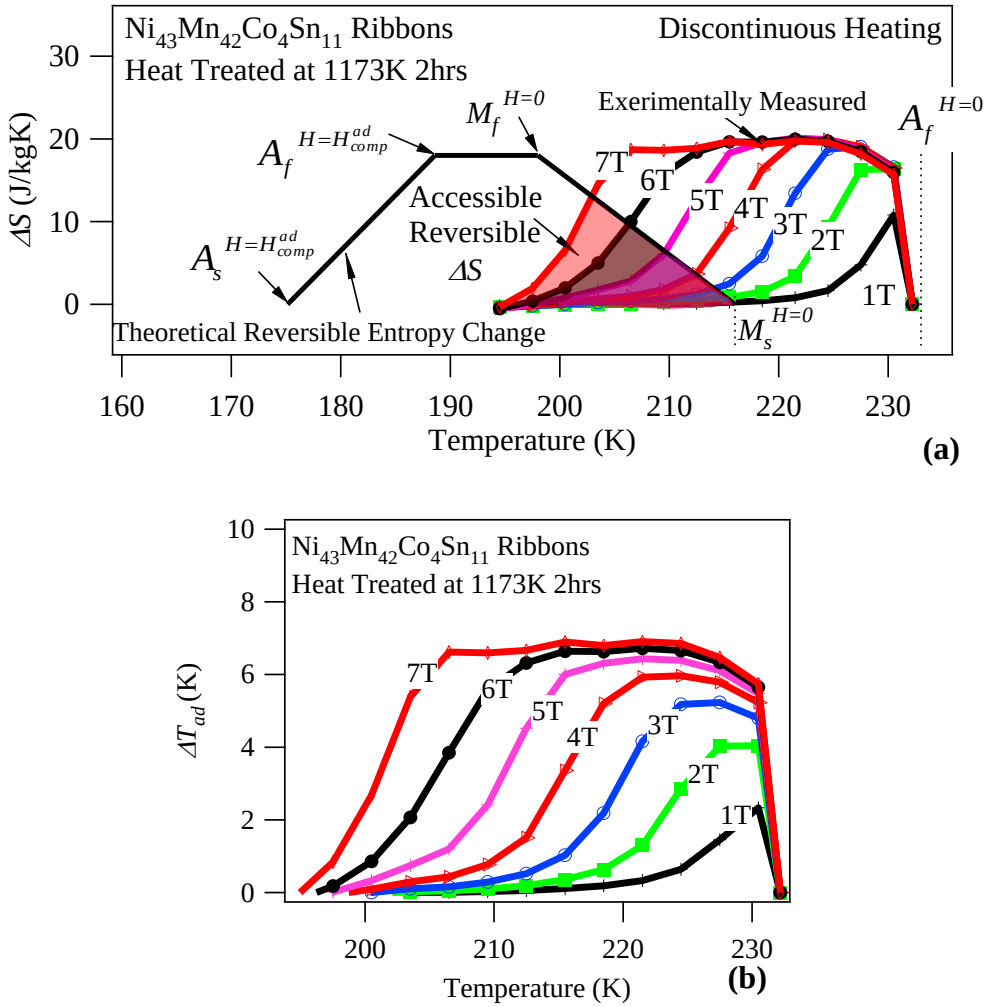

Figure 6-4: (a) Entropy change (ΔS) in the solutionized $Ni_{43}Mn_{42}Co_4Sn_{11}$ polycrystalline ribbon as a function of temperature around the martensitic transformation from the discontinuous heating protocol. The theoretical $\Delta S - T$ diagram from Fig. 4-4b has been drawn over the experimentally collected data as a black trapezoid. The corresponding adiabatic temperature changes are plotted in (b) per Eqn. (1.34) [50].

The T_{work} is determined from the data in Fig. 6-4a by the area of the overlapping theoretical and experimental $\Delta S - T$ curves (shaded area) with the hysteresis losses subtracted as defined in Eqn. (4.7). The applied fields, in this case, will produce very small

T_{work} values as only a fraction of the theoretical curve overlaps the experimentally captured one up to 7T. The maximum measured T_{work} value (overlapping of two curves) was found to be 74 J/kg under the applied field if 7T. However, the projected T_{work} of 389 J/kg was found using Eqn. (4.6).

Using the data in 6.4(a), ΔT_{ad} was computed with Eqn. (1.34) and is plotted in Fig. 6-4b. The data in Fig. 6-4b demonstrates that the SHT ribbons are capable of exhibiting nearly 4K temperatures changes by applying 2T and as much as 6K by applying 4T. Unfortunately, these temperature changes are not repeatable with field cycling due to the large thermal hysteresis. For example, to fully recover martensite on removing the field, the MMSMA must be at the M_f temperature depicted in the figure. At T = 198K, only about 2K can be generated by applying 7T. This is a very small caloric effect.

Finally, the discontinuous heating protocol from Chapter 2 was performed for the SHT+673K(RQ) ribbons and the $\Delta S - T$ diagram is shown in Fig. 6-5(a). The theoretical $\Delta S - T$ curve from the thermodynamic framework in Fig. 4-4 has also been drawn over the data. H_{req}, H_{comp}^{iso}, and H_{comp}^{ad} for the SHT+673K(RQ) ribbons were calculated to be 3.1T, 6.9T, and 9.5T, respectively, as shown in Table 6-1. The $\Delta S^{M \to A}$ value saturates near 19.7 J/kgK as computed from Eqn. (1.30). It is important to note that the SHT+673K(RQ) ribbons show a H_{comp}^{iso} of 6.9T. According to Eqn. (4.12), this means that an isothermal test at temperature M_f will produce a complete field-induced structural transformation with the application of 6.9T. This prediction is verified with Fig 6-5

because the 7T $\Delta S - T$ curve shows an entropy change of approximately 19J/kgK at temperature $M_f^{H=0}$ as indicated by point 1 in the figure.

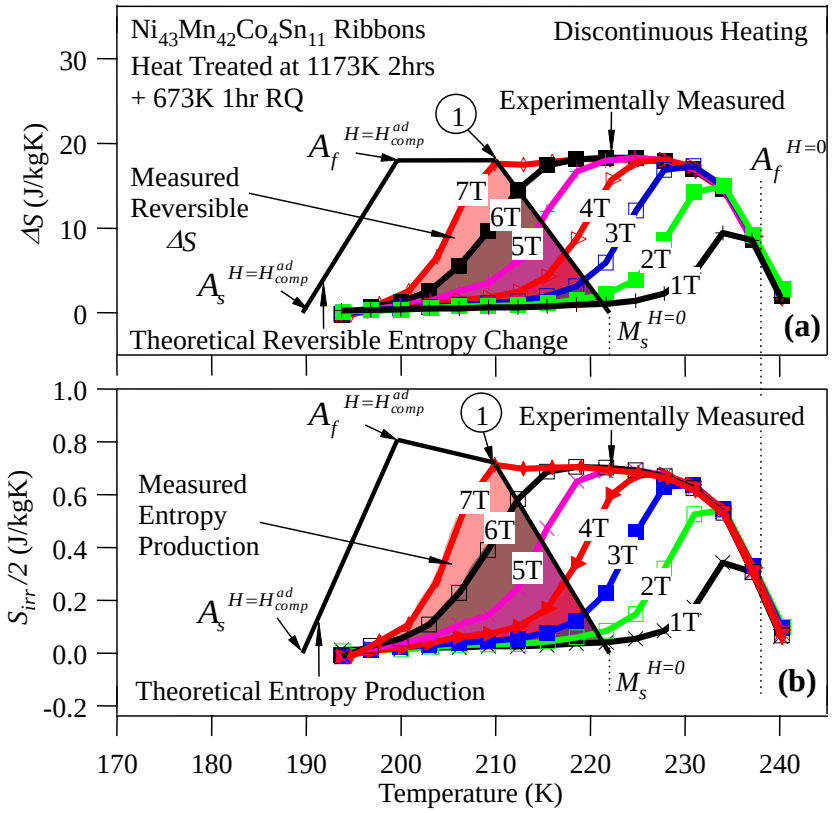

Figure 6-5: (a) Entropy change (ΔS) in the SHT+673K(RQ) ribbon as a function of temperature around the martensitic transformation from the discontinuous heating scheme. The theoretical $\Delta S - T$ diagram from Fig. 4-4(b) has been drawn over the experimentally collected data as a black trapezoid (b) Half the entropy production from the reverse *MT* for the same temperatures and field levels as shown in (a) [50].

Furthermore, the T_{work} for the SHT+673K(RQ) ribbons was calculated as the overlapping areas of the theoretical and experimental $\Delta S - T$ curves for each applied field level (shaded area) with hysteresis losses subtracted as defined in Eqn. 4.7. Figure 6-5(b)

shows $S_{irr}/2-T$ diagrams which were calculated using Eqn. (4.7). Since the $\Delta S-T$ curves saturate at $\Delta S^{M\to A}$ that is measured with DSC, the diagram in Fig. 6-5(a) can be used at every temperature and field level to yield a value for $\xi(H)\cdot\Delta S^{M\to A}$ in Eqn. (4.7). In other words, the $\Delta S-T$ curves in Fig. 6-5(a) were multiplied by ΔT_{hys} and divided by the temperature at each data point in which the isothermal test was conducted to produce the $S_{irr}/2-T$ diagrams.

To determine the T_{work}, in this and the SHT ribbon cases discussed earlier, the area of overlapping theoretical and measured $\Delta S-T$ curves were first determined, and then the overlapping area of the theoretical and measured $S_{irr}/2-T$ curves were subtracted at each field level. This assumes that the entropy production is a function of transformation volume fraction. The T_{work} results are plotted in Figure 6-6(a) for the SHT+673K (RQ) ribbons. The measured T_{work} value was found to be 234 J/kg at H_{comp}^{iso} as shown in Fig. 6-6a. The maximum projected T_{work}, however, should reach 385 J/kg under H_{comp}^{ad} considering all the terms in Eqn. (4.6). Although this projected T_{work} of the SHT+673K(RQ) ribbons is almost the same as that of the SHT ribbons (389 J/kg), the secondary heat treatment allows this high T_{work} to be reached under a smaller magnetic field than that of the SHT ribbons as shown by H_{comp}^{ad} values in Table 6-1. This improvement is attributed to the larger GS/t ratio and beneficial degree of $L2_1$ ordering that yields desired MCE properties as discussed in Chapter 5.

The T_{work} of $Ni_{43}Mn_{42}Co_4Sn_{11}$ heat treated ribbons is greater than other meta-magnetic SMAs that have been reported in the literature since we used a very simple parameter optimization approach to select a favorable microstructure and resulting desirable properties to maximize MCE. However, it is difficult to compare the results directly because most results in the literature compute the T_{work} in the conventional way which defines T_{hot} and T_{cold} arbitrarily at full width at half maximum of the $\Delta S - T$ curve [49]. These temperatures are often inside the thermal hysteresis range shown in Fig 4-4 and the values do not reflect reversible ΔS and T_{work} values. It was shown in Chapter 4 that the conventional way of calculating T_{work} is not correct for meta-magnetic SMAs.

$Ni_{43}Mn_{42}Co_4Sn_{11}$ SHT ribbons exhibit a T_{work} of 389 J/kg and from our isothermal tests, only 74 J/kg was accessible experimentally under 7T. The MCE performance of the solutionized ribbons was improved with secondary heat treatments whereby a T_{work} of 385 J/kg is achievable under an applied field of 9.5T. The SHT ribbons allow for a slightly larger T_{work} using special thermodynamic cycles because they also have a larger elastic temperature range. This, in turn, requires higher applied fields to transform the ribbon. The alloys in the literature such as $Ni_{50}Mn_{37}Sn_{13}$ (39J/kgK, 1.8T) [75], NiMnIn (130 J/kg, 3T) [78] have been reported to exhibit smaller T_{work} under smaller fields, but neither their measurement protocol nor heat capacity were reported.

Finally, η^{Latent} was computed with Eqn. (4.26) and is plotted for each heat treatment condition in Fig. 6-6b. Interestingly, the RQ samples exhibited a higher energy conversion efficiency than the FC treatments. It is believed this is due to the sharper

transition ranges exhibited by RQ samples. Interestingly, low temperature heat treatments increased the energy conversion efficiency by nearly 20%. The SHT + 673K 1hr. RQ was indeed the optimal heat treatment condition with the highest conversion efficiency.

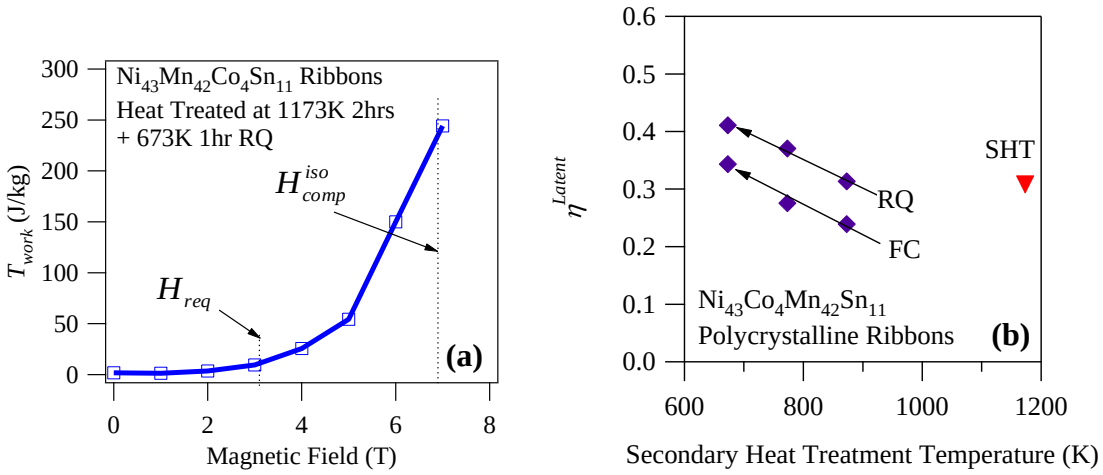

Figure 6-6: (a) Maximum thermal work of the SHT+673K(RQ) ribbons as a function of applied magnetic field. Values were computed from the data in Fig. 6-5a and b using the discontinuous heating protocol and (b) the η^{Latent} computed with Eqn. (4.26) for each heat treatment case [50].

6.2.3 Conclusions

In the present work, we demonstrate how $Ni_{43}Co_4Mn_{42}Sn_{11}$ can be used as solid-state refrigerant using the Brayton cycle in Fig. 4-3. From this cycle, the key material parameters, important for controlling MCE and refrigeration performance, were identified, such as the magnetic fields required to induce, and complete, the martensitic transformation, magnetization change across the transformation, transformation temperature range, and thermal hysteresis. The performance parameter, maximum thermal

work (T_{work}), was used for comparing the performance of meta-magnetic SMAs with different compositions and microstructures. It was shown that the conventional method of quantifying performance in MMSMAs by using the RCP is not a valid approach for MMSMAs and that the T_{work} should be used to quantify refrigeration performance across a first order transformation.

In attempt to validate the selection of the above materials parameters, a case study was conducted on a specific NiMnCoSn composition. The results indicated that these parameters can be optimized using simple heat treatments even in the compositions of meta-magnetic SMAs that show high $L2_1$ atomic stability. Atomic ordering was shown to change the transformation thermal hysteresis. The best performance parameters were achieved in $Ni_{43}Mn_{42}Co_4Sn_{11}$ polycrystalline ribbons when they were homogenized at 1173K and then annealed at 673K for 1 hr. followed by a rapid quenching in water. This was also demonstrated using Eqn. (4.26). Furthermore, the cooling method after the secondary heat treatments was shown to affect the meta-magnetic response and ultimately control the transformation range and thermal hysteresis.

More precisely, the effects of secondary heat treatments on the aforementioned materials parameters were studied in the $Ni_{43}Mn_{42}Co_4Sn_{11}$ melt-spun ribbons. Promoting atomic disorder decreased the thermal hysteresis. The elastic energy storage upon martensitic transformation was reduced by increasing the grain size to thickness ratio, which reduced the transformation range from 25K in the as-spun ribbons to only 10K in the heat treated ribbons. This effectively reduced the magnetic fields required to transform the materials and increased the operating temperature range of the refrigerant.

Finally, the relationships between the entropy change vs. temperature diagrams were discussed. Comparisons between theoretical and experimental entropy change vs. temperature curves were shown and used to demonstrate how the sample responses were improved by the optimization heat treatments. Ultimately, it was found that past reports on the MCE in meta-magnetic SMAs can still yield valuable information as long as the experimental protocol, martensitic transformation temperatures, and heat capacity are also presented so the T_{work} can be calculated accurately.

The key materials parameters proposed in this work provide a powerful tool for analyzing meta-magnetic SMA refrigerants as shown in the present work. The alloy composition and responses presented in this study indicate meta-magnetic SMAs can be used as solid state refrigerants. Moreover, further composition and microstructural optimization through thermal treatments can improve the transformation characteristics and thus, the refrigeration performance parameters for them to compete with conventional rare-earth based MCE materials, such as Gd alloys.

6.3 $Ni_{48}Mn_{38}In_{14}$

6.3.1 Introduction

In the following sections the magnetocaloric effects in NiMnIn and NiCoMnIn alloys in Tables 2-4, 2-5, and 2-6 are discussed in detail. The thermomagnetic responses of the alloys are presented as measured from SQUID magnetometry using FC and FH protocols. Using the thermomagnetization data, the magnetic Clausius-Clapeyron slopes, $\frac{dH}{dT}^{A_f}$, were extracted and plotted as a function of heat treatment. Other parameters in

Eqn. (4.26) were identified using calorimetry to determine the optimum heat treatment condition listed in the tables. Finally, entropy change diagrams were generated from measured magnetization data (using Eqn. (2.3)) which were then used to compute the adiabatic temperature change of the alloy with Eqn. (1.34).

6.3.2 Results

The thermomagnetic response of each heat treated alloy in Table 2-4 is shown in the Appendix. Each heat treatment case exhibits a magnetic Curie point near 300K in the austenite phase. Interestingly, these heat treatments only modestly change the M_s temperature. This small change is also depicted in Figure 5-3. Other differences observed between the responses include magnitudes of $\Delta M^{M \to A}$, thermal hysteresis, and transformation ranges. All of these parameters have been shown to influence the energy conversion efficiency as explained in Chapter 4 with Eqn. (4.26).

The magnetization changes across the martensitic transformation from each heat treatment case were identified for the 1T thermomagnetic curve and are plotted in Figure 6-7a. Interestingly, the solution heat treated case (SHT) exhibits one of the largest magnetization changes. Three hour secondary heat treating at 1073K results in a significant drop in the magnetization change. Secondary heat treatments at even lower temperatures tend to recover the magnetization change to levels comparable to the SHT case. This is attributed to promoting crystallographic ordering to $L2_1$ from B2 austenite [46]. Heat treating at 673K for 3 hours, the martensitic transformation becomes suppressed and the magnetization change is nearly zero. Further work must be performed to identify

the cause of the suppression of the transformation in these alloys, but this arrest can be achieved in both NiCoMnIn and NiMnIn alloys.

The A_f temperature Clausius-Clapeyron slopes for each 3 hour heat treated alloy was extracted from the data are shown in Figure 6-7b. As discussed in Eqn. (1.8) in Chapter 1, a decrease in the magnetization change (shown in Fig. 6-7a) must be accompanied by a decrease in the dT/dH slope due to a reduction in the magnetic Zeeman energy. As expected, this decrease with decreasing $\Delta M^{M\to A}$ is depicted in Fig. 6-7b. Promoting $L2_1$ ordering with lower temperature heat treatments results in an increase in $\Delta M^{M\to A}$ and therefore an increase in dT/dH.

Using Eqn. (2.2), the entropy change was computed for each heat treatment case. The entropy change across the martensitic transformation is plotted in Figure 6-7c. The SHT case exhibits the largest entropy change of approximately 24J/kgK. Lower temperature secondary heat treatments result in an initial drop in the entropy change followed by recovery. This is similar to the response in $\Delta M^{M\to A}$ in 6-7a. When the $\Delta M^{M\to A}$ is nearly zero from the 673K 3hr heat treatment, the entropy change is also computed to be nearly zero per the CC equation.

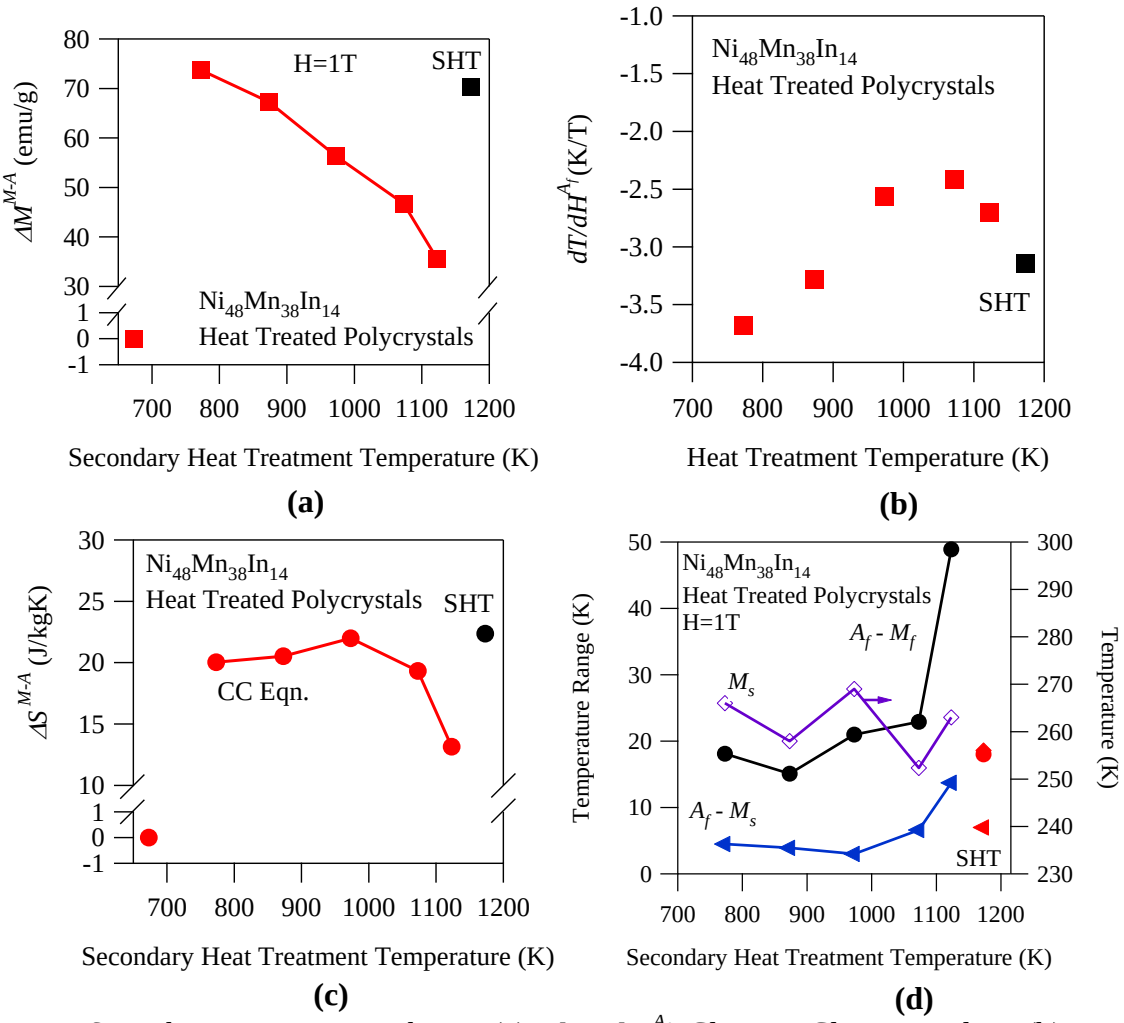

Figure 6-7: The magnetization change (a), dT / dH^{A_f} Clausius-Clapeyron slope (b), computed entropy change (c), and temperature ranges (d), for each 3 hour heat treated $Ni_{48}Mn_{38}In_{14}$ alloy. The Entropy change was computed from Eqn. (2.2) and temperature ranges were extracted from the thermomagnetization data in the Appendix.

Finally, the complete transformation ranges ($A_f - M_f$), the thermal hysteresis, $A_f - M_s$, and M_s are plotted in Fig. 6-7d for each heat treatment case. At once, the influence of the microstructurally stored elastic energy across the martensitic transformation is realized as indicated by the magnitude of $A_f - M_f$ [61]. From the SHT

+ 1073K 3hrs heat treatment case, the hysteresis and transition ranges are larger than the SHT case. In contrast to the $Ni_{45}Co_5Mn_{36.6}In_{13.4}$ alloy (Co5) in Chapter 5, a sharp increase is observed in $A_f - M_f$ with heat treatments slightly below the SHT temperature. In the Co5 alloy, the transformation ranges abruptly decrease when heat treated at a temperature slightly below 1173K. Therefore, the increase in the transition ranges may be attributed to some phenomenon other than vacancy concentration as was discussed in Chapter 5 for the Co-containing alloy. Perhaps crystallographic ordering at temperatures above some critical temperature influences the crystallographic compatibility, however, more work is needed to identify the cause of the increase in transition range.

Using the parameters in Fig. 6-7, η^{Latent} was computed for each heat treatment case to identify the relative magnetic to thermal energy conversion efficiency and is plotted in Fig. 6-8 as a function of secondary heat treatment temperature. Clearly, the $Ni_{48}Mn_{38}In_{14}$ alloy exhibits a dissimilar response in η^{Latent} to the cobalt containing alloy in Chapter 5. From Fig. 6-8, it is clear that the SHT case exhibits similar conversion efficiency to the alloys ordered toward $L2_1$ resulting from low temperature heat treatments. The η^{Latent} for the 673K 3hours heat treatment case, in Fig. 6-8, is zero because the martensitic transformation is suppressed, thus the entropy change across the transformation is nearly zero.

Two heat treatment cases were selected to construct entropy change vs. temperature diagrams on either side of the local minimum at 1123K in Fig. 6-8. The SHT case and the SHT + 973K 3hrs cases were selected to identify differences between the two, although they exhibit similar conversion efficiency. Per Fig. 6-7, SHT case exhibits

larger $\Delta M^{M\to A}$ and dT/dH, but both cases exhibit nearly the same entropy change, 20J/kgK. In the SHT + 973K 3hrs alloy, the $A_f - M_f$ range is larger by about 5 Kelvins.

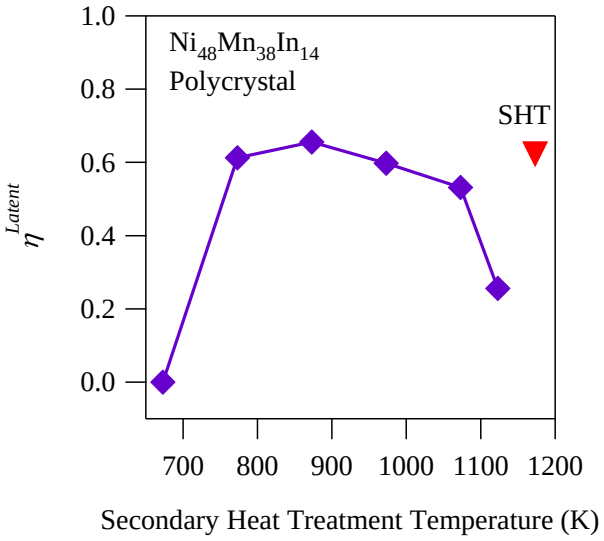

Figure 6-8: η^{Latent} as a function of 3 hour secondary heat treatment temperature computed from Eqn. (4.26) in $Ni_{48}Mn_{38}In_{14}$.

In Figure 6-9(a-c) the magnetization history on applying the magnetic field, the computed entropy change vs. temperature diagram (Eqn. 2.2), and the computed adiabatic temperature change (1.34), are shown for the SHT alloy, respectively. Here, the magnetization change is measured to be approximately 80-85emu/g under 3T or higher. Magnetization measurements were taken at intervals of 3Kelvin across the martensitic transformation range. The entropy change diagram in Fig. 6-9b indicates an entropy change of nearly 20J/kgK can be generated at 253K by applying 4T to the alloy. The entropy change diagram grows toward the left due to the negative CC slope, as expected.

The computed adiabatic temperature change, in Fig. 6-9c, demonstrates that the alloy will exhibit approximately 8K temperature change under 7T applied magnetic fields.

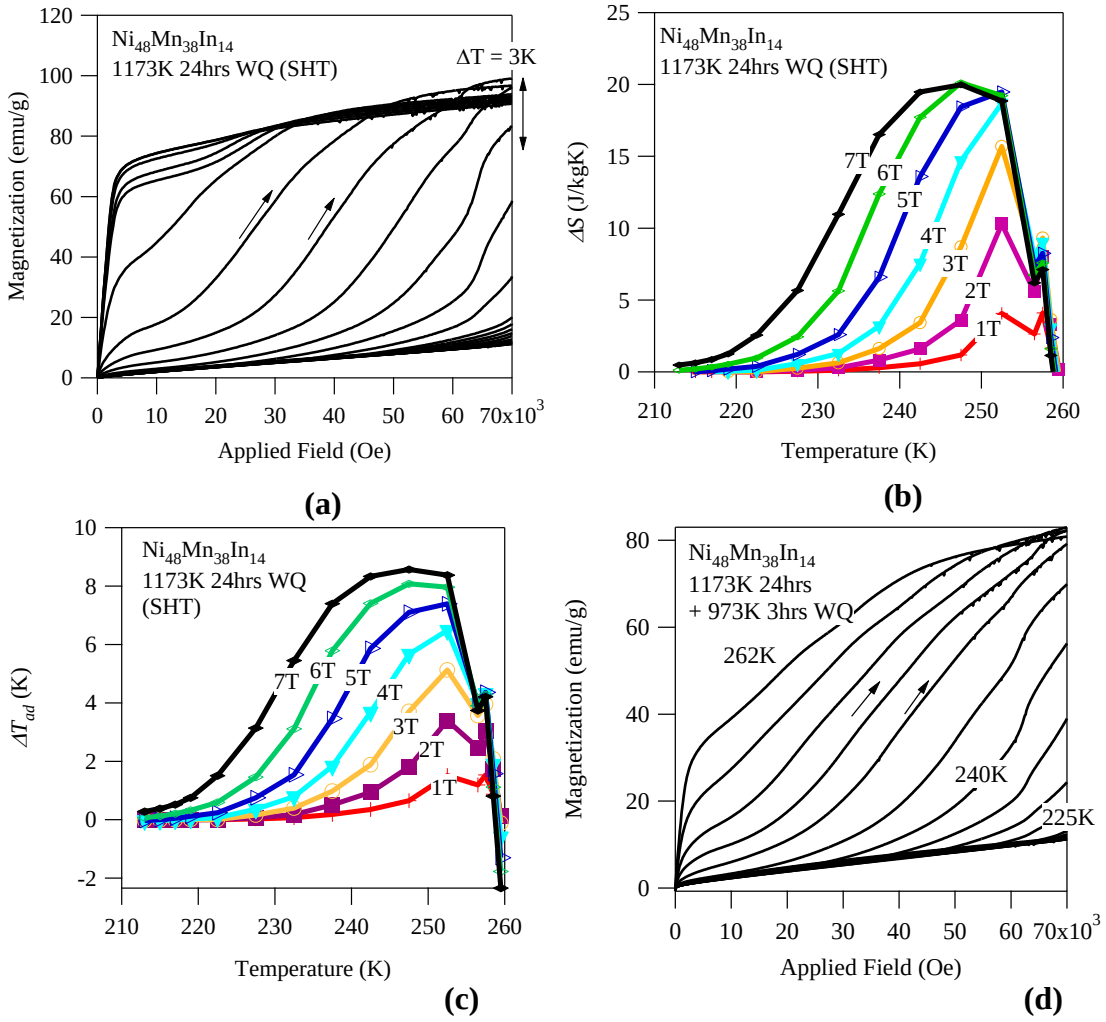

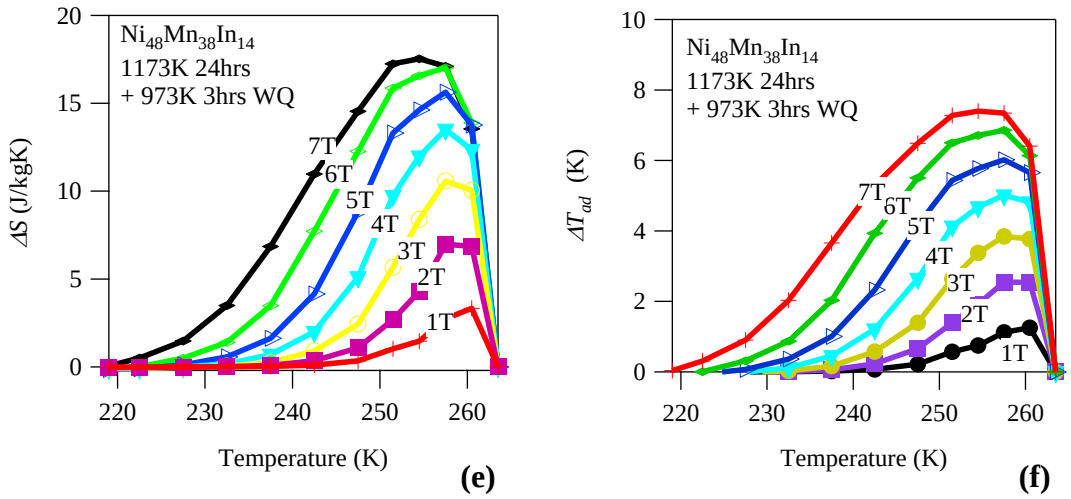

Figure 6-9: The magnetization history (a), computed entropy change (b), and computed temperature change (c) for the $Ni_{48}Mn_{38}In_{14}$ solution heat treated alloy and the magnetization history (d), computed entropy change (e), and computed temperature change (f) for the $Ni_{48}Mn_{38}In_{14}$ solution heat treated alloy subject to a secondary 973K 3hour WQ heat treatment. Entropy change diagrams were computed with Eqn. (2.2) and adiabatic temperature change with Eqn. (1.34).

In common MCE applications, only magnetic fields slightly below 2T can be applied to magnetocaloric metals with permanent magnets, and therefore, the SHT case would be expected to exhibit only 3K temperature change at 250K. Unfortunately, 250K is nearly equal to the A_s temperature for this alloy, and therefore, to achieve 3K temperature changes with field cycling, the sample must first be cooled below M_f to recover the martensite phase and then reheated to A_s before the field is re-ramped. In other words, the cyclic reversibility of the temperature change reported in Fig. 6-9c is very poor.

Similarly, the magnetizing responses for the SHT + 973K 3hrs heat treated alloy is plotted in 6-9d. This data analyzed with Eqn. (2.2) and the resulting entropy change diagram is plotted in Fig. 6-9e. Clearly, the entropy change is slightly lower than the SHT

case. In addition, the change in magnetization from applying 7T has also been reduced with ordering. It is believed that the entropy change in this alloy is reduced due to the additional elastic energy contribution to the driving force in Eqn. (1.8). Clearly, the martensitic transformation range in the SHT + 973K 3hrs heat treated alloy is larger than the SHT case, and in turn, decreases dT / dH .

With smaller dT / dH , the SHT + 973K 3hrs heat treated alloy requires larger magnetic fields than the SHT case to complete the martensitic transformation. This can be seen from the slopes of the magnetization responses in Fig. 6-9a and d. In the SHT + 973K 3hrs heat treated alloy, the magnetization vs. magnetic field (M-H) slope is smaller on applying field across the transition, indicating the transformation requires that magnetic fields be applied. In some cases, the transformation will progress with small fields. In this case, very large fields are needed. Nevertheless, the adiabatic temperature change was computed for this heat treatment case as shown in in Fig. 6-9f. Since the entropy change in this alloy is slightly smaller, the adiabatic temperature change is expected to be slightly smaller than the SHT case. Like the SHT case, however, the cyclic reversibility of the caloric response is very poor. In both alloys, approximately only 4K can be generated by cycling 0 to 7T at temperatures near M_f . The cyclic reversibility can be quantified with a 0.6 conversion efficiency parameter from Eqn. (4.26), whereas nearly 0.8 can be achieved in the NiCoMnIn alloy described in Chapter 5.

6.3.3 Conclusions

In conclusion, the $Ni_{48}Mn_{38}In_{14}$ alloy exhibits a dissimilar conversion efficiency response to the cobalt containing alloy in Chapter 5. Interestingly, very large elastic energy

is stored in the microstructure across the transformation in this alloy composition when quenched from temperatures near the SHT temperature. Lower temperature annealing then orders NiMnIn toward $L2_1$, and results in an increase in the conversion efficiency. On ordering to $L2_1$ from lower temperature heat treatments, the magnetization change across the transformation is recovered to nearly that of the SHT case. In this particular alloy composition, the SHT case is expected to outperform the other secondary annealing cases.

6.4 $Ni_{50}Mn_{36-X}In_{14+X}$ (X=0, 0.5, 1, 1.5):

6.4.1 Introduction

Initially, thermal treatments were employed on the $Ni_{50}Mn_{36}In_{14}$ alloy in attempts to modify the transformation temperatures as described in Chapters 2 and 5. The thermal treatment temperatures and times were tabulated in Table 2-5 for the $Ni_{50}Mn_{36}In_{14}$ alloy. Interestingly, these thermal treatments had minimal effect on the transformation temperatures, and therefore are not discussed here. It is believed that only small changes in the transformation temperatures resulted from thermal treatments because the austenite phase was paramagnetic, rather than the typical ferromagnetic phase. It is interesting to note that more ferromagnetic austenite phases result in higher tunability with thermal processing. That is, cobalt containing MMSMA that exhibit ferromagnetism in austenite seem to be the most sensitive to thermal treatment. Ferromagnetic NiMnIn alloys then exhibit the next lower level of sensitivity with thermal processing and, finally, the transformation characteristics in paramagnetic MMSMAs exhibit very little susceptibility

to thermal treatments. The thermomagnetic responses under 7T can be found in the Appendix for each heat treatment case of $Ni_{50}Mn_{36}In_{14}$.

Instead, the base alloy $Ni_{50}Mn_{36}In_{14}$ (at.%) was employed to generate a composition spread and identify the energy conversion efficiency from the resulting alloys of different composition in their solutionized conditions. Alloys were homogenized (solution heat treated) at 1173K for 24hours and quenched in water. Despite the fact that the Ni50 base alloy was of paramagnetic order in austenite, the martensitic transformation could still be observed from SQUID magnetometry due to its high sensitivity ($\sim 10^{-8}$emu) as shown in Fig. 6-10a. Very small magnetization changes were measured in this base alloy under 0.05T. Some recent work [79] suggested that perhaps the refrigerant capacity would be greatly increased by reducing the martensitic transformation temperature to the theoretical austenite Curie point. Here, we identify the magnetic to thermal energy conversion efficiency with η^{Latent} for alloys whose M_s is above, below, and nearly equal to the austenite T_{Curie}.

To reduce the M_s temperature in the base alloy, arc-melting was employed. High purity Ni, Mn, and In were added to achieve the desired composition spread. Wavelength dispersive spectroscopy (WDS) was employed to verify the composition of the alloys. SQUID magnetometry was used to identify the magnetic parameters in Eqn. (4.26), and the heat capacity was approximated using the universal Debye curve for the NiCoMnIn alloy in Fig. 5-19b. The Debye curve in Fig. 5-19b is a universal curve in units of Cal/molK, and assumes the Debye temperature is 322K. The transformation temperatures of the Ni50 base alloy were elevated. Therefore the heat capacity was assumed to equal

the saturated 3R (6cal/molK) vibrational limit. The thermomagnetization responses of the alloys in the composition spread are depicted in Figure 6-10a-d.

6.4.2 Results

As shown in Fig. 6-10a, the base alloy exhibits a small magnetic signal under 0.05T. Under 1T, the martensitic transformation can be identified by the thermal hysteresis around 350K. The magnetization change across the transformation was approximately 2emu/g in this case. Under 7T, the austenite phase is characterized by at most 20emu/g exhibiting a 15 emu/g magnetization change around the transition. Interestingly, the thermal hysteresis in this alloy is nearly 5K. According to the magnetic fitting in [79], the austenite phase was determined to be paramagnetic, and thus explains why small magnetization changes occur across transition.

On substituting indium (valence of 3e-) for manganese (valence of 7e-), the martensitic transformation temperatures decrease. This can be attributed to reducing the valence electron concentration per atom (e/a ratio) depicted in Fig. 5-1 and tabulated in Table 2-1. Decreased e/a ratios result in lower M_s temperatures. The projected austenite Curie temperature, T_{Curie}, of the base alloy is tabulated in Table 2-1 as 289K [79]. When only 0.5 at.% of Mn was replaced with In, the martensitic transformation temperature had decreased by about 10K, as shown in Fig. 6-10b. The thermal hysteresis in this alloy remained approximately the same as the base alloy. The magnetization change, on the other hand, had almost doubled, yet, the austenite phase was still expected to be paramagnetic because the M_s temperature was above the projected T_{Curie} of 289K.

Replacing 1 at.% Mn with In resulted in a larger decrease in M_s. In this alloy (see Fig. 6-10c) the M_s temperature had dropped about 50K from the base alloy and the transformation occurred around room temperature. Interestingly, this particular composition exhibited only 3K thermal hysteresis. The magnetization change across the transformation was, again, nearly doubled from the In14.5 at.% case. Finally, 1.5at.% of Mn was replaced for In. In this condition, the M_s temperature was reduced to 260K and the 0.05T thermomagnetic response exhibited approximately 10emu/g in austenite. It is believed lowering the M_s temperature resulted in a ferromagnetic austenite phase. Unfortunately, the thermal hysteresis also substantially increased when lowering the M_s temperature below T_{Curie}.

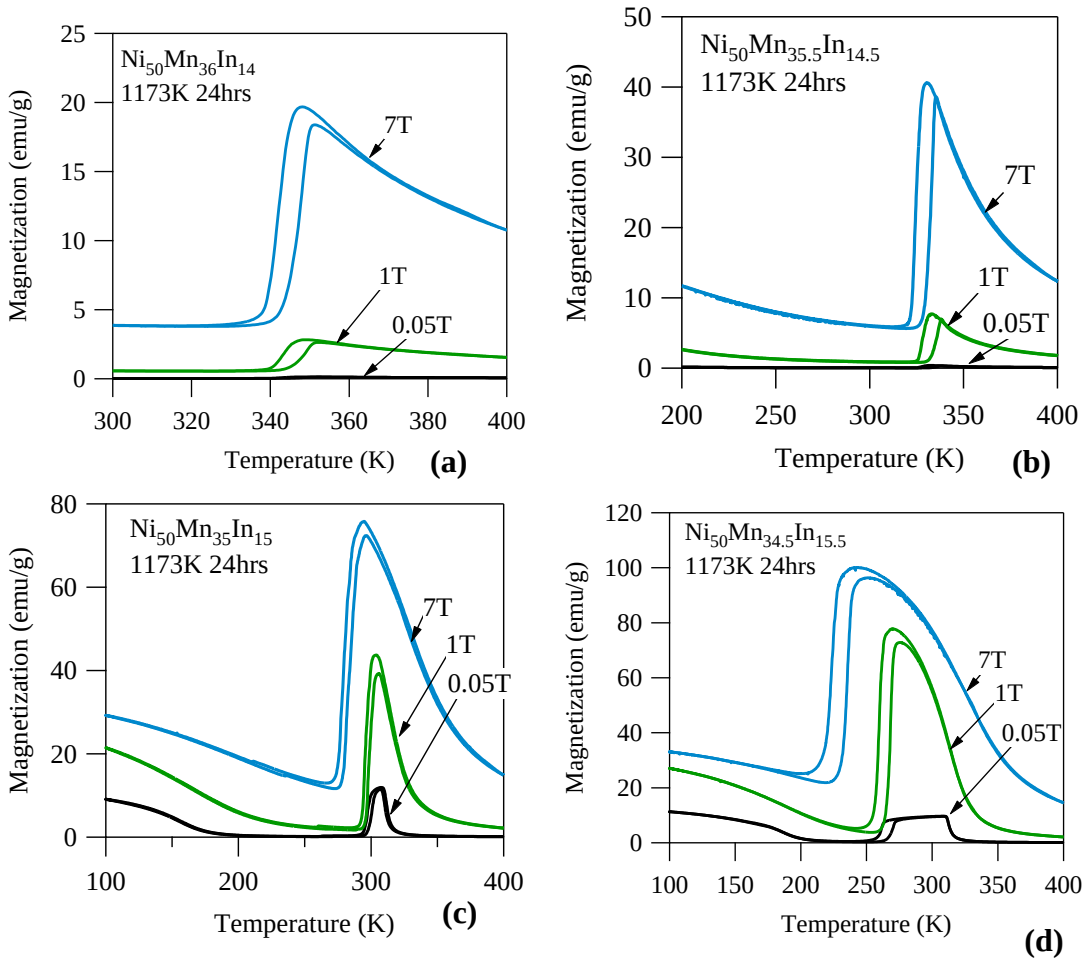

Figure 6-10: The 0.05T, 1T, and 7T field cooling (FC) and field heating (FH) thermomagnetic histories of solutionized $Ni_{50}Mn_{36}In_{14}$ (a), $Ni_{50}Mn_{35.5}In_{14.5}$ (b), $Ni_{50}Mn_{35}In_{15}$ (c), and $Ni_{50}Mn_{34.5}In_{15.5}$ (d) alloys.

Figure 6-11 depicts the thermomagnetic martensitic transformations under 7T of each alloys mentioned above. Interestingly, the T_{Curie} slightly increases on increasing In content as indicated by the increased magnetization levels at high temperatures in austenite. Clearly, the $Ni_{50}Mn_{35}In_{15}$ alloy exhibits the smallest thermal hysteresis. In fact, 3K thermal hysteresis under 7T is the smallest hysteresis observed in NiMnIn, to date [80].

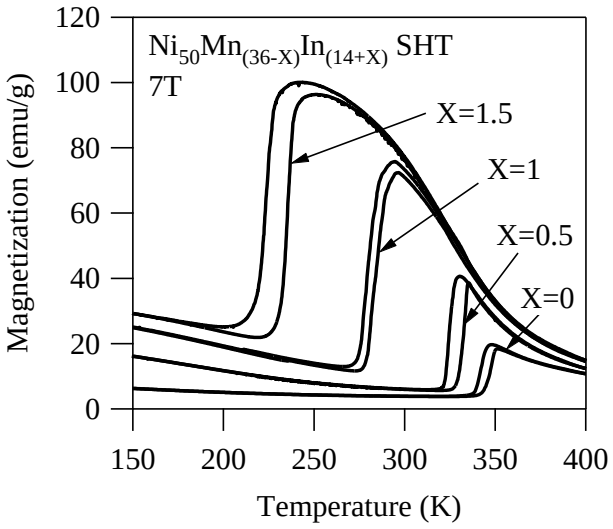

Figure 6-11: A comparison of the $Ni_{50}Mn_{(36-X)}In_{(14+X)}$ (X=0, 0.5, 1, and 1.5) thermomagnetic responses under 7T.

The parameters in Eqn. (4.26) were extracted from thermomagnetic data above and are plotted in Fig. 6-12 as a function of In content. Indium content, in these plots, correspond to that which was directly measured with WDS. No clear trends are identified from the few data points. However, the $A_f - M_f$, in 6-12a, was found to be minimum for the $Ni_{50}Mn_{35}In_{15}$ alloy. As expected, the $\Delta M^{M \to A}$ under 1T increases as In content increases and M_s decreases. As such, with larger magnetic Zeeman energy, the dT/dH also increases as discussed in Chapter 1. To fully identify the parameters in Eqn. (4.26), the heat capacity for this alloy was approximated using the Debye curve in 5-19b. It is important to note that the Debye curve in Fig. 5-19b neglects any magnetic contribution to the specific heat capacity and only predicts the vibrational contribution with a Debye temperature of 322K.

The resulting values for η^{Latent} are shown in Fig. 6-12c along with the entropy change across the martensitic transformation as computed using Eqn. (2.2). A very large value for the conversion efficiency was computed for the solutionized $Ni_{50}Mn_{35}In_{15}$ alloy of about 0.8. The base alloy and the others exhibited a conversion efficiency of about 0.6. Interestingly, the $Ni_{50}Mn_{35}In_{15}$ alloy exhibits the largest entropy change under 1T of all the fabricated alloys. It is believed a peak exists in the entropy change around 14.9at. % In content as demonstrated with the bell-curve fit. According to Eqn. (2.2) the entropy change can be computed with the parameters in Fig. 6-12b. For reasons unknown, the maximum in the entropy change corresponds to neither the maximum $\Delta M^{M\to A}$ nor the minimum dT/dH as would be expected with Eqn. (2.2). Since $\Delta M^{M\to A}$ influences the dT/dH through the magnetic Zeeman energy term discussed in Eqn. (1.8) in Chapter 1, other contributions to the free energy seem to influence the dT/dH, thus making the $Ni_{50}Mn_{35}In_{15}$ composition particularly well suited for MCE applications. Perhaps the small transition ranges in this composition reduce the $G_{el}^{A\to M}$ term in Eqn. (1.8) and therefore, some optimum is achieved in the $\Delta S^{M\to A}$. Further studies need to be performed to identify the cause of the peak in $\Delta S^{M\to A}$.

Finally, the MCE was measured in only the base alloy. This data was partially used in [79]. The very small dT/dH slope depicted in 6-12b resulted in a small amount of magnetic field induced transformation when applying up to 7T at any temperature. A few magnetization responses are shown in Fig. 6-12d. Next, Eqn. (2.3) was employed with the data shown in Fig. 6-12d to generate the entropy change diagram in Fig. 6-13a. As

expected, very small entropy changes were generated in this alloy due to the difficulty to transform the MMSMA under reasonable field levels.

Even though the entropy change is somewhat small compared to the other alloys discussed in this work, the reversibility of this alloy is better than most due to its small thermal hysteresis. The thermal hysteresis of the base alloy, is shown to be only 4K in Fig. 6-12a, and therefore, nearly repeatable entropy and adiabatic temperature changes can be achieved in this alloy with field cycling. The adiabatic temperature changes corresponding to the entorpy changes in Fig 6-13a were computed with Eqn. (1.34) and are plotted in Fig. 6-13b.

The computed adiabatic tempeature changes are nearly 4K with the application of 6T-7T. This is comparable to those attainable in the $Ni_{48}Mn_{38}In_{14}$ alloy discussed earlier. Even though the reversibility is better in the small hysteresis $Ni_{50}Mn_{36}In_{14}$ alloy, approximately the same magnitude temperature change can be achieved with field cycling.

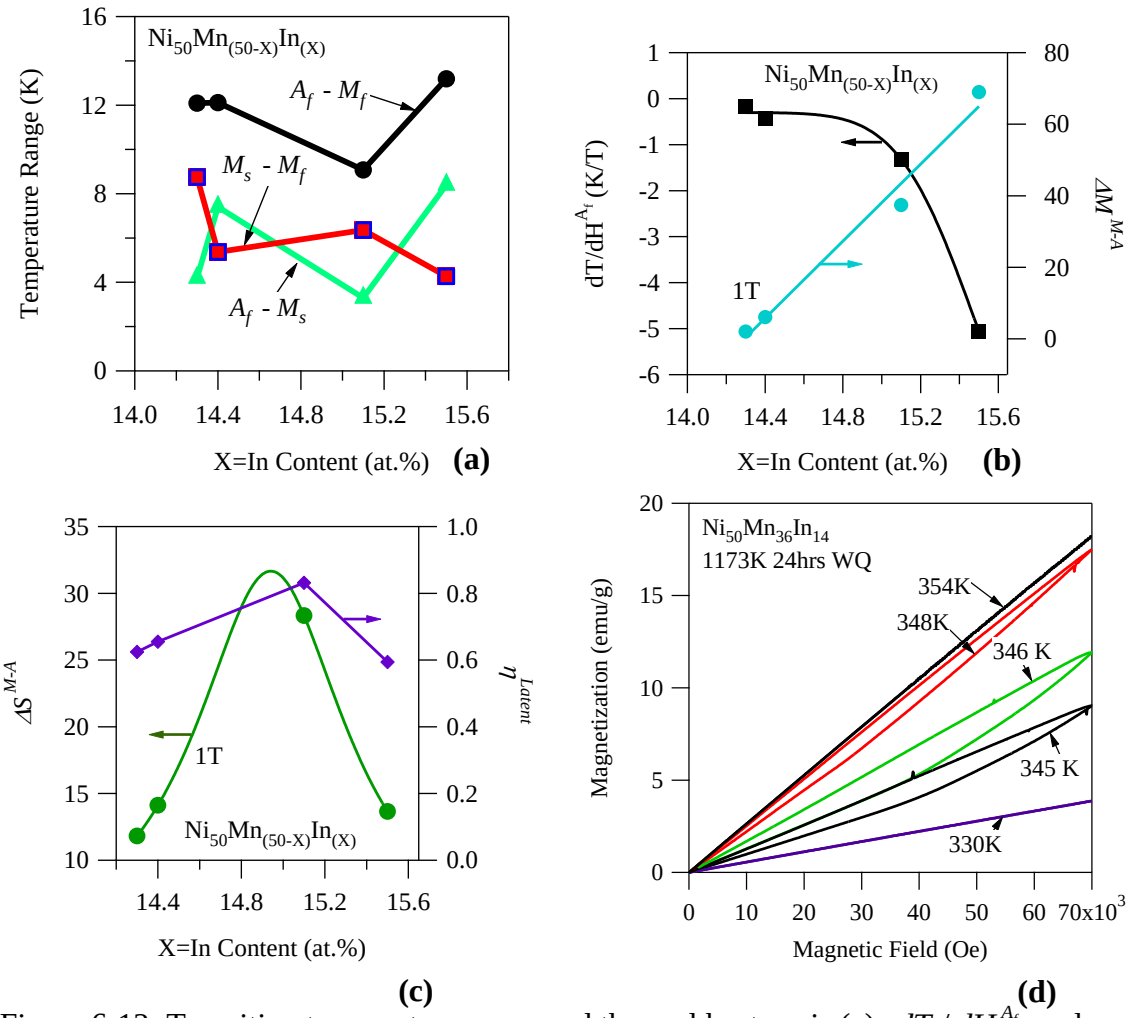

Figure 6-12: Transition temperature range and thermal hysteresis (a), dT/dH^{A_f} and $\Delta M^{M\rightarrow A}$ (b), $\Delta S^{M\rightarrow A}$ and η^{Latent} (c) as a function of indium content in $Ni_{50}Mn_{(50-X)}In_X$. A few magnetization responses a different temperatures are plotted in (d) for the solutionized $Ni_{50}Mn_{36}In_{14}$ alloy. $\Delta S^{M\rightarrow A}$ was computed with Eqn. (2.2) and η^{Latent} with Eqn. (4.26).

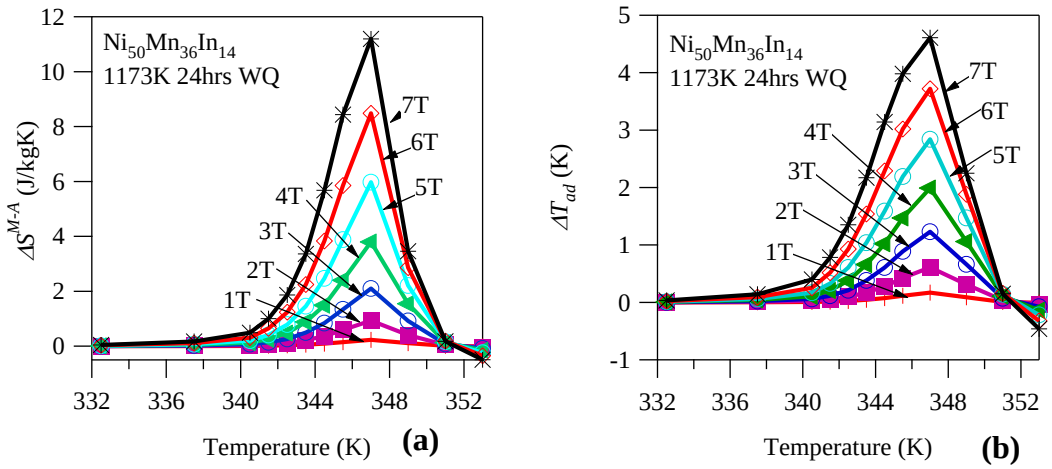

Figure 6-13: The entropy change versus temperature diagram computed with Eqn. (2.3) for the data shown in Fig. 6-12d (a), and the corresponding adiabatic temperature changes computed with Eqn. (1.34) for 0-7T (b).

6.4.3 Conclusions

In conclusion, modifying the composition of $Ni_{50}Mn_{36}In_{14}$ is an effective way of reducing thermal hysteresis and tuning the martensitic transformation to occur at a desired temperature. Replacing Mn with In in $Ni_{50}Mn_{36}In_{14}$, the magnetization change across the martensitic transformation increases as a result of decreasing the e/a ratio and M_s temperature. Around In14.9 at.%, a peak exists in the entropy change. This corresponds to a minimum in the thermal hysteresis, as well. More work must be performed to identify the MCE generated by the optimized $Ni_{50}Mn_{35}In_{15}$ alloy.

6.5 $Ni_{45}Co_5Mn_{36.6}In_{13.4}$ single crystals

In Chapter 5, the most promising heat treatment condition in $Ni_{45}Co_5Mn_{36.6}In_{13.4}$ was identified as SHT + 1073K 3hours. This heat treatment condition had resulted in

optimal materials parameters so that η^{Latent} from Eqn. (4.26) was maximal. Here, the MCE is measured for the optimal heat treat condition. In addition, a shorter duration heat treatment is identified that produces similar transformation properties in $Ni_{45}Co_5Mn_{36.6}In_{13.4}$ single crystals. The MCE is then studied in the short duration ordering treatment and the two are compared.

6.5.1 Results

In Figure 6-14 the thermomagnetization curves under 1, 3, 5, and 7T are shown for the optimized $Ni_{45}Co_5Mn_{36.6}In_{13.4}$ alloy. In this particular heat treatment, the transformation temperatures are around room temperature.

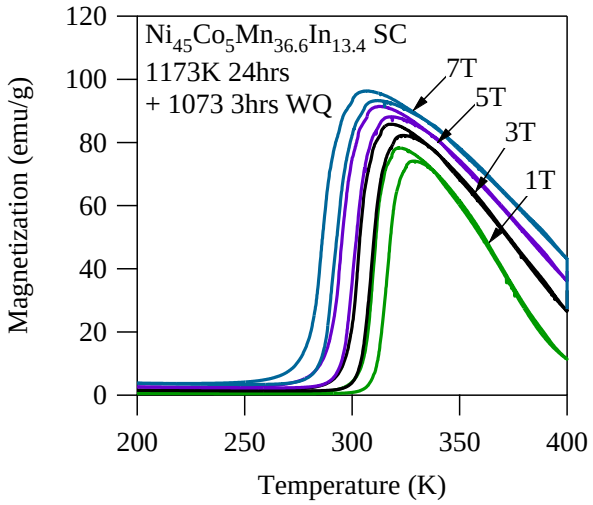

Figure 6-14: The 1T, 3T, 5T, and 7T, field cooling (FC)/field heating (FH) thermomagnetic responses of $Ni_{45}Co_5Mn_{36.6}In_{13.4}$ single crystals that had been heat treated at 1173K for 24hours followed by a secondary annealing treatment at 1073K for 3hours and then water quenched.

As shown in Fig 6-14, the thermal hysteresis in this heat treated alloy remained fairly constant at 8K regardless of the applied field level. In addition, the magnetization change for nearly all of the applied field levels was between 80-90emu/g. The martensite phase was found to be extremely non-magnetic as shown by the very low magnetization levels below the M_f temperatures.

According to the data in Chapter 5, the dH/dT in this alloy was neither maximum nor minimum. The resulting entropy change was computed with the CC equation to be nearly 25J/kgK. This entropy change, and the corresponding adiabatic temperature change were computed in Chapter 5 to be between -6K and -8K. These temperature changes can be driven with cyclic fields up to 6T in a thermally insulated sample. To identify how the entropy change is influenced by temperature, entropy change versus temperature diagrams were generated using Eqn. (2.3) as shown in Fig. 6-15a.

As shown in 6-15a, 4T is capable of generating about 20J/kgK at 300K. Since 308K is approximately equal to the M_f temperature in Fig. 6-14, the repeatability is very good with field cycling. Applying 5, 6, and 7T in this alloy at 300K does not generate larger entropy changes because the material is magnetically saturated and the isothermal transformation completes with nearly 4T. Due to the negative CC slope, applying larger magnetic fields allows the entropy change to be achieved at lower temperatures as depicted in Fig. 6-15.

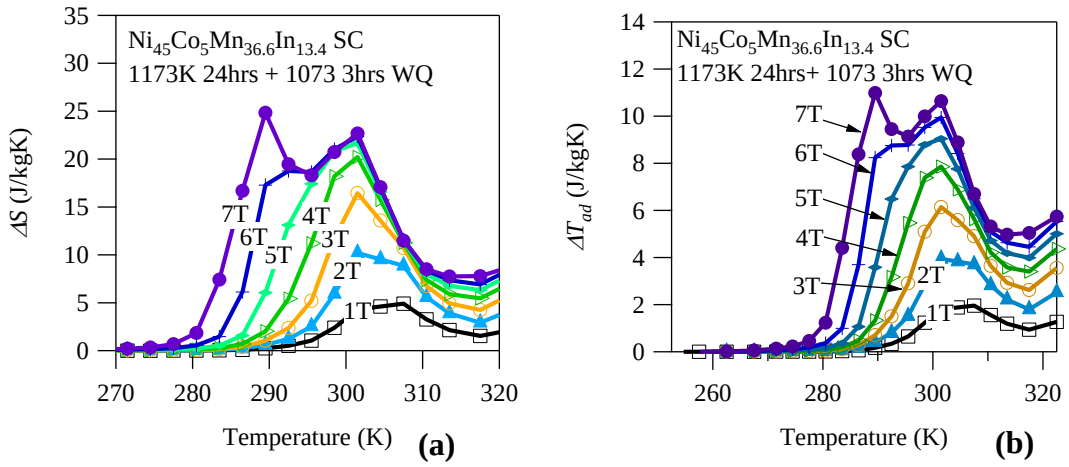

Figure 6-15: The entropy change versus temperature diagram (a) and the corresponding adiabatic temperature change (b) in $Ni_{45}Co_5Mn_{36.6}In_{13.4}$ single crystals heat treated at 1173K for 24hours and secondary annealed at 1073K for 3hours followed by quenching in water. Entropy change values were computed with Eqn. (2.3) and adiabatic temperature changes with (Eqn. 1.34).

In Fig. 6-15b, the adiabatic temperature changes are computed with Eqn. (1.34) from the data in 6-15a. The heat capacity data in Fig. 5-19b for the same sample was used to compute ΔT_{ad}. From this optimized heat treatment, the NiCoMnIn will change about 4K with the application of 2T. This is significant, as the same temperature change could be achieved in the $Ni_{50}Mn_{36}In_{14}$ sample in the previous section by applying 7T. Since M_f is nearly 308K, this temperature change should be repeatable with field cycling. Applying larger magnetic fields will further transform the MMSMA, thus larger adiabatic temperature changes will be generated. The data in Fig. 6-15b indicate that the MMSMA should change nearly 8K by applying up to 7T.

While working with NiMnIn alloys, it was realized that very short heat treatments are capable of ordering the NiCoMnIn single crystals [46, 75]. This was also seen with the

TEM images in Chapter 5 Figure 5-23. Therefore, a SHT crystal was heat treated at 873K for only 30min and then quenched in water. Surprisingly, this heat treatment resulted in martensitic transformation characteristics almost identical to the SHT + 1073K 3hrs WQ case. The thermomagnetization responses of the SHT + 873K 30 min WQ case are shown in Fig. 6-16.

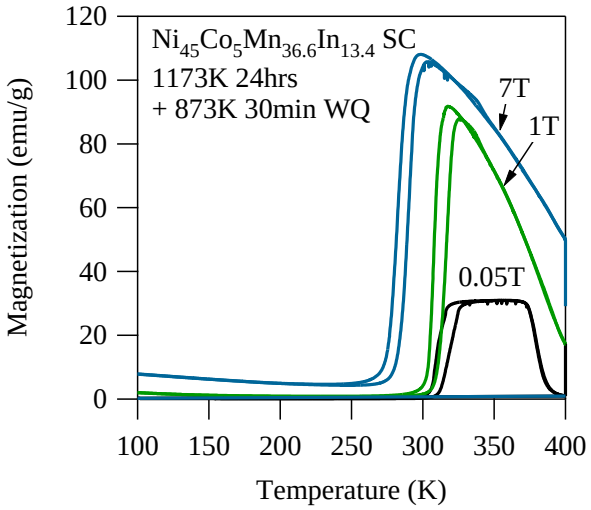

Figure 6-16: The 0.05T, 1T, and 7T thermomagnetic responses of $Ni_{45}Co_5Mn_{36.6}In_{13.4}$ single crystals that have been heat treated at 1173K for 24hours followed by a secondary heat treatment of 873K for 30mins.

When compared to the response in 6-14, it can be seen that the SHT + 873K 30 min WQ case exhibits slightly larger magnetization levels in A and M than the SHT + 1073K 3hrs WQ case, but nearly the same magnetization change across the martensitic transition. At the same time, the dT/dH is slightly larger. Here, $dT/dH = -4.3\text{K/T}$, but for the SHT + 1073K 3hrs WQ case, $dT/dH = -4.1\text{K/T}$. Thus, the $\Delta S^{M\rightarrow A}$ is lower in

the SHT + 873K 30min case. To identify the temperature dependence of $\Delta S^{M \to A}$ in the SHT + 873K 30min WQ alloy, Eqn. (2.3) was employed. The $\Delta S^{M \to A}$ is shown in Fig. 6-17a.

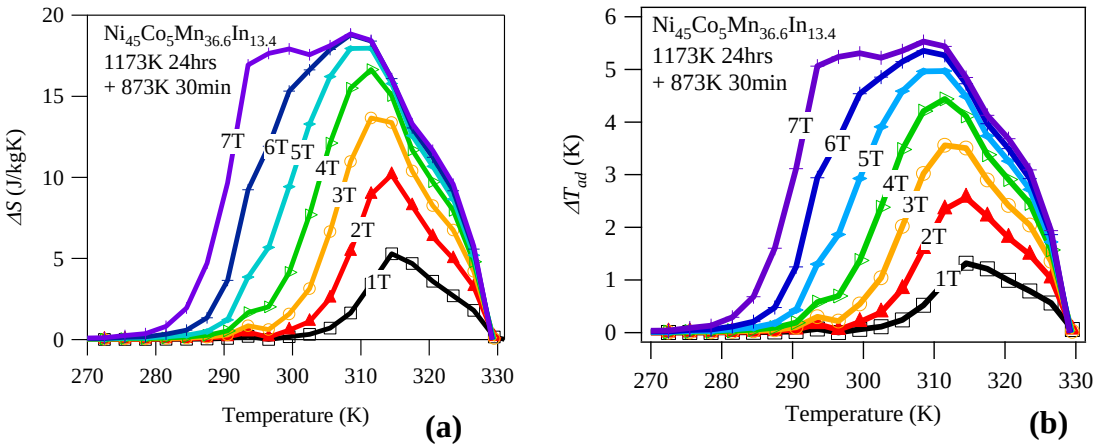

Figure 6-17: The entropy change (a) and adiabatic temperature change (b) as a function of temperature for the $Ni_{45}Co_5Mn_{36.6}In_{13.4}$ single crystals solutionized at 1173K for 24hours followed by a secondary heat treatment of 873K for 30mins. Entropy change value in (a) were computed with Eqn. (2.3) and adiabatic temperature change values in (b) were computed with Eqn. (1.34).

The computed adiabatic temperature changes corresponding to the entropy changes in Fig. 6-17a are shown in 6-17b. Only about 2K can be generated at the M_f temperature in this alloy (306K), which corresponds to half of what can be produced in the SHT + 1073K 3hrs heat treatment case. This is most likely a result of the smaller $\Delta S^{M \to A}$ in the 873K 30min alloy. Due to the higher cyclic reversibility in the SHT + 1073K 3hrs alloy, the maximum found in η^{Latent} (Fig. 5-20) is apparently an accurate metric for comparing the influence of heat treatments on a single MMSMA composition.

6.5.2 Achieving 1K thermal hysteresis in $Ni_{45}Co_5Mn_{36.6}In_{13.4}$ single crystals

To identify if 3 hour heat treatments were a sufficient duration to achieve thermodynamic equilibrium between B2 and $L2_1$ phases in NiCoMnIn, a one week secondary ordering heat treatment was performed at 873K. This temperature was nearly equal to the ordering temperature discussed in Chapter 5 (900K). Interestingly, the magnetothermal response in the 1 week secondary heat treatment was drastically different than the 3 hour (Figure A14) or 30minutes cases (Figure 6-16).

In Fig. 6-18, the thermomagnetization response of a SHT + 873K 1 week WQ sample is shown. Surprisingly, the 1 week heat treatment resulted in a 1K-3K thermal hysteresis. This low level of hysteresis has never before been observed in $Ni_{45}Co_5Mn_{36.6}In_{13.4}$ single crystals, and suggests that the MMSMAs heat treated for only 3 hours are in metastable equilibrium. The differences in their thermomagnetic responses are representative of their metastability.

Dark and bright field TEM imaging was performed on this particular heat treatment using the methods detailed in Chapter 5. The bright and dark field images (Fig. 6-19) suggests that the alloy is comprised of both B2 (dark) and L21 (bright) phases. However, the dark field image in 6-19b indicates that the alloy is mostly B2 ordered. Due to the differences between the thermal hystereses measured in SHT + 873K 1WK and SHT + 873K 30min cases, B2 APBs, which were clearly uniform as depicted in Fig. 5-23 and non-uniform in the 1W case of Fig. 6-19b, may contribute to structural dissipation across the transformation. More work, however, is needed to identify the cause of the small hysteresis measured from the 1WK heat treatment. In addition, the entropy change

versus temperature diagrams need to be generated to identify the cyclic reversibility of the FOPT.

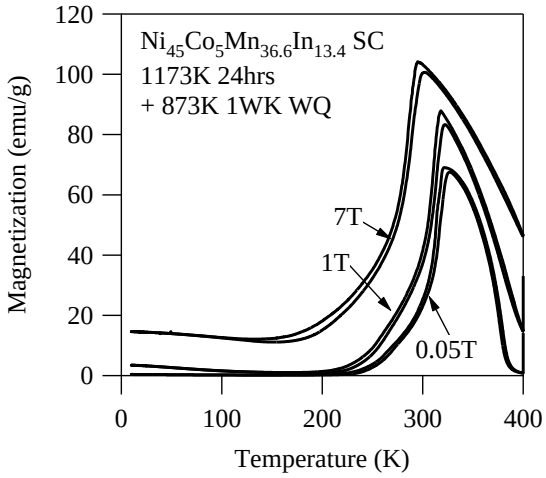

Figure 6-18: The 0.05T, 1T, and 7T thermomagnetic responses of $Ni_{45}Co_5Mn_{36.6}In_{13.4}$ single crystals solution heat treated at 1173K for 24 hours followed by a secondary heat treatment of 873K for 1 week.

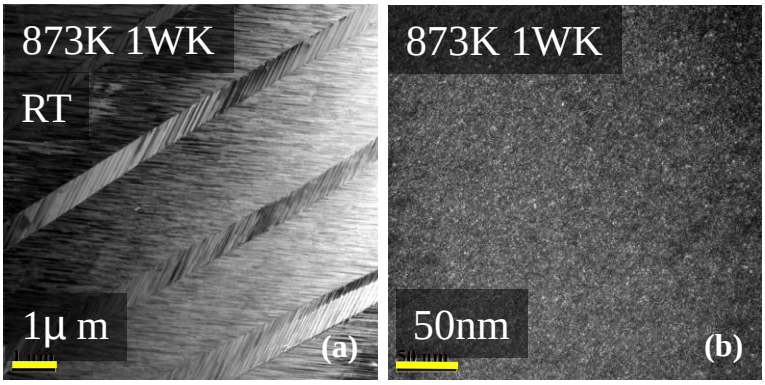

Figure 6-19: Transmission electron microscopy bright field micrograph of room temperature martensite (a) and $L2_1$ morphology in room temperature austenite (b) in a $Ni_{45}Co_5Mn_{36.6}In_{13.4}$ single crystal heat treated for 1173K for 24hours followed by a secondary heat treatment at 873K for 1 week quenched in water.

6.5.3 Conclusions

Two heat treatment cases of NiCoMnIn were investigated for the magnetocaloric effects. The three hour secondary heat treatments at 1073K were determined to be superior when compared to a 30min heat treatment at 873K due to the smaller $A_f - M_f$ temperature range and larger entropy change. With a brief critical analysis of the reversibility in these materials, Eqn. (4.26) was validated. In the optimum 1073K 3hrs case, it was determined that a 4K temperature change can be achieved at the M_f temperature with cycling only 2T. Higher field levels would result in larger temperature changes up to 8K. A specially selected 1 week long heat treatment was employed at 873K to determine if the MMSMA was in thermodynamic equilibrium when only heated for 3 hours. Only 3 hour treatments were identified as insufficient to stabilize the MMSMA response. Further investigations are required to fully understand and identify the mechanisms responsible for decreasing the thermal hysteresis to 1-3K from the typical 8K in all the other heat treatments. In addition, entropy change versus temperature diagrams are needed for this specially heat treated alloy to identify the influence of low hysteresis on the reversible MCE.

6.6 $Ni_{54}Fe_{19}Ga_{27}$ single crystals

This final section contains data describing the anisotropy of the giant elastocaloric effect (ECE) in $Ni_{54}Fe_{19}Ga_{27}$ single crystals. Directly measured adiabatic temperature changes are also presented and compared to those computed using the framework in Chapter 1. It is shown that when properly applied, the thermodynamic framework can

accurately predict the directly measured adiabatic temperature change from superelastic loading and that the most efficient loading direction for converting mechanical energy to thermal can be revealed with Eqn. (4.27). The giant elastocaloric effect offers an additional driving mechanism to transform the shape memory alloy, rather than a magnetic field, thus lending the possibility of implementing novel refrigeration cycles as discussed in Chapter 7.

6.6.1 Introduction

The $Ni_{54}Fe_{19}Ga_{27}$ (at%) alloy was fabricated to nominal composition using the Bridgman technique in an inert environment. In the as-grown state, this single crystal contained no γ phase [81] precipitates verified by optimal microscopy and no annealing was performed to promote their growth. Electro-discharge machining (EDM) was used to cut compression specimens of 4mm × 4mm × 8mm nominal dimensions in three different crystallographic compression orientations along the 8mm length. To determine stress-free martensitic transformation temperatures, the compression samples were heated and cooled at 5K/min in a superconducting quantum interference device – vibrating sample magnetometer (SQUID-VSM) around the martensitic transition (MT) and their magnetization was measured under 0.05T. The average of the transformation temperatures are reported in Table 6-2. Heat capacity measurements were performed on a small disk sample (EDM cut) using a quantum design physical property measurement system (PPMS) and heat capacity measurements were compared with those reported in literature for our alloy composition. The specific heat capacity (data not shown) for the alloy in this

study has been found to be approximately 405 J/kgK at A_f, which is also in reasonable agreement with previous work (425 J/kgK) for an alloy of the same composition [82].

Table 6-2: The martensitic transformation temperatures described in Figure 1-3a for $Ni_{54}Fe_{19}Ga_{27}$ (at.%).

Austenite Crystal Direction	M_f (K)	M_s (K)	A_s (K)	A_f (K)
[001] [123] [011]	275	280	284	289

To measure the stress-strain ($\sigma - \varepsilon$) curves used to compute entropy change with Eqn. (2.11), the isothermal superelastic (SE) response was measured in the [100], [123], and [011] austenite crystallographic compression directions. Uniaxial loading directions of the compression specimens were verified with x-ray diffraction by measuring peak locations on the sample compression face with Cu-K_α x-rays. Isothermal SE loading was performed from 253K to 353K in increasing increments of about 3K and the stress-strain response was recorded. Since each sample was initially at room temperature before testing and then cooled to 253K (below M_f) to begin the heating sequence, a mechanical load of 3000N was first applied to each sample upon reaching 253K to orient the self-modulated martensite that formed upon cooling to its stress-preferred state. The self-accommodation process was depicted in Fig. 1-1. This martensitic reorientation does not create a large entropy (or temperature) change because no latent heat is generated by orienting martensite. This step of the test sequence was performed to keep consistency with the

analysis described in Chapter 2. Since only the latent heat of the stress-induced transformation was to be quantified, and cycling stress would not generate self-accommodated martensite, the ECE resulting from martensitic reorientation was not considered.

After the initial detwinning of self-accommodated martensite, a constant 5-10 MPa preload was left on the sample during heating to the next temperature step, thus allowing the compression rods (see Fig. 2-9) to conduct heat to the sample through contact on the compression faces. Once the sample reached the target temperature on heating, the load was again ranged from 5-10MPa to 200MPa and back to 5-10MPa. This heating protocol is the equivalent experimental procedure followed by some magnetocaloric measurements [83].

The isothermal compression tests were performed using a screw-driven material testing system (MTS) with quasi-static displacement control condition (~equating to nearly 0.06 %ε/sec on the nominal sample dimensions) to prevent the sample from changing temperature as a result of the latent heat of the superelastic transformation. Despite the slow strain rate, temperature fluctuations of approximately 0.4K were measured during isothermal loading and unloading which were attributed to K-type thermocouple resolution and sensitivity. It is important that the temperature remained constant during tests as the superelastic $\sigma - \varepsilon$ curves were used to compute *isothermal* entropy change. To measure the *adiabatic* temperature change presented in the final section, the sample was loaded at 0.01mm/s (very quickly) so that the latent heat of

transformation could be monitored with the attached thermocouple prior to losing the heat to the pushrods, or the pushrods giving up heat to the sample.

Sample strain was measured using a MTS high temperature extensometer (HTEX) with ceramic tips held in place with a mechanical spring against the compression rods near the sample. Specimen surface temperature was actively measured every one second using a thermocouple fixed to the specimen's surface. The specimen and compression rods were insulated using thermal insulation (pyrogel) to prevent heat leaks to the environment. The isothermal superelastic $\sigma - \varepsilon$ responses were measured with the same acquisition rate (1Hz) such that temperature, stress, and strain could be compared at the same instant in time. For adiabatic measurements the acquisition rate was increased to 50Hz.

6.6.2 Results

Figure 6-20 shows the superelastic responses (SE) in the [123], [001], and [011] austenite directions at 288K, i.e. nearly A_f. Clearly, the [001] single crystal compression direction exhibits a single stage transition to approximately 5.5% transformation strain under stresses less than 50MPa. The [123] direction also exhibits a single stage transformation up to 4% strain. The [011] direction, however, is capable of exhibiting a two stage stress-induced martensitic transformation from austenite, A, to martensite, M_I, up to 3% strain and then from M_I to a second martensite, M_{II}, up to 5.5% strain. For the [011] direction, the label "A" indicates that the sample is first compressed in the austenite phase at A_f and "M" denotes martensite, M_{II} in the figure. Mechanical loading drives the A to M transformation as discussed in Chapter 1.

At a critical stress level, an A to M_I transformation is initiated. Further loading drives the A to M_I transformation to completion at σ_{comp}^{iso,M_I}. Loading beyond σ_{comp}^{iso,M_I} produces elastic deformation in M_I, and perhaps reorientation, until a second critical stress is reached around 200MPa. At this stress level, the $M_I \rightarrow M_{II}$ transformation occurs [32]. Finally, the elastic response of M_{II} is measured around 5.5% applied strain above $\sigma_{comp}^{iso,M_{II}}$. Mechanically unloading results in a completely reversible two stage transformation with mechanical hysteresis from both transitions, namely $\Delta\sigma_{hys}^{M_I}$ and $\Delta\sigma_{hys}^{M_{II}}$ as depicted in the figure. In the [001] and [123] compression directions, however, only a single stage reverse transformation is measured when loaded to 200MPa as shown in the inset.

Isothermal compression tests were performed at different temperatures and the critical stresses for the M to A transformation (those that generate cooling) were extracted and plotted with temperature. The critical stress (σ^{A_s}) vs. temperature phase diagram is shown in Figure 6-20b. Here, only the σ^{A_s} is plotted because the M to A transformation in NiFeGa is endothermic and generates cooling with mechanical unloading. As shown in Fig. 6-20b, the [123] loading direction exhibits the steepest $d\sigma^{A_s}/dT$ slope of 4.6MPa/K, followed by the [011] (for the $M_I \rightarrow A$ transformation) and the [001] of 4.4MPa/K and 3.0MPa/K, respectively. The CC slope of the $M_{II} \rightarrow M_I$ transformation observed in the [011] direction is also plotted in Fig. 6-20b. Interestingly, this slope is very small and negative.

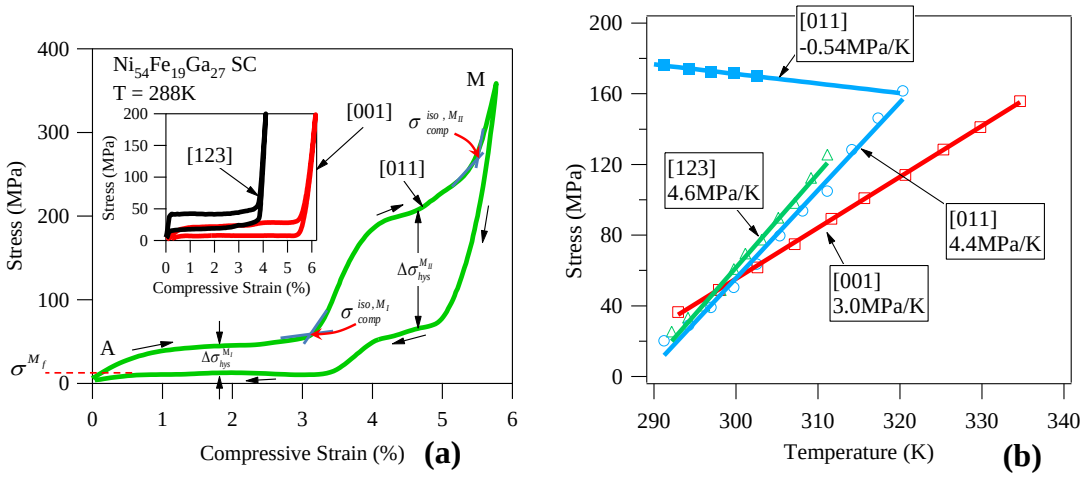

Figure 6-20: The superelastic responses of [011], [001], and [123] austenite crystal directions from compression at $T = 288K$ (a) and the A_s versus temperature phase diagram (b) for each loading direction.

According to Eqn. (2.5), the transformation strain can be multiplied by the CC slope to identify the transformation entropy change generated from superelastic loading. In Eqn. (2.5) the mass density, ρ, is needed and it was therefore approximated using a mass scale and compression sample volume. Using the data in Fig. 6-20, critical materials parameters for Eqn. (4.27) were extracted and tabulated in Table 6-3.

Table 6-3: The critical transformation characteristics in $Ni_{54}Fe_{19}Ga_{27}$ single crystals for the [001], [123], and [011] austenite crystal directions while loaded in compression. Stress hysteresis, $\Delta\sigma_{hys}\big|_{T=A_f}$, transformation strain, $\varepsilon_{tr}\big|_{T=A_f}$, and austenite moduli of elasticity, E_A, were extracted from the data in Fig. 6-20a.

Crystal Direction	ρ (kg/m3)	$\varepsilon_{tr}\big\|_{T=A_f}$ (%)	$d\sigma^{A_s}/dT$ (MPa/K)	$\Delta S^{M\to A}$ (J/kgK)	$\Delta\sigma_{hys}\big\|_{T=A_f}$ (MPa)	σ^{iso}_{comp} (MPa)	E_A (GPa)
[001]	8457	4.9	3.02	17.4	16	29	7.2
[123]		3.4	4.63	18.5	22	50	13.5
[011]		2.8^{I} 1.8^{II}	4.43^{I} -0.54^{II}	14.6 -0.97	32^{I} 145^{II}	56.3^{I} 258^{II}	9.4

[I]: First stage martensitic transition, [II]: Second stage martensitic transition.

In Table 6-3, mass density ρ, measured transformation strain $\varepsilon_{tr}\big|_{T=A_f}$, the CC slope $d\sigma^{A_s}/dT$, computed $\Delta S^{M\to A}$, measured stress hysteresis $\Delta\sigma_{hys}\big|_{T=A_f}$, and the austenite moduli of elasticity E_A, are tabulated for each crystal loading direction at T= A_f .

In each loading direction, the $\Delta S^{M\to A}$ was computed to be nearly 18J/kgK with the exception of the [011]. Due to the negative CC slope of the $M_I \to M_{II}$ transformation, the entropy change is opposite in sign to that generated by the $A \to M_I$. Thus, when applying the giant ECE in NiFeGa, the $M_I \to M_{II}$ transformation in the [011] direction should be avoided to generate the largest effect. In Table 6-3, the stress hysteresis at T= A_f, $\Delta\sigma_{hys}\big|_{T=A_f}$, is shown to be substantially different in each loading direction indicating that the mechanical-to-thermal energy conversion efficiency for each direction will also

different. Finally, it is interesting to note that the austenite moduli of elasticity are directly proportional to the magnitude of the $d\sigma^{A_s}/dT$, as predicted in Chapter 1 (Section 1.3.2).

Next, isothermal compression tests were performed up to 200MPa in each austenite loading direction. This maximal stress level was selected to prevent the $M_I \rightarrow M_{II}$ transition in [011] and is experimentally equivalent to arbitrarily selecting 7T for the peak field in MCE measurements. In Fig. 6-21a, isothermal stress-strain data are shown for the M to A (reverse) transformation in the [001] loading direction. These curves were used to compute an entropy change vs. temperature diagrams with Eqn. (2.11) and are plotted in Fig. 6-21b for different degrees of applied strain. Here, is it important to note that the entropy change curves in Fig. 6-21b need be expressed in terms of applied strain, instead of applied stress, due to the inability to integrate the ε with respect to σ, i.e. $\int \varepsilon d\sigma$. This is discussed in Chapter 2 . The $\varepsilon - \sigma$ response is not a valid function to integrate as shown by the decrease in stress near 1% strain of the $\varepsilon - \sigma$ curves in Fig. 6-21a. In other words, at T=289K, the $\varepsilon - \sigma$ response of the [001] direction exhibits the same stress value, σ, for two or more ε values. This results in the inability to integrate the $\varepsilon - \sigma$ curve, and instead, a different thermodynamic formula was derived in Chapter 2 to perform the analysis.

In some cases, as shown for the [123] loading direction in Fig. 6-22a, the $\varepsilon - \sigma$ response can be integrated. This is because no drop in stress is measured during mechanical testing and only one stress value corresponds to one strain value. Nevertheless, Eqn. (2.11) derived from Helmholtz free energy can be applied to either case, and

therefore, is more mathematically robust than the other expression derived from the Gibbs free energy in Eqn. (2.7). Here, only Eqn. (2.11) is implemented.

In Fig. 6-21b, 5% applied strain in the [001] direction corresponds to the full 18J/kgK predicted in Table 6-3. Similarly, in the [123] direction, about 18J/kgK is generated by loading up to 4% applied strain. The shape of the entropy change vs. temperature diagram in Fig. 6-22b indicates that only the peak entropy change can be generated at temperatures below 305K. This, of course, is only true up to 200MPa. The entropy change data exhibits this particular shape as a byproduct of only loading the MMSMA up to 200MPa. If a higher mechanical load was applied, superelasticity would be achieved at higher temperatures and, therefore, the entropy change of the transformation can be generated at higher temperatures. In fact, superelastic loading can be achieved at temperatures up to that which plastic deformation occurs, or the coexistence lines on a phase diagram intersect [32].

Finally, a similar magnitude for the entropy change between A and M_I was measured in the [011] austenite compression direction. The reverse $M_I \rightarrow A$ $\sigma - \varepsilon$ curves are shown at various temperatures. Clearly, these $\sigma - \varepsilon$ curves could not have been integrated as $\int \varepsilon d\sigma$, as mentioned before, and therefore Eqn. (2.11) was employed instead. Again, the entropy change diagram that results is a function of applied strain in Fig. 6-23b. If the second $M_{II} \rightarrow M_I$ transition was driven by larger mechanical loads in the [011] direction, the entropy change would be decreased as a result of the summative

nature of the ΔS and the negative CC slope of the $M_{II} \rightarrow M_I$ transition depicted in 6-20b.

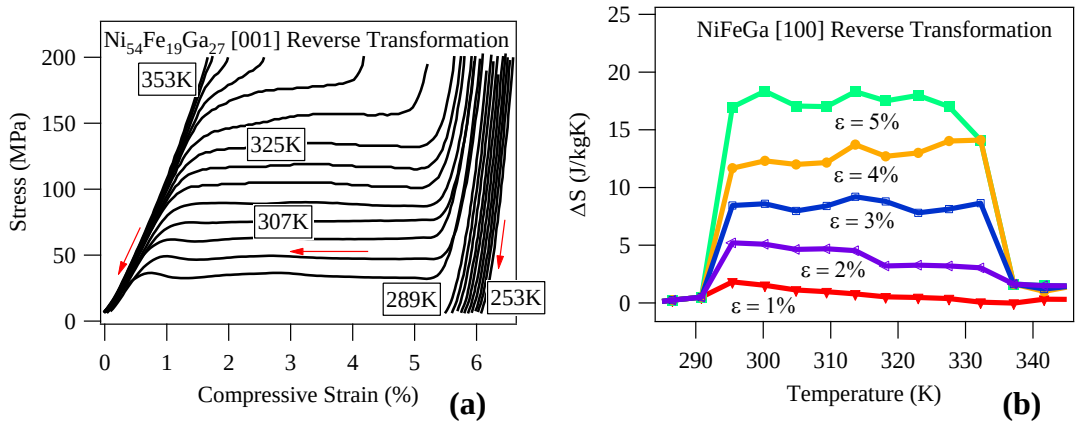

Figure 6-21: Mechanical unloading across the M to A transition in $Ni_{54}Fe_{19}Ga_{27}$ single crystals along the [001] austenite crystal direction (a) and the entropy change versus temperature diagram computed with Eqn. (2.11).

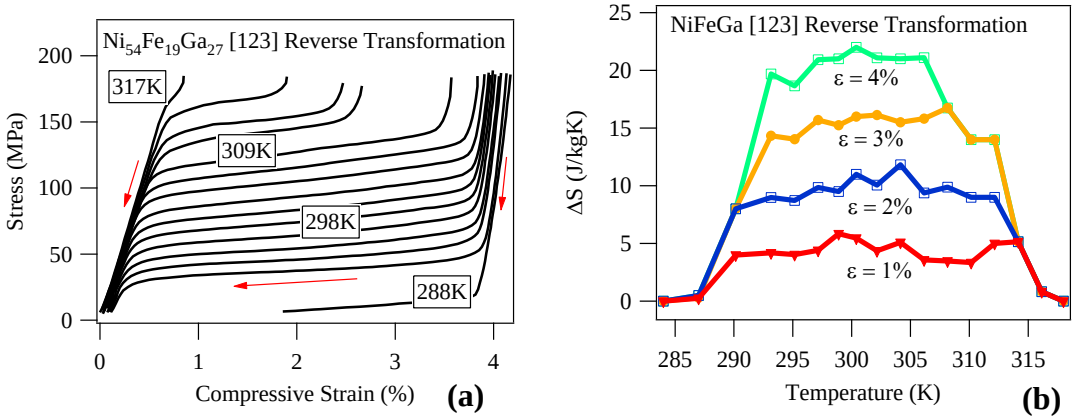

Figure 6-22: Mechanical unloading across the M to A transition in $Ni_{54}Fe_{19}Ga_{27}$ single crystals along the [123] austenite crystal direction (a) and the entropy change versus temperature diagram computed with Eqn. (2.11).

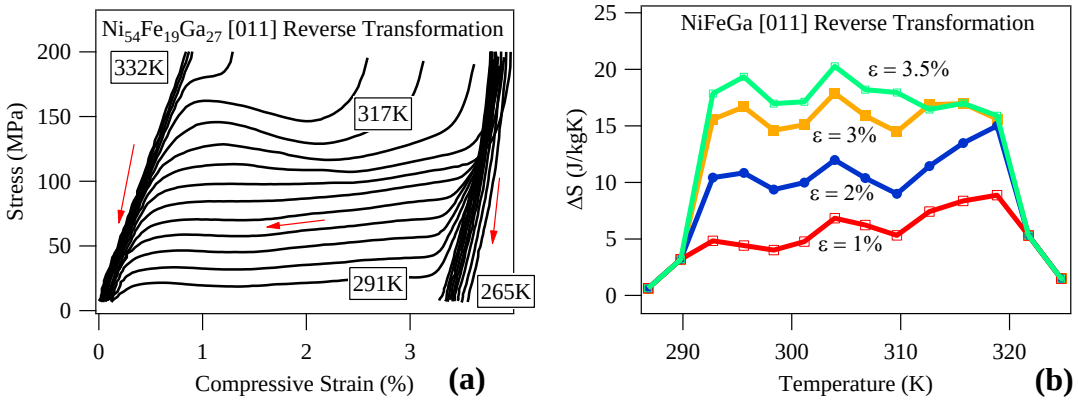

Figure 6-23: Mechanical unloading across the M to A transition in $Ni_{54}Fe_{19}Ga_{27}$ single crystals along the [011] austenite crystal direction (a) and the entropy change versus temperature diagram computed with Eqn. (2.11).

Next, to identify the mechanical to thermal energy conversion efficiency of the stress-induced transformation for each loading direction, the $\sigma - \varepsilon$ curves were integrated to quantify the magnitude of the mechanical dissipation. The mechanical dissipation, S_{irr}, was computed in units of J/kg as

$$S_{irr} = \frac{1}{T\rho}\left[\int_0^{\varepsilon} \sigma^{A\to M} d\varepsilon - \int_{\varepsilon}^{0} \sigma^{M\to A} d\varepsilon\right]. \tag{6.1}$$

at T= A_f. Eqn. (6.1) used the $\sigma - \varepsilon$ data for each loading direction in Fig. 6-20. The applied strain, ε, was used to approximate the percent of the martensitic transformation as $\%\ \text{transformation} = \varepsilon / \varepsilon_{total}$. S_{irr} was then plotted as a function of percent transformation (%) as shown in Fig. 6-24.

For complete transformation, the [001] austenite direction exhibited a larger hysteretic loss than the [123] loading direction despite the fact that the $\Delta\sigma_{hys}\big|_{T=A_f}$, in Table

6-3, is smaller in the [001] direction. The transformation strains seem to be partly responsible for the magnitudes of the dissipation. When mechanically loading only to 50% transformation, the [001] direction exhibits smaller hysteresis loss than the [123] direction. In the [011] direction, the $A \rightarrow M_I$ and the $M_I \rightarrow M_{II}$ transitions were considered to define a complete transformation. As expected, the [011] direction exhibits the largest hysteresis loss across the entire transformation interval corresponding to the large magnitude in $\Delta\sigma_{hys}$ in Table 6-3.

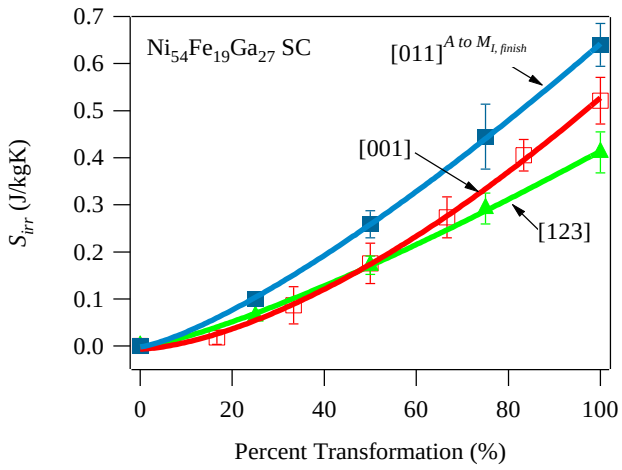

Figure 6-24: Dissipation computed from Eqn. (6.1) as a function of percent transformation. The percent transformation was approximated assuming $\varepsilon / \varepsilon_{total}$.

Finally, η was computed using Eqn. (4.3), and η^{Latent} with Eqn. (4.26). It should be noted that η from Eqn. (4.3) is not the same as η^{Latent} from Eqn. (4.26). η^{Latent} only accounts for half of the energy input needed for a complete thermodynamic cycle, whereas

Eqn. (4.3) accounts for the work performed by an entire cycle (applying and removing the mechanical force).

To determine η, W_{rev} was computed as described in Eqn. (4.1). ΔS_c was used from the plots in Figs. 6-21, 6-22, and 6-23 as the largest entropy change at the coolest temperatures. The ΔT in Eqn. (4.1) was assumed to equal ΔT_{ad} per the discussion in Chapter 4 and was computed to be 5.5K with the data in Table 6-3 and Eqn. (1.39). W_{real} in Eqn. (4.2) was computed using S_{irr} in Fig. 6.24 and the W_{rev}. In Eqn. (4.2) and the Q_l and Q_f contributions were neglected. Employing Eqns. (4.2) and (4.3), with the data shown in Figures 6-21 through 6-24, the conversion efficiency was computed as a function of percent transformation and is plotted in Fig. 6-25.

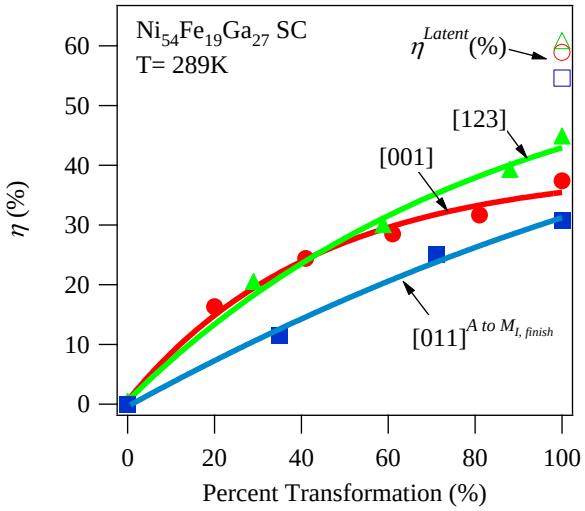

Figure 6-25: Transformation efficiency η computed with Eqn. (4.3) and η^{Latent} from Eqn. (4.27) for $Ni_{54}Fe_{19}Ga_{27}$ single crystals at 289K in [001], [123], and [011] austenite crystal directions as a function of percent transformation. η in Eqn. (4.3) was developed in [12].

In Fig. 6-25, the [123] compression direction exhibits a higher energy conversion efficiency for a complete transformation than the other compression directions. Up to 40% transformation the [001] single crystal exhibits a slightly better and nearly equal mechanical-to-thermal energy conversion efficiency than the [123] direction. This is attributed to the hysteresis loss in Fig. 6-25. The [011] exhibits a linear behavior and performs poorly, overall. A 45% efficiency is predicted for the [123] direction and a 35% efficiency for the [001] direction.

The magnitude of η is interesting to compare to η^{Latent} because η accounts for the energy applied to the shape memory alloy over a complete cycle, whereas η^{Latent} only accounts for energy applied and not that which is recovered on releasing the load as mentioned in Chapter 2. As a result of the differences between the two computational methods, η^{Latent} is larger in all the cases and is shown by transparent data points in Fig. 6-25. To compute η^{Latent}, the data in Table 6-3 were applied in Eqn. (4.27).

Although η^{Latent} over predicts the energy conversion ratio, the relative comparison between crystal directions is still accurate. η^{Latent} was defined assuming that the complete transformation occurs, and therefore is only plotted for 100% transformation. The [123] direction exhibits the best conversion efficiency. The over prediction is the result of how the energy input is computed in the denominator of Eqn. (4.3). Nevertheless, the η^{Latent} in Eqn. (4.27) can be used to accurately compare the relative energy conversion performance between single crystal shape memory alloys. The [123] direction is most efficient in converting mechanical energy to thermal. In the next section, the directly measured giant

ECEs in [123] and [001] single crystal loading directions are discussed and results are presented. These two directions were selected because they exhibited the highest energy conversion ratio per the above discussion.

6.6.3 Direct giant ECE measurement

The [123] and [001] austenite loading directions were mechanically loaded and unloaded at 0.01mm/s up to 200MPa at room temperature and their temperatures were recorded with time. The stress-strain responses are shown in Fig. 6-26a for six cycles. In Fig. 6-26a the [123] loading direction exhibited what looked to be substantial transformation hardening as a result of the adiabatic conditions.

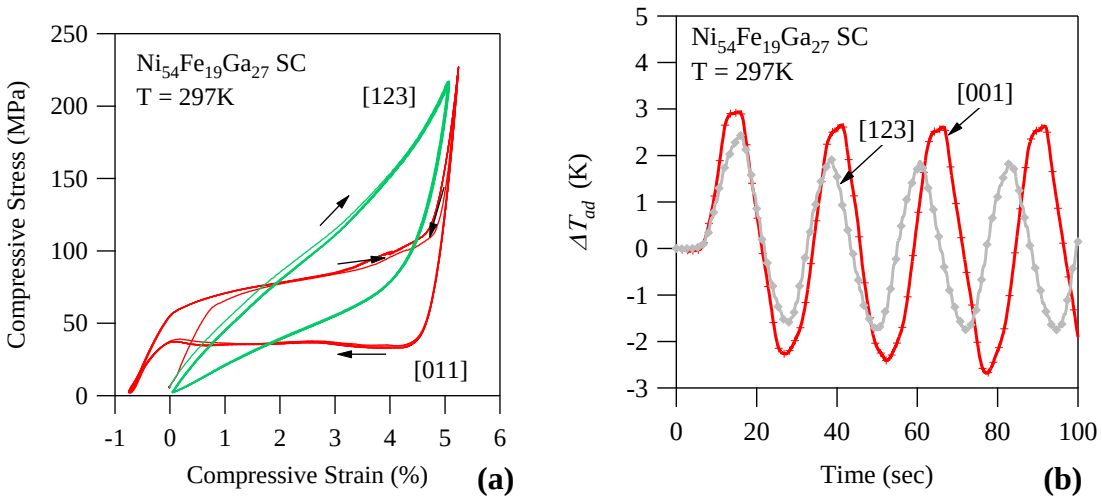

Figure 6-26: The adiabatic compressive stress-strain responses of $Ni_{54}Fe_{19}Ga_{27}$ [123] and [001] austenite crystal directions at 297K (a) and the measured adiabatic temperature changes (b) from the loading in (a).

The transformation hardening in the [123] single crystal is a result of the sample changing temperature across the stress-induced transformation and the increase in critical stresses as described by the CC slope in Table 6-3. On the other hand, the [001] direction may have exhibited smaller transformation hardening due to its smaller CC slope. Interestingly, the [001] single crystal exhibited over-recovery after its first cycle, indicating that the sample may not have been completely in the austenite phase at room temperature. In Figure 6-26b, the adiabatic temperature change is plotted for the mechanical cycling in Fig. 6-26a.

As shown in Fig. 6-26b, the mechanical loading, or A to M transition, generated about 2.5K temperature increase in both of the single crystals. This is a result of the exothermic forward martensitic transformation. Mechanical unloading was performed immediately after the sample was loaded to martensite, thus not allowing the sample to cool back to RT. On unloading, the sample cooled by approximately 5K in both single crystals. This agreed well with the predicted ΔT_{ad} of 5.5K computed with Eqn. (1.39).

6.6.4 Conclusions

$Ni_{54}Fe_{19}Ga_{27}$ single crystals were studied for their giant elastocaloric effects. The [001], [123], and [011] austenite crystal directions were found to generate an entropy change of nearly 18J/kgK around their stress-induced transformations and an adiabatic temperature change of 5.5K. Each loading direction exhibited a different magnitude of stress hysteresis, and therefore the mechanical to thermal energy conversion of each sample was different. The energy conversion efficiency, η, was computed using the

methods in [12], as well as with η^{Latent} developed in Eqn. (4.27). It was found that these parameters, although different in magnitude, predict that the ECE in the [123] austenite crystal direction outperforms the other directions tested in this study.

6.7 General conclusions

As demonstrated by the case studies in this chapter, the giant magnetocaloric and elastocaloric effects in MMSMAs can be simply quantified by the latent heat of the martensitic transformation. The transformation is then driven from M to A by a magnetic field, or A to M by a mechanical load. It was found that the η^{Latent} parameters defined by Eqns. (4.26) and (4.27) were capable of predicting the relative calorific performance between shape memory alloys of the same composition. In addition, different heat treatments and crystal loading directions were studied to quantify differences in the caloric effects.

The next chapter demonstrates that a combination of both driving forces, namely mechanical stress and applied magnetic field, can result in what is known as the stress-assisted magnetocaloric effect (SAMCE). It will be shown that when both driving forces are employed, the required magnitude of each is substantially reduced. As a result, the caloric effects generated by the martensitic transformation can be realized in everyday applications where magnetic fields below 2T and stresses below 60MPa can be employed to generate efficient cooling systems with magnetic shape memory alloy solid-state refrigerants.

CHAPTER VII

THE META-MAGNETIC RESPONSE OF MMSMA SINGLE CRYSTALS UNDER MECHANICAL STRESS AND MAGNETIC FIELD

7.1 Introduction

In the following chapter, the influence of high magnetic fields on the superelastic response in $Ni_{45}Co_5Mn_{36.6}In_{13.4}$ single crystals is identified. The custom MaTMeCh device was employed, as described in Chapter 3, with the aim of isolating the temperature-field-stress space in which the calorific effects are most pronounced. The influence of magnetic field on the austenite modulus of elasticity, energy dissipation across the transformation, and most importantly, the entropy change from the stress-induced martensitic transformation is quantified. The temperature and magnetic field dependence of each term in Eqn. (1.8) is investigated and their influence on the superelastic response is discussed.

Finally, a complete stress-assisted MFIT is demonstrated in $Ni_{45}Co_5Mn_{36.6}In_{13.4}$ single crystals. With the help of mechanical stress, magnetic fields below 1.5T prove to be sufficient to induce a complete martensitic transition. The complete stress-assisted MFIT (SAMFIT) is demonstrated in a region of the temperature-field-stress space where the entropy change is largest. This is an important finding, in that it opens the possibility of achieving larger caloric effects than those reported in more-expensive rare-earth MCE refrigerants. Additionally, in NiCoMnIn, these caloric effects can be tuned (see Chapter 5) to occur at a desired temperature.

7.2 The influence of magnetic field on superelasticity in $Ni_{45}Co_5Mn_{36.6}In_{13.4}$ single crystals

Figure 7-1 shows the superelastic response of a solution heat treated (SHT) NiCoMnIn [001] oriented single crystal in uniaxial compression. The A_f temperature of this particular sample was identified with SQUID magnetometry as -12°C, and therefore, the superelastic tests were performed at this temperature under different magnetic field levels. Each test exhibits full recovery. As shown in the figure, the sample was originally in the austenite phase and compression first resulted in the elastic response of austenite. At a critical stress, the stress-induced A to M transformation occurred. Each sample was only strained to 6.5% to protect its microstructural integrity. In doing so, the elastic response of the stress-induced martensite was not observed. On removing the applied stress, however, the elastic modulus could be identified. The reverse martensitic transformation took place and no significant irrecoverable strain was measured in any of the cases above 0T.

Under higher magnetic fields, the critical stress to transform the MMSMA from A to M increased. This is expected per the discussion in Chapter 1. With larger applied magnetic fields, the thermodynamic equilibrium temperature, T_0, exhibited a decrease thus requiring a higher mechanical load to trigger the transition, i.e. a larger chemical energy barrier had to be overcome by mechanical force. As shown in Fig. 7-1, the increase in critical stress is not linear below field levels of approximately 3T. Additionally, it is interesting to note that the larger applied field levels do not necessarily correspond to an increase or decrease in stress hysteresis nor an increase or decrease in transformation

hardening. Under these loading conditions, this particular sample exhibited a mechanically stable response under all the applied magnetic field levels.

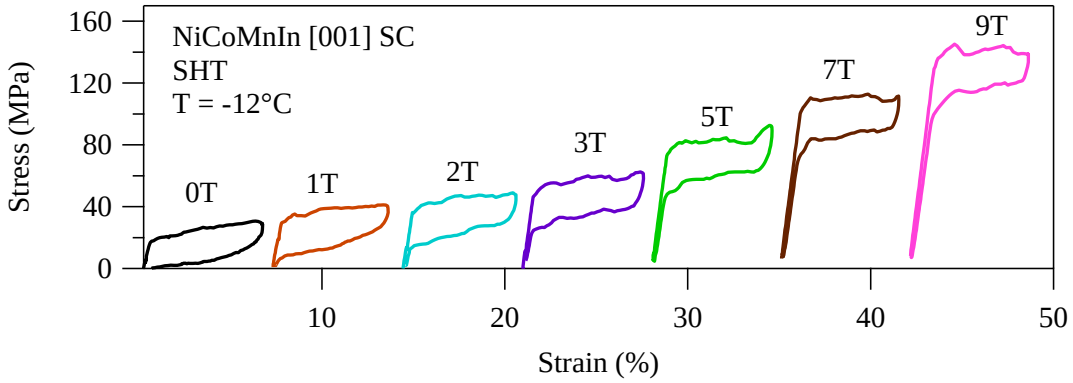

Figure 7-1: Superelastic responses of solutionized $Ni_{45}Co_5Mn_{36.6}In_{13.4}$ single crystals at -12°C under 0T, 1T, 2T, 3T, 5T, 7T, and 9T.

On the other hand, a similar compression sample was tested after being subject to a SHT + 600°C 30min heat treatment and the results are depicted in Figure 7-2. As shown in Fig. 7-2, the critical stresses increase with increasing field level, as expected. In contrast to the SHT case, this sample exhibited an increase in stress hysteresis with field. It is important to note that the SHT + 600°C 30min sample also exhibits significant transformation hardening compared to the SHT sample in Fig. 7-1. It is believed this is a result of the production of multiple or single martensite variants upon triggering the transformation with stress, however, more work must be performed to identify the influence of microstructural features on the mechanical behavior in these samples. Perhaps mechanical training influences martensite morphology.

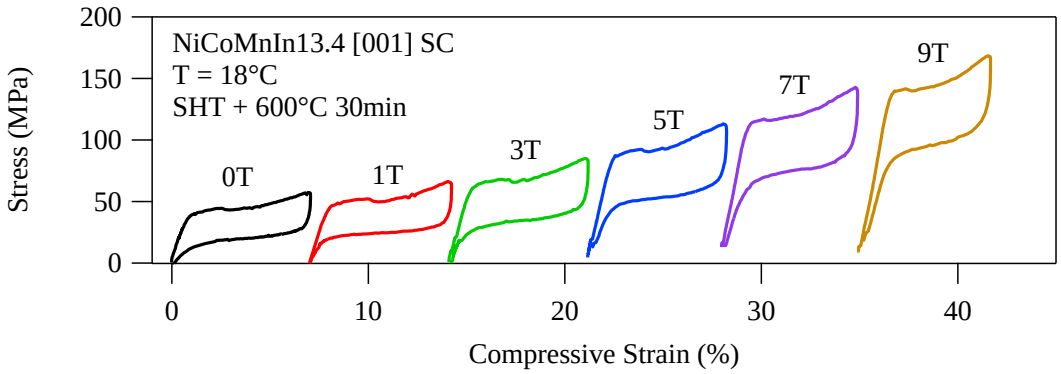

Figure 7-2: Superelastic responses of solutionized + 600°C 30min $Ni_{45}Co_5Mn_{36.6}In_{13.4}$ single crystals at 18°C under 0T, 1T, 2T, 3T, 5T, 7T, and 9T.

The critical stresses for the start of the A to M transformation, σ^{M_s}, were extracted from the data in Figures 7-1, 7-2, and the stress-strain curves in the Appendix. Phase diagrams were then plotted in Figure 7-3a and b for the SHT and SHT + 600°C 30min samples, respectively. As shown in Figure 7-3a, the slope of the critical stress (σ^{M_s})-temperature line decreases with higher applied fields and lower temperatures for the SHT alloy. This is of some importance, as the entropy change that defines the caloric effects influences the slope of these lines per Eqn. (2.5). Assuming the theoretical transformation strain of the stress-induced A to M transition (~6.24%) can be achieved under any field level and temperature [18], and that the mass density of our samples is nearly 8000kg/m^3, the entropy change from superelastic loading can be computed with Eqn. (2.5) as 17.6J/kgK under 0T and only 6.24J/kgK under 9T. These values were determined assuming the 0T and 9T CC slopes in Fig. 7-3a were 2.2MPa/K and 0.8MPa/K, respectively. At low temperatures, however, the 9T and 7T curves exhibit a further

decrease in the CC slopes. The decrease was neglected in the calculation, above, but will be discussed more later.

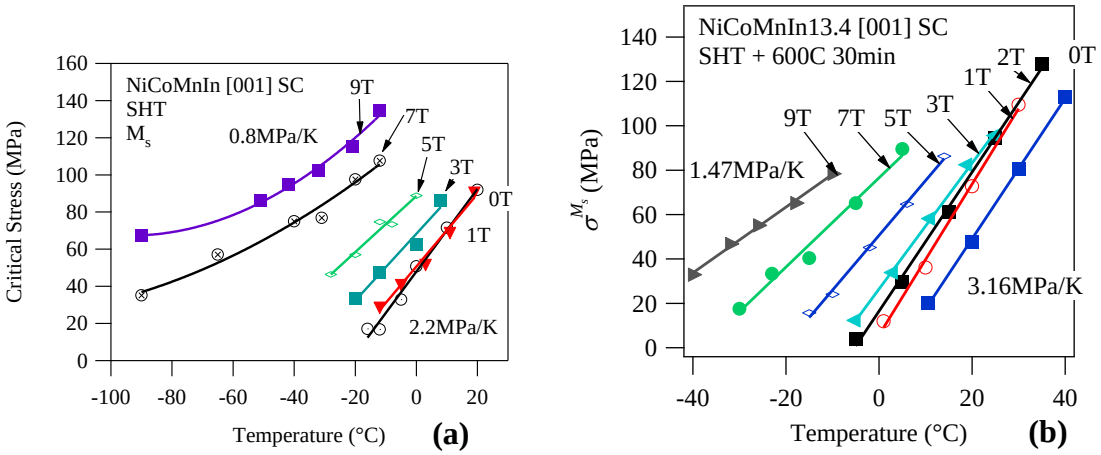

Figure 7-3: The σ^{M_s} versus temperature phase diagram for SHT(a) and SHT+600°C 30min(b) $Ni_{45}Co_5Mn_{36.6}In_{13.4}$ single crystal compression samples in the [001] austenite direction.

Similarly, the decrease in slope with increasing field is observed in the SHT + 600°C 30min sample as shown in Fig. 7-3b. In this particular sample, all of the slopes of the σ^{M_s} vs. temperature diagram are larger and show no apparent non-linearity as is observed for the SHT case at low temperatures. It is interesting to note that the CC diagram in Fig. 7-3b has been constructed for temperatures above -40°C, whereas that in Fig. 7-3a has been plotted down to -90°C. Again, assuming that the transformation strain is approximately 6.24% with a mass density of 8000kg/m^3 for the SHT + 600°C30min sample, the stress-induced entropy changes computed with Eqn. (2.5) and the slopes in Fig. 7-3b equate to 24.6J/kgK and 11.4J/kgK for 0T and 9T, respectively. Clearly, smaller

applied fields and higher transformation temperatures will result in larger entropy changes in these materials.

Using the superelastic data in Figs. 7-1 and 7-2, the magnetostress was computed for each heat treatment condition as shown in Figs. 7-4a and b.

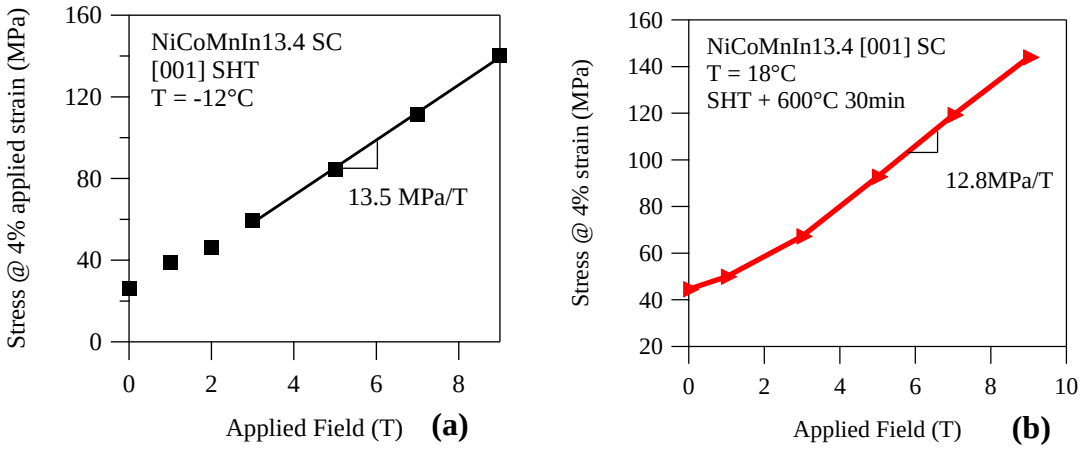

Figure 7-4: The magnetostress for SHT (a) and SHT+600°C 30min (b) $Ni_{45}Co_5Mn_{36.6}In_{13.4}$ single crystals along the austenite [001] direction.

The magnetostress was computed using the stress level at 4% applied strain under different field levels as described in [18]. Here, the SHT sample at -12°C exhibited a magnetostress of 13.5MPa/T and the SHT + 600°C 30min sample at 18°C, 12.8MPa/T. The difference between the magnetostress capabilities can be attributed to differences in the CC slopes in Fig. 7-3. More work is needed to identify the influence the temperature-field dependence of magnetostress.

In Eqn. (1.8), the elastic energy stored across the stress-induced transformation influences the shape memory behavior. As such, the austenite moduli of elasticity, E^A, were extracted from each superelastic test in the Appendix, Fig. 7-1, and 7-2, in an attempt to determine its field-temperature dependence. The E^A is plotted in Figs. 7-5a and b for the SHT and SHT + 600°C 30min cases, respectively, as a function of $T - M_s^H$. Here, T was the superelastic test temperature and M_s^H is the M_s temperature under field, H, which was identified by a linear extrapolation of the phase diagram lines in Fig. 7-3 to a critical stress of 0.

Although no clear trend is observed in either of the graphs for the field dependence on the E^A, a temperature dependence can be clearly seen. Temperatures much higher than M_s^H are accompanied with elastic hardening of austenite. To make this clear, all of the data points from Fig. 7-5 were plotted on a single graph as shown in Fig. 7-6.

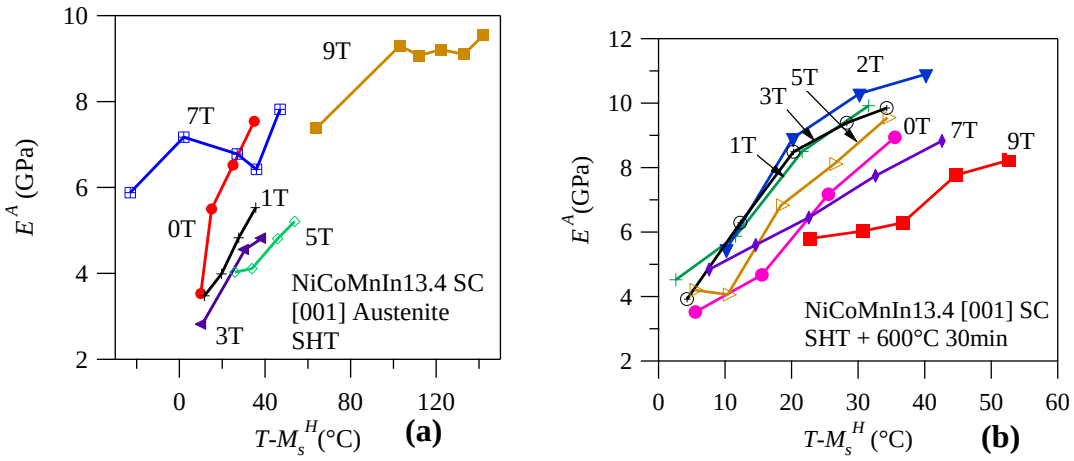

Figure 7-5: The elastic moduli if austenite in SHT (a) and SHT + 600°C 30min (b) $Ni_{45}Co_5Mn_{36.6}In_{13.4}$ single crystals in the [001] austenite direction as a function of temperature away from M_s^H .

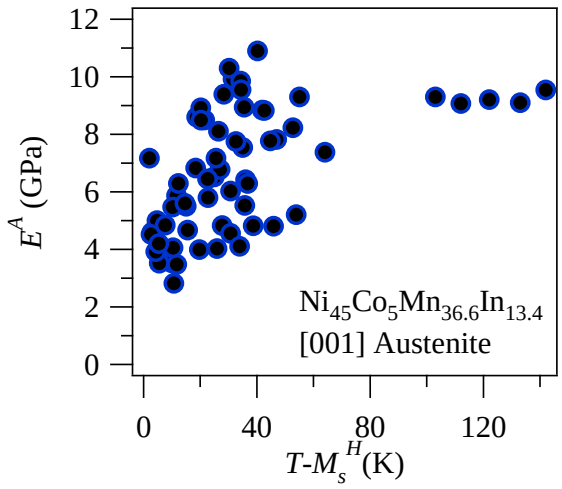

Figure 7-6: The elastic moduli if austenite in $Ni_{45}Co_5Mn_{36.6}In_{13.4}$ single crystals in the [001] austenite direction as a function of temperature away from M_s^H .

As shown in Fig. 7-6, approaching the M_s^H temperature is accompanied by elastic softening in austenite to nearly 4GPa or less. At temperatures 40K above the M_s^H temperatures, austenite exhibits an E^A of nearly 8-10GPa. This has been well documented [84], and has been related to the softening of phonons at the point of the transformation, mentioned earlier. More superelastic tests need to be performed to identify the influence of the E^A on the martensitic transformation characteristics.

Finally, the field-temperature dependence of mechanical dissipation was investigated. The areas of the stress-strain hysteresis loops (mechanical dissipation) were extracted from the data in the Appendix using a MATLAB script and IGOR integration software. The dissipation was computed using an expression similar to Eqn. (6.1). The mechanical dissipation was then plotted as a function of applied strain level and that corresponding to 6% applied strain was extracted for each superelastic test.

In Figure 7-7a and b, the dissipation at 6% applied strain is plotted for each field level and temperature in the SHT and SHT + 600°C 30min samples, respectively.

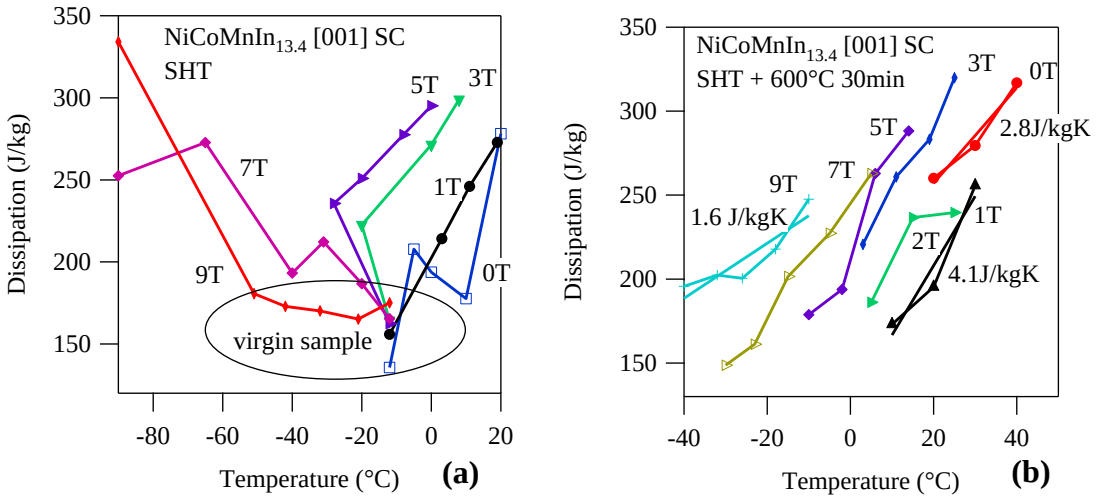

Figure 7-7: The mechanical dissipation from 6% applied strain in SHT (a) and SHT + 600°C 30min (b) $Ni_{45}Co_5Mn_{36.6}In_{13.4}$ single crystals compressed in the [001] austenite direction.

Interestingly, the SHT case (7-7a) exhibited small dissipation in a virgin sample. Subsequent training from repeated mechanical cycling increased the dissipation levels. In the SHT + 600°C 30min case, the sample exhibited larger dissipation losses over a majority of the test temperatures and field levels. From Fig. 7-7b, it can be seen that perhaps increasing the field levels corresponds to a decrease in dissipation, however, more data points are needed to corroborate the current data set. Additional tests will be performed to identify the influence of mechanical training on the dissipation resulting from superelastic loading.

To demonstrate the mechanical stability of the $Ni_{45}Co_5Mn_{36.6}In_{13.4}$ single crystals, superelastic cycling to different strain levels was performed at room temperature in the SHT + 600°C 30min sample under 0.01T. The stress - strain and magnetization - stress responses are shown in Figure 7-8a and b, respectively. Clearly, larger applied strain levels

correspond to larger stress hysteresis widths and greater degrees of transformation hardening. The stress hysteresis width at 4% applied strain was plotted as a function of compression strain in Fig. 7-8c.

At 2% applied strain the sample exhibits a stress hysteresis of only 20MPa, similar to the SHT case plotted in in Fig. 7-1. Upon reaching higher levels of strain up to 7%, the stress hysteresis doubles. Additionally, mechanical unloading at room temperature from higher applied strain levels was accompanied with irrecoverable strain, thus indicating the generation of plastic deformation during the stress-induced martensitic transformation. Due to the clear spread in the stress level at the finish of the M to A transition, σ^{A_f}, that results from different applied strain levels, the superelastic data from these tests could not yield reliable results to construct the σ^{A_f} vs. temperature phase diagrams. More superelastic data are needed on mechanically trained and untrained specimens to fully understand the field-temperature dependence of mechanical dissipation and stability of the superelastic response.

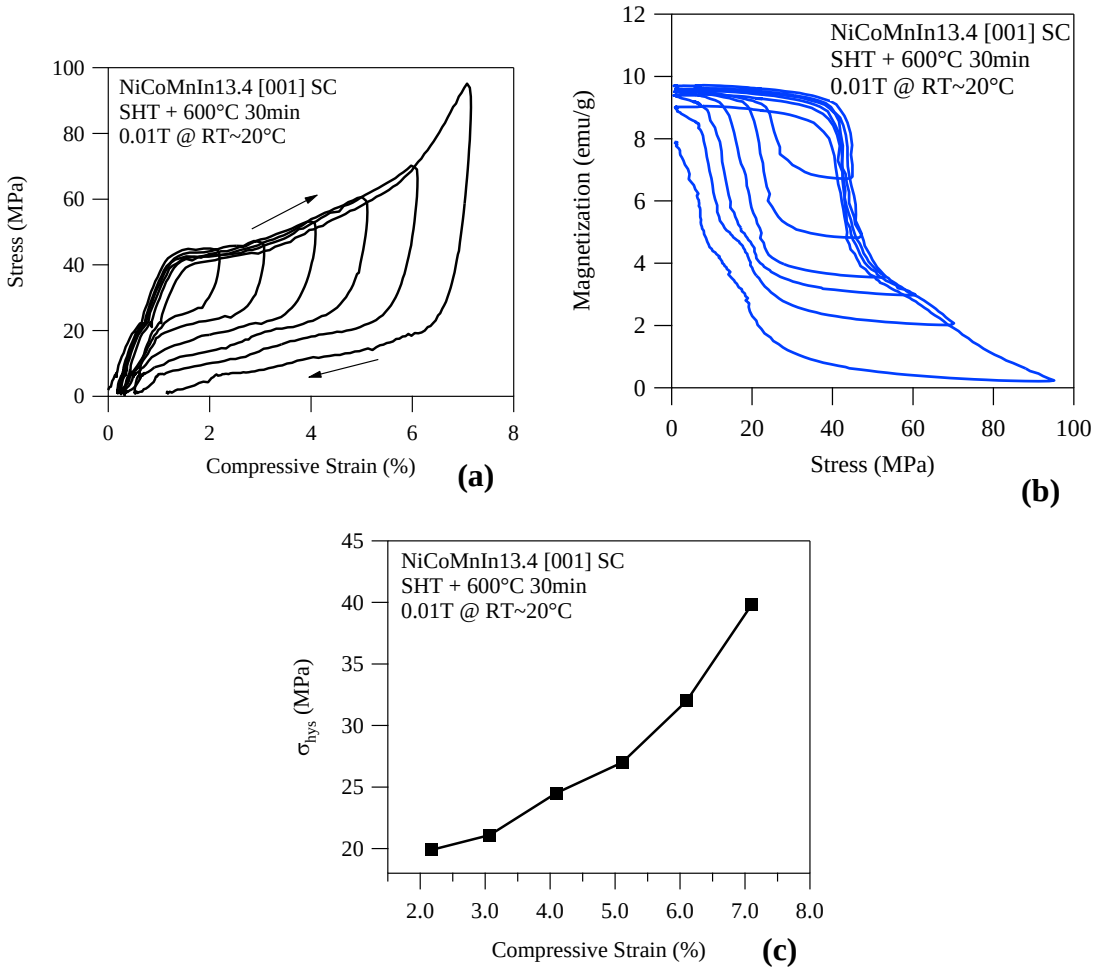

Figure 7-8: The stress-strain (a), magnetization-stress (b), and mechanical hysteresis versus compressive strain (c) responses of a SHT + 600°C 30min $Ni_{45}Co_5Mn_{36.6}In_{13.4}$ single crystal at room temperature under 0.01T.

In Chapter 1, superelasticity was explained using Eqn. (1.8) and Figure 1-4a. Here, we attempt to determine the cause of the non-linearity and field dependence in the CC slope shown in Fig. 7-3. For the discussion, the temperature-magnetic field dependence of each term of Eqn. (1.8) is discussed. Using a simple mathematical derivation, the mechanical CC slope shown in Fig. 7-3 can be quantified. It is well known that the first

term in Eqn. (1.8) is simply the difference between G^A and G^M at temperatures away from T_0. The second term can be defined as [85]

$$\Delta E_{mech} = \sigma_{cr}\varepsilon_{tr}, \tag{7.1}$$

where σ_{cr} is the critical stress at the onset of the A to M transformation and ε_{tr} is the transformation strain. The third term is the elastic energy stored across the martensite transition and can be approximated as [62]

$$\Delta G_{el}^{A\to M} = \frac{1}{2}V_0\mu\varepsilon_{tr}^2 \tag{7.2}$$

where V_0 is the molar volume and μ is the shear modulus. The shear modulus is directly proportional to the modulus of elasticity, E^A.

The fourth term in Eqn. (1.8) is the mechanical dissipation for each compression sample, discussed here, and was plotted Figs. 7-7a and b. Finally, the fifth term is the difference in magnetic Zeeman energy, and is defined as

$$\Delta G_{mag}^{A\to M} = \Delta M^{A\to M}\cdot H, \tag{7.3}$$

where $\Delta M^{A\to M}$ is the difference in magnetization between A and M phases, and H is the applied field. Eqn. (7.3) is the magnetic analog to Eqn. (7.1). Term 6 in Eqn. (1.8) is neglected as it is expected to be small in the cubic austenite phase.

Substituting Eqns. (7.1) – (7.3) into Eqn. (1.8) at $T = T_0$ results in $\Delta G_{ch} = 0$ and

$$0 = -\sigma_{cr}\varepsilon_{tr} + \frac{1}{2}V_0\mu\varepsilon_{tr}^2 + \Delta E_{irr} + \Delta M^{A\to M}\cdot H, \tag{7.4}$$

where the critical stress, σ_{cr}, can be explicitly solved as

$$\sigma_{cr} = \frac{\frac{1}{2}V_0 \mu \varepsilon_{tr}^2 + \Delta E_{irr} + \Delta M^{A\to M} \cdot H}{\varepsilon_{tr}}. \tag{7.5}$$

Differentiating Eqn. (7.5) with respect to temperature and assuming each term exhibits a temperature dependence leads to

$$\frac{d\sigma_{cr}}{dT} = \frac{d}{dT}\left(\frac{\frac{1}{2}V_0 \mu \varepsilon_{tr}^2 + \Delta E_{irr} + \Delta M^{A\to M} \cdot H}{\varepsilon_{tr}}\right), \tag{7.6}$$

which then simplifies to

$$\frac{d\sigma_{cr}}{dT} = \frac{d\left(V_0 \mu \varepsilon_{tr}\right)}{2dT} + \frac{d\Delta E_{irr}}{\varepsilon_{tr} dT} + \frac{d\left(\Delta M^{A\to M} \cdot H\right)}{\varepsilon_{tr} dT}. \tag{7.7}$$

Equation (7.7) demonstrates that the mechanical Clausius-Clapeyron slopes, in Fig. 7-3, are dependent on the temperature derivatives of the shear modulus and transformation strain, dissipation across the transition, and the magnetic Zeeman energy. Assuming the $\Delta M^{A\to M}$ and ε_{tr} are independent of temperature well below the magnetic Curie point of austenite, Eqn. (7.7) reduces to

$$\frac{d\sigma_{cr}}{dT} = \varepsilon_{tr}\frac{d\left(V_0 \mu\right)}{2dT} + \frac{d\Delta E_{irr}}{\varepsilon_{tr} dT} + \frac{\Delta M^{A\to M}}{\varepsilon_{tr}}\frac{dH}{dT}. \tag{7.8}$$

In the following sections, the temperature and field dependence of each term is investigated.

Term 1; the influence of the austenite elastic modulus

In Fig. 7-6, it was demonstrated that when temperatures were elevated beyond M_s^H, the E^A increased. As such, the temperature derivative of the elastic energy term in

Eqn. (7.8) is positive. It is believed that at lower temperatures the E^A is smaller, and therefore this term is reduced. This ultimately reduces the $\frac{d\sigma_{cr}}{dT}$. Nevertheless, more data points with less experimental scatter are needed to identify the influence of magnetic field, rather than temperature, on the first term of Eqn. (7.8).

Term 2; the influence of dissipation

Similarly, the temperature dependence of the mechanical dissipation increases with increasing temperature as shown in Figs. 7-7a and b. In Fig. 7-7a, mechanical training was observed to influence the stability of the superelastic response, and therefore, more data is needed to accurately define the magnetic field dependence of dissipation on the $\frac{d\sigma_{cr}}{dT}$ slope. At low temperatures, however, the dissipation is observed to decrease in Fig. 7-7b. This would also decrease the $\frac{d\sigma_{cr}}{dT}$ slope as shown in 7.3.

Term 3; the influence of the entropy change

Per Eqn. (2.2), the last term of Eqn. (7.8) is the entropy change across the martensitic transformation, as quantified for the magnetocaloric effect, divided by the transformation strain. As discussed in Chapter 1, the entropy change of the martensitic transformation can be extracted from magnetic data by multiplying $\frac{dH_{cr}}{dT}$ to $\Delta M^{A\rightarrow M}$. To probe at the decrease in $\frac{d\sigma_{cr}}{dT}$, the magnetic phase diagrams were constructed for both heat treatment cases in Figure 7-3 using thermomagnetization data obtained with SQUID magnetometry (see Chapter 2). These phase diagrams are depicted in Fig. 7-9a.

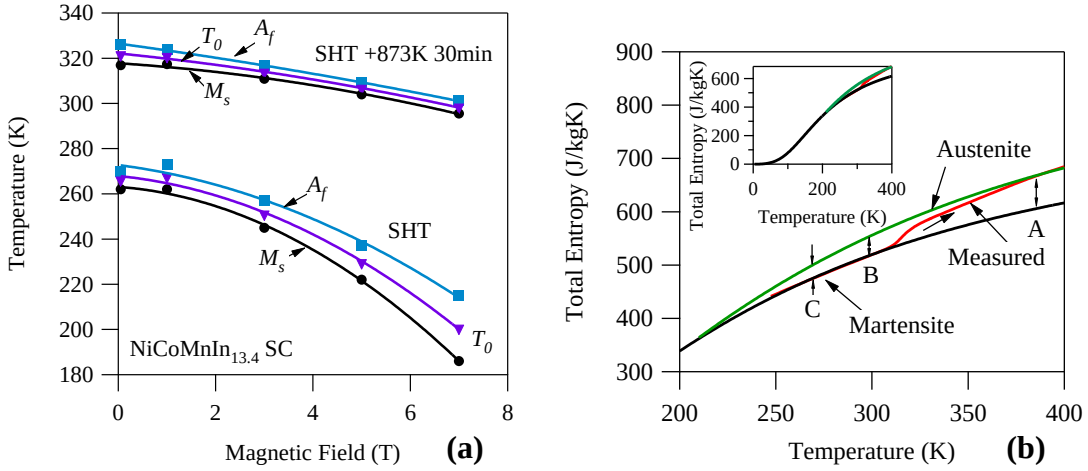

Figure 7-9: The magnetic phase diagram for SHT and SHT + 600°C 30min $Ni_{45}Co_5Mn_{36.6}In_{13.4}$ single crystals (a) and theoretical total entropy versus temperature curves for austenite and martensite phases from 0 to 400K (b).

As shown in Fig. 7-9a, the SHT sample exhibits a strong non-linearity under high fields and low temperatures. Additionally, the thermal hysteresis, defined here as $A_f - M_s$, increases at lower temperatures and high fields. The SQUID magnetometer only permitted measurements up to 7T. In the SHT + 873K 30min case, however, this non-linearity is smaller and the thermal hysteresis remains nearly constant under any field level. The data in Fig. 7-9a suggest that under higher field levels, the transition takes place at lower temperatures, as expected. At low temperatures, the $\frac{dH_{cr}}{dT}$ decreases. Per Eqn. (7.8), the decrease in $\frac{dH_{cr}}{dT}$ results in a decrease in $\frac{d\sigma_{cr}}{dT}$.

To explain why both $\frac{dH_{cr}}{dT}$ and $\frac{d\sigma_{cr}}{dT}$ decrease, Eqn. (2.2) and Fig. 7-9b need to be considered. In Fig. 7-9b, the approximate total entropy curves for martensite and

austenite phases are plotted as predicted with the Debye model. The measured total entropy on heating across the martensitic transition, in a SHT sample, is plotted between the two Debye curves. It is important to note that the Debye model only accounts for the vibrational entropy contribution. The austenite phase was modeled to exhibit a larger Debye temperature than martensite, resulting in a difference in total entropy between the two phases at elevated temperatures. The martensitic transformation is indicated on the plot with the measured heating curve. Note, Eqn. (2.2) is used for computing the entropy difference between M and A phases as depicted by the curves in Fig. 7-9b.

At lower temperatures (points $A \rightarrow B \rightarrow C$), the entropy difference between A and M phases decreases. It is believed that at lower temperatures, the entropy of each phase converges at some temperature. At lower temperatures, the entropy difference between the M and A phases tend to decrease and is currently not fully understood. Ultimately, applying magnetic fields to a MMSMA decreases the temperature at which the transformation occurs. This decrease in T_0 , in turn, results in a decrease in $\Delta S^{A \rightarrow M}$ as described by Eqn. (2.2). If the transformation strain remains nearly constant, as was demonstrated by the superelastic curves, herein, the decrease in $\Delta S^{A \rightarrow M}$ must result in a decrease in $\frac{d\sigma_{cr}}{dT}$.

This finding suggests that the NiCoMnIn shape memory alloys that transform at high temperatures will exhibit larger caloric effects than those that transform at low temperatures. The increase in the entropy difference between the two phases is desirable, however, the resulting adiabatic temperature change at higher temperatures may be

reduced compared to those that transform at low temperatures simply due to the elevated heat capacity (see Eqn. (1.34)). Nevertheless, NiCoMnIn single crystals are capable of exhibiting a giant caloric effect near, or away from room temperature, and the specific heat capacity within this temperature range varies between 325-450J/kgK, as shown in Fig. 5-19b. The adiabatic temperature changes computed in Fig. 5-21a demonstrate that the SHT or SHT + 600°C 30min alloys will exhibit between 6-8K temperature changes upon a complete transformation.

In conclusion, the magnetic field and temperature dependence of each of the terms in Eqn. (1.8) on the mechanical Clausius-Clapeyron slope was investigated. The influence of temperature on dissipation and elastic modulus of austenite was clearly determined, however the magnetic field dependence still remains unclear. The decrease in the mechanical CC slope was attributed to the decrease in entropy difference between M and A phases at low temperatures, thus indicating transforming MMSMAs at higher temperatures will result in a larger caloric effect. Unfortunately, higher temperatures also result in higher mechanical dissipation. Further studies will be performed to identify if dissipation can be reduced under high magnetic field levels.

The next section demonstrates the stress-assisted magnetic field induced transformation (SAMFIT) in $Ni_{45}Co_5Mn_{36.6}In_{13.4}$ [001] single crystals. The stress-temperature-field space was selected for these measurements considering the above discussions and data. Temperatures near $M_s^{H=0}$ were employed to minimize hysteresis and dissipation losses. Additionally, the required mechanical forces and magnetic fields are minimal nearest to this temperature. The SHT + 600°C 30min sample exhibited a higher

transformation temperature, and therefore a higher entropy change than the SHT sample. In the following section, both heat treatments are subject to mixed loading conditions to measure their multiferroic responses across SAMFITs.

7.3 The stress-assisted magnetocaloric effect

In the above section, the temperature-field space was identified where mixed loading conditions would be the most effective at minimizing both stress and field requirements while maintaining a high degree of entropy change. In this section, the martensitic transition in the $Ni_{45}Co_5Mn_{36.6}In_{13.4}$ [001] single crystals is triggered using a magnetic field. However, uniaxial stress is not held constant between forward and reverse transformations. This is known as stress-assisted magnetic field induced transformation. Here, the process is demonstrated in SHT and SHT + 600°C 30min heat treated single crystals.

Figure 7-10a demonstrates the stress and magnetic field history applied to a $Ni_{45}Co_5Mn_{36.6}In_{13.4}$ SHT + 600°C 30min compression specimen during a stress-assisted magnetic field induced transition (SAMFIT). At time $t = 0$, the sample is uniaxially preloaded along the [001] austenite direction up to approximately 52MPa (see point 1) under 0T. Next, the mechanical load is decreased to 30MPa from point 1 to point 2. This stress level equals that which the sample will transform from the M phase back to the A phase at 18°C, i.e. the $\sigma^{A_s}_{T=18^\circ C}$. While the stress is held constant at 30MPa, the magnetic field is ramped from 0T to 3T as illustrated from point 2 to 3. After reaching 3T, the field is held constant, and the mechanical load is increased again to 52MPa (point 3-4). While the stress is held constant at 52MPa, the field is discharged to 0T. This is illustrated from

point 4 to 5. This process can be repeated cyclically. For cyclic operation, the loading illustrated through points 2-5 should be repeated.

Figure 7-10b is the measured stress-strain response resulting from the loading path detailed in Fig. 7-10a. Numbered points in 7-10b correspond to the same stress-field state in 7-10a. Interestingly, loading the MMSMA in this way does not lead to a notable decrease in the mechanical hysteresis. Careful inspection of Fig. 7-10b indicates that the M to A transformation results from applying the magnetic field (MFIT), and the A to M transformation is driven by removing the magnetic field. As shown in Fig. 7-10b, nearly 6% transformation strain is achieved by applying 3T to the mechanically pre-loaded MMSMA specimen.

The compressive strain versus applied magnetic field is plotted in Figure 7-10c. Again, the points are labeled corresponding to the loading in 7-10a. In 7-10c, nearly 6% transformation strain is achieved by applying 3T to the MMSMA. Under 2T, only 3.5% transformation strain is reached. Using these strains with Eqn. (2.5), assuming a mass density of 8000kg/m^3, and the $\frac{d\sigma_{cr}}{dT}$ in Fig. 7-3b (3.1MPa/K), the entropy change is computed to be 23J/kgK and 13.5J/kgK, respectively. The entropy change of 23J/kgK matches those reported in Fig. 6-15a for magnetic fields up to 7T. It seems that with only 3T, employing stress-assisted transformations lends the ability to completely transform the MMSMA under reduced field levels.

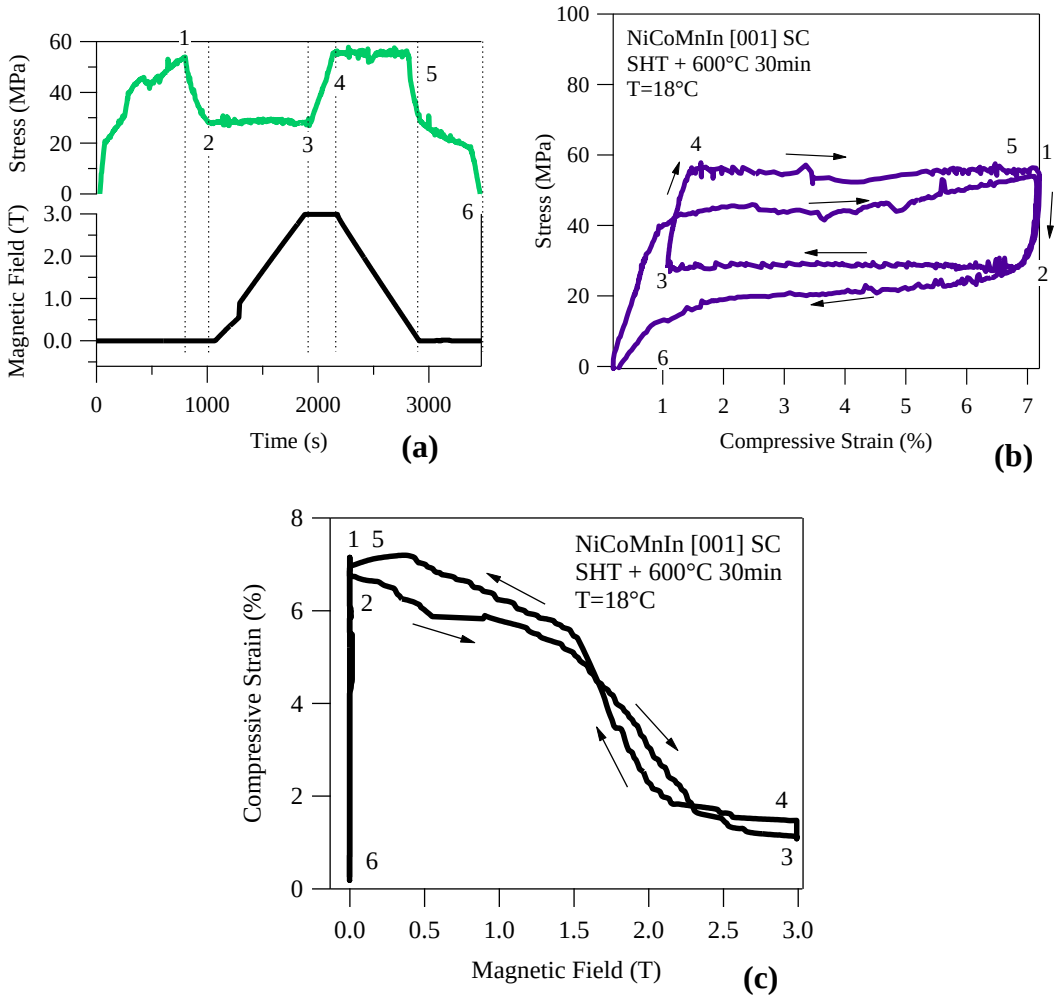

Figure 7-10: The stress and magnetic field loading history (a), stress-strain response (b) and strain-magnetic field response (c) across a stress-assisted magnetic field induced transformation in $Ni_{45}Co_5Mn_{36.6}In_{13.4}$ single crystals in the [001] austenite direction.

In Fig. 7-11a, the magnetic field induced strain is plotted for the same single crystal while a constant 52MPa was loaded on the sample during applying and releasing the field. On the same graph, the data from Fig. 7-10c is shown. In the case of the constant mechanical load, the magnetic field hysteresis is nearly 4T. If mixed loading conditions are employed, as illustrated in Fig. 7-10a, the magnetic field hysteresis is reduced to nearly

zero. Additionally, the same transformation strain is achieved no matter the loading sequence, i.e. if mechanical stress is held constant or changes mid-cycle. Clearly, the benefit of employing mixed loading sequences on MMSMA is the reduction of required magnetic field to complete the martensitic transformation.

Since the cyclic repeatability of steps 2-5 illustrated in Figure 7-10a are required in refrigeration processes, 5 cycles were carried out on the same compression sample to identify if the MMSMA specimen could perform consistently under multiple cycles. The cyclic tests were only performed up to 2T because this field level can be generated by permanent magnets and the test is more representative of application. The stress-strain data for the 5 cycles are plotted in Figure 7-11b. The pre-cycle compression test (red curve) was performed to identify the critical stresses for cycling the fields. Next, the sample was mechanically preloaded to a stress-induced martensite state and then unloaded to the $\sigma^{A_s}_{T=18^\circ C}$ state. The stress and field were then cycled as described above and the stress-strain data were recorded. The numbers overlaid on the data in 7-11b indicate the cycle number of the stress-strain history.

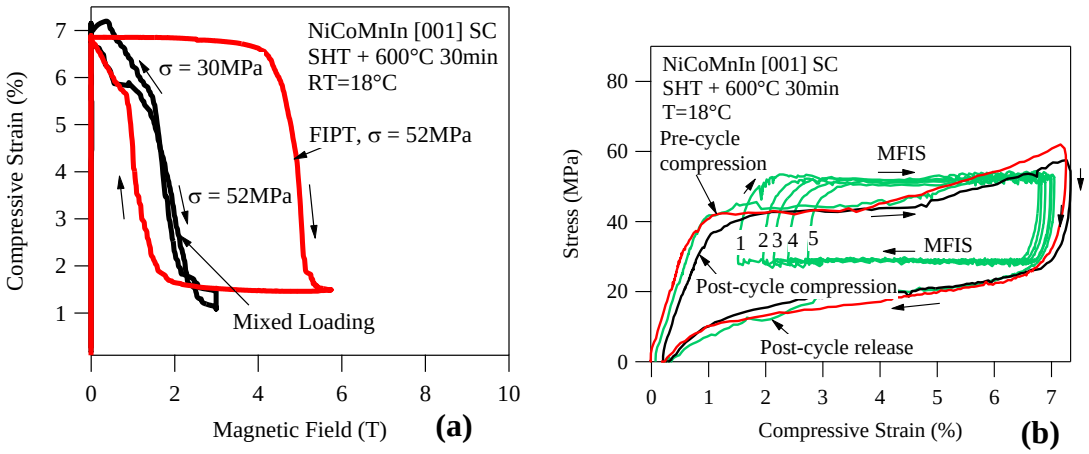

Figure 7-11: The strain versus magnetic field in SHT + 600°C 30min $Ni_{45}Co_5Mn_{36.6}In_{13.4}$ single crystals in the [001] austenite direction for MFIT and SAMFIT(a), and the stress-strain response from SAMFIT cycling (b).

Over the course of 5 cycles, the magnetic field induced strain (MFIS) decreased from 5.14% to 4.1%. More cycles were not carried out due to the length of time required for such cycling. It is believed that eventually the MFIS would reach an equilibrium value as the sample was trained from the loading sequence. Mechanical training in these alloys tends to increase the transformation hardening and, therefore, less MFIS is achieved. Smaller MFISs were generated with field cycling due to the mechanical instability of the single crystals. More work is needed to verify the influence of temperature and strain level on the mechanical instability.

Nevertheless, achieving 4% transformation strain under a cyclic 2T is significant. To demonstrate the maximum potential of the NiCoMnIn single crystals, a virgin (untrained) SHT sample was tested up to only 2T under the loading sequence described in Fig. 7-10a. Only one cycle was performed to prevent mechanical training. Figure 7-12a

shows the stress-strain response at -10°C, i.e. the measured A_f temperature of the virgin SHT sample. In this sample, the upper and lower mechanical stresses for SAMFIT were identified to be 35MPa and 17MPa, respectively. The field was only charged to 2T.

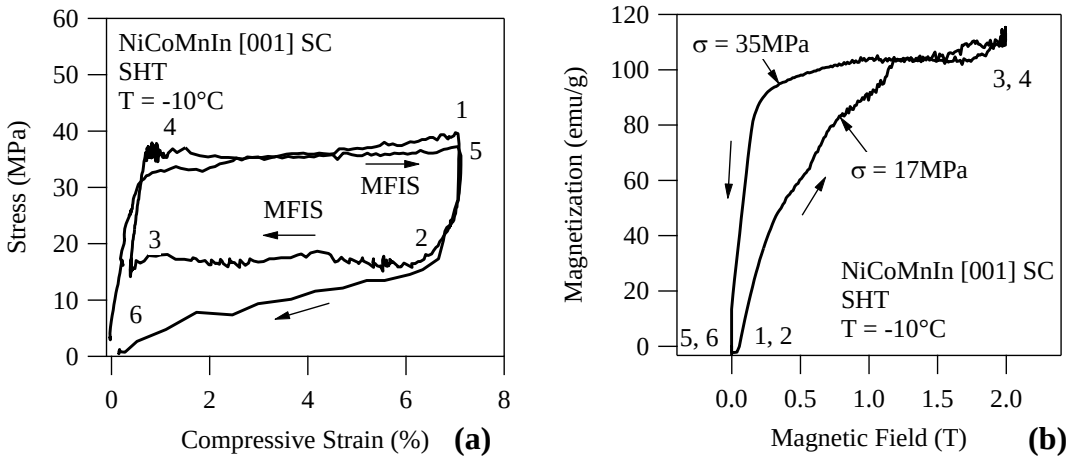

Figure 7-12: The stress-strain response of a SHT $Ni_{45}Co_5Mn_{36.6}In_{13.4}$ single crystal (a) and the measured magnetization response (b) in the [001] austenite direction.

As shown by the stress-strain response in 7-12a, the transformation hardening was small and the stress hysteresis was nearly 18MPa. From point 2 to 3, the NiCoMnIn single crystal transformed completely under 17MPa. The measured magnetization is plotted in Fig. 7-12b which also suggests that the complete transformation took place. Under 2T, the austenite phase should be magnetically saturated, and therefore, 100emu/g is an appropriate magnetization level for a saturated ferromagnetic phase. Amazingly, the complete martensitic transformation was achieved under a magnetic field level as small as 1.3T.

Finally, the compressive strain versus applied magnetic field response is shown in Figure 7-13. Like the magnetic response in Fig. 7-12b, the MFIS reaches a maximum of 5.35% under 1.3T. Unloading the magnetic field under 35MPa (point 4 to 5) did not initiate the A to M transformation until the field was completely reduced to zero. Irrespective of the field level needed to generate the return transition, the SHT virgin NiCoMnIn compression sample was shown to exhibit a complete SAMFIT under a magnetic field of 1.3T. To the author's knowledge, this has never before been experimentally demonstrated and was made possible by the MaTMeCh device.

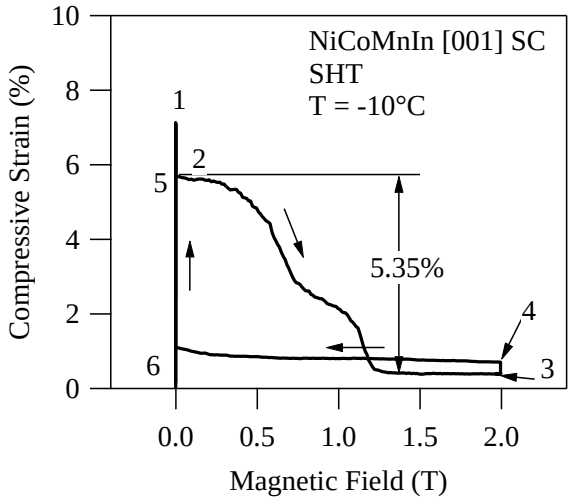

Figure 7-13: The strain versus magnetic field response of a SHT $Ni_{45}Co_5Mn_{36.6}In_{13.4}$ single crystal loaded along the [001] austenite direction. A complete martensitic transformation is demonstrated with magnetic field levels below 1.5T.

In the previous section, 5.35% transformation strain was measured as a result of applying only 1.3T to a NiCoMnIn single crystal. The entropy change corresponding to this SAMFIT can be computed using Eqn. (2.5) with the CC slope in Fig. 7-3a. Under 0-

2T, the CC slope was determined to be 2.2MPa/K. With a computed mass density of 8081kg/m^3, the resulting entropy change is 14.5J/kgK. The MMSMA should cool by nearly 6-8K per Eqn. (1.34). Achieving temperature changes this large by applying only 1.3T is substantial and has never before be realized with these alloys. This capability is better than those exhibited by common rare-earth containing MCE compounds. Additionally, the martensitic transformation in MMSMAs offers a tunable transformation such that a single composition can be employed across a range of temperatures.

In Table 7-1, common magnetocaloric compounds are tabulated alongside their adiabatic temperature changes attainable under 2T at the magnetic Curie temperatures [48]. In the table, Curie temperatures are referred to as 'operating temperatures'. Additionally, the cost to melt 1kg of the magnetocaloric substance is tabulated. Cost was computed by converting the compound composition to wt.% and identifying the mass needed to melt 1kg. The cost was computed with raw pieces or granules with at least 99.9% purity from Alfa-Aesar.com.

As shown by the ΔT_{ad} in Table 7-1, common MCE materials can produce between 2-7K temperature changes at their operating temperature. Their operating temperatures are clearly dependent on composition. Some compounds that exhibit small adiabatic temperature changes are exceedingly expensive. Perhaps the compounds exhibiting low operating temperatures can be employed in cryogenic laboratory applications, and therefore the cost is not a major consideration. When compared to the $Ni_{45}Co_5Mn_{36.6}In_{13.4}$ alloy at the bottom of the table, the potential of employing a MMSMA in solid-state refrigeration applications becomes clear.

Table 7-1: Adiabatic temperature change values (MCE) of various metal compounds from [48] under 2T applied magnetic field and their operating (Curie) temperatures. $Ni_{45}Co_5Mn_{36.6}In_{13.4}$ is appended to the bottom to demonstrate its relative capabilities.

Compound (at.%)	ΔT_{ad} (K)	Operating Temperature (K)	Cost ($/kg)*
$TbAl_2$	2.2	108	22,202
$DyAl_2$	3.6	63.3	4,775
$HoAl_2$	4.6	31	11,559
Gd_3Al_2	2.4	281	5,049
GdZn	3	270	3,995
Gd_3In	2	191	5,400
$DyNi_2$	4	20	3,787
Y_2Fe_{17}	2.3	307	1,332
Lu_2Fe_{17}	0.6	263	40,467
$LaFe_{11.44}Si_{1.56}$	7.5	188	2,250
$TbCo_2$	1.9	231	17,256
$DyCo_2$	4.4	138	3,864
$ErCo_2$	3.2	35	11,050
$Gd_5Si_2Ge_2$	7.4	276	6,376
Gd	4.8	294	5,620
$Ni_{45}Co_5Mn_{36.6}In_{13.4}$	6†	250-350K††	1,218

*Cost was determined from 99.9% pure raw elements on alfa.com using wt.% as computed from at.% given in the table.
†Achieved with 2T under SAMFIT
††Tunable with heat treatment

When comparing NiCoMnIn to an alloy of similar cost, such as Y_2Fe_{17}, Table 7-1 demonstrates that $Ni_{45}Co_5Mn_{36.6}In_{13.4}$ exhibits an advantage in that the operating temperature can be tuned. Similarly, the large ΔT_{ad} in $LaFe_{11.44}Si_{1.56}$ is impressive, however, it will only perform at 188K and is double the cost of $Ni_{45}Co_5Mn_{36.6}In_{13.4}$. Clearly, $Ni_{45}Co_5Mn_{36.6}In_{13.4}$ has the potential to become a competitive candidate for solid-state cooling applications. Without the experimental evidences shown and discussed above, the material's potential would have remained unclear.

For the first time, a complete martensitic transformation was driven in $Ni_{45}Co_5Mn_{36.6}In_{13.4}$ with a magnetic field below 1.3T. Using mechanical loading between field-ramping, the martensitic transformation was shown to be cyclical. When compared to more common non-SMA magnetocaloric compounds, NiCoMnIn exhibits a clear advantage in cost and ability. Unfortunately, experimental evidences suggest that mechanical training hinders the cyclic performance of the alloy. Further studies are underway to identify ways to avoid excessive transformation hardening and the evolution of mechanical hysteresis in these alloys.

7.4 Conclusions

The preceding chapter demonstrated the potential of employing $Ni_{45}Co_5Mn_{36.6}In_{13.4}$ single crystals for near-room temperature refrigeration applications. Mechanical phase diagrams were plotted using superelastic data under various magnetic fields and temperatures. A non-linearity developed in the phase diagram slopes at low temperatures. Using non-equilibrium thermodynamics, different contributions to this non-linear behavior were identified and discussed. The main cause of the non-linearity was determined to be a decrease in the difference between the entropy of austenite and martensite phases at low temperatures. Applying magnetic fields reduced the transformation temperatures, and in turn, reduced the entropy difference between the phases. Nevertheless, further studies are underway to identify the magnetic field dependence of the elastic moduli of austenite, structural dissipation, and elastic energy storage across the transition which all contribute to the thermodynamics surrounding the martensitic transformation.

Finally, a complete first order phase transformation was generated in $Ni_{45}Co_5Mn_{36.6}In_{13.4}$ single crystals for the first time under 1.3T. To achieve the complete transformation, mechanical stress was applied in between field ramping, thus reducing or eliminating magnetic hysteresis. This discovery opens the possibility of a new type of refrigeration system that employs the stress-assisted magnetocaloric effect in magnetic shape memory alloys. Although the mechanical stability of these materials was demonstrated to be somewhat poor, more studies are underway to identify loading sequences that prevent the evolution of transformation hardening and an increase in stress hysteresis. Despite the poor mechanical stability in $Ni_{45}Co_5Mn_{36.6}In_{13.4}$, a comparison between other rare-earth containing MCE refrigerants was made. Clearly, $Ni_{45}Co_5Mn_{36.6}In_{13.4}$ offers advantages over other refrigerants due to their cost, operating temperatures, and adiabatic temperature changes.

CHAPTER VIII

GENERAL CONCLUSIONS AND FUTURE WORK

In the beginning of this work, a completely reversible magnetic field induced transformation in NiCoMnIn single crystals had never before been achieved with a magnetic field below 2T. Different methods of reducing the high magnetic field requirement were initially discussed. They included finding optimum alloy compositions, tuning microstructures with heat treatments, and finally, employing mixed stress and magnetic field loading conditions with the aim of reducing magnetic hysteresis.

With the former, a few thermodynamic frameworks were developed that indicated an increase in relative energy conversion efficiency and refrigeration performance of heat treated alloys. Although the relative energy conversion performances of the shape memory alloys were increased with heat treatments, the alloys were still unable to completely transform under 2T. Nevertheless, a few of these heat treated alloys exhibited substantially reduced dissipative losses across their martensitic transformations which merits further investigation. For example, $Ni_{45}Co_5Mn_{36.6}In_{13.4}$ single crystals were demonstrated to exhibit only 1K thermal hysteresis with carefully selected heat treatments. Additionally, a NiMnIn alloy with only 3K thermal hysteresis was identified. In either of these cases, the alloys maintained a reasonable entropy change from the first order martensitic phase transformation and should be the subject of further studies.

There is still much work to be done to improve and understand the microstructures of meta-magnetic shape memory alloys. It still remains unclear why Co containing alloys exhibit a higher degree of tunability than their non-Co containing counterparts.

Additionally, the arrest behavior in NiMnIn alloys is still not completely understood. Future work should be performed to identify the atomic mobility in these alloys and to build a clearer picture of the time-temperature-transformation dependence of their $L2_1$ to B2 transition.

Different contributions to the free energy around the martensitic transformation were discussed and manipulated with heat treatments. Varying degrees of long range $L2_1$/B2 orders in single crystal $Ni_{45}Co_5Mn_{36.6}In_{13.4}$ were demonstrated to influence the magnetic to thermal energy conversion efficiency. It was determined that a B2 ordered alloy exhibited the highest energy conversion efficiency, and therefore, is most favorable in magnetocaloric applications. With low annealing temperatures, however, it was found that some mixture of $L2_1$ and B2 causes the martensitic transformation to become interrupted. With TEM dark field images, a microstructural contrast difference was observed within $L2_1$ morphology in arrested alloys. Before this work, the contrast differences in the $L2_1$ morphologies had never before been observed.

A common finding in all the work, herein, is that the entropy changes from martensitic transformations decrease when the transformation temperatures are lowered. The physical cause of this decrease is currently not fully understood. In the greater picture, this implies that the shape memory alloys are only suitable for refrigeration within a set temperature interval; their operating temperature can be tuned to occur within this interval via heat treatments. If the M_s temperature is shifted too low, the transformation may become arrested and will not proceed by simple heating/cooling. In order to trigger the

martensitic transformation at low temperatures, mechanical stress can be employed, but the entropy change generated by the martensitic transformation will be small.

A magneto-thermo-mechanical characterization (MaTMeCh) device was developed, herein, to probe at the multiferroic couplings in NiCoMnIn single crystals. This device offered the capability of simultaneously measuring compressive strain, stress, temperature, and the average magnetization within a longitudinally magnetized shape memory alloy specimen. These measurements were the first of their kind up to 9T while down to -90°C. Additionally, the capabilities of the test rig facilitated cyclic stress-assisted magnetic field induced transformations. The results ultimately lead to a complete martensitic transformation under 1.3T.

The MaTMeCh device facilitated data acquisition with the potential to change the way scientists and engineers think about solid-state refrigeration. A cost analysis of some common magnetocaloric refrigerants was performed, and when compared to that of NiCoMnIn, the shape memory alloy was shown to offer the same temperature change of more expensive compounds. In addition, the operating temperature of a single composition in NiCoMnIn can be tuned to occur at any temperature within an interval of nearly 100K. Currently, the author is developing a stress-assisted magnetocaloric refrigeration device that employs this new technology.

Although the complete transition in NiCoMnIn single crystals can be driven with magnetic fields below 2T, the magnetic field dependence of the transformation hardening, austenite modulus of elasticity, and dissipation across the martensitic transition are still

not completely understood. Further investigations are currently underway with the MaTMeCh device to identify the field dependence of these materials parameters.

REFERENCES

[1] P.P. Weiss, A. Le phenomene magnetocalorique, Journal of Physics (Paris) 5 (1917) 6.

[2] A. Smith, Who discovered the magnetocaloric effect?, European Physical Journal H 38 (2013) 507-517.

[3] P. Debye, Some observations on magnetisation at a low temperature, Ann Phys-Berlin 81 (1926) 1154-1160.

[4] W.F. Giauque, A thermodynamic treatment of certain magnetic effects. A proposed method of producing temperatures considerably below, 1° absolute, J Am Chem Soc 49 (1927) 1864-1870.

[5] M.J. Molina and F.S. Rowland, Stratospheric sink for chlorofluoromethanes - chlorine atomic-catalysed destruction of ozone, Nature 249 (1974) 810-812.

[6] The montreal protocol on substances that deplete the ozone layer, www.epa.gov/ozone/intpol/ (2015).

[7] V.K. Pecharsky and K.A. Gschneidner, Giant magnetocaloric effect in Gd-5(Si2Ge2), Phys Rev Lett 78 (1997) 4494-4497.

[8] C. Zimm, A. Jastrab, A. Sternberg, V. Pecharsky, K. Gschneidner, M. Osborne, I. Anderson, Description and performance of a near-room temperature magnetic refrigerator, Adv Cryog Eng 43 (1998) 1759-1766.

[9] R. Kainuma, Y. Imano, W. Ito, Y. Sutou, H. Morito, S. Okamoto, O. Kitakami, K. Oikawa, A. Fujita, T. Kanomata, K. Ishida, Magnetic-field-induced shape recovery by reverse phase transformation, Nature 439 (2006) 957-960.

[10] E. Bonnot, R. Romero, L. Manosa, E. Vives, A. Planes, Elastocaloric effect associated with the martensitic transition in shape-memory alloys, Phys Rev Lett 100 (2008) 125901.

[11] E. Warburg, Magnetische Untersuchungen, Ann der Physik 8 (1881) 141-164.

[12] M.E. Wood and W.H. Potter, General-analysis of magnetic refrigeration and its optimization using a new concept - Maximization of refrigerant capacity, Cryogenics 25 (1985) 667-683.

[13] L.C. Chang and T.A. Read, Trans. of the Amer Inst of Mining, Metall and Pet Eng 189 (1951) 47.

[14] W.J. Buehler, R.C. Wiley, J.V. Gilfrich, Effect of low-temperature phase changes on mechanical properties of alloys near composition TiNi, J Appl Phys 34 (1963) 1475.

[15] K. Otsuka and C.M. Wayman, Shape memory materials, Cambridge University Press, Cambridge; New York, 1998.

[16] R.T. DeHoff, Thermodynamics in materials science, 2nd Ed., Taylor & Francis Group, Boca Raton, 2006.

[17] J. Ortin and A. Planes, Thermodynamic analysis of thermal measurements in thermoelastic martensitic transformations, Acta Metall Mater 36 (1988) 1873-1889.

[18] H.E. Karaca, I. Karaman, B. Basaran, Y. Ren, Y.I. Chumlyakov, H.J. Maier, Magnetic field-induced phase transformation in NiMnColn magnetic shape-memory alloys-A new actuation mechanism with large work output, Adv Funct Mater 19 (2009) 983-998.

[19] B. Kiefer, D.C. Lagoudas, Magnetic field-induced martensitic variant reorientation in magnetic shape memory alloys, Philos Mag 85 (2005) 4289-4329.

[20] R.C. O'Handley, S.J. Murray, M. Marioni, H. Nembach, S.M. Allen, Phenomenology of giant magnetic-field-induced strain in ferromagnetic shape-memory materials, J Appl Phys 87 (2000) 4712-4717.

[21] J. Liu, K. Skokov, O. Gutfleisch, Magnetostructural transition and adiabatic temperature change in Mn-Co-Ge magnetic refrigerants, Scripta Mater 66 (2012) 642-645.

[22] W. Zhu, E.K. Liu, L. Feng, X.D. Tang, J.L. Chen, G.H. Wu, H.Y. Liu, F.B. Meng, H.Z. Luo, Magnetic-field-induced transformation in FeMnGa alloys, Appl Phys Lett 95 (2009) 222512.

[23] E.M. Fernald, Elements of thermodynamics, with special reference to applications in engineering. 2d ed., McGraw-Hill Book Company, inc., New York and London, (1938).

[24] C. Truesdell, U.S. Naval Research Laboratory, (1949).

[25] S. Gama, A.A. Coelho, A. de Campos, A.M.G. Carvalho, F.C.G. Gandra, P.J. von Ranke, N.A. de Oliveira, Pressure-induced colossal magnetocaloric effect in MnAs, Phys Rev Lett 93 (2004) 237202.

[26] G. Porcari, S. Fabbrici, C. Pernechele, F. Albertini, M. Buzzi, A. Paoluzi, J. Kamarad, Z. Arnold, M. Solzi, Reverse magnetostructural transformation and adiabatic temperature change in Co- and In-substituted Ni-Mn-Ga alloys, Phys Rev B 85 (2012) 024414.

[27] J. Liu, T. Gottschall, K.P. Skokov, J.D. Moore, O. Gutfleisch, Giant magnetocaloric effect driven by structural transitions, Nat Mater 11 (2012) 620-626.

[28] I. Titov, M. Acet, M. Farle, D. Gonzalez-Alonso, L. Manosa, A. Planes, T. Krenke, Hysteresis effects in the inverse magnetocaloric effect in martensitic Ni-Mn-In and Ni-Mn-Sn, J Appl Phys 112 (2012) 073914.

[29] Y.J. Huang, Q.D. Hu, N. Bruno, I. Karaman, J.G. Li, Influence of grain boundary on pseudoelasticity in highly-oriented polycrystalline Ni52Fe17Ga27Co4 ferromagnetic shape memory alloy, Mater Lett 114 (2014) 11-14.

[30] A. Planes, L. Manosa, M. Acet, Magnetocaloric effect and its relation to shape-memory properties in ferromagnetic Heusler alloys, J Phys-Condens Mat 21 (2009) 233201.

[31] A.K. Ugural, Advanced and applied elasticity. 4th ed., Pearson Education, Castleton, NY, 2003.

[32] E.E. Timofeeva, E.Y. Panchenko, Y.I. Chumlyakov, H. Maier, Development of thermoelastic martensitic transformations in ferromagnetic [011]-oriented NiFeGa single crystals in compression, Russian Physics Journal 54 (2012) 1427-1430.

[33] S.Y. Yu, Z.H. Liu, G.D. Liu, J.L. Chen, Z.X. Cao, G.H. Wu, B. Zhang, X.X. Zhang, Large magnetoresistance in single-crystalline Ni50Mn50-xInx alloys (x=14-16) upon martensitic transformation, Appl Phys Lett 89 (2006) 162503.

[34] B.M. Wang, Y. Liu, L. Wang, S.L. Huang, Y. Zhao, Y. Yang, H. Zhang, Exchange bias and its training effect in the martensitic state of bulk polycrystalline Ni49.5Mn34.5In16, J Appl Phys 104 (2008) 043916.

[35] X.B. Ren, Strain glass and ferroic glass - Unusual properties from glassy nano-domains, Phys Status Solidi B 251 (2014) 1982-1992.

[36] T.W. Shield, Magnetomechanical testing machine for ferromagnetic shape-memory alloys, Rev Sci Instrum 74 (2003) 4077-4088.

[37] K. Haldar, D.C. Lagoudas, I. Karaman, Magnetic field-induced martensitic phase transformation in magnetic shape memory alloys: Modeling and experiments, J Mech Phys Solids 69 (2014) 33-66.

[38] N.M. Bruno, C. Ciocanel, H.P. Feigenbaum, A. Waldauer, A theoretical and experimental investigation of power harvesting using the NiMnGa martensite reorientation mechanism, Smart Mater Struct 21 (2012) 094018.

[39] T. Krenke, M. Acet, E.F. Wassermann, X. Moya, L. Manosa, A. Planes, Martensitic transitions and the nature of ferromagnetism in the austenitic and martensitic states of Ni-Mn-Sn alloys, Phys Rev B 72 (2005) 014412.

[40] V. Srivastava, X.A. Chen, R.D. James, Hysteresis and unusual magnetic properties in the singular Heusler alloy Ni45Co5Mn40Sn10, Appl Phys Lett 97 (2010) 014101.

[41] Y. Chumlyakov, E. Panchenko, I. Kireeva, I. Karaman, H. Sehitoglu, H.J. Maier, A. Tverdokhlebova, A. Ovsyannikov, Orientation dependence and tension/compression asymmetry of shape memory effect and superelasticity in ferromagnetic Co40Ni33Al27, Co49Ni21Ga30 and Ni54Fe19Ga27 single crystals, Mat Sci Eng a-Struct 481 (2008) 95-100.

[42] P.J. Shamberger, F.S. Ohuchi, Hysteresis of the martensitic phase transition in magnetocaloric-effect Ni-Mn-Sn alloys, Phys Rev B 79 (2009) 144407.

[43] R.D. James, K.F. Hane, Martensitic transformations and shape-memory materials, Acta Mater 48 (2000) 197-222.

[44] D.X. Chen, E. Pardo, A. Sanchez, Demagnetizing factors of rectangular prisms and ellipsoids, IEEE T Magn 38 (2002) 1742-1752.

[45] M. Acet, E.F. Wassermann, Magnetic Interactions in Ni-Mn-Based Magnetic Shape-Memory Heusler Alloys, Adv Eng Mater 14 (2012) 523-529.

[46] V. Recarte, J.I. Perez-Landazabal, V. Sanchez-Alarcos, J.A. Rodriguez-Velamazan, Dependence of the martensitic transformation and magnetic transition on the atomic order in Ni-Mn-In metamagnetic shape memory alloys, Acta Mater 60 (2012) 1937-1945.

[47] B.F. Lu, F. Xiao, A. Yan, J. Liu, Elastocaloric effect in a textured polycrystalline Ni-Mn-In-Co metamagnetic shape memory alloy, Appl Phys Lett 105 (2014) 161905.

[48] A.M. Spichkin, Y.I. Tishin, The magnetocaloric effect and its applications, Instit of Phys Pub, Bristol and Philadelphia, (2003).

[49] K.A. Gschneidner, V.K. Pecharsky, Magnetocaloric materials, Annu Rev Mater Sci 30 (2000) 387-429.

[50] N.M. Bruno, C. Yegin, I. Karaman, J.H. Chen, J.H. Ross, J. Liu, J.G. Li. The effect of heat treatments on Ni43Mn42Co4Sn11 meta-magnetic shape memory alloys for magnetic refrigeration, Acta Mater 74 (2014) 66-84.

[51] V. Recarte, J.I. Perez-Landazabal, S. Kustov, E. Cesari, Entropy change linked to the magnetic field induced martensitic transformation in a Ni-Mn-In-Co shape memory alloy, J Appl Phys 107 (2010) 053501.

[52] X. Moya, A. Planes, S. Aksoy, M. Acet, E.F. Wassermann, T. Krenke, Phys Rev B 75 (2007) 184412.

[53] F. Guillou, H. Yibole, G. Porcari, L. Zhang, N.H. van Dijk, E. Bruck, Magnetocaloric effect, cyclability and coefficient of refrigerant performance in the MnFe(P, Si, B) system, J Appl Phys 116 (2014) 063903.

[54] A. Planes, J. Vinals, V. Torra, Effect of atomic order on a martensitic-transformation, Philos Mag A 48 (1983) 501-508.

[55] E. Castan, E. Vives, L. Manosa, A. Planes, A. Saxena, Disorder in magnetic and structural transitions: pretransitional phenomena and kinetics, Mag and Struct in Funct Mater 79 (2005) 27-48.

[56] I. Takeuchi, O.O. Famodu, J.C. Read, M.A. Aronova, K.S. Chang, C. Craciunescu, S.E. Lofland, M. Wuttig, F.C. Wellstood, L. Knauss, A. Orozco, Identification of novel compositions of ferromagnetic shape-memory alloys using composition spreads, Nat Mater 2 (2003) 180-184.

[57] T. Krenke, X. Moya, S. Aksoy, M. Acet, P. Entel, L. Manosa, A. Planes, Y. Elerman, A. Yucel, E.F. Wassermann, Electronic aspects of the martensitic transition in Ni-Mn based Heusler alloys, J Magn Magn Mater 310 (2007) 2788-2789.

[58] P. Entel, S. Sahoo, M. Siewert, M.E. Gruner, H.C. Herper, D. Comtesse, M. Acet, V.D. Buchelnikov, V.V. Sokolovskiy, First-principles investigations of caloric effects in ferroic materials, AIP Conf Proc 1461 (2012) 11-23.

[59] I. Dvorak, E.B. Hawbolt, Transformational elasticity in a polycrystalline Cu-Zn-Sn alloy, Metall Trans 6 (1975) 95-99.

[60] M. Somerday, R.J. Comstock, J.A. Wert, Effect of grain size on the observed pseudoelastic behavior of a Cu-Zn-Al shape memory alloy, Metall Mater Trans A 28 (1997) 2335-2341.

[61] M. Ahlers, R. Pascual, R. Rapacioli, W. Arneodo, Transformation hardening and energy-dissipation in martensitic beta-brass, Mater Sci Eng 27 (1977) 49-55.

[62] R.J. Cohen and M. Salzbrenner, On the thermodynamics of thermoelastic martensitic transformations, Acta Metall Mater 27 (1978) 739-748.

[63] J.A. Monroe, J. Cruz-Perez, C. Yegin, I. Karaman, A.B. Geltmacher, R.K. Everett, R. Kainuma, Magnetic response of porous NiCoMnSn metamagnetic shape memory alloys fabricated using solid-state replication, Scripta Mater 67 (2012) 116-119.

[64] J. Liu, T.G. Woodcock, N. Scheerbaum, O. Gutfleisch, Influence of annealing on magnetic field-induced structural transformation and magnetocaloric effect in Ni-Mn-In-Co ribbons, Acta Mater 57 (2009) 4911-4920.

[65] J.H. Huang and E. Rosen, Determination of gibbs free-energies of formation for the silicates MnSiO3, Mn2SiO4 and Mn7SiO12 in the temperature-range 1000-1350-K by solid-state emf-measurements, Phys Chem Miner 21 (1994) 228-233.

[66] T.B. Reed, Free energy of formation of binary compounds, Cambridge, MA; M.I.T. Press, (1971).

[67] V. Recarte, J.I. Perez-Landazabal, V. Sanchez-Alarcos, V. Zablotskii, E. Cesari, S. Kustov, Entropy change linked to the martensitic transformation in metamagnetic shape memory alloys, Acta Mater 60 (2012) 3168-3175.

[68] A. Planes, L. Manosa, E. Vives, J. Rodriguez-Carvajal, M. Morin, G. Guenin, J.L. Macqueron, Neutron-Diffraction Study of Long-Range Atomic Order in Cu-Zn-Al Shape Memory Alloys, J Phys-Condens Mat 4 (1992) 553-559.

[69] W. Ito, M. Nagasako, R.Y. Umetsu, R. Kainuma, T. Kanomata, K. Ishida, Atomic ordering and magnetic properties in the Ni45Co5Mn36.7In13.3 metamagnetic shape memory alloy, Appl Phys Lett 93 (2008) 232503.

[70] T. Fukuda, T. Kakeshita, Y.H. Lee, An interpretation of the kinetics of martensitic transformation in a Ni45Co5Mn36.5In13.5 alloy, Acta Mater 81 (2014) 121-127.

[71] N.A. de Oliveira, P.J. von Ranke, Physics Reports 489 (2010) 89-159.

[72] W. Ito, K. Ito, R.Y. Umetsu, R. Kainuma, K. Koyama, K. Watanabe, A. Fujita, K. Oikawa, K. Ishida, T. Kanomata, Kinetic arrest of martensitic transformation in the NiCoMnIn metamagnetic shape memory alloy, Appl Phys Lett 92 (2008) 021908.

[73] Y. Murakami, K. Yanagisawa, K. Niitsu, H.S. Park, T. Matsuda, R. Kainuma, D. Shindo, A. Tonomura, Determination of magnetic flux density at the nanometer-scale antiphase boundary in Heusler alloy Ni50Mn25Al12.5Ga12.5, Acta Mater 61 (2013) 2095-2101.

[74] S.M. Allen, J.W. Cahn, Microscopic theory for antiphase boundary motion and its application to antiphase domain coarsening, Acta Metall Mater 27 (1979) 1085-1095.

[75] D.Z. Wu, S.C. Xue, J. Frenzel, G. Eggeler, Q.J. Zhai, H.X. Zheng, Atomic ordering effect in Ni50Mn37Sn13 magnetocaloric ribbons, Mat Sci Eng a-Struct 534 (2012) 568-572.

[76] S. Aksoy, M. Acet, P.P. Deen, L. Manosa, A. Planes, Magnetic correlations in martensitic Ni-Mn-based Heusler shape-memory alloys: Neutron polarization analysis, Phys Rev B 79 (2009) 212401.

[77] L. Tan, A. Kreyssig, S. Nandi, S. Jia, Y.B. Lee, J.C. Lang, Z. Islam, T.A. Lograsso, D.L. Schlagel, V.K. Pecharsky, K.A. Gschneidner, P.C. Canfield, B.N. Harmon, R.J. McQueeney, A.I. Goldman, Spin-flop transition in Gd(5)Ge(4) observed by x-ray resonant magnetic scattering and first-principles calculations of magnetic anisotropy, Phys Rev B 77 (2008) 064425.

[78] R. Caballero-Flores, T. Sanchez, W.O. Rosa, J. Garcia, L. Gonzalez-Legarreta, D. Serantes, V.M. Prida, L. Escoda, J.J. Sunol, B. Hernando, On tuning the magnetocaloric effect in Ni-Mn-In Heusler alloy ribbons with thermal treatment, J Alloy Compd 545 (2012) 216-221.

[79] J.H. Chen, N.M. Bruno, I. Karaman, Y.J. Huang, J.G. Li, J.H. Ross, Calorimetric and magnetic study for Ni50Mn36In14 and relative cooling power in paramagnetic inverse magnetocaloric systems, J Appl Phys 116 (2014) 203901.

[80] E. Stern-Taulats, P.O. Castillo-Villa, L. Manosa, C. Frontera, S. Pramanick, S. Majumdar, A. Planes, Magnetocaloric effect in the low hysteresis Ni-Mn-In metamagnetic shape-memory Heusler alloy, J Appl Phys 115 (2014) 173907.

[81] R.F. Hamilton, C. Efstathiou, H. Sehitoglu, Y. Chumlyakov, Thermal and stress-induced martensitic transformations in NiFeGa single crystals under tension and compression, Scripta Mater 54 (2006) 465-469.

[82] O. Heczko, S. Fahler, T.M. Vasilchikova, T.N. Voloshok, K.V. Klimov, Y.I. Chumlyakov, A.N. Vasiliev, Thermodynamic, kinetic, and magnetic properties of a Ni(54)Fe(19)Ga(27) magnetic shape-memory single crystal, Phys Rev B 77 (2008) 174402.

[83] M.K. Chattopadhyay, V.K. Sharma, S.B. Roy, Thermomagnetic history dependence of magnetocaloric effect in Ni(50)Mn(34)In(16), Appl Phys Lett 92 (2008) 022503.

[84] H. Seiner, J. Kopecek, P. Sedlak, L. Bodnarova, M. Landa, P. Sedmak, O. Heczko, Microstructure, martensitic transformation and anomalies in c '-softening in Co-Ni-Al ferromagnetic shape memory alloys, Acta Mater 61 (2013) 5869-5876.

[85] I.V. Kireeva, C. Picornell, J. Pons, I.V. Kretinina, Y.I. Chumlyakov, E. Cesari, Effect of oriented gamma ' precipitates on shape memory effect and superelasticity in Co-Ni-Ga single crystals, Acta Mater 68 (2014) 127-139.

A.1 Thermomagnetic history of $Ni_{48}Mn_{38}In_{14}$ alloys

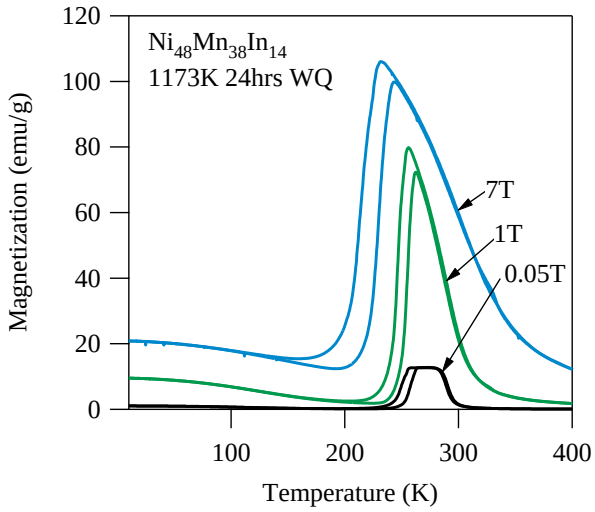

Figure A1: Thermomagnetic response of SHT $Ni_{48}Mn_{38}In_{14}$ (at.%) polycrystals under 0.05T, 1T, and 7T. Samples were heated to 400K under zero field and were then field cooled (FC) and field heated (FH).

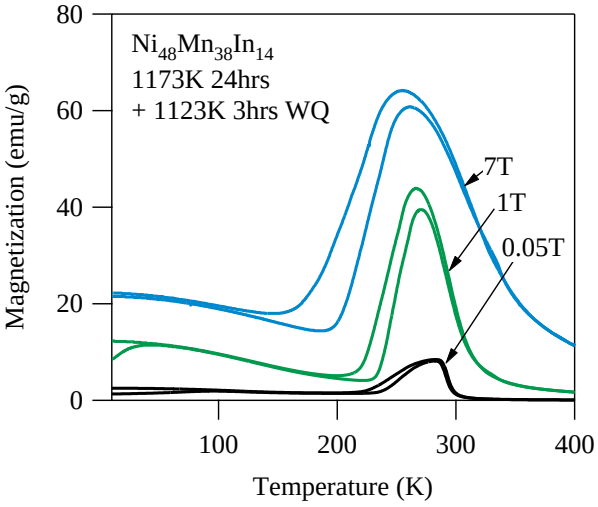

Figure A2: Thermomagnetic response of SHT + 1123K 3hrs WQ $Ni_{48}Mn_{38}In_{14}$ (at.%) polycrystals under 0.05T, 1T, and 7T. Samples were cooled to 10K under zero field (ZFC). The field was then applied and the temperature was increased to 400K under field. The sample was subsequently cooled in field (FC).

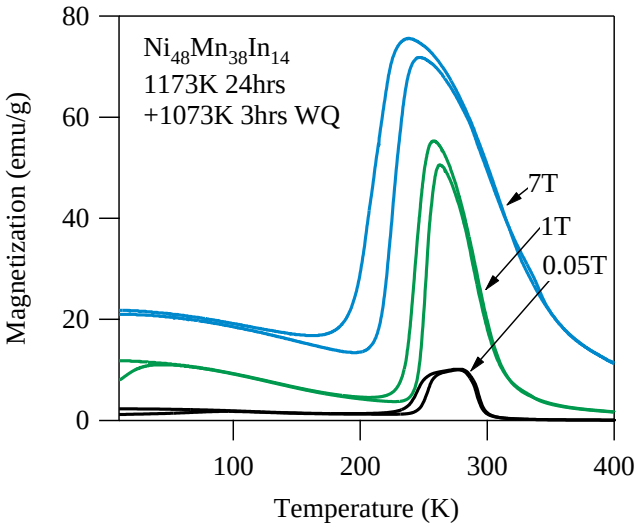

Figure A3: Thermomagnetic response of SHT + 1073K 3hrs WQ $Ni_{48}Mn_{38}In_{14}$ (at.%) polycrystals under 0.05T, 1T, and 7T. Samples were cooled to 10K under zero field (ZFC). The field was then applied and the temperature was increased to 400K under field. The sample was subsequently cooled in field (FC).

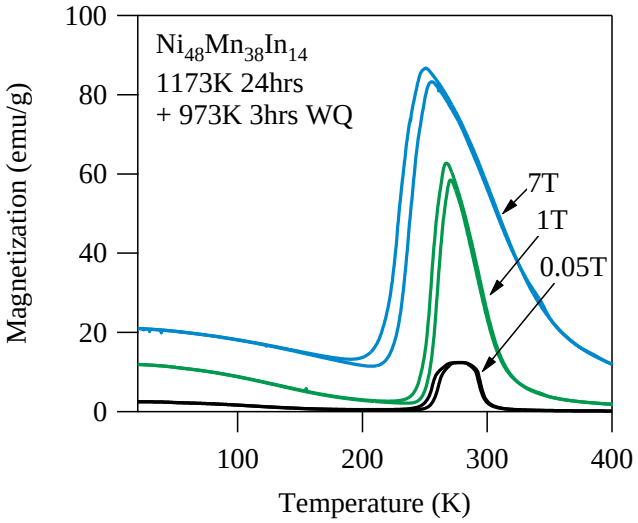

Figure A4: Thermomagnetic response of SHT + 973K 3hrs WQ $Ni_{48}Mn_{38}In_{14}$ (at.%) polycrystals under 0.05T, 1T, and 7T. Samples were heated to 400K under zero field and were then field cooled (FC) and field heated (FH).

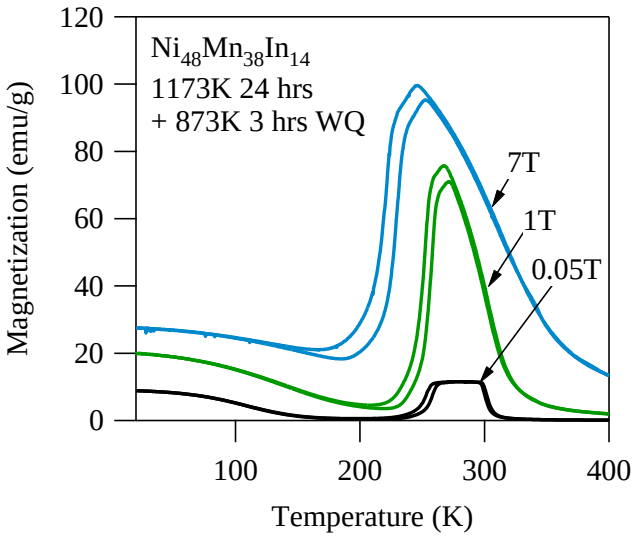

Figure A5: Thermomagnetic response of SHT + 873K 3hrs WQ $Ni_{48}Mn_{38}In_{14}$ (at.%) polycrystals under 0.05T, 1T, and 7T. Samples were heated to 400K under zero field and were then field cooled (FC) and field heated (FH).

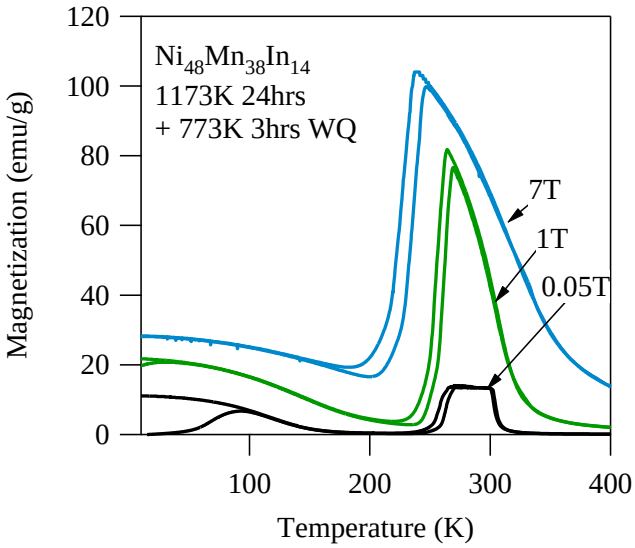

Figure A6: Thermomagnetic response of SHT + 773K 3hrs WQ $Ni_{48}Mn_{38}In_{14}$ (at.%) polycrystals under 0.05T, 1T, and 7T. Samples were cooled to 10K under zero field (ZFC). The field was then applied and the temperature was increased to 400K under field. The sample was subsequently cooled in field (FC).

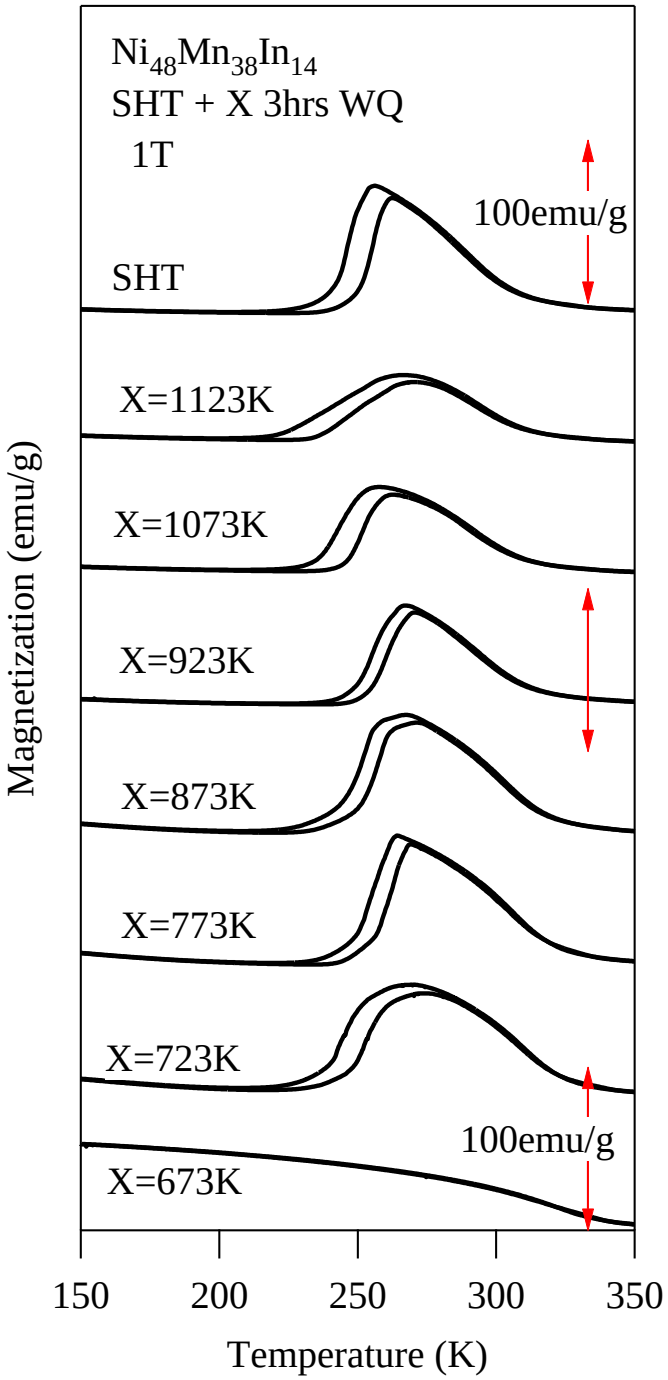

Figure A7: Thermomagnetic responses of heat treated $Ni_{48}Mn_{38}In_{14}$ (at.%) polycrystals under 1T. Samples were heated to 400K under zero field and were then field cooled (FC) and field heated (FH).

Thermomagnetic history of Ni50Mn36In14

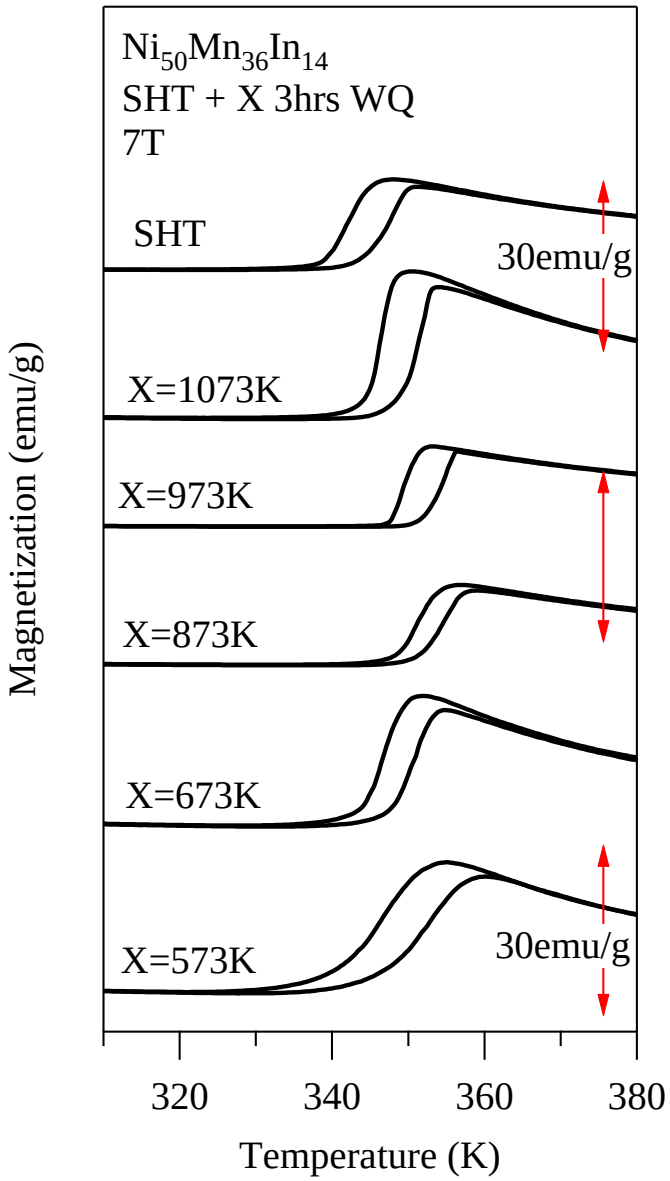

Figure A8: Thermomagnetic responses of heat treated $Ni_{50}Mn_{36}In_{14}$ (at.%) polycrystals under 7T. Samples were heated to 400K under zero field and were then field cooled (FC) and field heated (FH).

Thermomagnetic history of $Ni_{45}Co_5Mn_{36.6}In$ heat treated alloys

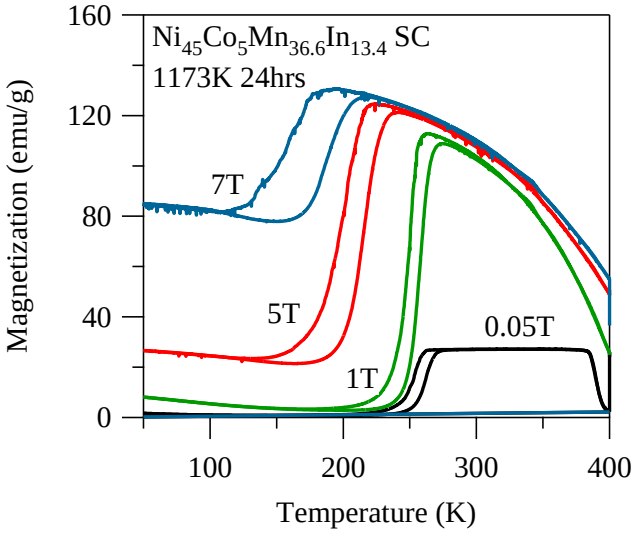

Figure A9: Thermomagnetic response of SHT $Ni_{45}Co_5Mn_{36.6}In_{13.4}$ (at.%) single crystals under 0.05T, 1T, 5T, and 7T. Samples were heated to 400K under zero field and were then field cooled (FC) and field heated (FH).

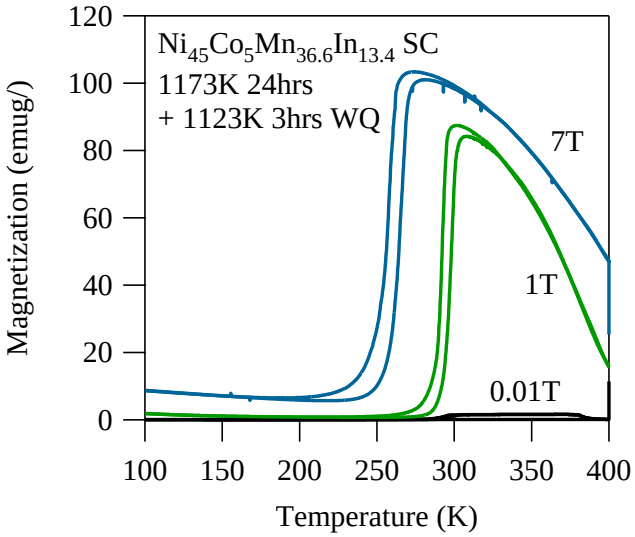

Figure A10: Thermomagnetic response of SHT + 1123K 3hrs WQ $Ni_{45}Co_5Mn_{36.6}In_{13.4}$ (at.%) single crystals under 0.01T, 1T, and 7T. Samples were heated to 400K under zero field and were then field cooled (FC) and field heated (FH).

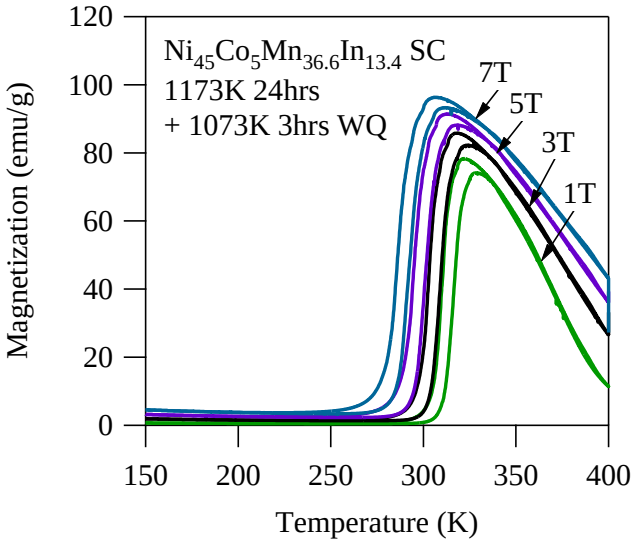

Figure A11: Thermomagnetic response of SHT + 1073K 3hrs WQ $Ni_{45}Co_5Mn_{36.6}In_{13.4}$ (at.%) single crystals under 0.01T, 1T, and 7T. Samples were heated to 400K under zero field and were then field cooled (FC) and field heated (FH).

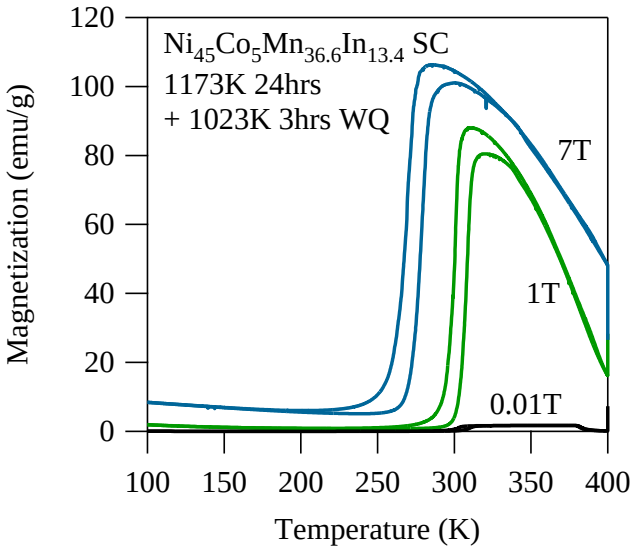

Figure A12: Thermomagnetic response of SHT + 1023K 3hrs WQ $Ni_{45}Co_5Mn_{36.6}In_{13.4}$ (at.%) single crystals under 0.01T, 1T, and 7T. Samples were heated to 400K under zero field and were then field cooled (FC) and field heated (FH).

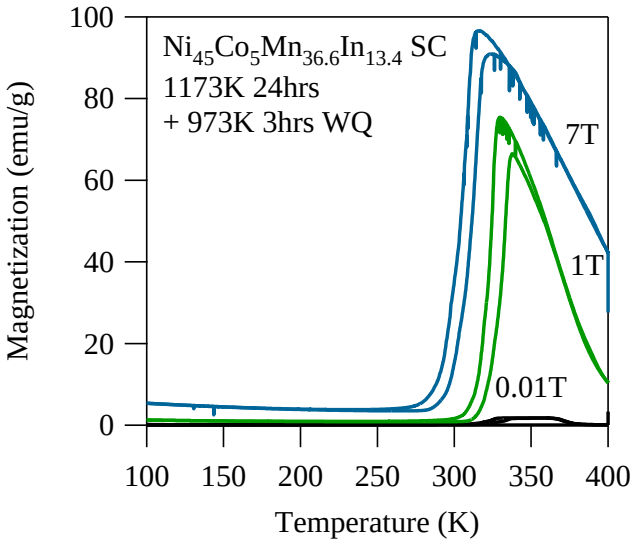

Figure A13: Thermomagnetic response of SHT + 973K 3hrs WQ $Ni_{45}Co_5Mn_{36.6}In_{13.4}$ (at.%) single crystals under 0.01T, 1T, and 7T. Samples were heated to 400K under zero field and were then field cooled (FC) and field heated (FH).

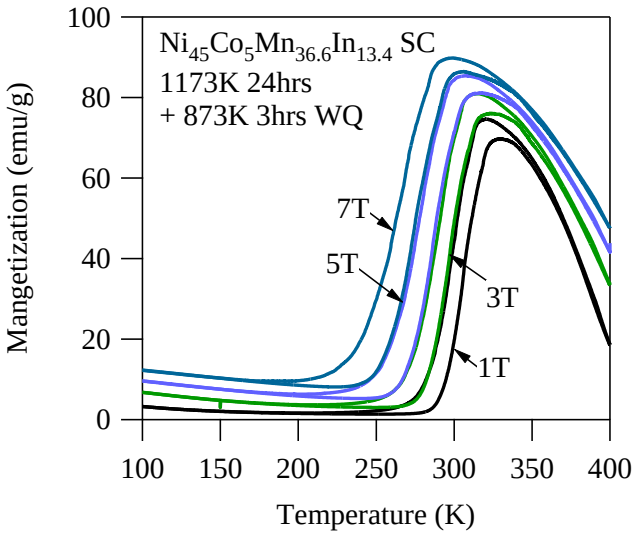

Figure A14: Thermomagnetic response of SHT + 873K 3hrs WQ $Ni_{45}Co_5Mn_{36.6}In_{13.4}$ (at.%) single crystals under 1T, 3T, 5T,and 7T. Samples were heated to 400K under zero field and were then field cooled (FC) and field heated (FH).

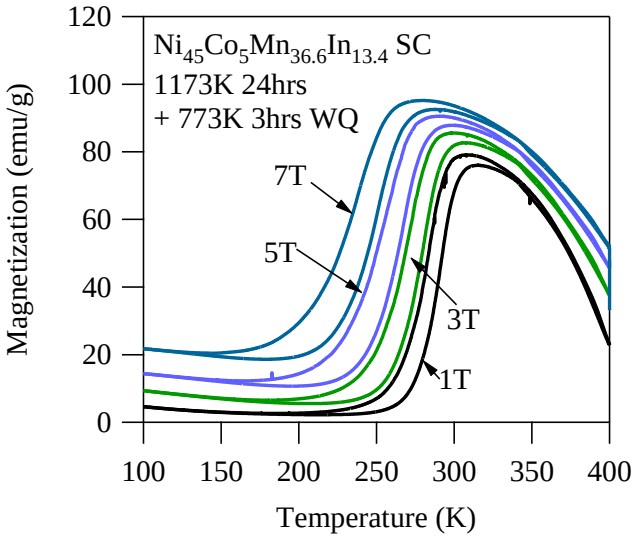

Figure A15: Thermomagnetic response of SHT + 773K 3hrs WQ $Ni_{45}Co_5Mn_{36.6}In_{13.4}$ (at.%) single crystals under 1T, 3T, 5T,and 7T. Samples were heated to 400K under zero field and were then field cooled (FC) and field heated (FH).

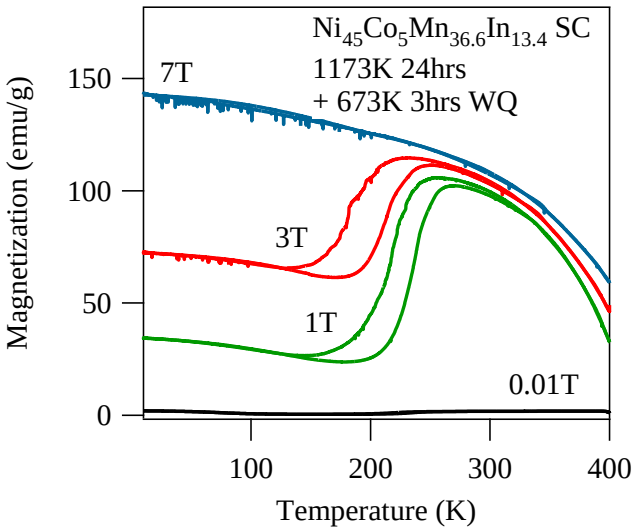

Figure A16: Thermomagnetic response of SHT + 673K 3hrs WQ $Ni_{45}Co_5Mn_{36.6}In_{13.4}$ (at.%) single crystals under 0.01T, 1T, 3T,and 7T. Samples were heated to 400K under zero field and were then field cooled (FC) and field heated (FH).

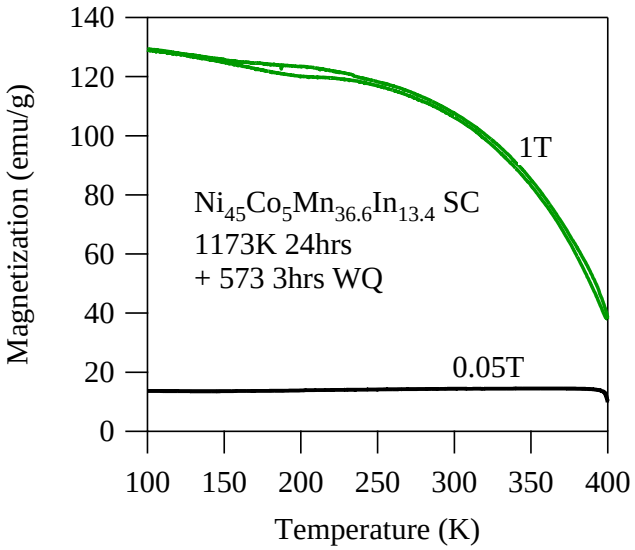

Figure A17: Thermomagnetic response of SHT + 573K 3hrs WQ $Ni_{45}Co_5Mn_{36.6}In_{13.4}$ (at.%) single crystals under 0.05T and 1T. Samples were heated to 400K under zero field and were then field cooled (FC) and field heated (FH).

Isofield Stress-Strain response of Ni45Co5Mn36.6In13.4 SHT single crystals along the [001] austenite crystal direction

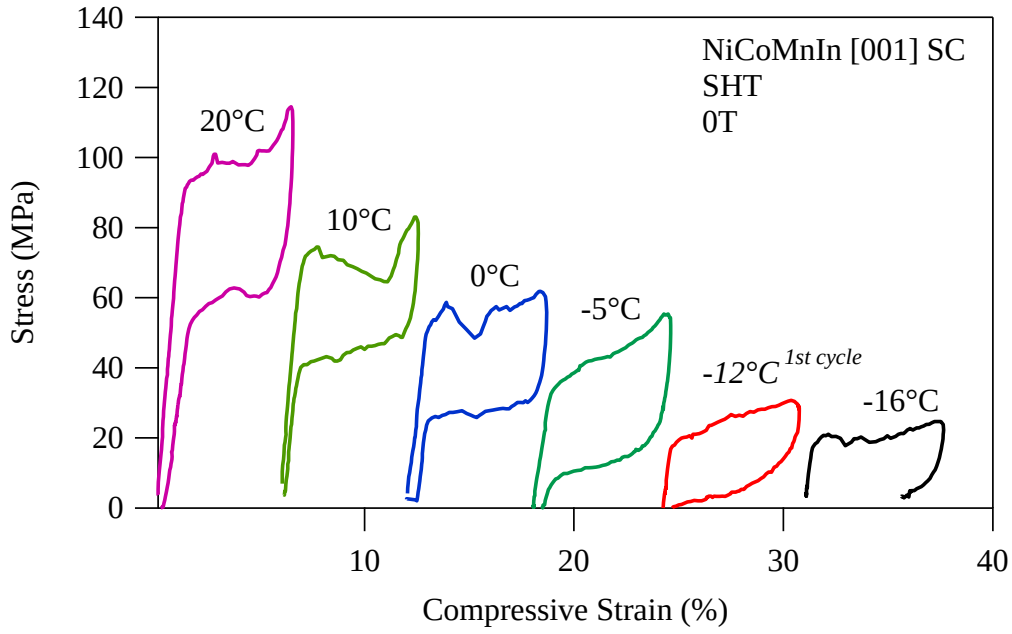

Figure A18: Superelastic compression response of SHT $Ni_{45}Co_5Mn_{36.6}In_{13.4}$ (at.%) in the [001] austenite direction under 0T at 20°C, 10°C, 0°C, -5°C, -12°C, and -16°C.

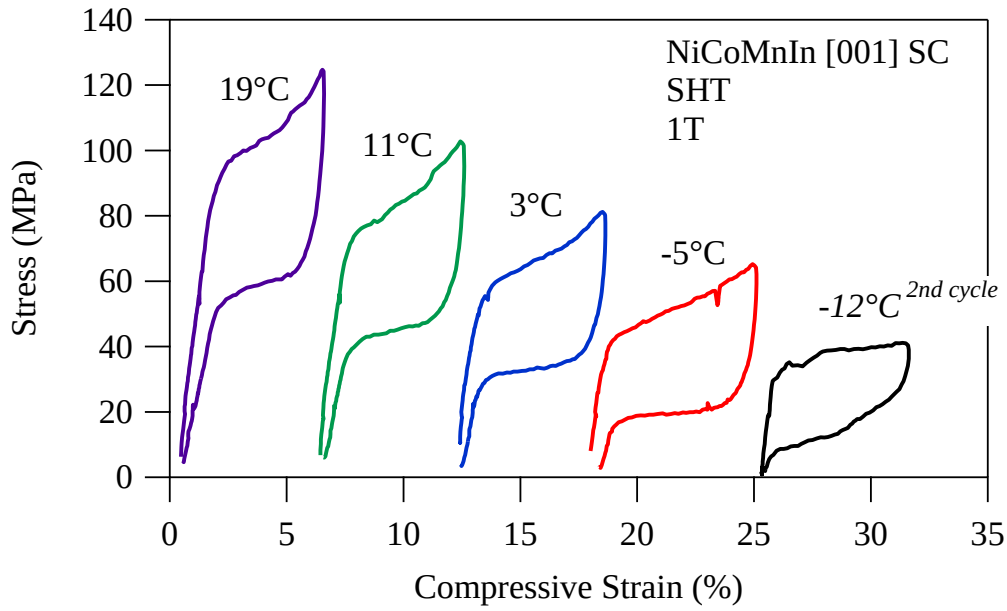

Figure A19: Superelastic compression response of SHT $Ni_{45}Co_5Mn_{36.6}In_{13.4}$ (at.%) in the [001] austenite direction under 1T at 19°C, 11°C, 3°C, -5°C, and -12°C.

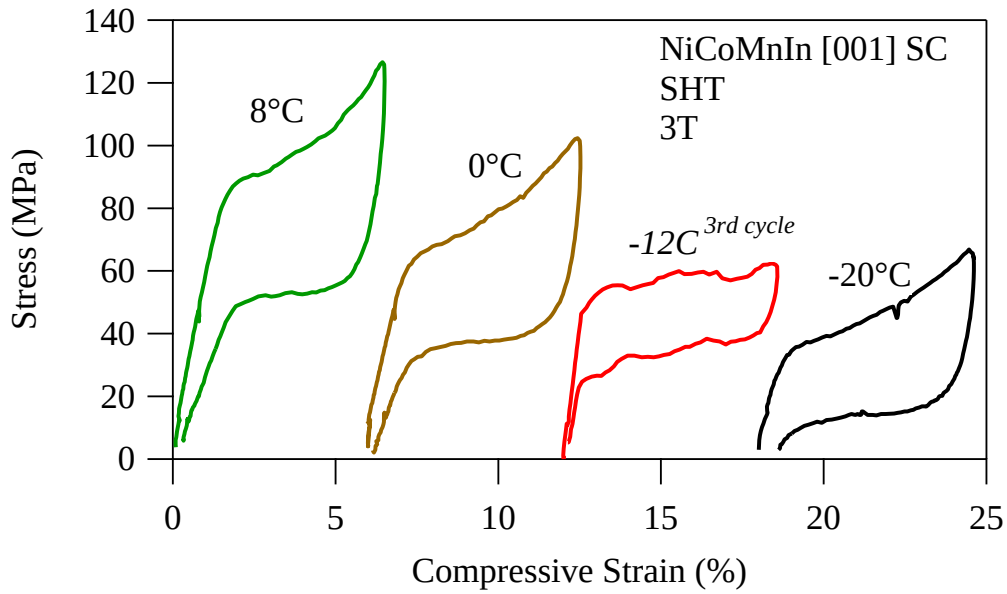

Figure A20: Superelastic compression response of SHT $Ni_{45}Co_5Mn_{36.6}In_{13.4}$ (at.%) in the [001] austenite direction under 3T at 8°C, 0°C, -12°C, and -20°C.

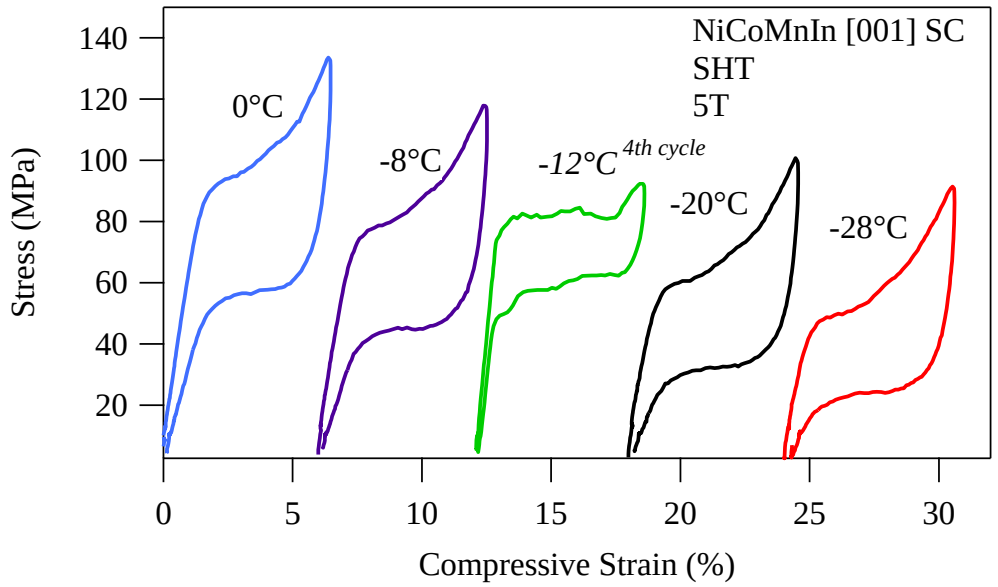

Figure A21: Superelastic compression response of SHT $Ni_{45}Co_5Mn_{36.6}In_{13.4}$ (at.%) in the [001] austenite direction under 5T at 0°C, -8°C, -12°C, -20°C, and -28°C.

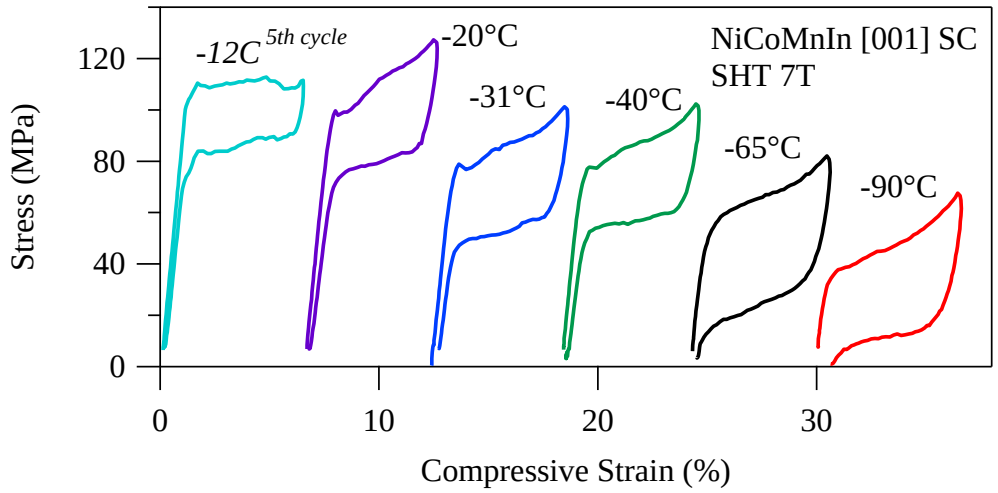

Figure A22: Superelastic compression response of SHT $Ni_{45}Co_5Mn_{36.6}In_{13.4}$ (at.%) in the [001] austenite direction under 7T at -12°C, -20°C, -31°C, -40°C, -65°C , and -90°C.

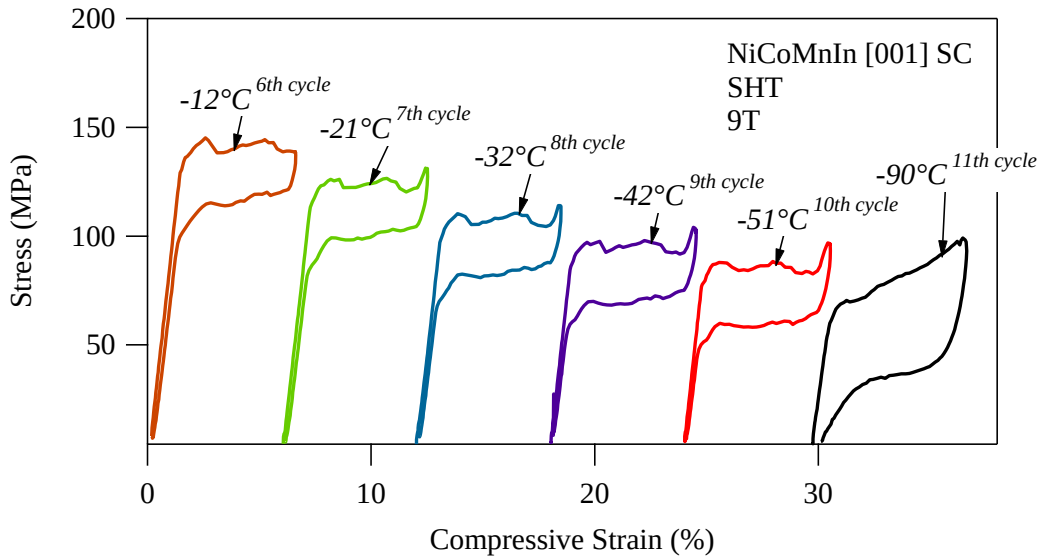

Figure A23: Superelastic compression response of SHT $Ni_{45}Co_5Mn_{36.6}In_{13.4}$ (at.%) in the [001] austenite direction under 9T at -12°C, -21°C, -32°C, -42°C, -51°C , and -90°C.

Isofield Stress-Strain response of $Ni_{45}Co_5Mn_{36.6}In_{13.4}$ SHT+600°C 30min single crystals along the [001] austenite crystal direction

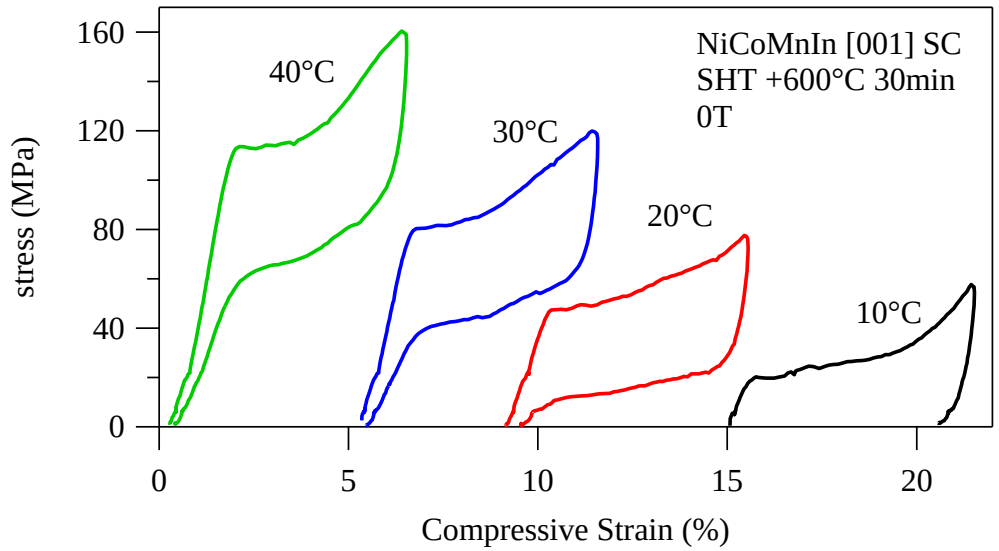

Figure A24: Superelastic compression response of SHT + 600°C 30min $Ni_{45}Co_5Mn_{36.6}In_{13.4}$ (at.%) in the [001] austenite direction under 0T at 40°C, 30°C, 20°C, and 10°C.

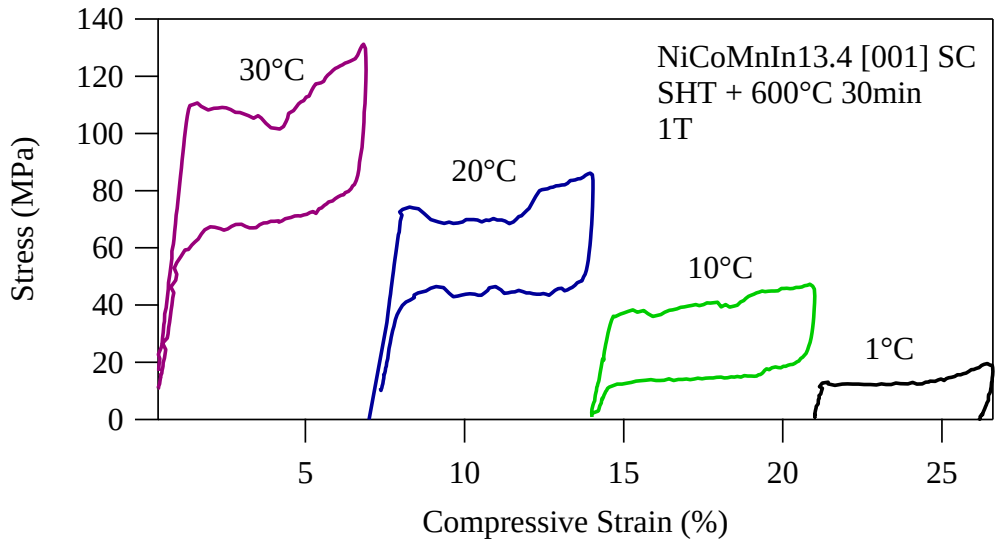

Figure A25: Superelastic compression response of SHT + 600°C 30min $Ni_{45}Co_5Mn_{36.6}In_{13.4}$ (at.%) in the [001] austenite direction under 1T at 30°C, 20°C, 10°C, and 1°C.

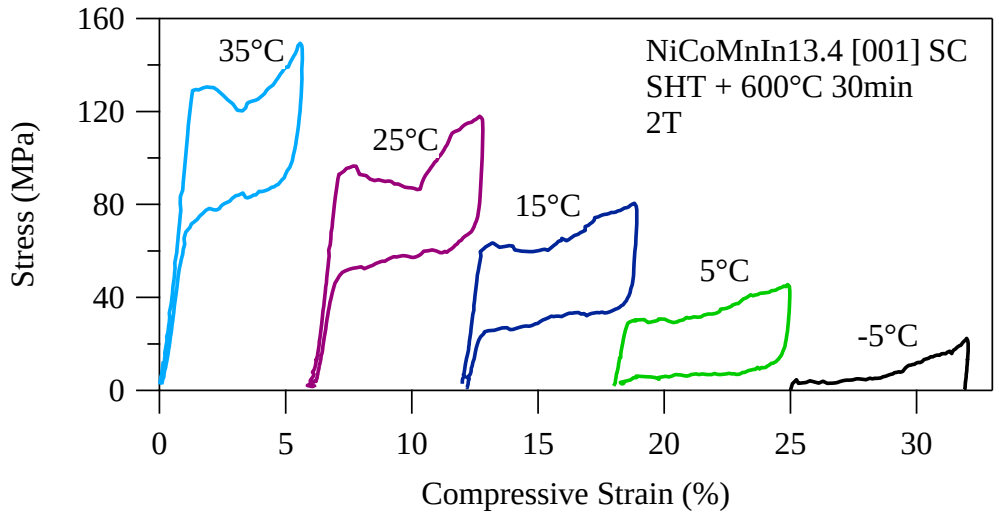

Figure A26: Superelastic compression response of SHT + 600°C 30min $Ni_{45}Co_5Mn_{36.6}In_{13.4}$ (at.%) in the [001] austenite direction under 2T at 35°C, 25°C, 15°C, 5°C, and -5°C.

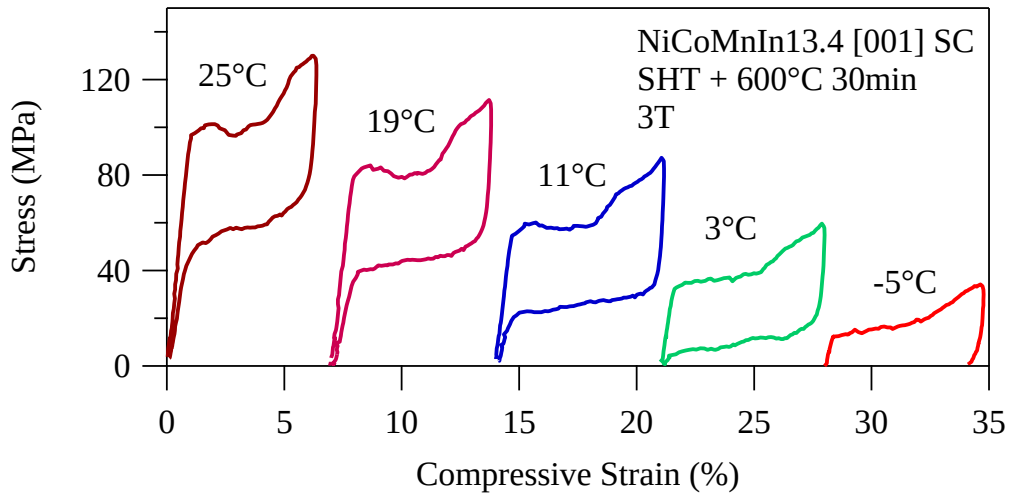

Figure A27: Superelastic compression response of SHT + 600°C 30min $Ni_{45}Co_5Mn_{36.6}In_{13.4}$ (at.%) in the [001] austenite direction under 3T at 25°C, 19°C, 11°C, 3°C, and -5°C.

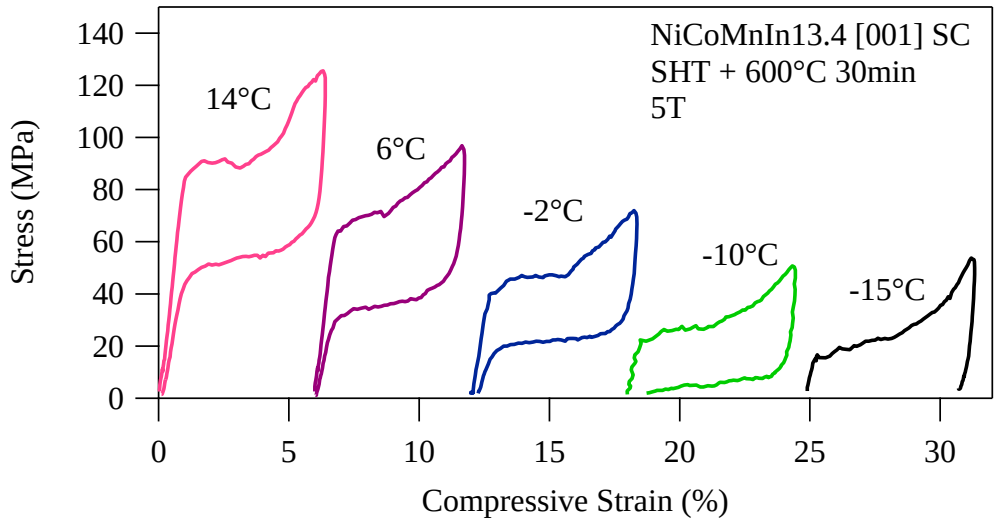

Figure A28: Superelastic compression response of SHT + 600°C 30min $Ni_{45}Co_5Mn_{36.6}In_{13.4}$ (at.%) in the [001] austenite direction under 5T at 14°C, 6°C, -2°C, -10°C, and -15°C.

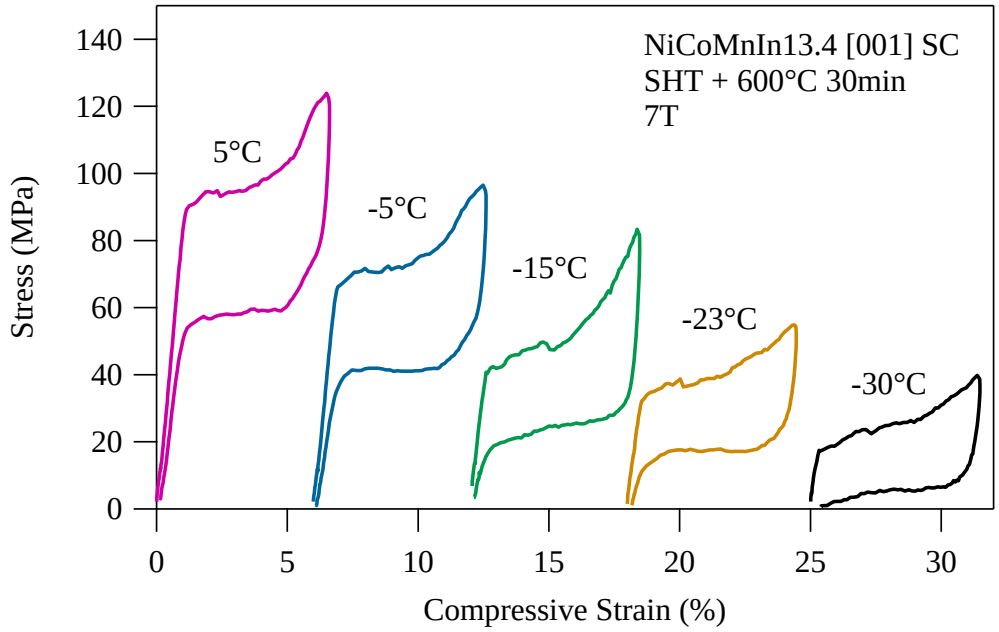

Figure A29: Superelastic compression response of SHT + 600°C 30min $Ni_{45}Co_5Mn_{36.6}In_{13.4}$ (at.%) in the [001] austenite direction under 7T at 5°C, -5°C, -15°C, -23°C, and -30°C.

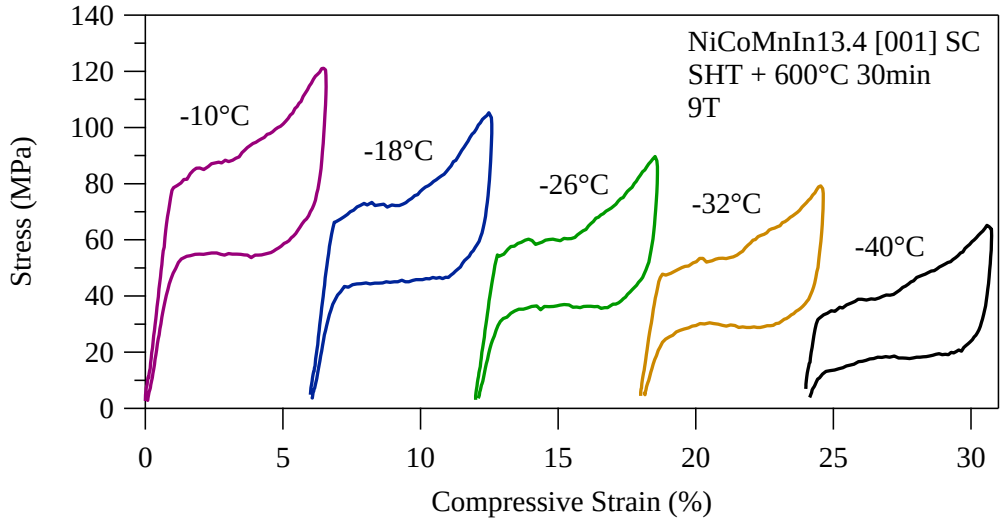

Figure A30: Superelastic compression response of SHT + 600°C 30min $Ni_{45}Co_5Mn_{36.6}In_{13.4}$ (at.%) in the [001] austenite direction under 9T at -10°C, -18°C, -26°C, -32°C, and -40°C.

Table of Replacement parts for MaTMeCh Device

Table A1: Replacement parts for MaTMeCh apparatus

Company	Item Description	Product #	Qty.	Unit Price	Total Price
Mechatronic Techniques Inc.	Linear Actuator	Custom	1	8167	8167.5
Conax Technologies	6 T type thermocouple vacuum feedthrough	HD18-450(6K)MPGAT,24/24	1	449	449
Conax Technologies	12 copper lead wire vacuum feedthrough	HD18-450(12CU)MPGAT,24/24	1	449	449
Omega Engineering	(24BIT USB 16SE/8DE CH MODCE)	OMB-DAQ-2408	1	599	599
Omega Engineering	1/16 DIN RAMP & SOAK CTRL	CN8202-R1-R2-AL1	1	3.69	369
Engineered Spring Products	0.147 Titanium Spring	Custom	3	125	375
Bass Tool & Supply	NTK TNG-43 SX5 T0220 CERAMIC INSERT	RNG-43-SX5	3	13.12	39.36
Palma Tool & Die	TOP CAP	Custom	1	2361	2361
Palma Tool & Die	TOP ROD	Custom	1	554	554
Palma Tool & Die	PROBE ARMS (PAIR)	Custom	1	834	834
Palma Tool & Die	SPINE	Custom	1	86	86
Palma Tool & Die	SIDES (PAIR)	Custom	2	59	118
Palma Tool & Die	ARM RODS	Custom	4	63.5	254
Palma Tool & Die	THREADED ARM RODS	Custom	2	318.5	637
Palma Tool & Die	SEAT	Custom	1	992	992
Palma Tool & Die	BOTTOM ROD	Custom	1	970	970
Palma Tool & Die	BOTTOM CAP	Custom	1	3416	3416
Palma Tool & Die	BOTTOM PLATE	Custom	1	698	698
Palma Tool & Die	BASE PLATE	Custom	1	503	503
Palma Tool & Die	TUBE	Custom	1	3376	3376
Palma Tool & Die	Bottom Rod	Custom	1	215	215

Palma Tool & Die	Upper Rod	Custom	1	525	525
Bomas Machine	Al2O3 Ceramic Seat	Custom	5	78	390
McMaster-Carr	18-8 Stainless Steel Low Head Socket Cap Screw	93615A410	1	5.93	5.93
McMaster-Carr	Type 316 Stainless Steel 37 Degree Flared Tube Fitting	50715K162	2	11.25	22.5
McMaster-Carr	Bronze Precision Acme Round Nut	95072A109	3	32.92	98.76
McMaster-Carr	Type 316 Stainless Steel General Purpose Acme Threaded Rod	97014A315	2	65.17	130.34
McMaster-Carr	Brass General Purpose Acme Square Nut	95270A114	3	6.89	20.67
McMaster-Carr	Easy-Bend Aluminum Tubing	5177K621	2	14.12	28.24
McMaster-Carr	Plastic Dowel Pin	97155A319	1	3.2	3.2
McMaster-Carr	Clean & Bagged Cryogenic Solenoid Valve	7902K41	1	245.4	245.41
McMaster-Carr	Ultra-Thin Heat Sheet	35475K363	3	43.64	130.92
McMaster-Carr	Buna-N O-Ring	9452K156	1	8.5	8.5
McMaster-Carr	Buna-N O-Ring	9452K126	1	11.31	11.31
McMaster-Carr	External Retaining Ring	98410A725	1	9.9	9.9
McMaster-Carr	Flexible White Tubing Made With Teflon PTFE	51155K42	1	13.7	13.7
McMaster-Carr	Pressure Transducer	3196K5	1	176.1	176.1
McMaster-Carr	Quick-Assembly Brass 45 Degree Flared Fitting	50635K511	3	3.48	10.44
McMaster-Carr	Dow Corning High-Vacuum Grease	2966K52	1	26.68	26.68
McMaster-Carr	Buna-N O-Ring	9452K185	1	4.15	4.15
McMaster-Carr	Type 316 SS 37 Degree Flared Tube Fitting Adapter	50715K162	2	7.53	15.06
McMaster-Carr	Bronze Precision Acme Round Nut	95072A109	3	32.92	98.76
McMaster-Carr	Type 316 SS General Purpose ACME Threaded Rod	97014A315	2	65.17	130.34
McMaster-Carr	Brass General Purpose Acme Square Nut	95270A114	3	6.89	20.67
McMaster-Carr	Brass General Purpose Acme Cylinder Nut	95100A103	2	5.94	11.88
McMaster-Carr	Miniature Metal-Handle Screwdriver	7026A11	1	5.71	5.71
McMaster-Carr	Nonmarring Tweezers	6182A22	1	38.51	38.51
McMaster-Carr	Formable 260 Brass, Rod, 3mm Diameter, 300mm long	88605K48	1	3.59	3.59
ChinaTiScrew.com/AliExpress	Titanium Screw M1.6X6 DIN 912 Socket Head		1	44	44
ChinaTiScrew.com/AliExpress	Titanium Screw M2.5X6 DIN 912 Socket Head		1	30	30

Gearmo	USB to RS485/RS422 Converter	GM-482422	1	42.94	42.94
		Approximate total cost of MATMECH			27765

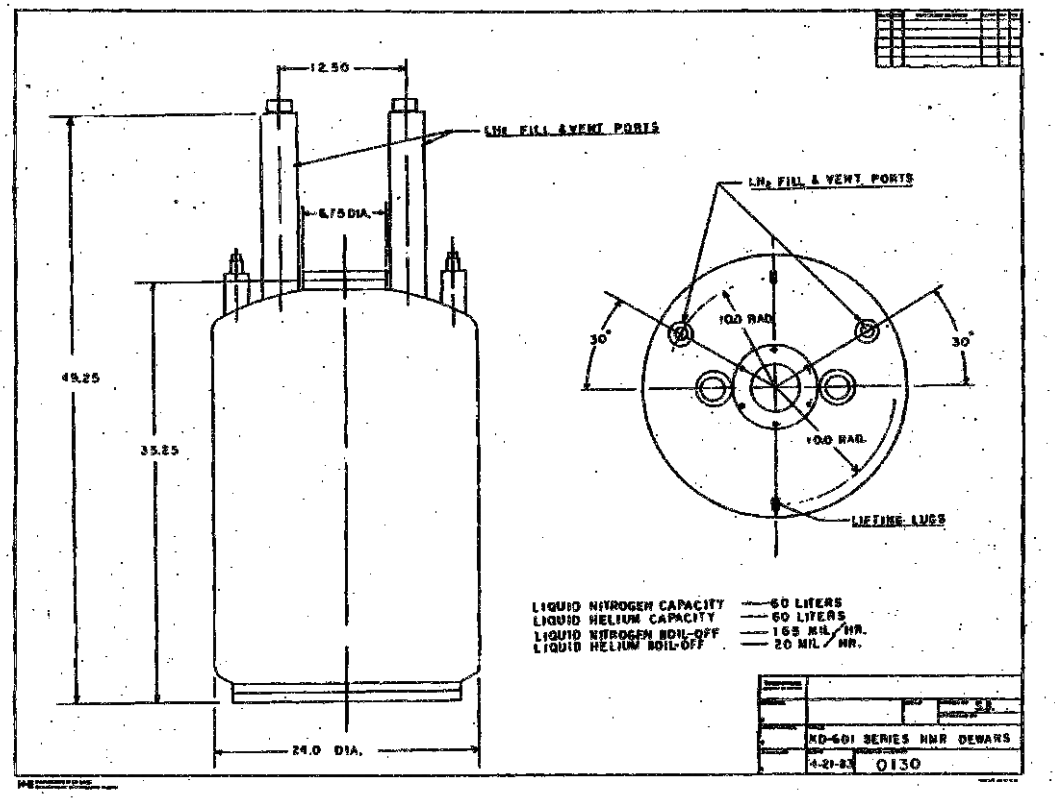

Figure A31: NMR magnet liquid helium dewar for MaTMeCh device design specifications.

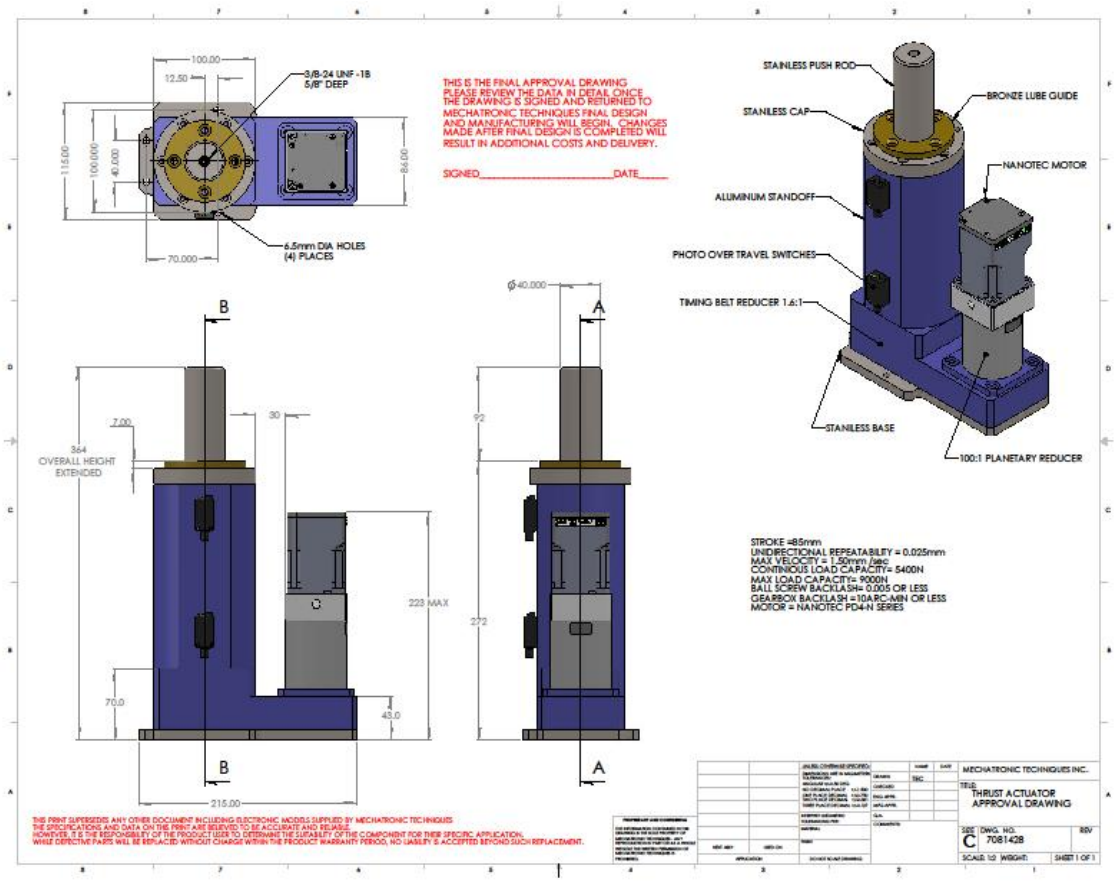

Figure A32: Approval drawing for custom spindle drive actuator for MaTMeCh apparatus.